HD

NATIONAL AERONAUTICS AND SPACE ADMINISTRATION

Space Programs Summary 37-51, Vol. II

The Deep Space Network

For the Period March 1 to April 30, 1968

GPO PRICE $ _____
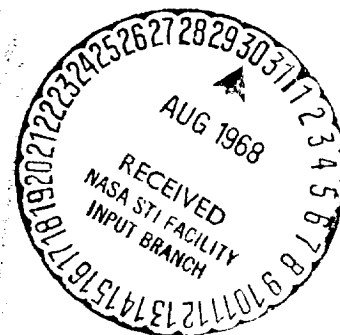
CFSTI PRICE(S) $ _____

Hard copy (HC) ___ *3-00*

Microfiche (MF) ___ *.65*

ff 653 July 65

JET PROPULSION LABORATORY
CALIFORNIA INSTITUTE OF TECHNOLOGY
PASADENA, CALIFORNIA

May 31, 1968

NATIONAL AERONAUTICS AND SPACE ADMINISTRATION

Space Programs Summary 37-51, Vol. II

The Deep Space Network

For the Period March 1 to April 30, 1968

JET PROPULSION LABORATORY
CALIFORNIA INSTITUTE OF TECHNOLOGY
PASADENA, CALIFORNIA

May 31, 1968

SPACE PROGRAMS SUMMARY 37-51, VOL. II

Preface

The Space Programs Summary is a bimonthly publication that presents a review of engineering and scientific work performed, or managed, by the Jet Propulsion Laboratory for the National Aeronautics and Space Administration during a two-month period. Beginning with the 37-47 series, the Space Programs Summary is composed of four volumes:

Vol. I.   *Flight Projects* (Unclassified)

Vol. II.   *The Deep Space Network* (Unclassified)

Vol. III.   *Supporting Research and Advanced Development* (Unclassified)

Vol. IV.   *Flight Projects and Supporting Research and Advanced Development* (Confidential)

Approved by:

W. H. Pickering, *Director*
Jet Propulsion Laboratory

Contents

Contents (contd)

Contents (contd)

Contents (contd)

I. Introduction

A. Description of the DSN

The Deep Space Network (DSN), established by the NASA Office of Tracking and Data Acquisition under the system management and technical direction of JPL, is responsible for two-way communications with unmanned spacecraft traveling approximately 10,000 mi from earth to interplanetary distances. It supports, or has supported, the following NASA deep space exploration projects: *Ranger, Surveyor, Mariner* Venus 1962, *Mariner* Mars 1964, *Mariner* Venus 67, and *Mariner* Mars 1969 (JPL); *Lunar Orbiter* (Langley Research Center); *Pioneer* (Ames Research Center); and *Apollo* (Manned Spacecraft Center), as backup to the Manned Space Flight Network (MSFN). The DSN is distinct from other NASA networks such as the MSFN, which has primary responsibility for tracking the manned spacecraft of the *Apollo* Project, and the Space Tracking and Data Acquisition Network (STADAN), which tracks earth-orbiting scientific and communications satellites.

The three basic functions performed by the DSN in support of each flight project are as follows:

(1) *Tracking.* Accomplished by radio communication with the spacecraft, tracking provides such metric data as angles, radial velocity, and range (distance from the earth to the spacecraft).

(2) *Data acquisition.* Using the same radio link, the data acquisition function consists of the recovery of information from the spacecraft in the form of telemetry, namely, the engineering measurements recorded by the spacecraft and the scientific data obtained by the onboard instruments.

(3) *Command.* Using the same radio link, the command function involves sending information to the spacecraft to initiate equipment which, for example, operates propulsion systems for changing the trajectory of the spacecraft, changes data transmission rate to earth, or reprograms onboard computers which determine the sequence of spacecraft engineering events.

The DSN can be characterized as a set of the following systems: (1) telemetry, (2) tracking, (3) command, (4) monitoring, (5) simulation, and (6) operations control. Alternately, it can be considered as being comprised of three facilities: the Deep Space Instrumentation Facility (DSIF), the Ground Communications Facility (GCF), and the Space Flight Operations Facility (SFOF).

The DSIF is a worldwide set of deep space stations (DSSs) that provide basic radio communications with spacecraft. These stations and the deep space communications complexes (DSCCs) they comprise are as follows:

Pioneer, Echo, and Mars DSSs (and Venus DSS, described later), comprising the Goldstone DSCC in California; Woomera, Tidbinbilla, and Booroomba[1] DSSs, comprising the Canberra DSCC in Australia; Johannesburg DSS in South Africa; and Robledo, Cebreros, and Rio Cofio[1] DSSs, comprising the Madrid DSCC in Spain. The overseas stations are normally staffed and operated by government agencies of the respective countries, with some assistance from U.S. support personnel.

In addition, the DSIF operates a spacecraft monitoring station at Cape Kennedy, which is used for verifying flight-spacecraft/DSN compatibility prior to launch, and a flight-project/tracking and data system interface laboratory at JPL, which is used during the development of the spacecraft to assure a design compatible with the network. A spacecraft guidance and command station on Ascension Island serves to track the spacecraft in the latter part of the launch trajectory while the spacecraft is relatively low in altitude.

To enable continuous radio contact with spacecraft, the stations are located approximately 120 deg apart in longitude; thus, a spacecraft in flight is always within the field-of-view of at least one station, and for several hours each day may be seen by two stations. Furthermore, since most spacecraft on deep space missions travel within 30 deg of the equatorial plane, the stations are located within latitudes of 45 deg north or south of the equator.

Radio contact with a spacecraft usually begins when the spacecraft is on the launch vehicle at Cape Kennedy, and it is maintained throughout the mission. The early part of the trajectory is covered by selected network stations of the Air Force Eastern Test Range (AFETR) which are managed by the Goddard Space Flight Center. Normally, two-way communications are established between the spacecraft and the DSN within 30 min after the spacecraft has been injected into lunar, interplanetary, or planetary flight. The Cape Kennedy DSS, having supported the preflight compatibility tests, monitors the spacecraft continuously during the launch phase until it passes over the local horizon. The deep space phase begins with acquisition by either the Johannesburg, Woomera, or Tidbinbilla DSS. These stations, with large antennas, low-noise phase-lock receiving systems, and high-power transmitters, provide radio communications to the end of the flight. By international agreement, the

[1] Not yet authorized.

radio frequencies assigned for these functions are 2290–2300 MHz for spacecraft-to-earth downlink data transmission and 2110–2120 MHz for earth-to-spacecraft command and uplink data transmission.

To maintain a state-of-the-art capability, research and advanced development work on new components and systems has been conducted continuously at JPL since the establishment of the DSN. To support this work, the Goldstone DSCC has a research and development facility designated the Venus DSS, at which the feasibility of new equipment and techniques to be introduced into the operational network is demonstrated. When a new piece of equipment or new technique has been accepted for integration into the network, it is classed as Goldstone duplicate standard (GSDS), thus standardizing the design and operation of identical items throughout the network.

The GCF, using, in part, facilities of the worldwide NASA Communications Facility (NASCOM, managed and directed by the Goddard Space Flight Center), provides voice, high-speed data, and teletype communications between all stations of the network. Communications between the Goldstone DSCC and the SFOF are provided by a microwave system leased from common carriers. This microwave link has made possible the transmission, in real time, of video data received at the Goldstone DSCC to the SFOF and then to commercial TV systems, as was done during the *Ranger* and *Surveyor* missions.

The SFOF, located at JPL, receives data from all of the tracking stations and processes that information required by the flight project to conduct flight operations. Voice and data channels are distributed throughout the facility, and the following equipment and services are provided: (1) data-processing equipment for the real-time handling and display of tracking and telemetry data; (2) real-time and non-real-time telemetry processing; (3) simulation equipment for flight projects, as well as for network use in training of personnel; (4) monitoring equipment for evaluation of network performance in near-real time; (5) operations control consoles and status and operational display facilities required for the conduct of flight operations; and (6) technical areas for flight project personnel who analyze spacecraft performance, trajectories, and generation of commands, as well as support services required to carry out those functions, such as internal communications by telephone, intercom, public address, closed-circuit TV, documentation, and

reproduction of data packages. The SFOF is equipped to support many spacecraft in flight and those under test in preparation for flight; e.g., over a 24-h period during 1967, as many as eight spacecraft in flight or in operational-readiness tests for flight were supported by the SFOF.

Thus, the DSN simultaneously conducts research and development for support of future flight projects, implements demonstrated capabilities for support of the more immediate flight projects, and provides direct support for the currently active missions, while accommodating differences in the individual projects. In this and future issues of the SPS, Vol. II, the current technical activities of the DSN in these three general categories will be reported under the following subject areas:

Introduction
    Description of the DSN
    Description of DSN Systems

Mission Support
    Introduction
    Interplanetary Flight Projects
    Planetary Flight Projects
    Manned Space Flight Project

Advanced Engineering
    Tracking and Navigational Accuracy Analysis
    Communications System Research
    Tracking and Data Acquisition Elements Research
    Supporting Research and Technology

Development and Implementation
    SFOF Development
    GCF Development
    DSIF Development
    DSN Project and System Development

Operations and Facilities
    DSN Operations and Analyses
    SFOF Operations
    GCF Operations
    DSIF Operations
    Facility Engineering

In the subsection entitled "Description of DSN Systems," the status of recent developments for each of the six DSN systems listed above will be described. The more fundamental research carried out in support of the DSN is reported in Vol. III of the SPS, and JPL flight project activities for those missions supported by the DSN are reported in Vol. I.

B. Description of DSN Systems

1. Tracking Data System, R. E. Holzman

a. Functions. The DSN tracking data system (TDS) consists of those elements of the DSN which provide validated ultra-accurate tracking data to the flight projects, as well as prediction information necessary for continued acquisition of the spacecraft signal. The general functions performed to provide these data are tracking data acquisition, data handling, data transmission, and data processing. Figure 1 shows the general tracking data flow. The functions are almost totally project-independent; differences from project to project are manifested as differences in configuration, rather than differences in processing.

b. System elements. The physical subsystems of the DSIF that are part of, or contribute to the operation of, the TDS are (Fig. 2):

(1) DSS receiver subsystem.

(2) Ranging subsystem.

(3) Servo subsystem.

(4) Antenna pointing subsystem.

(5) Frequency and timing subsystem.

(6) Tracking data handling subsystem.

Those of the GCF are:

(1) DSS/GCF interface equipment.

(2) Teletype channels of NASCOM.

(3) SFOF/GCF interface equipment.

Those of the SFOF are (Fig. 3):

(1) IBM 7044 input/output processor.

(2) IBM 7044 pseudo-residual processor.

(3) IBM 7094 mission-independent editor.

(4) Tracking data processor.

(5) Prediction program.

(6) Input/output and display devices.
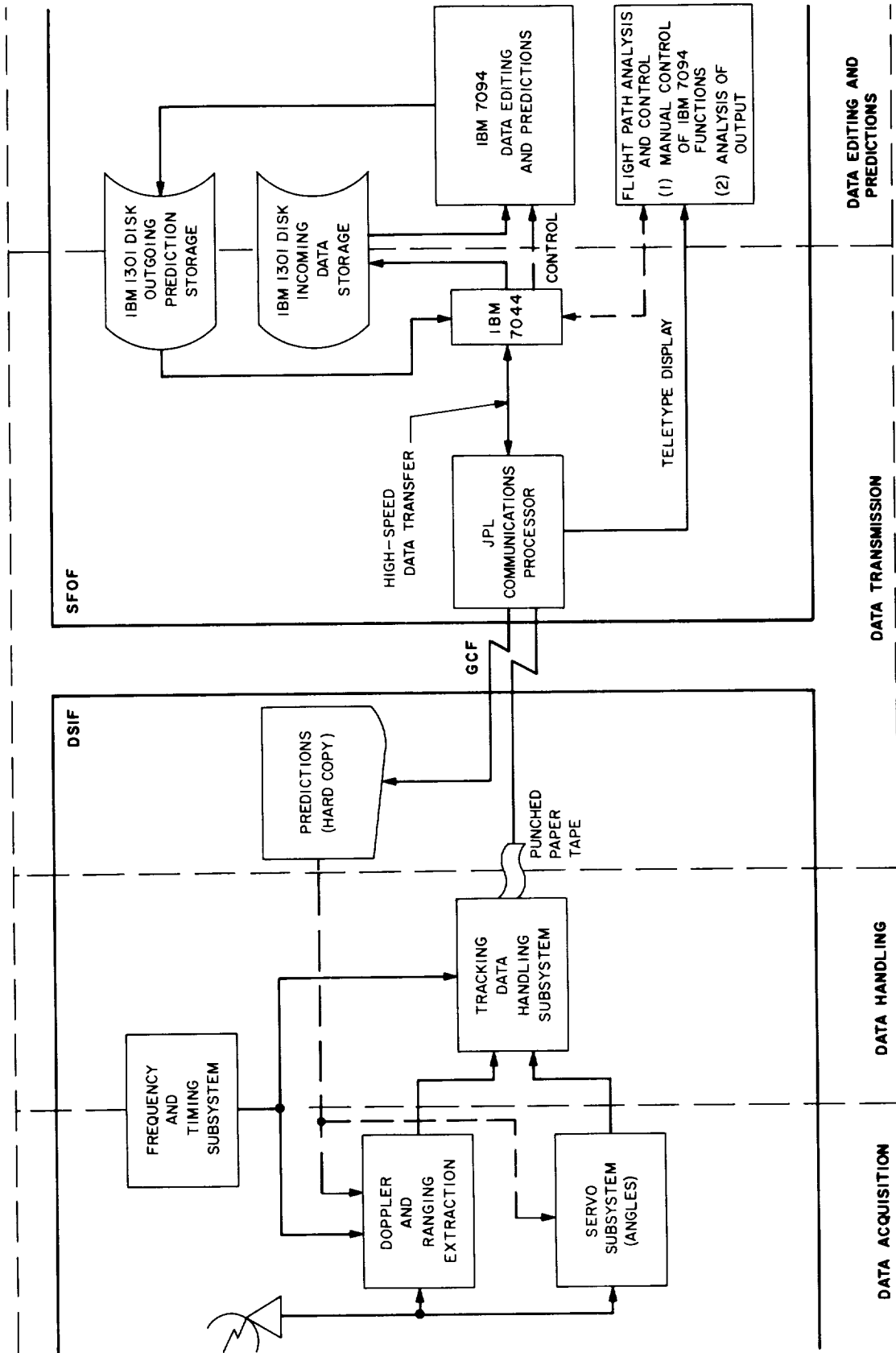
Fig. 1. DSN tracking data system
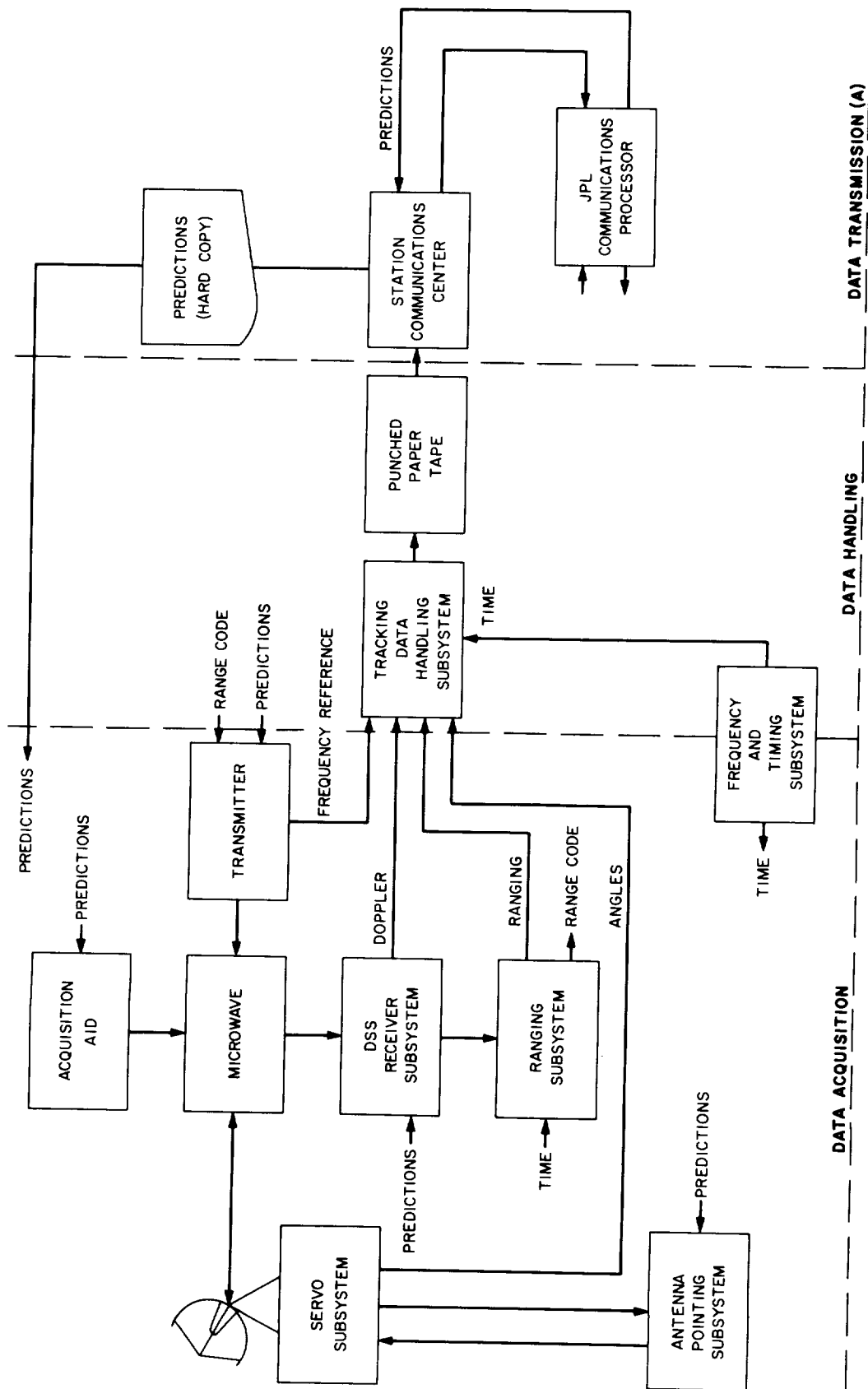
Fig. 2. DSIF data handling system
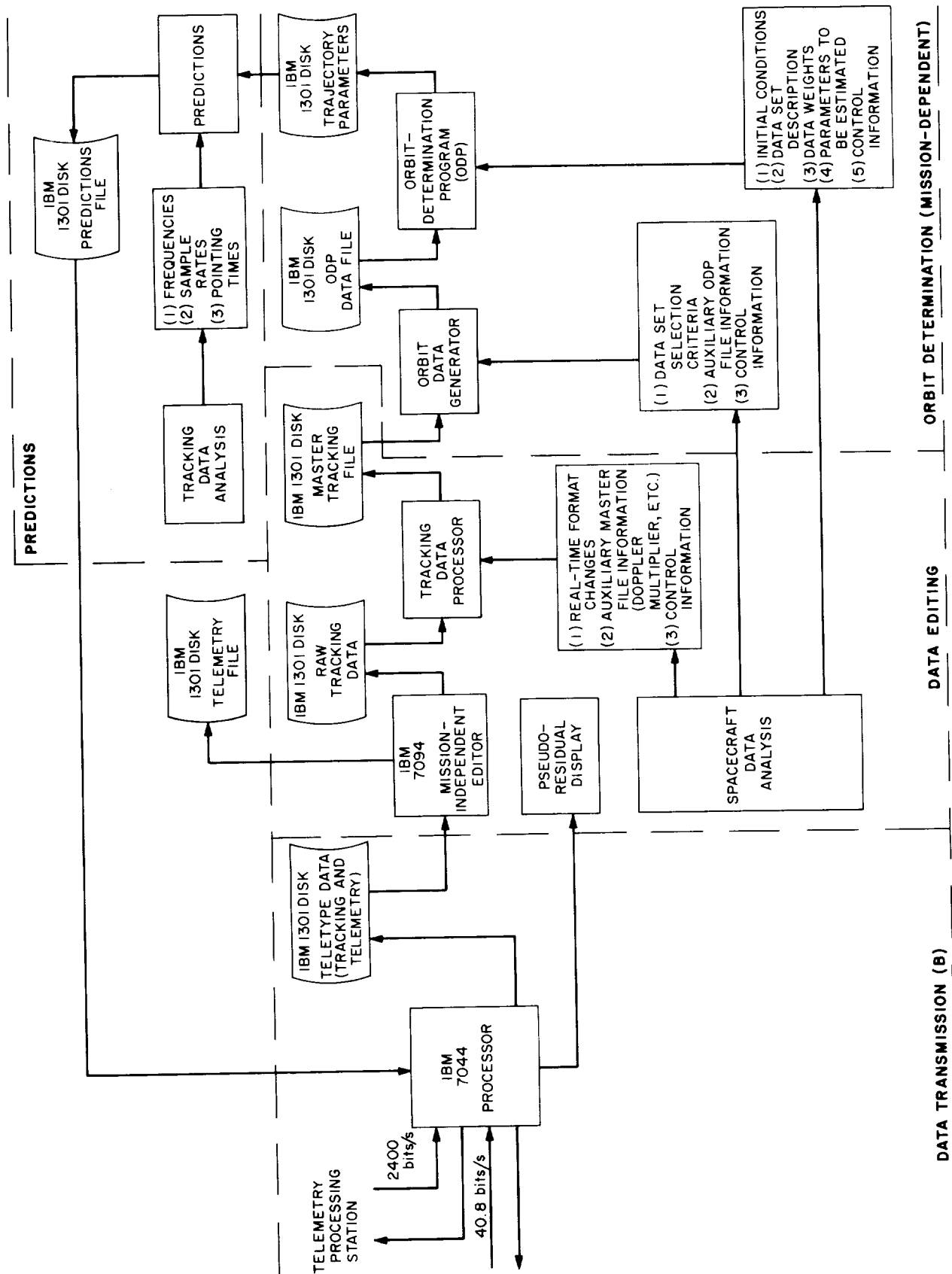
Fig. 3. SFOF data handling system

c. System operation/subsystem description

Tracking data acquisition. The data acquisition function varies by data type as follows:

(1) *Doppler and digital resolver data.* Doppler data and digital resolver data (representing instantaneous phase of the doppler signal) are derived by comparing the received signal with a reference signal (obtained from the transmitter signal if the station is transmitting to the spacecraft).

(2) *Angle data.* Angle data for both antenna axes are derived from shaft encoders attached to the antenna.

(3) *Ranging data.* A measurement of the round-trip transmission time to the spacecraft is provided by the ranging subsystem.

Under normal conditions, most spacecraft tracking is automatic; however, at the start of each pass and at the times of transmitter "hand-over," certain tasks must be performed by various station operators. Some of these manual activities will be eliminated by new subsystems currently being designed and developed. For tracking data acquisition, a computer-programmed local oscillator/exciter is presently being considered for network implementation (SPS 37-46, Vol. III, pp. 157–159).

Tracking data handling. Signals from the servo subsystem (angle data), the receiver subsystem (doppler and digital resolver data), the transmitter subsystem (transmitter frequency), and the ranging subsystem (ranging data) are fed to the tracking data handling (TDH) subsystem for digitizing and formatting. Automatic indications of data condition are also fed to the TDH subsystem from the other subsystems.

The prime function of the TDH subsystem at each DSS is that of counting doppler; in addition, it acts as the assembly and formatting center for the other tracking data at the DSS. The TDH subsystem processes, displays, records, and encodes the DSIF tracking data and doppler information for teletype transmission. The above data, as well as time and associated identification information, are provided in digital form. The representation is in standard five-level Baudot code punched onto paper tape.

The major components of the TDH subsystem are:

(1) *Angle encoder.* The angle encoder provides, in digital form, the local hour angle and declination angle of the antenna. The angle data are made available

to the punch and can also be transmitted to other areas of the station.

(2) *Doppler encoder.* The doppler encoder provides a doppler count and voltage-controlled oscillator (VCO) frequency count. These data are made available to the punch and can also be transmitted to other station users. Input signals to the doppler encoder are furnished by the station receiver and transmitter subsystems.

(3) *Sample rate selector.* The sample rate selector controls the data sample rate by generating time and angle sampling commands. These commands control the rate at which the doppler and ranging counters are read out and the angle encoders are sampled. Precise timing information is supplied by the station frequency and timing subsystem. Data may be sampled at multiples of 1 sec from 1 sample/sec to 1 sample/9 sec and simultaneously at multiples of 10 sec from 1 sample/10 sec to 1 sample/90 sec.

(4) *Punch and distributor.* Data are furnished to the punch from the angle, doppler, and VCO frequency encoders; time information is furnished by the frequency and timing subsystem; and ranging data are furnished by the ranging subsystem. Data are punched in one of a number of standard formats and are available for distribution to other areas of the station. Distribution is normally made to the digital instrumentation subsystem of the DSN monitor system.

The paper tapes on which the data are punched are accumulated at the station communications center for periodic mailing to the SFOF. The station paper tapes may be used for Master Data Library purposes, since these data are potentially of higher quality than data transmitted to the SFOF in real time. Transmission errors occur at intervals more or less dependent on the quality of the lines between the station and the SFOF. Special high-rate data may also be taken for special DSN inherent accuracy applications; these data are included with data mailed to the SFOF and are processed in detail.

Plans for improving the TDH subsystem were described in SPS 37-46. Testing of the prototype subsystem is anticipated to begin in 1969.

Tracking data transmission. The teletype paper tape is read in the station communications center. NASCOM headers are inserted manually into the data stream, which

is carried by 100-word/min lines into the NASCOM and transmitted to the JPL communications center for routing by the JPL communications processor (CP). The CP forwards the data by 40.8-kbit/s lines to all operating strings of the SFOF data processing system. In addition, the CP sends images of the data stream to teletype line printers in the SFOF by 100-word/min lines, as requested by operations personnel. Future developments include upgrading of data transmission to the highspeed data lines (2400 bits/s).

Tracking data processing. The general flow of tracking and prediction data through the SFOF data processing system (DPS) is shown in Fig. 4; a more detailed description of the DPS appeared in SPS 37-46, Vol. III, pp. 164–172. Hand-carried tape operations (represented by dashed lines in Fig. 4) occur for predictions and raw data in the Mode 3 and 4 configuration and for the residual prediction tape in all modes. The raw data and prediction formats are identical on both tape and disk in order to provide program compatibility.

(1) *IBM 7044 input/output processor.* The flow of tracking data through the IBM 7044 buffers and the programs that operate on the data are shown in Fig. 4. One message segment (one teletype line of Baudot-coded information) is sent from the CP to the IBM 7044 at a time. The CP recognizes carriage-return/line-feed combinations (the last two characters of each line) and establishes a line on that basis. The contents of the wired buffer are three control words followed by the message segment. The Baudot characters are stored at 6 characters/word, 5 bits/character, right-justified. The last word of the block contains the block checksum.

The trap supervisor (TRSP) handles the trap generated by the CP, adds several control words, puts the data as a logical record into the raw data buffer (RWDB) and the communications processor input buffer (CPIB), and turns on the CP input program (CPIP). The RWDB is the buffer from which all input data are logged onto the tape and disk. It is written in 450-word physical records to be processed by the mission-independent editor in the IBM 7094.

The CPIP sorts all input data into the appropriate buffers and turns on the appropriate program. In the case of tracking data, this is buffer TRKB and program TRKP, the pseudo-residual program described below. Similar buffers and programs exist for monitor, command, and telemetry data.

(2) *IBM 7044 pseudo-residual processor.* The IBM 7044 performs a validation function, that of pseudo-residual processing, in addition to its primary data transmission function. As each tracking point enters the IBM 7044, a tape containing predictions is read and interpolated, and residuals and statistics are calculated and logged on tape. Up to 9 doppler and 100 other residuals can be calculated. The required residuals are entered in the form: identification number, spacecraft number, station number, and residual type (plus rejection sigma, size of sequential and noise estimate tables, order of curve fit, and transmitting station for three-way doppler for doppler residuals only). A user requests a display by referring to the format number, which in turn has been initialized to reference specific identification numbers. Any of the above-mentioned parameters may be changed in real time by entering them in the display request.

(3) *IBM 7094 mission-independent editor (MIED).* The MIED reads the 450-word records written by the IBM 7044 and distributes the logical records (message segments) according to the data type. Tracking data go into two separate sequential files on disk to be handled by the respective tracking data processor for each of the two allowable missions. The output is written in 225-word physical records.

The MIED for the current IBM 7094 system has an output format different from that of the previous IBM 7094 system. To maintain the established interface between the transmission and data editing (tracking data processing) functions, a subroutine has been added which converts from the new format to the old format as a last step before the output file is written. The correlation between the MIED output file and the editing program input file is given at editor initialization time along with several other parameters, such as spacecraft identification.

Work is currently under way to enable the MIED to process high-speed tracking data.

(4) *Tracking data processor (TDP).* The TDP is a user program which can run automatically or under user control. It accesses the raw data file written by the MIED and generates a master tracking data file on disk. Data samples are checked for format and data consistency and converted from Baudot (teletype) code to binary form before being merged onto the master file. The TDP also has the capability for reading data such as Hollerith (punched card code) information from punched cards, binary-coded-decimal or Baudot-coded (teletype) data from magnetic tape, or the IBM 7044 log tape. These
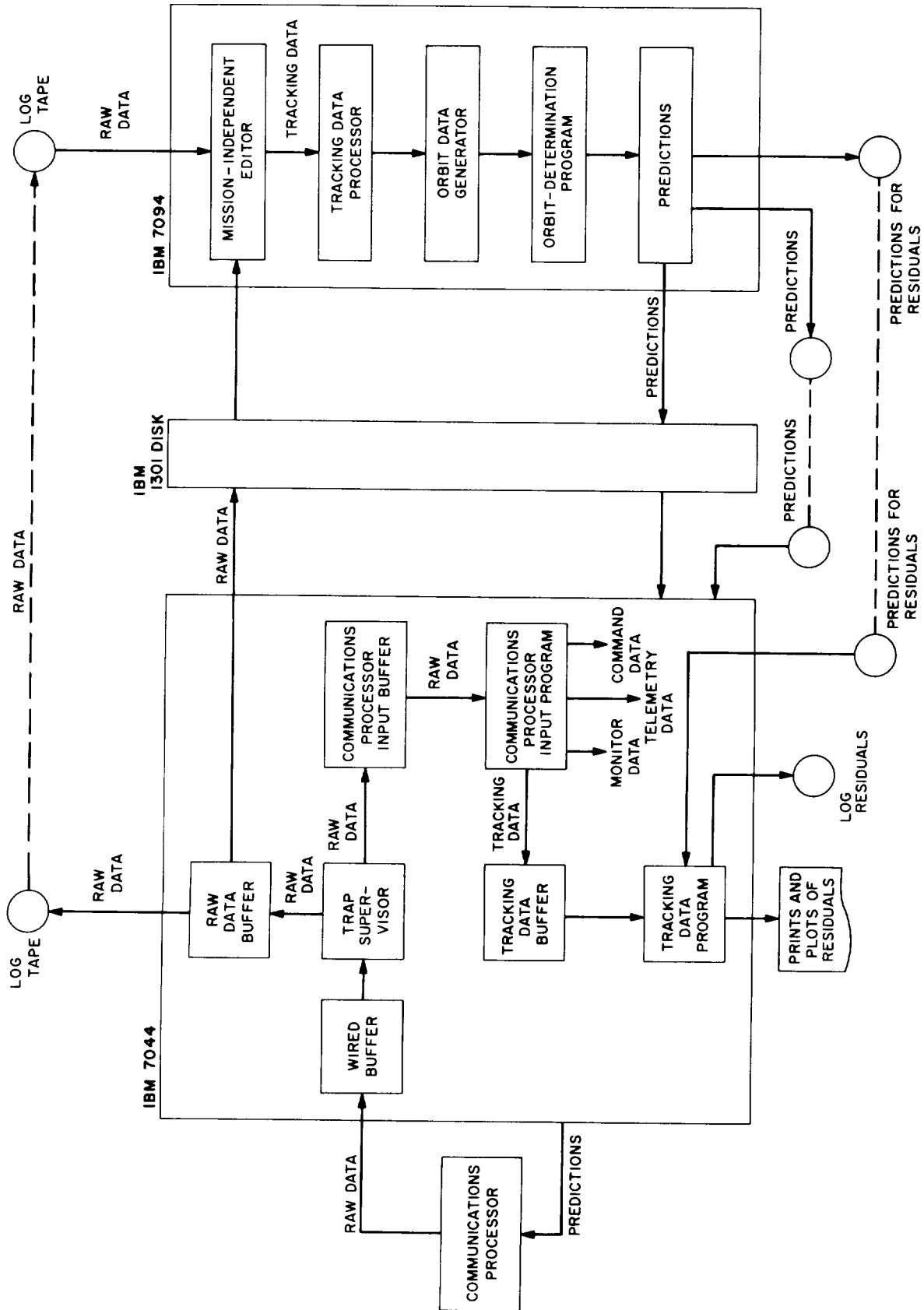
Fig. 4. Tracking and prediction data flow through the DPS

options are normally executed as backup or, during the cruise mode, as prime data sources. Capability exists in the SFOF to record data punched in teletype tape onto magnetic tape, using the Digital Equipment Corp. PDP-7 computer in the telemetry processing station (TPS). The teletype data are converted to a binary-coded-decimal data tape by a PDP-7 program. In this mode, the TDP does not require the IBM 7044 or the MIED to process tracking data, and it is not required to run in an SFOF system mode. Work is currently under way to simplify the interface between the TDS and the flight project by increasing the amount of information stored on the master tracking data file.

(5) *Prediction program.* The IBM 7094 prediction program produces a file of predictions on tape and/or disk. When a disk file is closed, the user can have it transmitted to any site or teleprinter. Predictions are routinely produced for the IBM 7044 pseudo-residual program. The IBM 7044 can read a prediction file from tape and transmit it to the stations in either Mode 2 or Mode 3.

On a transmit request, the IBM 7044 reads the prediction file from tape or disk, generates NASCOM headers from information contained in the transmit message, inserts them at appropriate intervals, and sends the data to the CP.

II. Mission Support

A. Introduction

The DSN, as part of the Tracking and Data System (TDS) for a flight project, is normally assigned to support the deep-space phase of each mission. Thus far, responsibility for providing TDS support from liftoff until the end of the mission has been assigned to the JPL Office of Tracking and Data Acquisition. A TDS Manager, appointed by the Office of Tracking and Data Acquisition for each flight project, works with the JPL technical staff at the AFETR to coordinate the support of the AFETR, MSFN, and NASCOM with certain elements of the DSN needed for the near-earth-phase support. A DSN Manager and DSN Project Engineer, together with appropriate personnel from the DSIF, GCF, and SFOF, form a design team for the planning and operational phases of flight support. A typical functional organization chart for operations was shown in Fig. 1, p. 16, in SPS 37-50, Vol. II.

Mission operations design is accomplished in a closely coordinated effort by the Mission Operations System (MOS) and TDS Managers. Mission operations, an activity distinct from the management element MOS, includes: (1) a data system, (2) a software system, and (3) an operations system. The data system includes all earth-based equipment provided by all systems of the flight project for the receipt, handling, transmission, pro-

cessing, and display of spacecraft data and related data during mission operations. Except for relatively small amounts of mission-dependent equipment supplied by the flight project, all equipment is provided and operated by the DSN. In the near-earth phase, facilities of the AFETR and the MSFN are included. The DSN also operates and maintains the mission-dependent equipment.

The software system includes all computer programs and associated documentation. The mission-independent software is provided as part of the DSN support. The mission-dependent software developed by the flight project is operated and maintained for the project by the DSN.

The operations system includes the personnel, plans, and procedures provided by both the MOS and TDS which are required for execution of the mission operations. The mission operations design organization is supported by the DSN in the manner shown in Fig. 2, p. 17, in SPS 37-50, Vol. II. The DSN Project Engineer heads a design team composed of project engineers from various elements of the DSIF, GCF, and SFOF. This team is primarily concerned with the data system defined above. The designs of the other systems are the responsibilities of the software system design team and the mission operations design team. The DSN supports these activities through its representative, the DSN Project Engineer.

The mission operations design process which the DSN supports was shown in Fig. 3, p. 18, in SPS 37-50, Vol. II. From the Project Development Plan and the Mission Plan and Requirements are derived the guidelines for operational planning and the project requirements for TDS support. The mission operations design team formulates system-level functional requirements for the data, software, and operations systems. From these requirements, as well as from the TDS support requirements, the DSN design team formulates the DSN configuration to be used in support of the project. It also supports, through the DSN Project Engineer, the activities of the software and mission operations design teams in designing the software and operations systems. The interface definitions are accomplished by working groups from these design teams.

The TDS support required by the project is formulated in the Support Instrumentation Requirements Document (SIRD) and the Project Requirements Document (PRD). The PRD states project requirements for support by the U.S. Department of Defense through the AFETR. The NASA Support Plan (NSP) responds to the SIRD in describing the DSN, NASCOM, and MSFN support.

B. Interplanetary Flight Projects

1. Pioneer VII Mission Support, A. J. Siegmeth

a. DSN commitment for Pioneer VII mission support. Due to the excellent performance of the *Pioneer VI* spacecraft and the larger-than-anticipated amount of scientific data obtained during the mission, the DSN tracking and data acquisition support requirements and commitments were increased for the *Pioneer VII* mission. The functional organization for the DSN mission support operations shown in Fig. 1, p. 16, in SPS 37-50, Vol. II.

DSIF commitment. The Pioneer, Echo, Tidbinbilla, and Johannesburg DSSs equipped with *Pioneer* ground operational equipment (GOE), were assigned for support of the *Pioneer VII* mission. With GOE, the spacecraft can be commanded by the DSSs into desired modes of operation, bit rates, calibration, and maneuvers, and telemetry data can be sent during the pass to verify proper operation of the spacecraft and its scientific instruments. In addition, at these stations all telemetry data are recorded on magnetic tapes for future processing. These magnetic tapes are the only complete data record for a given pass.

The Pioneer and Echo DSSs were the prime stations committed for the nominal phase of the mission. The DSN support commitment for these stations was one

tracking pass per day during the first 4 days after launch, one maximum pass[1] per day from 5 days until 30 days after launch, and two maximum passes per week thereafter. The Tidbinbilla DSS was committed for one tracking pass per day during the first 4 days after launch, and one maximum pass per day from 5 to 30 days after launch. The services of the Johannesburg DSS were planned on an "if available" basis. It was requested that, during the first 4 days after launch, the Johannesburg DSS should be available for one tracking pass each day.

In addition, the Woomera, Robledo, and Cebreros DSSs, without GOE, were to be available for support during the mission in a record mode only. The Ascension Island DSS, record mode only, was committed for one full tracking pass after launch. These stations can record the data in the same manner as the stations with GOE; however, data sampling and command transmission during such passes are not possible.

The Cape Kennedy DSS was also committed for *Pioneer VII* mission support to make possible the spacecraft RF compatibility verification tests.

Beginning 31 days after launch, five maximum tracking passes per week were planned, using any combination of the following stations: Pioneer, Echo, Woomera, Tidbinbilla, Johannesburg, Robledo, and Cebreros. It was also planned, within the limits of DSN loading and station availability, to use any or all of the DSSs to provide a minimum average coverage of the equivalent of one pass per day beginning 31 days after launch until the end of the mission.

Since the main objective of the mission was to collect scientific data relative to interplanetary phenomena, special emphasis was given to support during solar flare activities. The DSN commitment stated that, in the event of Class II or greater solar flare events, continuous tracking and data acquisition coverage would be provided.

It was also agreed that the *Pioneer VII* spacecraft tracking coverage from the stations equipped with 85-ft antennas would be terminated at the time when the 8-bit/s telemetry data were distorted by a bit error rate of 10^{-3} (one error in 1000 detected bits or 0.1% error) or larger, making further telemetry acquisition effort impractical. Telemetry data with a bit error rate of 10^{-2} would be acceptable to the *Pioneer* Project. If available

---

[1] The length of a maximum tracking pass is defined by the direct visibility duration of the spacecraft, limited only by the terrain and antenna hardware constraints.

error correction techniques would be applied, meaningful readout of measurements generated by the flight instruments would be possible.

It was also planned to provide tracking and data acquisition support from the Mars DSS after the phase-out of support by the 85-ft-antenna stations. This station, at the time the *Pioneer VII* commitments were made, was not fully completed and was not given an operational status; therefore, this facility was made available on a "best effort" basis.

It was planned in the SIRD and NSP issued in 1967 to have daily tracks available at the Mars DSS for each *Pioneer* mission. Due to the limitations of a single station capability, the support ratio between the *Pioneer VI* and *VII* missions at the Mars DSS was to be coordinated by the *Pioneer* Project for the best utilization of all spacecraft instruments.

GCF commitment. Four full duplex teletype circuits and one voice circuit between the SFOF and the Echo, Tidbinbilla, Johannesburg, and any other scheduled DSSs were assigned as part of the GCF *Pioneer VII* mission support, subject to circuit priorities. It was also planned to furnish during launch operations three full duplex teletype and three voice circuits between the SFOF and the JPL communications center at Cape Kennedy and three full duplex teletype and voice circuits between the SFOF and the Cape Kennedy DSS.

SFOF commitment. The *Pioneer* mission support area in the SFOF was committed for the Space Flight Operations Director and his team to direct, during launch operations, all elements of space flight operations, spacecraft performance analysis and command (SPAC), and space science analysis and command (SSAC) functions. It was also planned that the Flight Path Analysis and Command (FPAC) Team would perform all prelaunch and postlaunch computations necessary for orbit determination and predictions. The SFOF was committed to generate medium-accuracy orbits, based upon tracking data received from the DSSs; provide continuous data validation; and render any other services necessary to make a reliable spacecraft acquisition as soon as possible and have precision orbit data available to meet the required accuracies. A further commitment was to furnish the *Pioneer* Project the best possible telemetry data.

b. DSN support during launch preparations and the near-earth phase of the Pioneer VII mission. To prepare for a successful *Pioneer VII* launch, FPAC tests, an SPAC/SSAC acceptance test, FPAC acceptance tests,

SFOF integration tests, DSS/AFETR integration tests, and two operations readiness tests were performed from June 16 to August 15, 1966. After the completion of these tests, DSN and tracking-data-system readiness reviews were conducted.

Prelaunch checkout and launch preparation of the spacecraft and its scientific instruments were conducted by *Pioneer* Project personnel at Building AN at the Cape Kennedy Air Force Station. During this period, performance and verification tests of the RF link between the spacecraft and the Cape Kennedy DSS were performed. This DSS contained mission-independent and mission-dependent equipment (*Pioneer* GOE) identical to that at standard DSSs.

During prelaunch countdown, the Cape Kennedy DSS received telemetry data from the spacecraft and continuously monitored the spacecraft communications subsystem performance and the compatibility of the subsystem with the DSN. The direction and status monitoring of the DSN was performed at the SFOF. Also, the performance of the spacecraft and its scientific instruments was analyzed at the SFOF from spacecraft telemetry data teletyped from the Cape Kennedy DSS. These activities served as backup to similar tasks performed at Building AN.

Pioneer VII was launched at 15:20:17 GMT on August 17, 1966. During the near-earth phase of the mission, the AFETR network metric-tracked the launch vehicle and received telemetry data from both the spacecraft and the launch vehicle. The spacecraft telemetry data were recorded on magnetic tape for later processing and analysis. The tracking data were teletyped immediately and continuously to the real-time computer facility at the Cape Kennedy Air Force Station, where the characteristics of the trajectory were calculated for predictions to be used for the initial DSN acquisition of the spacecraft's S-band signal. Similar activities were performed at the SFOF, using the AFETR tracking data.

The MSFN collected metric tracking and telemetry data from the *Delta* second stage on C-band. The metric tracking data were obtained by three MSFN stations, and the telemetry data by six. Two orbits were covered 200 min after launch.

The Cape Kennedy DSS tracked the spacecraft's S-band signal and supplied telemetry information, using its GOE and telemetry command processor, to the *Pioneer* mission support area at the SFOF until 190 s after launch, at which time it lost lock. The Ascension

Island DSS locked onto the S-band signal of *Pioneer VII* at 15:40:15 GMT (30 s after this station's rise) and recorded it for over 7 min, at which time the spacecraft reached horizon.

The first lock at the Johannesburg DSS was established 47 min after launch, approximately 90 s after the 10-deg elevation angle was reached. The Johannesburg DSS was in auto-track at 15:49:40 GMT. The signal strength was −133 dBmW, and the S-band acquisition aid was utilized. Two-way lock was established at 61 min, 50 s after launch at the same station, using the S-band cassegrain monopulse feed. The signal strength was approximately −100 dBmW.

At 16:21 GMT the signal at the Johannesburg DSS dropped rapidly to −115 dBmW. Therefore, tracking was transferred to the Tidbinbilla DSS at 16:25:30 GMT. This station locked-up in a two-way mode 1 min, 30 s later. At 16:35 GMT, there was a momentary loss of lock on the downlink. The lock was again re-established in 30 s. Tracking was transferred from the Tidbinbilla DSS back to the Johannesburg DSS 1 h, 41 min after launch. Since firm tracking and data acquisition of the *Pioneer VII* S-band signal had been established, the near-earth support phase of the mission was considered successfully completed.

During this phase, the SFOF provided all necessary services, functions, and equipment. The FPAC Team made computations of the parking orbit, which was nominal. The SFOF-computed orbit, available 35 min after launch, was used as a backup to the AFETR-computed orbit. The deviation between the two orbits was within the required accuracy limits. The computation of the solar orbit started 1 h after launch, utilizing two-way tracking data from the Johannesburg and Tidbinbilla DSSs. The first computed solar orbit, available approximately 2 h after launch, was used immediately to generate new predictions for the DSSs. Three more orbits were generated within 20 h after launch, utilizing two-way tracking data from the Johannesburg, Tidbinbilla, and Pioneer DSSs. All four orbits were very similar and the fit to the available data was almost perfect.

The GCF supplied all necessary support prior to, during, and after the launch of *Pioneer VII*.

c. *DSN support during the deep space phase of the Pioneer VII mission.* All committed tracking and data acquisition services were furnished to the *Pioneer* Project to make available almost continuous telemetry infor-

mation with the lowest bit error rate, as well as the necessary two-way doppler tracking information required to update the orbit parameters and generate frequency predictions for the DSSs. Figure 1 summarizes the tracking and data acquisition support rendered by the DSN from the *Pioneer VII* launch until the eighth week of 1968. During the 6-mo-long nominal mission, not only have the minimum requirements and commitments been met, but a considerable amount of additional support has also been furnished.

The fixed earth–sun line heliocentric trajectory of *Pioneer VII* is shown on Fig. 2. The time ticks drawn on the trajectory represent the spacecraft's position on the first day of each given month. The *Pioneer VII* telemetry threshold ranges are displayed for the standard and the experimental advanced 85-ft-antenna DSSs (Johannesburg and Echo), as well as for the 210-ft-antenna Mars DSS. The free-space attenuation scale can be used as a relative measure.

During the nominal mission, the principal tracking and data acquisition support was provided by the 85-ft-antenna DSSs equipped with the *Pioneer* GOE: Johannesburg, Echo, and Tidbinbilla. In addition, the Pioneer DSS also provided support utilizing the microwave link between the Pioneer and Echo DSSs and the multiple-mission support area at the Echo DSS. This configuration made possible the demodulation of the telemetry signals received by the Pioneer DSS S-band receiver with the *Pioneer* GOE located at the Echo DSS, thus expanding the usage of the only *Pioneer* GOE in the Goldstone DSCC.

This mode of operation was necessary to meet the *Pioneer* tracking and data acquisition support requirements and commitments without conflicting with the mission support of *Lunar Orbiter I* (launched August 10, 1966), provided by the Echo, Woomera, and Robledo DSSs. The *Lunar Orbiter II* (launched November 6, 1966) and *Lunar Orbiter III* (launched February 5, 1967) missions were supported by the same stations. Therefore, the *Pioneer VII* support from the Goldstone DSCC between the *Lunar Orbiter* missions was provided by the Echo DSS; at other times, the Pioneer DSS was used. Though the *Surveyor II* launch on September 20, 1966, further increased the DSN load, any possible support conflicts were resolved without affecting the DSN support of the *Pioneer VII* mission.

During the first 10 days after launch, the Johannesburg, Tidbinbilla, and Pioneer DSSs furnished 100% coverage
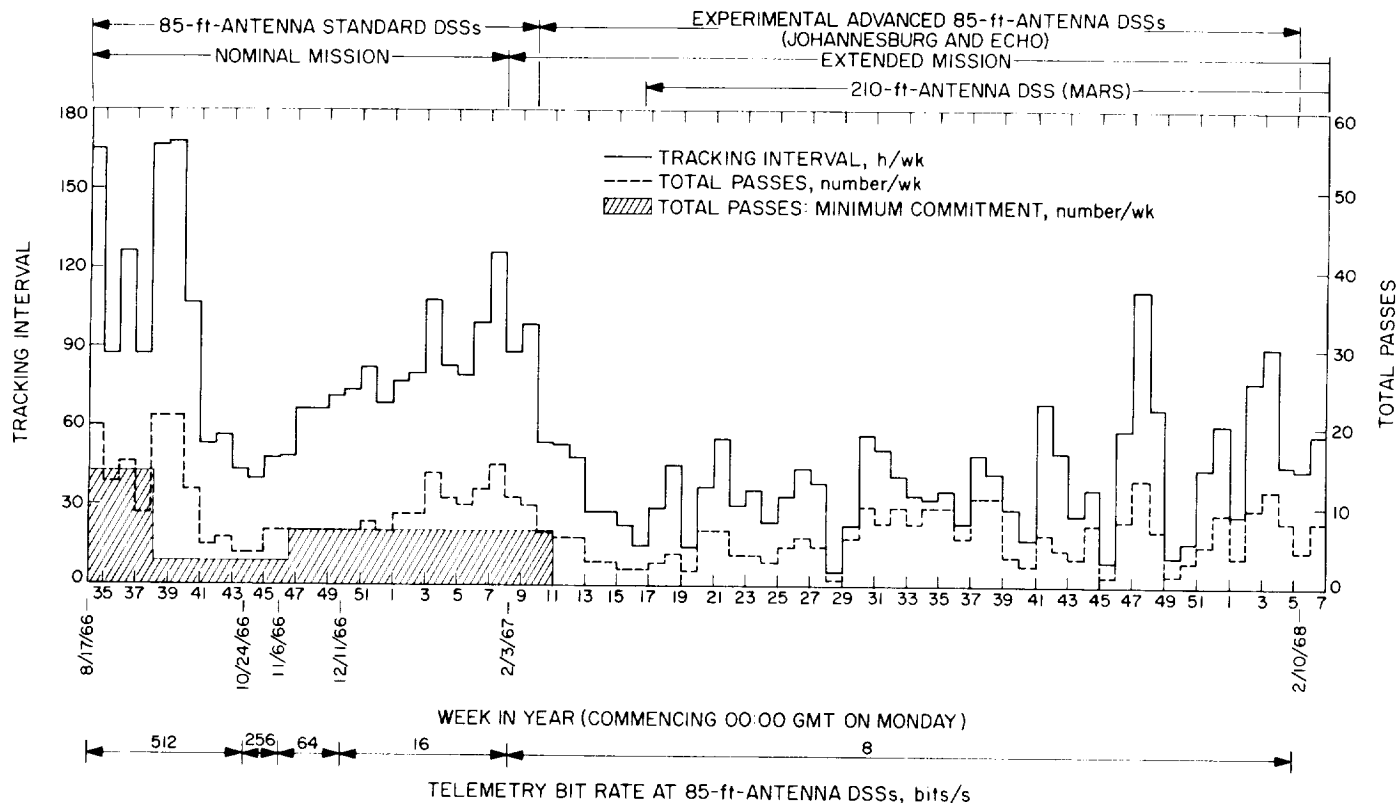
Fig. 1. DSN operational support of *Pioneer VII* mission: weekly tracking passes and hours and minimum commitment during the nominal mission

for the *Pioneer VII* mission. The Pioneer DSS sent the commands for the Type II orientation maneuver during the second pass. These commands rotated the spacecraft about the sun–probe line and stopped it at that orientation which resulted in the greatest signal strength at earth. At this position, the spin axis was known to be normal to the plane of the earth, sun, and probe. During this maneuver, the spacecraft antenna radiation pattern was plotted, and the spacecraft spin axis was positioned to receive the greatest signal strength at the tracking stations around the earth.

From 11 to 33 days after launch, the DSN provided, on the average, two passes per day (the minimum commitment). To detect sun radiation anomalies, *Pioneer VII* traveled through the geomagnetospheric tail of the earth, starting 34 days after launch. During this syzygy configuration, 100% tracking coverage was provided by the Echo, Woomera, and Cebreros DSSs. On October 1, the syzygy coverage of *Pioneer VII* was completed.

The telemetry data acquisition threshold of a 0.1% bit error rate was reached at the standard 85-ft-antenna

stations on March 21, 1967. Prior to that date, the DSN initiated supporting-research-and-technology efforts to improve the *Pioneer* telemetry threshold capabilities of the 85-ft-antenna network. This was the only way to further increase support capabilities without being forced to continue support using only the 210-ft antenna at the Mars DSS, which was already tracking *Pioneer VI*.

The first hardware modified to improve the telemetry detection threshold was tested at the Echo DSS during March. The 12-Hz S-band carrier tracking loop bandwidth was narrowed to 5 Hz and later to 3 Hz. In a receive, one-way mode only, the bit error rate was lowered from 0.1% to approximately 0.02%. Also, the system noise temperature of the Echo DSS was decreased. A specially designed waveguide bypass was installed that removed electrically the antenna diplexer and two waveguide switches from the microwave feed assembly. This change of the regular configuration decreased the system noise temperature by 11.5°K to approximately 29°K. Accordingly, the threshold improvement was 1.5 dB. These improvements made possible the Echo DSS support of the *Pioneer VII* mission during April. The telemetry bit error rate was within the acceptable limit.
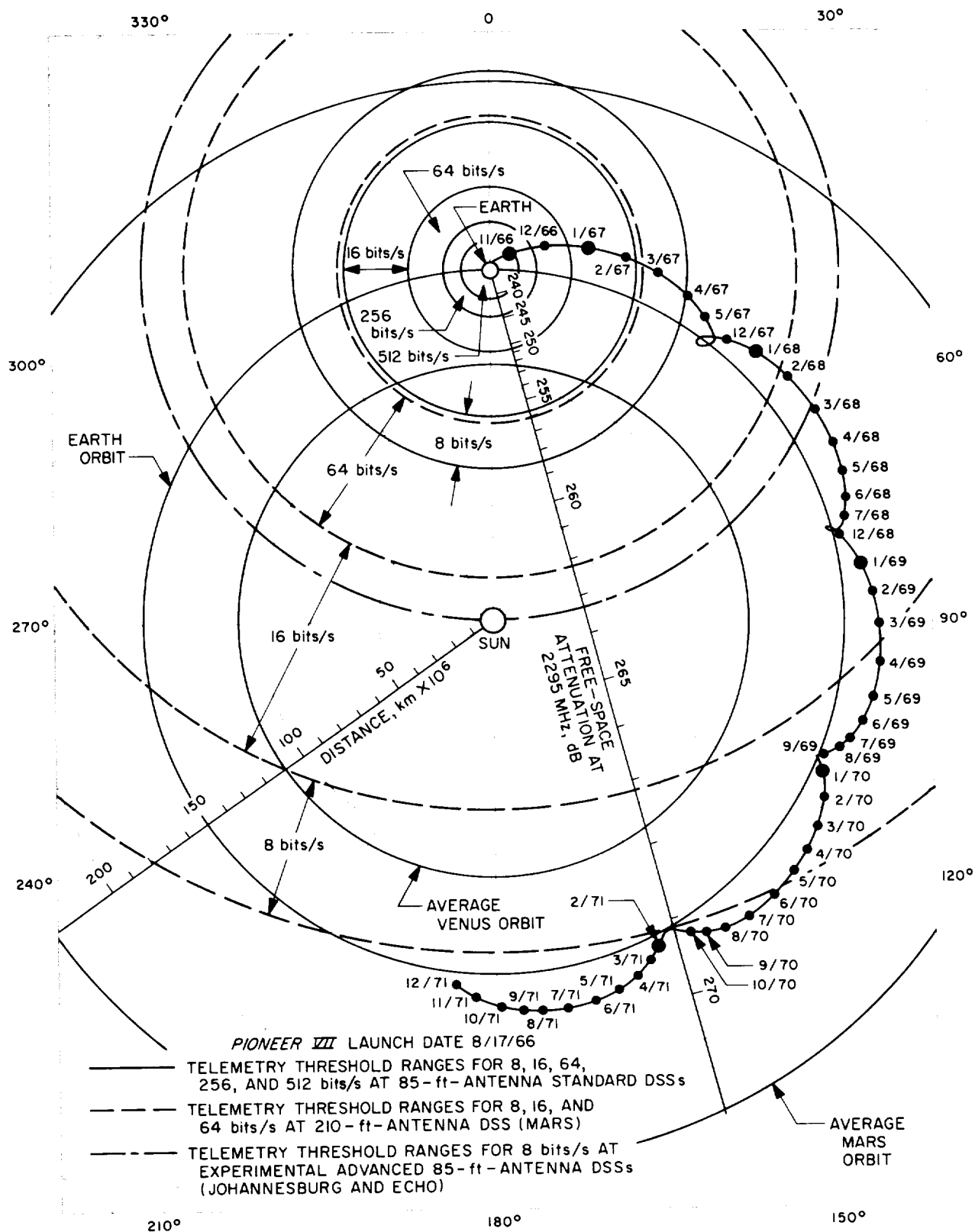
Fig. 2. Fixed earth—sun line heliocentric trajectory of *Pioneer VII* and telemetry threshold ranges

During the first 2 wk of May, the DSN supported the *Pioneer VII* mission from the Venus DSS, which has a system noise temperature of 30°K and a 3-Hz carrier tracking loop bandwidth. The linear polarized feedhorn of this station made possible a signal enhancement of about 3 dB. It should be noted that the *Pioneer* spacecraft transmit linearly polarized S-band signals and the standard 85-ft antenna DSSs have circularly polarized feedhorns. This configuration causes a 3-dB polarization loss at the standard stations, which have been optimized to track planetary spacecraft which operate with circularly polarized signals. The quoted threshold features of the Venus DSS made it possible to track *Pioneer VII* telemetry signals with no bit errors at an 8-bit/s rate.

During the second half of May, the *Pioneer VII* mission was supported by the Johannesburg DSS. A 3-Hz tracking loop bandwidth capability had been incorporated, and a special waveguide modification had been made. In this configuration, the station was limited to receive-only operation. The system noise temperature after the waveguide bypass installation was lowered to approximately 33.1°K; the standard noise temperature of this station is 42.5°K. The receiver threshold after both modifications was −177.5 dBmW; the receiver threshold in a standard configuration at the same station is approximately −173.5 dBmW. The overall system improvement due to both modifications, as derived using the parity error rate improvement, was equivalent to approximately 2.5 dB, of which 1.1 dB was attributed to reduced system temperature and the remainder to the 3-Hz tracking loop bandwidth.

Figure 3a shows the bit error rates obtained at the Johannesburg DSS during the latter part of May. The bit error rate for a normal pass was relatively constant for the middle of the pass, with a duration of approximately 4–6 h. The increase in error rate on either side of midpass was attributed to the noise contribution of the relatively large side-lobe sensitivity caused by damage to the antenna's surface from hail storms. The antenna surface panels were replaced, and the bit error rate of the *Pioneer VII* telemetry subsequently improved, as shown in Fig. 3b. The Mars DSS also provided support during the same period and obtained telemetry with bit rates of 64 and 16 bits/s and a very low bit error rate.

From July until the end of 1967, the *Pioneer VII* mission was supported mostly by the Johannesburg and Mars DSSs. During the launch activities at the Johannesburg DSS for the *Surveyor IV–VII* and *Lunar Orbiter V* missions, only the Mars DSS was used for *Pioneer VII* tracking and data acquisition support.

The desire for increased 85-ft-antenna station support for *Pioneer VII* resulted in the development of a polarizer for the cassegrain feeds. The test data for a research-and-development model indicated an approximate 3-dB improvement in signal level at both receive and transmit frequencies. This polarizer converted the standard circular feed to a linear feed. It was installed at the Johannesburg DSS during November 1967, and its performance has been very satisfactory. An acceptable telemetry bit error rate was obtained until February 1968, at which time the spacecraft–earth range started to increase rapidly and *Pioneer VII* support by the experimental advanced 85-ft-antenna Johannesburg DSS was phased out. Since that time, the *Pioneer VII* mission has been supported, on a daily basis, by the Mars DSS, which has the capability to support the mission until its termination.

Thus, the *Pioneer VII* mission support by 85-ft-antenna stations was extended approximately 10 mo after the standard 85-ft-antenna network reached its telemetry threshold limit. This improvement made possible not only more tracking and data acquisition support for *Pioneer VI* at the Mars DSS, but also approximately 850 additional tracking hours of *Pioneer VII* mission support during a time when the DSN was supporting 12 other lunar and planetary missions.

The *Pioneer VII* telemetry system transmits scientific and engineering data at five discrete bit rates ranging from 512 to 8 bits/s. During the first 18 mo after launch, *Pioneer VII* collected nearly 2.2×10^9 bits of telemetry information: 72%, scientific information; 6%, engineering data; and the rest, parity check and data identification. Throughout the flight, *Pioneer VII* operated primarily in the sampled real-time data transmission mode. All received data bits were recorded on an original master magnetic tape, and sampled telemetry data were transmitted in near-real time, using teletype lines, to the SFOF and the *Pioneer* Mission Operations Center at Ames Research Center. The *Pioneer* Project's Space Flight Operations Team used these data for "quick-look" and operational control purposes.

The spacecraft's duty-cycle storage mode[2] was used during the times the DSN was unable to furnish tracking

---

[2]In this mode the DSN is not receiving telemetry from the spacecraft, and the data are being stored on the spacecraft. It is the least desirable type of data retrieval method because the spacecraft memory unit has limited capacity and because a *portion of* the subsequent tracking period of a station must be reserved for playback. At the lowest bit rate, the time for playback can amount to 32 min.
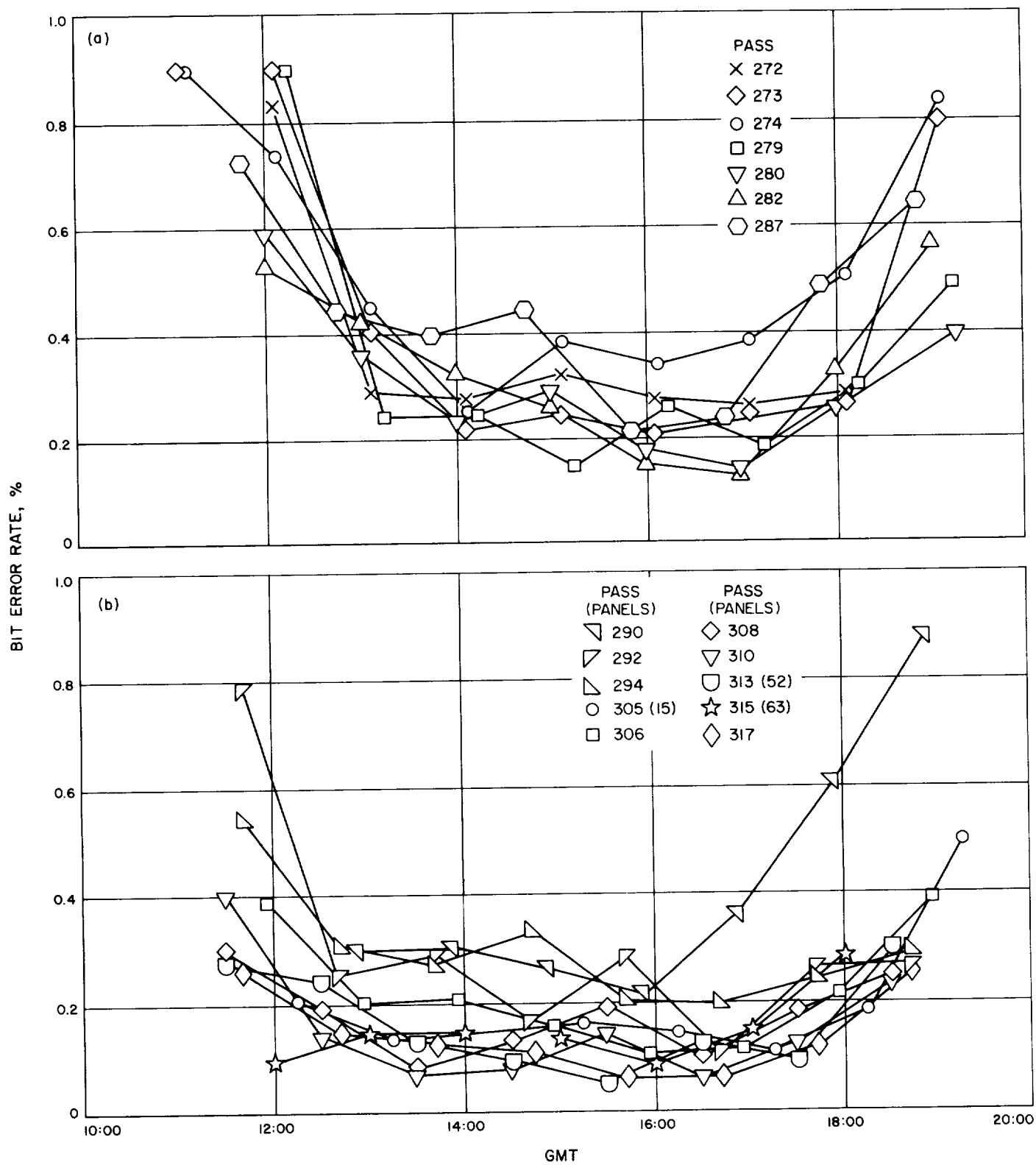
Fig. 3. *Pioneer VII* telemetry bit error rates estimated at the Johannesburg DSS: (a) May 15–31, 1967; (b) June 1–30, 1967
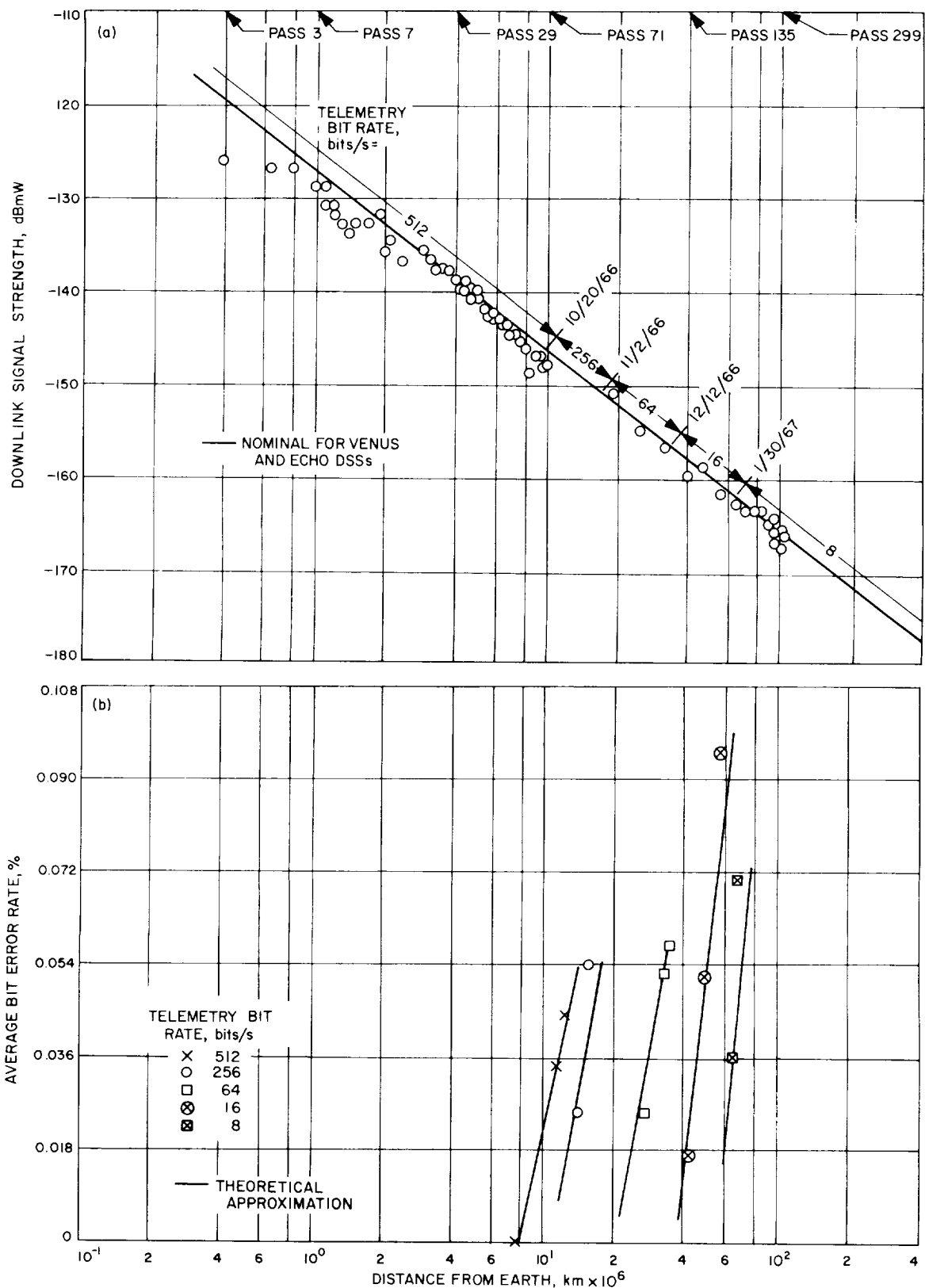
Fig. 4. Performance characteristics of S-band communications downlink using standard 85-ft-antenna DSSs

and data acquisition support. Less than 0.1% of the total data was received in this mode.

Every phase of the mission thus far has been very successful, and all flight instruments are still operating and continuously sending back excellent data on fields and particles. Based on its performance thus far, the estimated total lifetime of the *Pioneer VII* spacecraft is 5 yr. This nominal lifetime is used in DSN planning to estimate the future tracking and data acquisition support necessary for the mission.

The onboard S-band communications equipment (i.e., the Channel 6 and Channel 7 spacecraft receivers and the transmitter) is still performing within the tolerances of the given specifications. The performance characteristics of the S-band communications downlink, using the standard 85-ft-antenna DSSs, are plotted in Fig. 4. The S-band receiver input carrier level measurements at the Venus and Echo DSSs agree with the nominal values of the *Pioneer* communications systems design (given in Table 1, p. 23, in SPS 37-50, Vol. II).

The approximate cutoff dates of the *Pioneer VII* telemetry bit rates are also very close to the predicted values. The measured average telemetry bit error rates are in the vicinity of the theoretical approximation.

C. Planetary Flight Projects

1. Mariner V Extended Mission Operations Support,

D. J. Mudgway

It is estimated that *Mariner V* (developed under the *Mariner* Venus 67 Project) will survive from 3 to 6 yr on the basis of the known gas-depletion rate and the spacecraft's past history and that, approximately once every 13 mo, *Mariner V* will be within DSN tracking range for about 6 mo. The times during which the spacecraft is expected to be within communications range of the DSSs are shown in Fig. 5.

To take advantage of this opportunity for gathering additional scientific and engineering data, the *Mariner* Extended Mission Operations (MEMO) Project is being established.[3] A DSN Manager has been appointed; he will be supported by a DSN Project Engineer plus an engi-

---

[3]*Proposal for Mariner V Extended Mission Operations,* Jan. 10, 1968 (JPL internal document).

neering and operations team comprised of technical personnel from the DSIF, SFOF, and GCF.

The DSN proposes to meet the basic support requirements with the Mars DSS 210-ft antenna and the Robledo DSS 85-ft antenna. During the 210-ft-antenna visibility period, seven 4-h passes per week will be required by the Project; during the 85-ft-antenna visibility periods, seven 8-h passes per week will be required. The existing ground telemetry system from the previous *Mariner V* activities will be utilized. Command capability will be provided with the standard *Mariner V* read–write–verify system.

Some ranging passes on a "best effort" basis will also be provided from the Mars DSS, using the existing R&D planetary ranging equipment.

Additional support is planned on a "best effort" basis, using the DSSs scheduled to support the *Mariner* Mars 1969 missions. For this support, the newly developed multiple-mission telemetry system will be employed, using a specially modified telemetry-command-processor software program to make the system compatible with the *Mariner V* data format. This will permit the existing *Mariner V* software to be used for outputting the data from the telemetry command processor to the communications lines in the original format; hence, no changes will be required to the IBM 7044 data processing system in the SFOF.

Because of the impending new automatic-data-switching-system modifications, arrangements are being made to bypass the block multiplexers and error decoder–encoders at both the DSS and SFOF ends of the communications circuits. This will allow the MEMO high-speed data stream to enter the telemetry processing system for reformatting and subsequently pass to the IBM 7044 without any need for additional software.

Command capability by the DSSs scheduled to support the *Mariner* Mars 1969 missions is to be provided for MEMO by a slightly modified read–write–verify system, which can be readily converted to the *Mariner V* configuration by the insertion of an appropriate card.

A mission support area has been assigned in the SFOF, and planning layouts have been made of the communications and display facilities for this area.
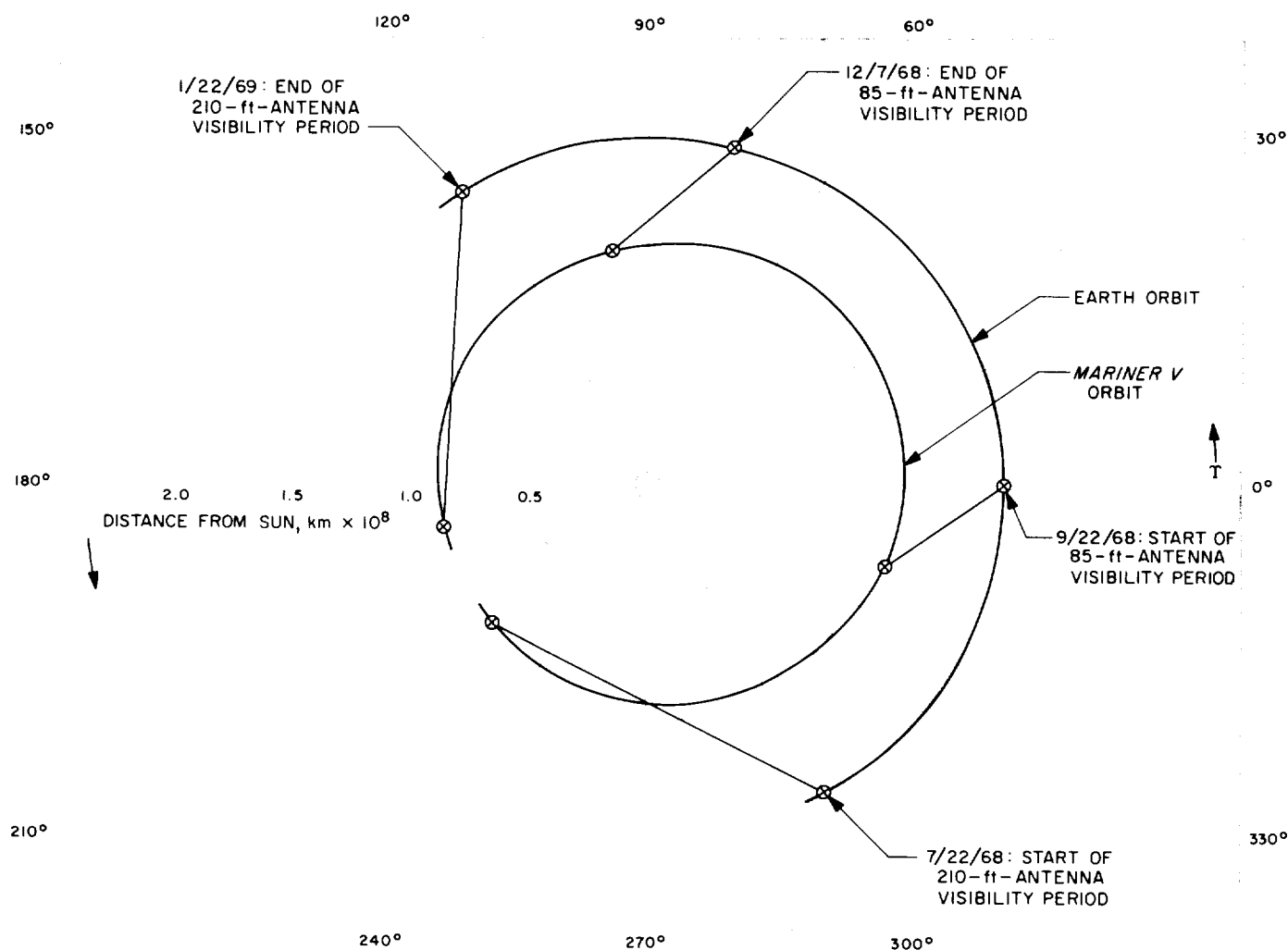
Fig. 5. Heliocentric view of Mariner V trajectory during 1968–1969 tracking opportunity

D. Manned Space Flight Project

1. Apollo Mission Support, P. S. Goodwin

a. Introduction. The DSN support furnished to the MSFN for the Apollo Project from the early equipment procurement and implementation through the operational support provided during the *Apollo 4* (launched November 9, 1967) and *Apollo 5* (launched January 22, 1968) missions was described in SPS 37-50, Vol. II, pp. 27–33. The support provided during the April 4, 1968 launch and subsequent flight of *Apollo 6* (AS-502) is described here.

b. Apollo 6 mission description. The *Apollo 6* mission was the second unmanned test of the giant *Saturn V* launch vehicle, which for this mission carried an instrumented, developmental spacecraft and an inert lunar module test article. The nominal *Apollo 6* mission profile was to be very similar to that of its predecessor, the

highly successful *Apollo 4*. The significant difference between the two mission profiles was that the *Apollo 6* third stage, the S-*IVB*, was to burn to full lunar injection velocity and target for a theoretical moon. The spacecraft [i.e., the command and service module (CSM)] was to separate shortly after injection and perform a braking maneuver to limit its apogee to approximately 12,000 nmi. The CSM was programmed to burn its propulsion system on the downward leg so as to re-enter the earth's atmosphere at a simulated lunar return velocity in a final test of the spacecraft's heat shield. However, two significant anomalies occurred that prevented the accomplishment of all of the mission objectives and affected the support provided by both the MSFN and the DSN. While these anomalies, discussed below, are probably not related, their combined effect was to greatly alter the combined MSFN/DSN post-lunar-injection test plan for this mission.

Premature shutdown of two of the five J-2 engines in the S-II second stage during the launch phase. In itself, the first anomaly had minimal effect upon the network's ability to acquire the spacecraft in earth orbit, because the S-IVB stage's first burn compensated for the velocity deficiencies created by the second-stage engine failure. The resulting earth orbit was somewhat elliptical (96 nmi by 196 nmi) but within the network's acquisition capabilities.

Failure of the J-2 engine in the S-IVB third stage to restart for the lunar injection burn. The second anomaly had the more significant effect upon the combined MSFN/DSN support plans. As a result of the S-IVB restart failure, an alternate mission plan was put into execution. The CSM was immediately separated from the S-IVB third stage, and the spacecraft's propulsion system was ignited to drive the CSM to near its intended apogee. In so doing, its fuel was depleted to such an extent that the CSM could not accelerate to lunar return velocity on the downward leg and was forced to land in a secondary recovery area. There it was successfully recovered by the Carrier *USS Okinawa.* In the meantime, the S-IVB remained in its 96-nmi by 196-nmi elliptical earth orbit, invalidating the preflight nominal acquisition information at the stations until new acquisition messages were received.

c. Cape Kennedy DSS support for Apollo 6 mission.
As was the case with *Apollo 4* and *5,* the Cape Kennedy DSS provided informal assistance to the MSFN station on Merritt Island during the countdown and launch of *Apollo 6.* The station was configured in a manner identical to that for the *Apollo 4* mission (SPS 37-50, Vol. II, p. 31); i.e., the CSM S-band downlink would be received at the Cape Kennedy DSS, and the detected phase-modulated telemetry baseband would be relayed to the MSFN station on Merritt Island for processing should multipath or flame attenuation cause reception difficulties at Merritt Island that possibly might not be experienced at the Cape Kennedy DSS. Activities at Cape Kennedy started with a countdown demonstration test 96 h before liftoff and proceeded through the terminal count and subsequent launch of *Apollo 6* at 12:00:01 GMT on April 4, 1968. During this period, the Cape Kennedy DSS observed the received signal on a spectrum analyser, took Polaroid pictures, and reported signal strength data to the MSFN station on Merritt Island. The received signal at the Cape Kennedy DSS was nominal, based on *Apollo 4* countdown experience, being −74 dBmW at 40 s after liftoff. A momentary dropout occurred 2 min, 31 s after liftoff, but the signal was im-

mediately recovered at a signal strength of −116 dBmW. Signals in the range of −106 to −124 dBmW were then received until 8 min after liftoff, when signal strength dropped to −140 dBmW. Loss of signal occurred 9 min, 14 s after liftoff on the launch pass.

d. Ascension Island DSS support for Apollo 6 mission.
Preparations for the *Apollo 6* mission at the DSN Ascension Island DSS officially started at 00:00 GMT on February 29, 1968, with the establishment of configuration control of the station in the MSFN configuration. In reality, the station had remained in the MSFN configuration since the *Apollo 4* mission and had participated in a practice exercise with *Apollo 5* (SPS 37-50, Vol. II, p. 32). During the time between the *Apollo 5* tracking and the launch of *Apollo 6,* the Ascension Island DSS participated in all requested MSFN prelaunch tests, network simulations, and *Test and Training Satellite (TATS)* tracks. A configuration freeze was established at 00:00 GMT on March 12, at which time the Ascension Island DSS went on "mission status," thereby joining the MSFN Ascension Island station in responding to the *Apollo* Project's scheduling requests. From this time through launch, the Ascension Island DSS reported "status green."

The Ascension Island DSS was formally committed to the MSFN for *Apollo 6* mission support, since the nominal mission profile required two antennas at Ascension Island after the planned lunar injection: one to cover the CSM and the other to cover the S-IVB stage. The MSFN Ascension Island station was assigned to the former vehicle, while the DSN Ascension Island DSS was assigned to the latter vehicle. Had the S-IVB injection burn been nominal, the Ascension Island DSS would have experienced a 12-h pass, tracking the S-IVB/IU stage[4] starting with the third orbital revolution. (The first and second orbital revolutions were not visible to Ascension Island.) Since the S-IVB did not restart for the lunar-injection engine burn at the end of the second orbital revolution, its subsequent passes over Ascension Island were all earth-orbital-type tracks, as noted below.

The restart anomaly occurred at the beginning of the third orbital revolution, just minutes before the expected CSM and S-IVB acquisition-of-signal times for the two Ascension Island stations. Because the CSM propulsion system was ignited to place the spacecraft in a near-standard, high-apogee elliptical orbit, the MSFN Ascension Island station was able to acquire the CSM at almost the expected time. The Ascension Island DSS

[4]The instrumentation unit (*IU*) is that part of the S-IVB stage that contains the VHF beacon and S-band transponder.

searched for the S-IVB/IU at its preflight nominal arrival azimuth bearing until well after its predicted arrival time. Having failed to detect the S-IVB/IU, the Ascension Island DSS next searched in the vicinity of the CSM, using verbally reported look angles from the MSFN Ascension Island station, again without success. After an estimated 2 min into the pass, the VHF telemetry antenna at the MSFN Ascension Island station acquired the S-IVB/IU VHF telemetry signals and relayed the vehicle's position to the Ascension Island DSS. The late "arrival" of the S-IVB, due to the restart anomaly, had created an almost 180-deg azimuth bearing difference in station look angles between the CSM and S-IVB/IU by the time the latter's signals were acquired.

Despite this confused start, the Ascension Island DSS successfully completed 6 min, 9 s of main beam autotrack on the S-IVB/IU in the third orbital revolution. The Ascension Island DSS first acquired the S-IVB/IU at 15:33:07 GMT on its acquisition antenna system (Fig. 10, p. 30, in SPS 37-50, Vol. II) and then transferred to the main-beam autotrack mode 6 s later. The signal strength at the acquisition-of-signal time was −85 dBmW —a strong signal. The Ascension Island DSS was successful in sending several commands and performing several ranging measurements, even though the third orbital revolution was a short earth-orbital pass. The signal strength at the loss-of-signal time was −120 dBmW.

Using verbal acquisition data provided by the MSFN station, the Ascension Island DSS rapidly acquired the S-IVB/IU on the fourth orbital revolution at 17:07:41 GMT, transferring to the main beam at 17:09:20 GMT. The signal strength at that time was −100 dBmW. The track was successful during the entire pass, which terminated at 17:15:17 GMT with loss of signal. An attempt was made to track the S-IVB/IU again on the fifth revolution, but the vehicle's orbit progression caused the track to follow the station's horizon, with the result that the Ascension Island DSS had only intermittent signal lock.

During the foregoing time period, the Ascension Island DSS tracking data were sent in real time to the SFOF, where they were inspected and manually checked for accuracy. The tracking data were also forwarded to Goldstone DSCC for processing through the system data analysis (SDA) computers which had been set up to perform a real-time evaluation. However, the accurate set of injection conditions required by the SDA program to perform an analysis was not available in time due to the anomalies in the mission. Therefore, the SDA-accumulated raw data were retained for postflight analy-

sis. The manual analysis of the tracking data did not disclose any particular problem areas, and the doppler counter problem mentioned in SPS 37-50 appeared to have been corrected.

Concurrently with the Ascension Island DSS's S-IVB activity, the MSFN Ascension Island station tracked the CSM in its high-apogee orbit, thereby fulfilling the Project's requirement for two-antenna coverage from Ascension Island. The high-apogee CSM pass (third orbital revolution) lasted 4 h, 11.5 min, which meant that the MSFN station's loss-of-signal time on the CSM was after the fifth orbital revolution of the S-IVB, which was the last revolution visible until the orbit precessed sufficiently to reappear over Ascension Island. Since the latter would occur well after the CSM loss of signal, the Manned Spacecraft Center released the Ascension Island DSS from further support to Apollo 6 at 19:00 GMT on April 4.

e. Apollo 6 mission support by DSS MSFN wings. The planned S-IVB/IU post-injection trajectory of Apollo 6 provided an excellent opportunity to exercise both the prime MSFN 85-ft-antenna stations and the backup 85-ft-antenna stations with MSFN wings in a simulated Apollo lunar-mission-type trajectory. The MSFN requested, and the DSN concurred, that the DSN stations with MSFN wings be scheduled to track Apollo 6 on a "best-effort" basis, consistent with the DSN commitments to other flight projects. Also, it was mutually recognized that the angular-tracking-rate limitation of the DSN 85-ft antennas might preclude continuous coverage on certain pre-injection earth-orbital passes; however, it was considered a worthwhile experiment to determine how well the DSN stations with MSFN wings could handle such a pass. Consequently, the MSFN developed a special "wing-prime evaluation plan" to:

(1) Evaluate the performance of the 85-ft-antenna stations.

(2) Evaluate the current operational procedures at the 85-ft-antenna stations.

(3) Provide valuable training for the 85-ft-antenna station crews.

As will be discussed below, the wing–prime evaluation plan produced relatively little data due to the Apollo 6 mission anomalies. Though the full effect of these anomalies has not yet been assessed, it is reasonable to expect that the evaluation tests will be repeated on a future suitable mission.

Pioneer DSS MSFN wing. Like the Goldstone MSFN (85-ft-antenna) Station, the MSFN wing at the Pioneer DSS (Fig. 8, p. 28, in SPS 37-50, Vol. II) contains two complete receiving and transmitting systems to simultaneously communicate with the CSM and the S-*IVB* whenever they are mutually within the beam. Acquisition of the *Apollo 6* spacecraft in earth orbit required four operators, though in critical mission phases up to six operators can be employed. The *Apollo* spacecraft are acquired by pointing the antenna at the expected horizon bearing angle, while the transmitter/exciter operator sweeps the uplink frequency in such a manner as to "capture" the spacecraft transponder, which in turn causes the downlink to be similarly swept in frequency. The station's receiver operators tune to a frequency offset from the nominal by the expected doppler shift and await capture by the sweeping downlink. Two-way capture is detected by the resulting sweep of the station receiver, which is nearly synchronous with the exciter

sweep. (The offset is proportional to the signal's round-trip time.) After two-way capture, the exciter sweep is decayed to the nominal uplink frequency, and the transmitter is locked to the rubidium frequency standard. Good-quality two-way tracking data are then obtained.

Although the premission nominal trajectory predicted that the first orbital revolution pass over the Goldstone MSFN Station and the Pioneer DSS would be quite close to the stations' horizon, it was felt that the second orbital revolution would be sufficiently high to afford a reasonable time to execute part of the wing–prime evaluation plan, yet not so high as to create overly excessive antenna rates. The *Apollo 6* earth-orbital insertion anomaly caused the first orbital revolution pass to be near-perigee, with the result that the track was within the Pioneer DSS antenna's predicted limits for most of the pass. The Pioneer DSS MSFN wing passively tracked (three-way with the Goldstone MSFN Station) during the second

Fig. 6. MSFN wing at Tidbinbilla DSS

orbital revolution, though some data were lost around the time *Apollo 6* crossed the station's meridian due to the higher-than-anticipated angular rates. The evaluation activity scheduled for the post-injection *S-IVB* trajectory was cancelled when the engine did not restart. Pioneer DSS did, however, passively track the *S-IVB*, which was still in earth orbit on the third revolution.

With the cancellation of this wing–prime evaluation plan, the Pioneer DSS MSFN wing was released from further *Apollo 6* support, and the configuration freeze (established 00:00 GMT on March 31) was terminated at 18:40 GMT on April 4.

Tidbinbilla DSS MSFN wing. In contrast to the Pioneer DSS MSFN wing, the Tidbinbilla DSS MSFN wing (Fig. 6) was expected to experience a reasonable view of *Apollo 6* on the first orbital revolution, but not on the second. Due to the insertion anomaly which placed the earth-orbital-phase apogee (196 nmi) near Australia, both revolutions were tracked, with neither exceeding the station antenna's angular-rate capability. All scheduled wing–prime evaluation plan "handovers" between the Tidbinbilla DSS MSFN wing and the prime Honeysuckle (Canberra) MSFN Station were accomplished during the first orbital revolution. Since the stations had not been expected to have good visibility of *Apollo 6* on the second revolution, no handovers were scheduled. The MSFN Honeysuckle Station maintained two-way lock and the

Tidbinbilla DSS MSFN wing maintained three-way lock throughout the second-orbital-revolution pass. The MSFN reported no problems on either pass, and preliminary indications were that the evaluation-plan data would be satisfactory. The injection-burn *Apollo 6* anomaly cancelled further evaluation tests at the Tidbinbilla DSS MSFN wing, and the station was released from "mission status." The configuration freeze (established 00:00 GMT on March 31) was terminated at 18:40 GMT on April 4.

Robledo DSS MSFN wing. Had the *Apollo 6* mission been nominal, the prime Madrid MSFN Station and the Robledo DSS MSFN wing (Fig. 7) would have had 8.5-h view period of the injected *S-IVB*; hence, the wing–prime evaluation plan tests were concentrated heavily at these stations. Due to its northerly latitude, Madrid was not scheduled to see either the first or the second earth-orbital passes. Even so, both stations were staffed and ready during the countdown and launch of *Apollo 6* and remained in a ready condition throughout the mission. Because the injection burn did not occur, neither station had visibility of either the *S-IVB/IU* or the CSM,[5] and with the cancellation of the evaluation plan, Robledo was released from "mission status." The configuration freeze (established 00:00 GMT on March 31) was terminated at 18:40 GMT on April 4.

---

[5]The mission profile was such that Madrid would not have CSM visibility, even on the high-apogee pass.
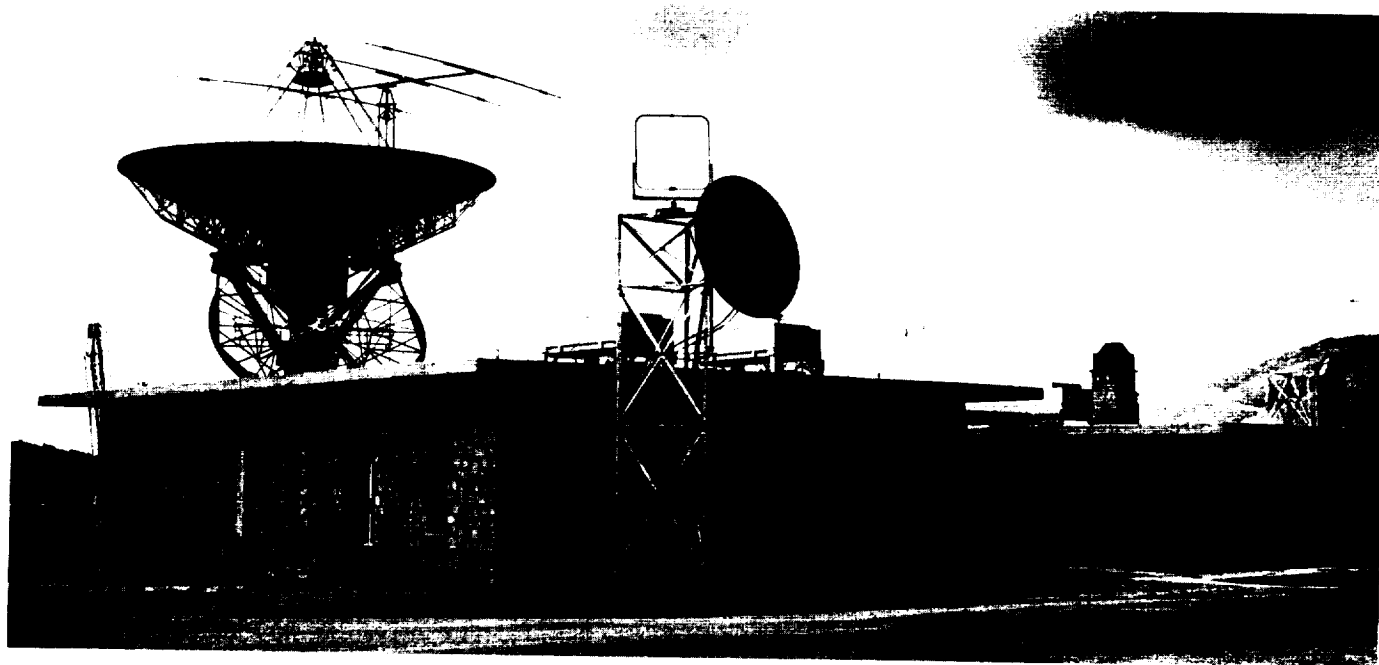
Fig. 7. MSFN wing at Robledo DSS

III. Advanced Engineering

A. Tracking and Navigational Accuracy Analysis

1. DSN Inherent Accuracy Project, *T. W. Hamilton and D. W. Trask*

The DSN Inherent Accuracy Project was formally established by the DSN Executive Committee in July 1965. The objectives of the project are:

(1) Determination (and verification) of the inherent accuracy of the DSN as a radio navigation instrument for lunar and planetary missions.

(2) Formulation of designs and plans for refining this accuracy to its practical limits.

Achievement of these goals is the joint responsibility of the telecommunications and systems divisions of JPL. To this end, regular monthly meetings are held to coordinate and initiate relevant activities. The project leader and his assistant (from the systems and telecommunications divisions, respectively) report to the DSN Executive Committee, and are authorized to task project members to (1) conduct analyses of proposed experiments, (2) prepare reports on current work, and (3) write descriptions of proposed experiments. The project is further authorized to deal directly with those flight projects using the DSN regarding data-gathering procedures that bear on inherent accuracy.

The various data types and tracking modes provided by the DSIF in support of lunar and planetary missions are discussed in SPS 37-39, Vol. III, pp. 6–8. Technical work directly related to the Inherent Accuracy Project is presented in SPS 37-38, Vol. III, and in subsequent *Deep Space Network* SPS volumes, and is continued in the following sections of this volume.

Considerable progress has been made in the analysis of the doppler residual anomalies of lunar-orbiting spacecraft since the previous status report of this investigation (SPS 37-47, Vol. II, pp. 13–15). One particularly fruitful area is a correlation of the doppler residuals with the spacecraft sub-lunar track. These two-way doppler residual anomalies commonly reach a magnitude of 100 mm/s which is large compared to the normal "visible" doppler noise of 0.1 mm/s. However, the size of these anomalies is consistent with what could be expected from local variations in mass distribution relatively near the lunar surface.

Subsection 2 shows that with respect to the same sub-lunar region, the residuals are similar for different orbits of the same spacecraft as well as for two different spacecraft. Previous investigations that looked for these correlations met with little success primarily due to two reasons: First, the existing lunar maps lack both the resolution and accuracy necessary to obtain a 1:1 correlation

between the mass distribution, as shown on the maps, with the actual residual anomalies. This analysis only establishes the similarities of residuals from spacecraft flying over the same region and is not a correlation between the residuals and features as shown on the lunar maps. Second, the doppler residuals become a function of the data span fit if either a too long or too short data arc is processed. This analysis found that, between these bounds, the doppler residuals become relatively invariant with the data span and, hopefully, directly reflect the lunar gravity anomalies in the vicinity of the spacecraft sub-lunar region.

Subsection 3 extends the work reported in SPS 37-50, Vol. II on an analytical procedure for determining the approximate accuracy obtainable from two-way doppler tracking of a deep-space probe during the early stages of planetary encounter when the effect of the target planet is still negligible. This subsection further describes how the effect of the target planet's gravity can be incorporated into the approximate solution, permitting an accurate estimate of the navigational accuracy throughout the planetary encounter phase. As in *Subsection 2*, favorable comparisons are made with the more time-consuming but sophisticated orbit determination programs. The ability to rapidly compute such navigational accuracy estimates considerably simplifies the study of guidance requirements for future missions.

Next, *Subsection 4* describes the determination of the selenographic location of *Surveyor VII*, the geographic location of the DSS, the utilization of tracking data obtained during the post-lunar touchdown phase of this mission, and the sensitivity of these solutions as a function of the recent lunar ephemeris improvements. This analysis parallels that of *Surveyor VI* reported in SPS 37-50, Vol. II, pp. 110–124. As with *Surveyor VI*, the two-way doppler "observed minus computed" residuals sets exhibit long-term periodicity and diurnal signatures. The long-term periodicities are lunar-ephemeris-dependent, while the diurnal signature has a number of suspected causes, among which are imperfections in the tropospheric refraction corrections applied to the doppler, ionospheric charged particle effects (not taken into account in this analysis), and the remaining inadequacies in the lunar motion model.

Spacecraft navigational capability depends not only on the ability to model the force exerted on the spacecraft by the solar system, but also on the modeling of forces generated within the spacecraft (e.g., gas leakage from the spacecraft). Aspects of this problem are discussed in *Subsections 5* and *6*. *Subsection 5* describes the effect of gas venting from the infrared spectrometer that will take place during the encounter phase of the *Mariner* Mars 1969 mission. This effect is expected to exceed 100 mm/s as compared to the 0.4 mm/s expected "visible" noise on the two-way doppler data during this time period. *Subsection 6* discusses a dynamic programming technique for computing the angular momentum that is transferred in cross directions when firing unbalanced attitude control jets, and is an extension of the work described in SPS 37-47, Vol. II, pp. 21–27.

2. Consistency of Lunar Orbiter Residuals With Trajectory and Local Gravity Effects,
P. M. Muller and W. L. Sjogren

a. Introduction. This subsection describes one phase of the effort devoted to analyzing the doppler tracking data from the five NASA *Lunar Orbiter* missions in which residuals of 100 mm/s have been observed. These residuals are three orders of magnitude larger than the previously observed lunar spacecraft tracking data residuals. There are two primary goals: (1) to obtain a description of the moon's gravity field for scientific interest and application, and (2) to obtain a representation of the moon's gravity field adequate for *Apollo* operations. A discussion of possible applications to *Apollo* and other scientific areas is given.

To date, the scientific analysis has proceeded with the immediate objective of determining the zonal and low-degree tesseral harmonics which describe the large scale variations from sphericity; however, for *Apollo* applications, more localized effects appear to be important since precise short-term prediction of spacecraft position is a requirement. The low-degree harmonics are apparently not adequate for this purpose.

A more intensive study of the short period fluctuation in the doppler data was initiated as it was noticed throughout the *Lunar Orbiter* Project that the doppler data exhibited short period fluctuations that could not be accounted for by any moon model then available. This suggested that either (1) the doppler data was in error, (2) the doppler data was being analyzed incorrectly, or (3) the moon is rougher than was anticipated. By a process of elimination, it is concluded in Ref. 1 that the moon was probably rougher in the sense that there are harmonic coefficients of high order large enough to affect the doppler data.

Short period effects suggested correlation with surface features of the moon, or at least with positions on the

Table 1. Probe conditions in selenocentric Cartesian coordinates

Source	III-E 1-B*	III-E 1-A	III-E 2-D	III-E 2-C	III-E 3	III-E 4-B	III-E 4-A	I-B 1	I-B 2	II-B	IV-C	V-C
x	•	-2038.527	•	-1951.21	1864.971	•	-435.091	2327.34	2055.469	2435.14	-5518.539	-588.6738
y		222.756		576.80091	-32.9292		-1363.37	-346.9167	-2306.28	1513.20	1166.0388	-1184.352
z		-48.4853		281.3003	262.0641		-1310.581	431.3395	-367.888	1080.60	107.51312	-2648.3518
Dx		-0.080334		-0.450305	-0.092526		1.563907	-0.371742	0.562046	-0.96697	0.1203467	0.3988729
Dy		-1.107033		-1.032102	1.222368		-0.334627	1.388035	0.879622	0.591078	0.17154097	1.0701989
Dz		-1.01804		-1.007199	1.101003		-0.058935	0.4370867	0.4750692	0.360331	-0.622698	-0.2735364
Epoch and time, h:m:s		Aug. 30, 1967 20:55:00		Aug. 31, 1967 00:50:01	Sep. 5, 1967 15:05:00		Sep. 5, 1967 18:50:00	Aug. 25, 1966 16:02:00	Aug. 26, 1966 05:19:00	Nov. 23, 1966 05:45:00	Jun. 13, 1967 20:28:00	Aug. 13, 1967 10:05:00
Latitude, deg		-2.805		1.96629	7.01308		-20.96	12.0989	9.2030	7.0447	-2.6104	-42.4594
Longitude, deg		251.132		235.8874	2.6391		254.28	270.72	219.34	210.667	192.925	199.9674
Pericenter passage, km		143.6		144.0	132.0		132.38	40.02	40.639	44.0	68.3	96.1
Epoch of pericenter passage, date; h:m:s		Aug. 30, 1967 21:54:57.3		Aug. 31, 1967 02:15:54.3	Sep. 5, 1967 17:05:16		Sep. 5, 1967 19:15:46.3	Aug. 25, 1966 16:32:53.8	Aug. 26, 1966 06:18:05.6	Nov. 23, 1966 06:40:59.9	Jun. 13, 1967 22:59:49.1	Aug. 13, 1967 11:05:45.96
Eccentricity		0.043696		0.043754	0.049471		0.0492825	0.33383	0.333538	0.338188	0.518333	0.276820
Inclination, deg		20.91		20.95	21.01		20.975	12.119	12.01	11.875	85.4	96.1
Semimajor axis, km		1967.8		1967.93	1968.31		1967.619	2669.39	2669.80	2689.64	3753.148	2536.123
Lon period		57.8		55.8	332.9		331.1	2.0	334.7	32.0	10.9	15.3
Lat period		-2.0		-2.0	-4.0		-3.95	-1.06	-1.166	7.5	-5.2	1.6
Period, min		130.55		130.56	130.54		130.54	206.41	206.38	208.62	344.0	191.1

* III-E 1-B — Lunar Orbiter III; phase B, data package 1, plot B (JPL numbering system).

° III-E 1-B, III-E 1-D, and III-E 4-B are one orbit following III-E 1-A, III-E 2-C and III-E 4-A, respectively.

lunar surface, but early attempts at finding such correlations were unsuccessful. However, a breakthrough in this direction was effected when the *Lunar Orbiter III* final phase (III-E) data were analyzed. It was discovered that when doppler residuals from single-orbit data fits were examined, the resulting residuals correlated closely with positions on the moon, and were consistent from orbit to orbit. Two factors were necessary for this correlation: (1) the use of only one orbit of data in the orbit determination, and (2) the use of a simple harmonic model of the moon (e.g., spherical or triaxial moon).

b. Background. The authors believed the basic hypothesis that the tracking data residuals could be correlated with the spacecraft sub-lunar trajectory. A simple calculation relates spacecraft accelerations, as determined from the residuals, to the accelerations one could reasonably expect from the variations in lunar terrain.

The observation of residuals such as those in Fig. 1 yields common variations of 0.5 Hz in a period of 5 min. This corresponds to an acceleration of 0.1 mm/s^2 and is equivalent to a perturbing mass equal to 10^{-6} that of the moon at a distance of 190 km, i.e., $m = ar^2$. This amount of mass-differential is contained in a depression 100 $\times$ 100 $\times$ 2 km (lunar density = 3.3).

These numbers are in good agreement with the observed condition of the lunar surface. If the local irregu-

larities are large enough to cause the perturbations, perhaps they are also responsible.

Figure 2 shows the variations caused by a set of alternating mass points that are 10^{-6} the lunar mass, equally spaced in time on the lunar surface, directly below a spacecraft trajectory (*Lunar Orbiter III* [III-E]). They were produced by differencing the doppler obtained from a spherical moon trajectory (unperturbed) and the perturbed trajectory resulting from the mass points. Table 1 lists orbital characteristics for all trajectories studied.

Figure 1 indicates another clue to the applicable method. A glance at the plot shows that the residual frequencies range between 5 and 15 cycles per orbit. This is far too high to be handled by the current harmonic models for the moon which only go up to degree 4 to 7. Figures 1, 3, and 4 compare single-precision orbit determination program (SPODP) fits to the same data using triaxial, COSPAR, and JPL No. 87 harmonic sets. (The coefficients are listed in Table 2.) The first model was used in this study due to its superiority for short arcs. The larger harmonic models were intended to fit the longer arcs. They are applied well in that context, but fail to adequately fit short arcs.

Additional confirmation of the residual frequencies is contained in Fig. 5 which is a harmonic spectrum of the residuals plotted in Fig. 1. The lack of low-order frequency
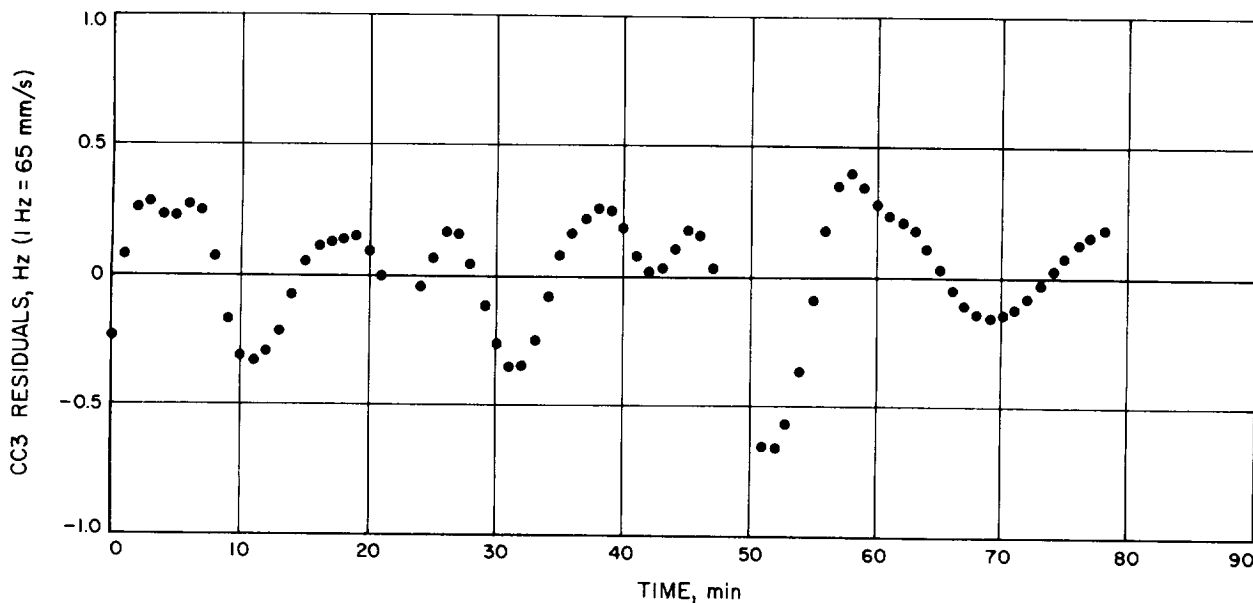
Fig. 1. ODP fit to one orbit III-E-3 using triaxial moon

is due to the short data span, but the plot is representative of the highest frequency residuals observed. It strongly indicates that low-order harmonic expansions of the lunar field will not improve the short arc fits.
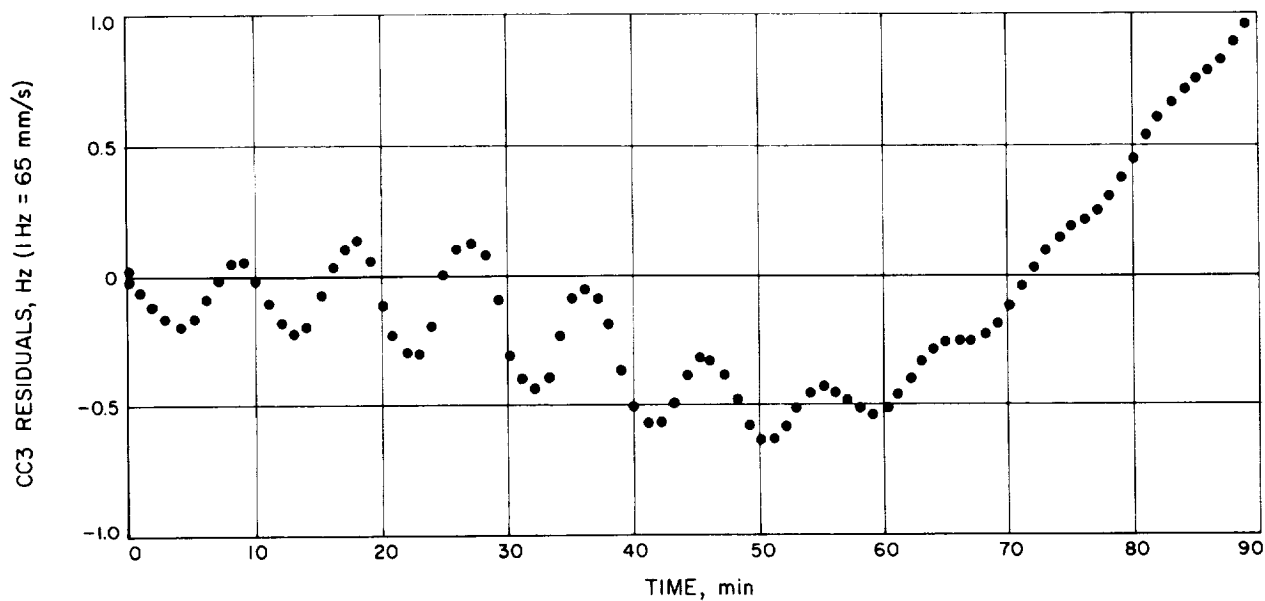
Fig. 2. Integrated trajectory residuals
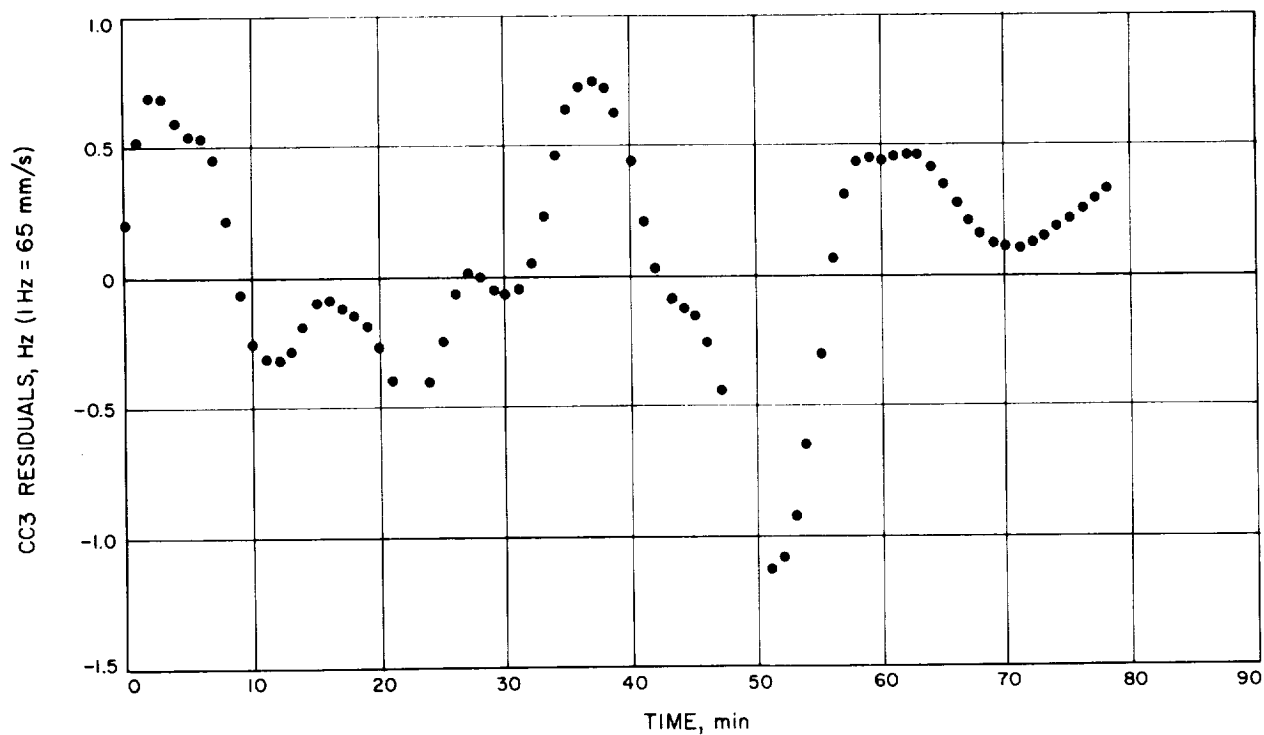
Fig. 3. Fit to one orbit III-E-3 using COSPAR harmonics
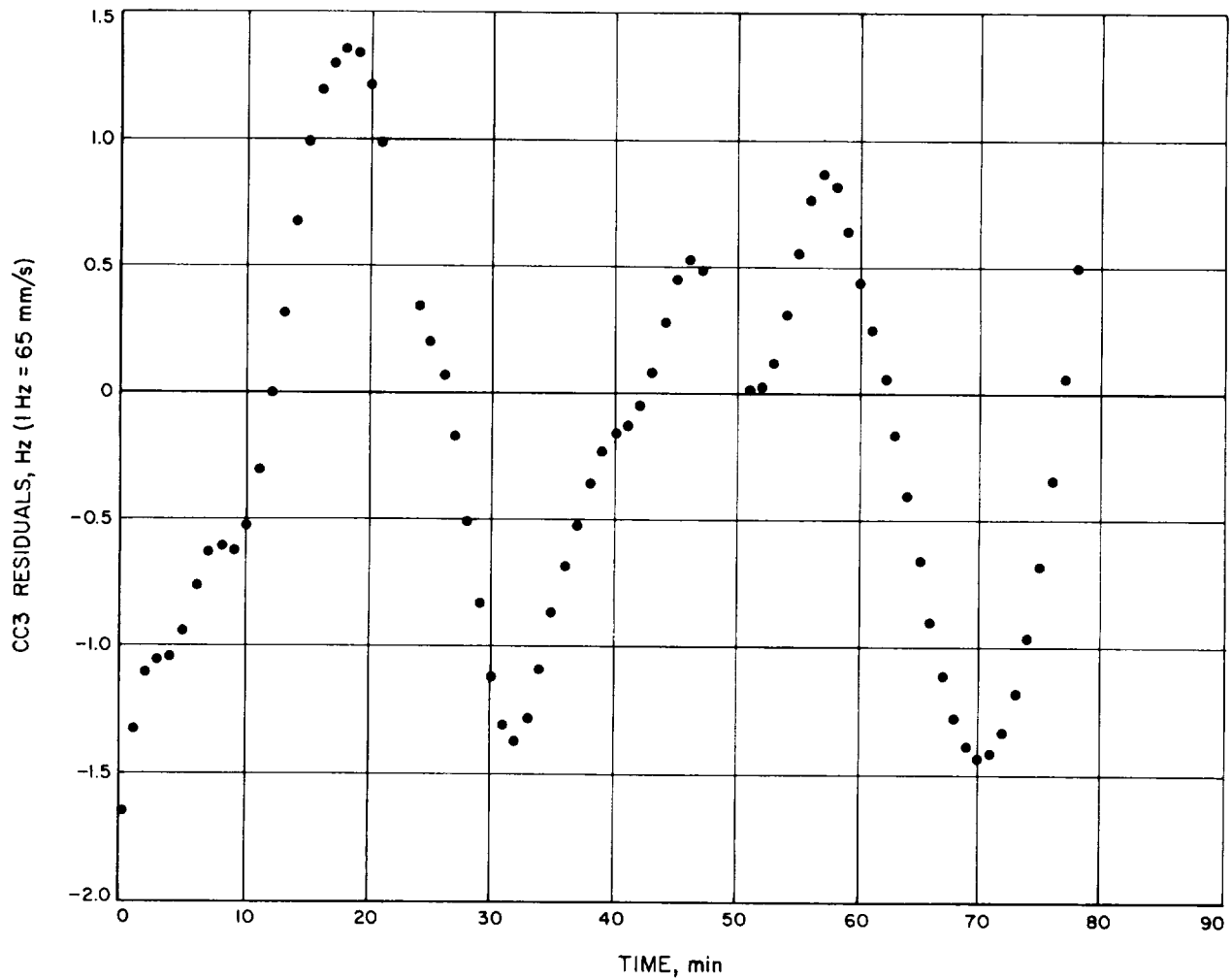
Fig. 4. Fit to one orbit III-E-3 using JPL No. 87 harmonics

Fig. 5. Relative harmonic spectrum for III-E-3 one-orbit residuals
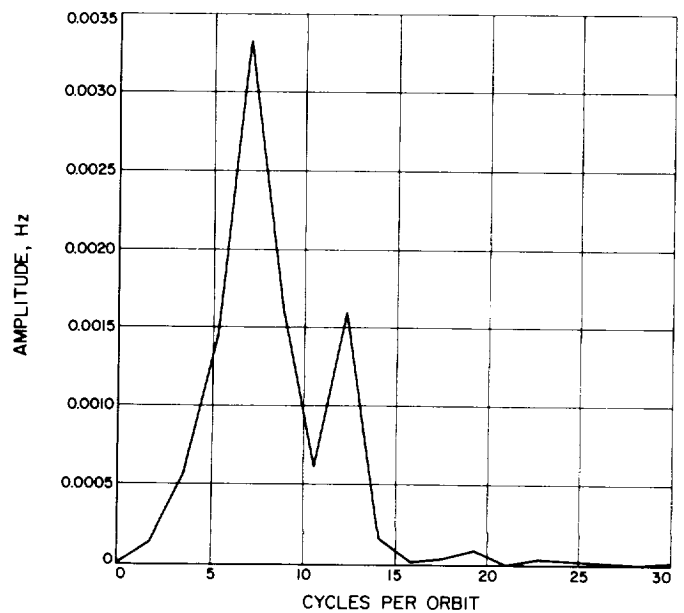
Table 2. Lunar harmonic coefficient sets

Nominal triaxial					
J_{20} = 0.2073E-3			C_{22} = 0.2030E-4		
COSPAR[a]					
J_{20}	0.2059E-3	C_{22}	0.2042E-4	S_{21}	0.8E-6
30	0.3373E-4	32	0.1294E-4	22	−0.342E-5
40	−0.79799999E-5	33	0.317E-5	31	0.1762E-4
50	0.55049999E-4	42	0.11E-6	32	−0.147E-5
		43	−0.81999999E-6	33	−0.43E-6
		44	0.69999999E-7	41	0.391E-5
		51	−0.38499999E-5	42	0.72E-6
		52	0.342E-5	43	−0.1E-7
		53	−0.70999999E-6	44	0.11E-6
		54	−0.8E-7	51	0.82899999E-5
		55	−0.3E-7	52	−0.203E-5
				53	−0.77999999E-6
				54	−0.13E-6
				55	0.3E-7
JPL No. 87[b]					
J_{20}	0.1907793E-3	C_{21}	0.25866226E-5	S_{21}	0.27363695E-5
30	0.20475193E-4	22	0.89647364E-5	22	−0.10877982E-4
40	−0.13195038E-4	31	0.33962867E-4	31	0.10463113E-4
50	−0.20221297E-5	32	−0.40269495E-6	32	0.304146E-5
60	0.13716878E-4	33	0.41107037E-5	33	−0.30990218E-5
70	−0.40089559E-4	41	−0.10998270E-4	41	0.78724356E-5
80	0.20652902E-4	42	0.42089126E-5	42	0.52514076E-6
		43	0.23212521E-5	43	−0.10259718E-5
		44	−0.58859199E-6	44	−0.20105803E-6

[a]IQSY/COSPAR Assemblies, London, England, July, 1967.

[b]An interim set of coefficients; not necessarily definitive (supplied by J. Lorell, Section 311).

c. Method. There are three basic categories for residual errors after the fit to a spacecraft trajectory:

(1) Gravity, solar pressure, gas jets, and other forces that act directly upon the spacecraft.

(2) Errors and physical deformations affecting the data tracking system, i.e., temperature couples to the transponder or tropospheric refraction.

(3) Software problems wherein the computer programs introduce residuals because of model limitations or program errors.

Error sources in category (3) would be eliminated by producing the same residuals with an independent program such as a polynomial fit to the raw tracking data. Forces and effects in category (2), and those in category (1), except for lunar gravity,[1] would be eliminated if spacecraft produced the same residuals when flying simi-

[1]Coupling between gravity-gradient forces on the spacecraft with gas-jet reactions was eliminated in Ref. 1 because of insufficient amplitude.

lar trajectories. This study was undertaken using the above approach.

Fits to single orbits were used throughout, employing a basic (spherical or triaxial) potential model. As noted in *Paragraph a*, this was a necessary constraint in order to produce consistent fits which could fruitfully be compared.

d. Results. Before comparison of the residuals could be made with confidence, it was first necessary to demonstrate that the SPODP (Ref. 2) could produce consistent solutions. Earlier attempts to compare residuals (using 2 to 3 orbit fits) were unsuccessful because the SPODP will not consistently fit the same data region unless the data span is one orbit or less. Studies of the SPODP limitations for longer arcs are in progress at the present time, and results of that work will be reported later.

To demonstrate consistency, short *Apollo*-type (III-E, eccentricity ≈ 0.) arcs were fit using different epochs and lengths of data span. Results are shown in Fig. 6. This agreement gave confidence in comparisons between trajectories providing the outlined fitting policy was followed.

For the independent software, a new program and system (devised by Drs. P. Dyer and S. McReynolds of Section 311) was employed. It fits a polynomial directly to the raw doppler data, removing the station motion with a second degree polynomial, and the spacecraft motion with a second order elliptical function based upon the period of the orbit involved.[2] The scheme is documented in a JPL Technical Report[3] that also contains a repetition of the experiments in order to eliminate the possibility of coincidence.

The residuals shown in Figs. 7 and 8, which compare the sample trajectories, have been plotted with respect to an adjusted time parameter. In each case, the epoch has been altered to be a point at which the two trajectories are most nearly above the same lunar location. This was done to show the residual agreement as a function of the sub-lunar trajectory. It was discovered that the epoch difference could be arrived at either by consulting the trajectory listings from SPODP or by simply overlaying the original plots and reading the time difference. This

[2]A number of earlier attempts to fit the raw doppler at JPL had failed, and success of this particular system is considered by the author to have been a significant advancement.

[3]Muller, P. M., and Sjogren, W. L., "Consistency of Lunar Orbiter Residuals With Trajectory and Local Gravity Effects," Technical Report 32-1307 (in preparation).

agreement confirmed the contention that the residuals are tied to the lunar surface.

Figure 7 by itself covers the heart of the study. Plot (a) of Fig. 7 is a fit to an *Apollo*-type orbit (low eccentricity), *Lunar Orbiter III*, Phase E (*Apollo* trajectory), data pack-

age 1 (an arbitrary JPL numbering system to identify the data ranges; e.g., III-E 1-A as in Table 1). Plot (b) is another ODP fit, but to the same spacecraft just two orbits later. The trajectories differ by only 100 km, with a perilune of 150 km, and so are essentially identical as far as the perturbations are concerned.
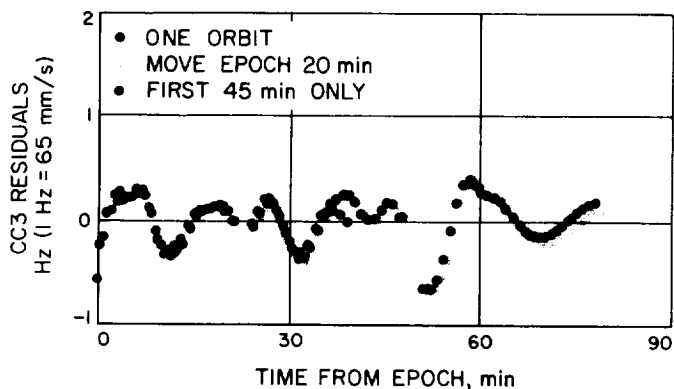
Fig. 6. ODP fit to III-E-3

TIME, min
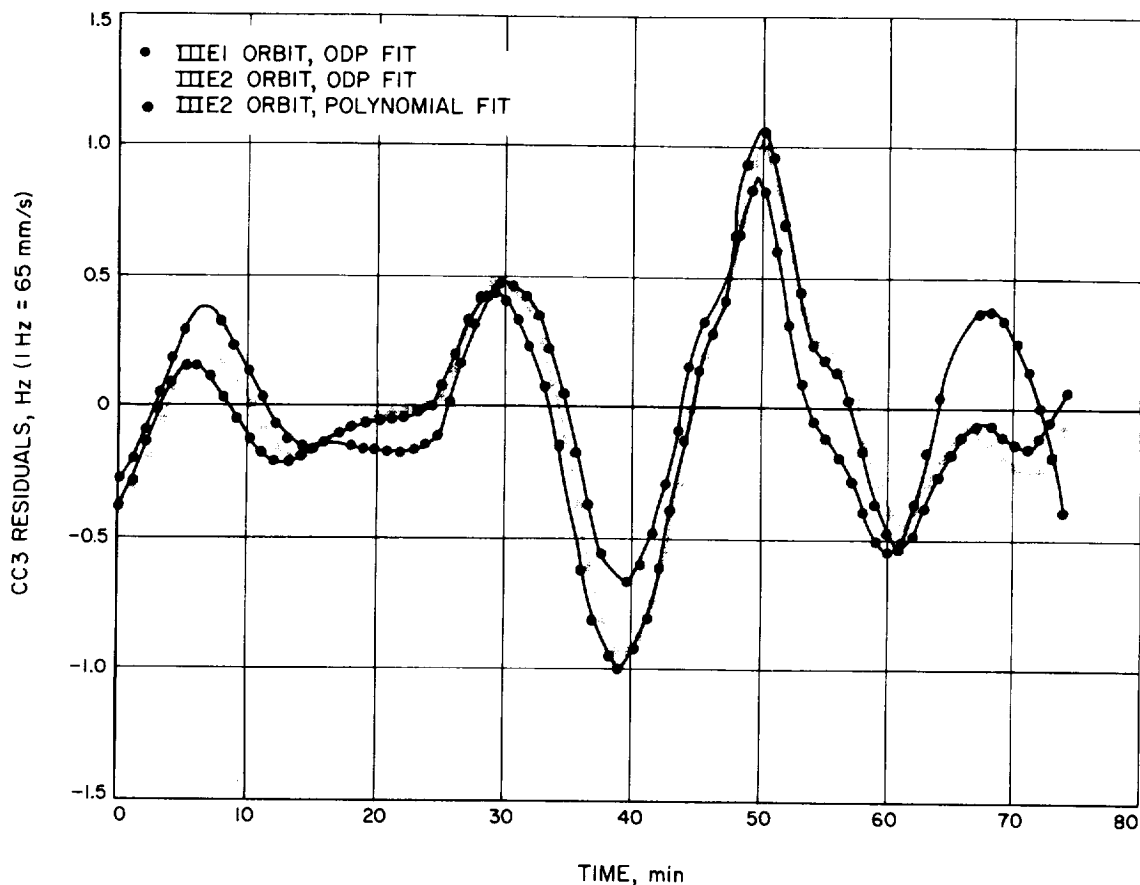
Fig. 7. Comparison of III-E-1 and III-E-2 residuals
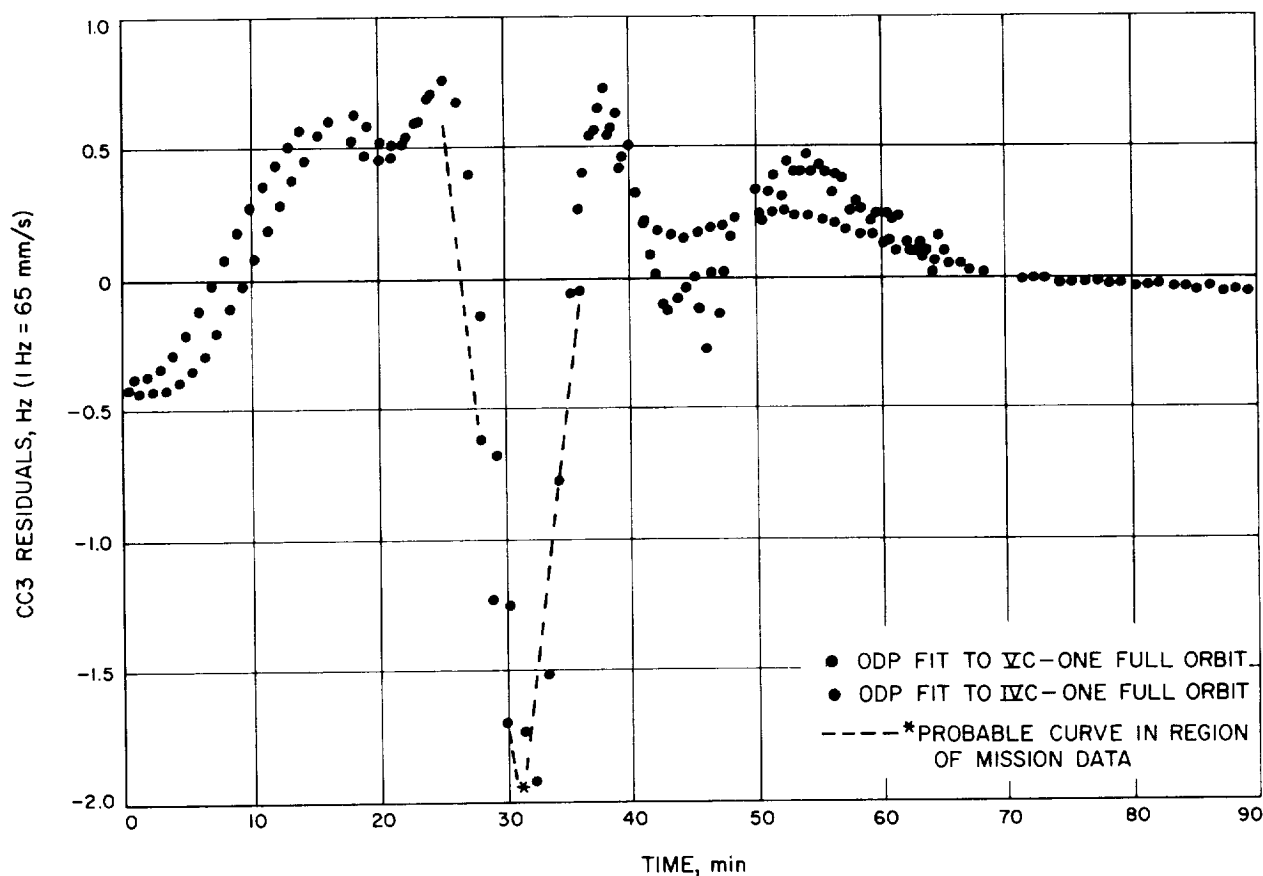
Fig. 8. Comparison of IV-C and V-C residuals

Plot (c) of Fig. 7 is a polynomial fit to the same data as plot (b). The agreement between this independent software system and SPODP eliminates both as a possible cause of the residuals. The independent software check builds confidence that SPODP is yielding the true residuals.[1]

Figure 1 is the same spacecraft some 5 days later. The change in residuals from Fig. 7 indicate that they do vary with time.

The final test is two different spacecraft flying similar trajectories, weeks apart. That case is illustrated in Fig. 8 with two high-eccentricity polar orbiters, Lunar Orbiters

IV C and *V* C, respectively. The two trajectories differ by some 120 km, and perilune is of the same order. As shown in Table 1, the orbital parameters, most notably eccentricity, differ substantially. The sub-lunar trajectory, however, is similar, and that fact manifests itself in the agreement between residuals. The very large plunge in the residuals constitutes the most spectacular example observed in the study. Other comparisons are given (see Footnote 3) with similar results.

Many of the largest residual signatures were successfully matched (by W. Sjogren of Section 311) with visible features on the moon such as maria and rough highlands. These large residual variations appear, therefore, to correlate with the largest lunar elevation changes.

This does not imply that *all* residuals correlate in this manner, and, in fact, the author failed to find consistent correlations between the more typical residual signatures and elevations indicated on the lunar maps.

e. Possible applications to future work. Under the assumption that the doppler residuals from each orbit of

---

[1] "True" residuals are those directly attributable to, and correlated with, the sub-lunar trajectory and are invariant under changes to the fit-epoch and data span within the guidelines (one orbit maximum, basic harmonics). The polynomial fits show both that the software is acceptable and that the observed residuals are true in the above sense. J. Lorell and W. L. Sjogren (Ref. 1) obtained a favorable comparison between the JPL and Langley Research Center programs for two orbit fits, and thereby had previously eliminated gross program failure as the cause.

a *Lunar Orbiter* spacecraft are a direct measure of the local gravitational field, the immediate plan is to estimate some small set of mass points along the trajectory of a single orbit. If this is successful, the independent reduction of many sequential orbits will be attempted. As a mass-grid is built up from these solutions, consistency (or the lack thereof) can be demonstrated.

If consistent and successful, these solutions could be statically reduced to a high-order harmonic set (as proposed by J. Lorell of Section 311). In addition, it might be possible to directly correlate the derivatives of the doppler signatures with local terrain and/or gravity. Either way, it may well turn out that *Lunar Orbiter* was an excellent "flying gravimeter."

The problem of the hidden side of the moon remains, since there are no data available to solve it directly. All proposed indirect methods of solution appear to fall back upon measuring variations in orbital parameters or spacecraft coordinates over many orbits. In order to fit arcs of two or more orbits, it may be possible to solve out the effect of the unseen lunar surface by considering its total effect to be a solve-for instantaneous spacecraft maneuver. This might permit an improved fit to more than a single orbit, but will not solve the hidden side problem except for the single arc in question.

The *Apollo* Project is concerned with the accuracy of short-arc fit-prediction capabilities. A considerable effort will be made to attain an improvement of at least one magnitude in this area, which appears to be the real strength of the short-arc point-mass approach.

f. Conclusions. In order to obtain consistent residuals, SPODP must be run with data arcs of one orbit and minimal (triaxial or spherical) harmonic coefficients. Using that approach, the residuals from one spacecraft correlate with those from another, providing they fly the same or similar sub-lunar trajectories. This ties the residuals to the local lunar gravitational field.

The frequencies observed in the residuals are too high to be effectively included in an harmonic expansion of the lunar potential unless the order of the model can be increased substantially. This further suggests the need for a different lunar potential model and a different approach to the problem if improvement in the fitting or predicting is to be achieved. It is possible that such a model would

best be derived directly from analysis of the residuals or solving for a mass-point grid on the lunar surface.

References

1. Lorell, J., and Sjogren, W. L., *Lunar Orbiter Data Analysis*, TR 32-1220. Jet Propulsion Laboratory, Pasadena, Calif., Nov. 15, 1967.

2. Warner, M. R., and Nead, M. W., *SPODP—Single Precision Orbit Determination Program*, Technical Memorandum 33-204. Jet Propulsion Laboratory, Pasadena, Calif., Feb. 15, 1965.

3. The Effect of Target Planet Gravity on the Estimate of Navigational Accuracy for a Deep Space Probe During the Planetary Encounter Phase,

L. Kingsland, Jr. and W. E. Bollman

a. Introduction. A previous article (SPS 37-50, Vol. II, pp. 90–93), discussed an analytical procedure for determining the approximate accuracy obtainable from the two-way doppler tracking of a deep space probe during the early stages of planetary encounter, when the effect of the target planet's gravity is still negligible. This article will describe how the effect of the target planet's gravity can be incorporated into the approximate solution, permitting an accurate estimate of navigational accuracy throughout the planetary encounter phase.

b. Background. The procedure for finding the estimate of navigational accuracy is similar to that of the previous SPS article and is reviewed below:

(1) The range rate between the observer on earth and the spacecraft is approximated by the Hamilton–Melbourne expression (SPS 37-39, Vol. III, pp. 18–23):

$$\dot{\rho} \approx \dot{r} + \omega r_s \cos \delta \sin \omega (t - t_0)$$

where $\dot{r}$ is the range rate between the center of the earth and the spacecraft and $\omega r_s \cos \delta \sin \omega (t - t_0)$ represents the approximate velocity component of the tracking station with respect to the earth's center along the direction to the spacecraft.

(2) The state variables to be estimated are the encounter parameters expressed in the **B** system:

$$\mathbf{B \cdot T}, \mathbf{B \cdot R}, T_r, C_3, \mathbf{S \cdot T}, \mathbf{S \cdot R}$$

(3) The partial derivatives of range rate with respect to the encounter parameters, Q, have the form of

$$\frac{\partial \dot{\rho}}{\partial Q_j} = a_j + b_j \cos \omega (t - t_0) + c_j \sin \omega (t - t_0)$$

(4) Obtain the partial derivatives of the observable $\dot{\rho}$ with respect to the n parameters to be estimated

$$\phi_{i_0} = \frac{\partial \dot{\rho}}{\partial Q_1}, \cdots , \frac{\partial \dot{\rho}}{\partial Q_n} \ (n \times 1 \text{ vector})$$

(5) The vector of partials is multiplied by itself and by a 1×1 weighting matrix $1/\sigma_i^2$, to form the matrix

$$J_i^* = \frac{1}{\sigma_i^2} \phi_{i_0}{}^T$$

(6) J_i^* is added to the accumulated matrix

$$J^* = J_1^* + J_2^* + \cdots + J_{i-1}^*$$

The effect of adding each term of the J_i^* matrix to the accumulating J^* matrix over one tracking pass is approximated by integrating each element of the J^* matrix over the duration of the pass. Integration of the sine and cosine terms produces constants which depend on the tracking pass duration. The coefficients a_j, b_j, and c_j, however, vary with time as the spacecraft approaches the planet and are therefore computed at sufficiently frequent intervals throughout the approach phase so that the J^* matrix is reasonably well approximated.

(7) Given an *a priori* covariance matrix, $\tilde{\Gamma}$, of the parameters to be estimated, the estimated covariance matrix is obtained as

$$\Gamma = (J^* + \tilde{\Gamma}^{-1})^{-1}$$

c. Method of solution. The partial derivative $\partial\dot{\rho}/\partial Q_j$ of step 3 is computed from

$$\frac{\partial \dot{\rho}}{\partial Q_j} \cong \left(\frac{\partial \dot{\rho}}{\partial Q_j}\right)_1 + \Delta \tag{1}$$

where

$\left(\dfrac{\partial \dot{\rho}}{\partial Q_j}\right)_1$ = the partial derivative assuming the spacecraft's trajectory is that of a heliocentric conic and the planet's mass is negligible. The procedure for computing this partial derivative was discussed in SPS 37-50, Vol. II, pp. 90–93.

Δ = the increment of the partial derivative due to the effect of the planet's gravitational attraction

$$\Delta = \left(\frac{\partial \dot{\rho}}{\partial Q_j}\right)_2 - \left(\frac{\partial \dot{\rho}}{\partial Q_j}\right)_3 \tag{2}$$

$\left(\dfrac{\partial \dot{\rho}}{\partial Q_j}\right)_2$ = the partial derivative assuming hyperbolic conic motion of the spacecraft with respect to the planet and assuming the velocity of the planet with respect to the center of the earth is a constant, thus neglecting the heliocentric motion of the spacecraft.

$\left(\dfrac{\partial \dot{\rho}}{\partial Q_j}\right)_3$ = the partial derivative assuming constant spacecraft velocity with respect to a massless planet and assuming the velocity of the planet with respect to the center of the earth is a constant, again neglecting the heliocentric motion of the spacecraft.

The effects of heliocentric conic motion are dominant during the early phases of encounter, but the effect of the planet's gravity becomes dominant closer to the time of encounter. The method described above permits a smooth transition in the computation of partial derivatives between the heliocentric and the planet-centered phases of the encounter.

d. Planet-centered computations. The equation for $\dot{r}$ that is used for the computation of $(\partial r/\partial Q_j)_2$ during the planet-centered phase is

$$\dot{r} = \frac{(\dot{\mathbf{R}}_p + \dot{\mathbf{R}}_{s/p}) \cdot \mathbf{r}}{|\mathbf{r}|} \tag{3}$$

where

$\mathbf{R}_p$ = the vector from the center of the earth to the planet

$\mathbf{R}_{s/p}$ = the vector from the planet to the spacecraft

$\mathbf{r}$ = the vector from the center of the earth to the spacecraft
$= (\mathbf{R}_p + \mathbf{R}_{s/p})$ (4)

Figure 9 shows the vector diagram for range rate near the planet. The vector expressions for radius and velocity of the spacecraft with respect to the planet referenced to the planet-centered $\hat{R}, \hat{S}, \hat{T}$ coordinate system are

$$\mathbf{R}_{s/p} = R_{s/p}\cos\alpha\,\hat{S} + R_{s/p}\sin\alpha\cos\theta\,\hat{T}$$
$$+ R_{s/p}\sin\alpha\sin\theta\,\hat{R} \tag{5}$$

EARTH
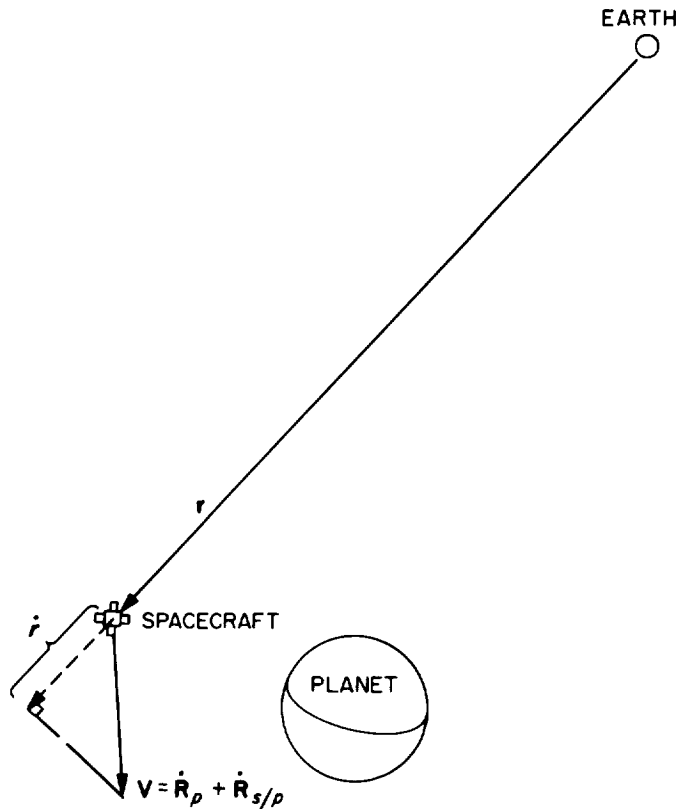
Fig. 9. Range-rate vector diagram

$$\dot{\mathbf{R}}_{s/p} = \left(V_\infty + \frac{\mu}{bV_\infty} \sin \alpha \right) \widehat{S} + \frac{\mu}{bV_\infty} (\cos \alpha - 1) \cos \theta \, \widehat{T}$$

$$+ \frac{\mu}{bV_\infty} (\cos \alpha - 1) \sin \theta \, \widehat{R} \tag{6}$$

where

$\widehat{S}$ = a unit vector along the approach asymptote

$\widehat{T}$ = a unit vector perpendicular to S and parallel to a given reference plane (such as the ecliptic)

$\widehat{R} = \widehat{S} \times \widehat{T}$, unit vector

α = the planet-centered angle measured from $-\widehat{S}$ to $\bar{R}_{s/p}$

b = the miss parameter

V_∞ = the hyperbolic excess speed

μ = the gravitational constant of the planet

θ = the orientation of the trajectory aiming point, measured clockwise from the $\widehat{T}$ axis to the miss parameter $\bar{b}$

These parameters are depicted in Fig. 10.

Substituting Eqs. (4), (5), and (6) into Eq. (3) yields:

$$\dot{r} = \frac{1}{r} \left[\dot{\mathbf{R}}_p \cdot \widehat{S} + V_\infty + \frac{\mu}{bV_\infty} \sin \alpha \right] [\mathbf{R}_p \cdot \widehat{S} - R_{s/p} \cos \alpha]$$

$$+ \frac{1}{r} \left[\dot{\mathbf{R}}_p \cdot \widehat{T} + \frac{\mu}{bV_\infty} (\cos \alpha - 1)(\cos \theta) \right]$$

$$\times [\mathbf{R}_p \cdot \widehat{T} + R_{s/p} \sin \alpha \cos \theta]$$

$$+ \frac{1}{r} \left[\dot{\mathbf{R}}_p \cdot \widehat{R} + \frac{\mu}{bV_\infty} (\cos \alpha - 1)(\sin \theta) \right]$$

$$\times [\mathbf{R}_p \cdot \widehat{R} + R_{s/p} \sin \alpha \sin \theta] \tag{7}$$

where

$$r = [R_p^2 + R_{s/p}^2 - 2(\mathbf{R}_p \cdot \widehat{S})(R_{s/p} \cos \alpha)$$

$$+ 2(\mathbf{R}_p \cdot \widehat{T})(R_{s/p} \sin \alpha \cos \theta)$$

$$+ 2(\mathbf{R}_p \cdot \widehat{R})(R_{s/p} \sin \alpha \sin \theta)]^{1/2} \tag{8}$$

The partial derivatives of $\dot{r}$, with respect to the encounter parameters, can then be obtained using the following equations relating elements of a hyperbolic orbit:

$$R_{s/p} = \frac{b^2}{a \left(1 + \dfrac{b}{a} \sin \alpha - \cos \alpha \right)} = a(e \cosh F - 1)$$

$$t - t_e = (-F + e \sinh F) \left(\frac{a^3}{\mu} \right)^{1/2}$$

$$e = \frac{(a^2 + b^2)^{1/2}}{a}$$

where

$a = \mu/V_\infty^2$, semi-major axis of the hyperbolic orbit

F = eccentric anomaly of the hyperbola

t = time of observation

t_e = time of closest approach (periapsis passage) of spacecraft to planet

e. Mariner Venus 67 example. An estimate of navigational accuracy was calculated for conditions corresponding to an orbit accuracy study performed for the planetary encounter phase of *Mariner* Venus 67.[5] The nominal trajectory considered was for a June 17, 1967 Venus arrival.

[5]Pease, G. E., "*Mariner* Venus 67 Orbit Determination Characteristics and Accuracy," June 9, 1967, (JPL internal document).
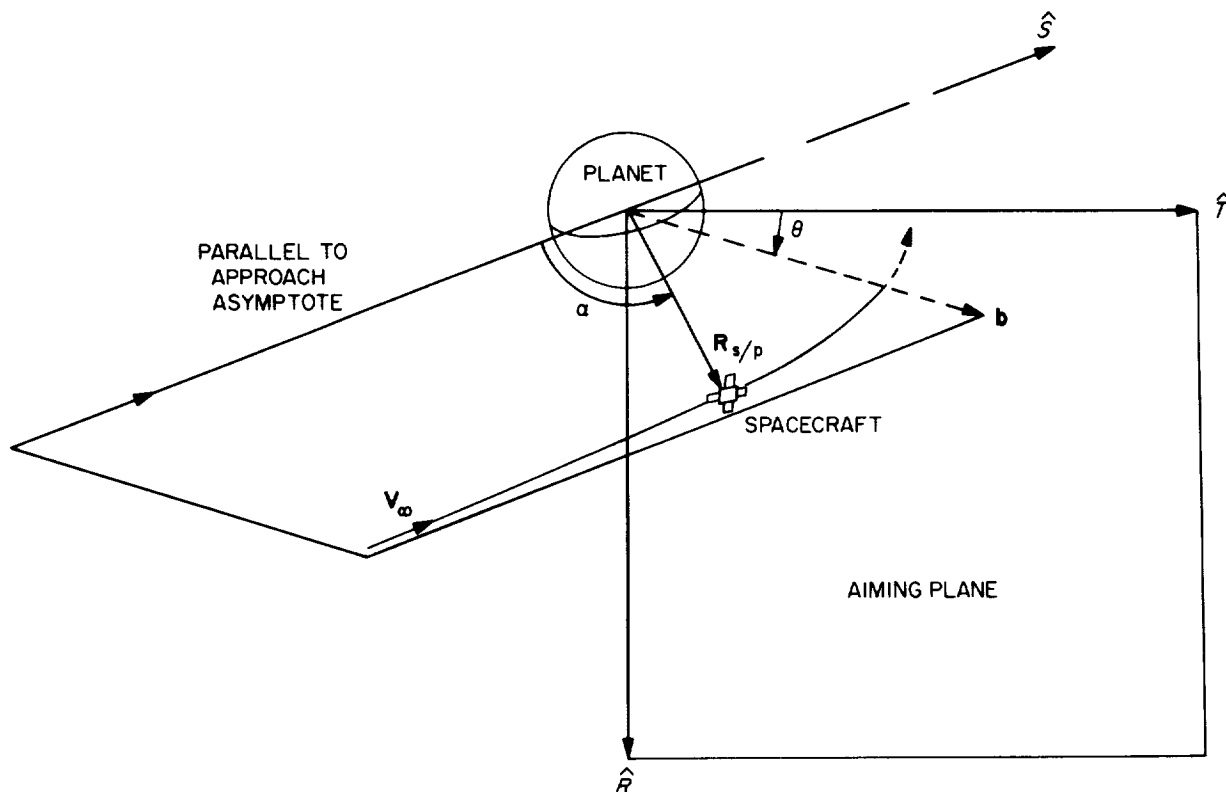
Fig. 10. Hyperbolic parameters

This example is a continuation of the example given in SPS 37-50, Vol. II, pp. .90–93, in which only the far-encounter phase was considered. The following *a priori* uncertainties were assumed:

$$\sigma_x, \sigma_y, \sigma_z = 1000 \text{ km}$$

$$\sigma_{\dot{x}}, \sigma_{\dot{y}}, \sigma_{\dot{z}} = 1 \text{ km/s}$$

$$\sigma_{\text{stn rad}} = 24 \text{ m}$$

$$\sigma_{\text{stn lon}} = 0.0005 \text{ deg}$$

The encounter parameters were as follows:

$$b = 25,000 \text{ km}$$

$$V_\infty = 3.113 \text{ km/s}$$

$$\theta = -32 \text{ deg}$$

Two stations tracking from E — 9 days and a data noise of $\sigma_{\dot{\rho}} = 0.005$ m/s were assumed. The results of the approximate solution are plotted in Figs. 11 and 12 for comparison with those obtained from the single-precision

orbit determination program (SPODP). Calculation of the estimate was performed on an IBM 1620 computer in double precision. Total required computation time for the data shown was about 40 min.

The results indicate reasonably good agreement with results obtained from the SPODP. The major difference is that the SPODP results indicated a fairly sharp transition in the uncertainty ellipse at E — 1 day, while the approximate solution resulted in a more gradual transition. However, the initial and final sizes and orientations of the uncertainty ellipse were reproduced with remarkable accuracy.

f. Conclusion. The approximate solution technique described in this article appears to offer a useful and practical procedure for performing navigational accuracy studies. Using relatively simple and rapid computation procedures, it produces orbit determination accuracy estimates that demonstrate fairly good agreement with those obtained from more complex and time-consuming orbit determination programs during both the distant approach and the near-planet phases of a planetary encounter sequence.
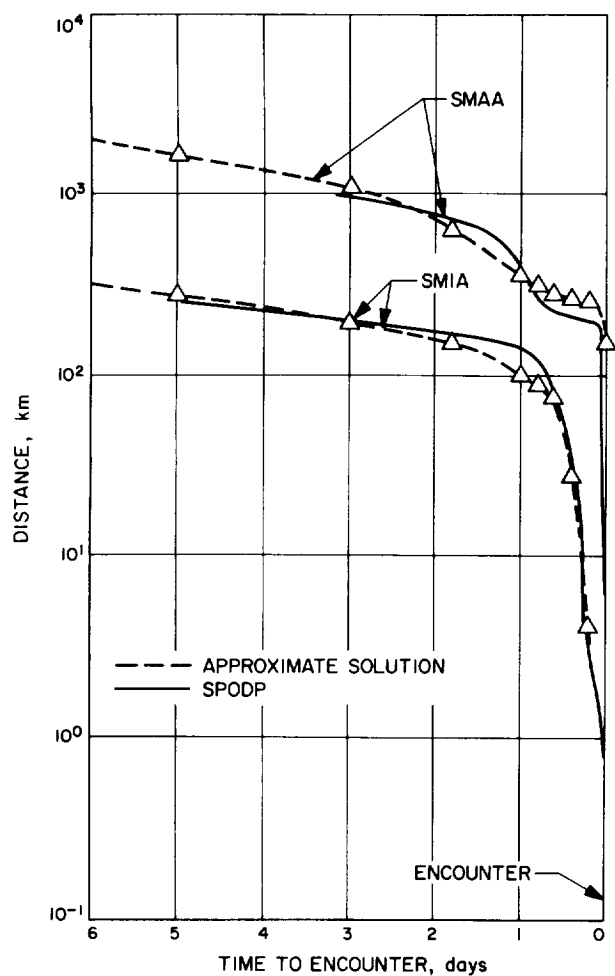
Fig. 11. Semimajor axis (SMAA) and semiminor
axis (SMIA) from doppler tracking
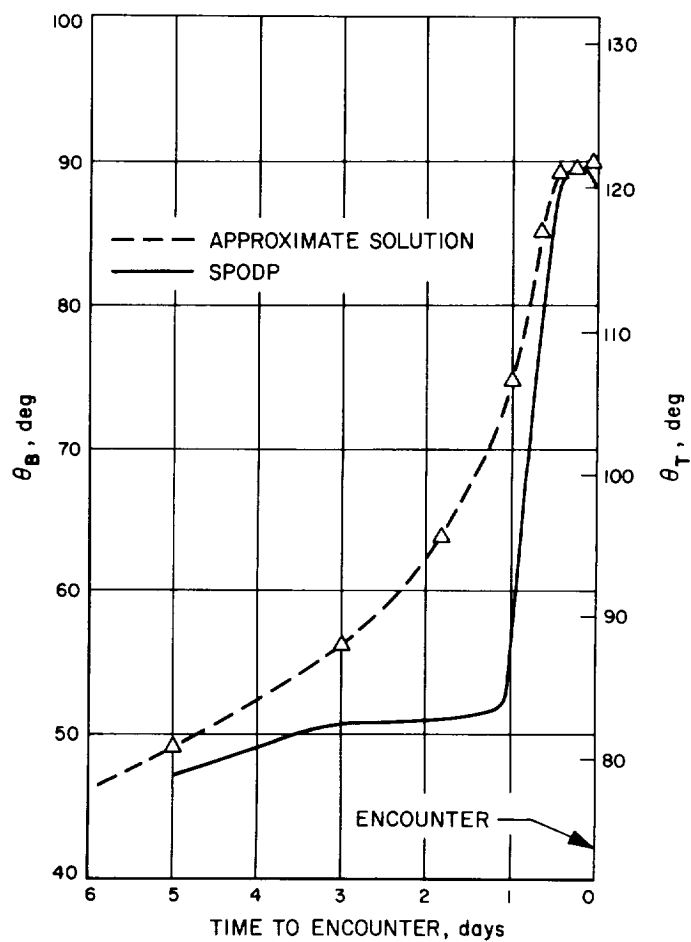
Fig. 12. Orientation of SMAA to B and T
from doppler tracking

4. Surveyor VII: Post-Lunar Touchdown Tracking Data Analysis, F. B. Winn

a. Introduction. The "observed minus computed" (O − C) residual sets exhibited long-term periodicities and diurnal signatures when *Surveyor VII* doppler data were reduced using the single-precision orbit determination program (SPODP) (Ref. 1). The long-term periodicities are lunar ephemeris dependent. The diurnal signatures result from tropospheric refraction (deficient modeling), ionospheric charged particle effects (not modeled), or the lunar motion model (deficient modeling).

b. Long-term periodicities. Two lunar ephemerides were employed in conjunction with one established scrubbed *Surveyor VII* tracking data sample. The two ephemerides employed were Lunar Ephemeris 4 (LE 4)

(Ref. 2) and Lunar Ephemeris 5 (LE 5) (Ref. 3 and SPS 37-48, Vol. III, pp. 33–39).

Lunar Ephemeris 4 can be regarded as the modern evolved Brown lunar theory. This ephemeris has recently been discovered to have radial components of position and velocity which deviate from observations (SPS 37-49, Vol. II, pp. 4–6 and SPS 37-50, Vol. II, pp. 93–97).

Lunar Ephemeris 5 is a numerical integration of the equations of motion which uses LE 4 positions as input observables (Ref. 4). Essentially, this amounts to a smoothed LE 4 which is gravitationally consistent.

The O − C residual long-term periodicities represent lunar motion modeling errors. Both LE 4 and LE 5 exhibit this trait. The long-term periodicities induced by
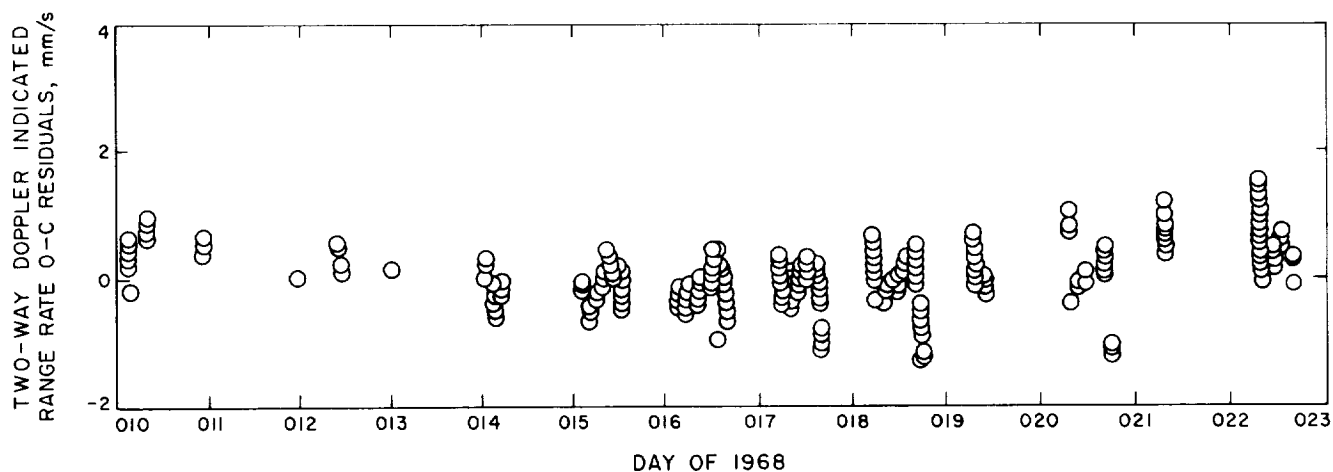
Fig. 13. Pioneer DSS O − C residuals (using DE 29/LE 5) for Surveyor VII
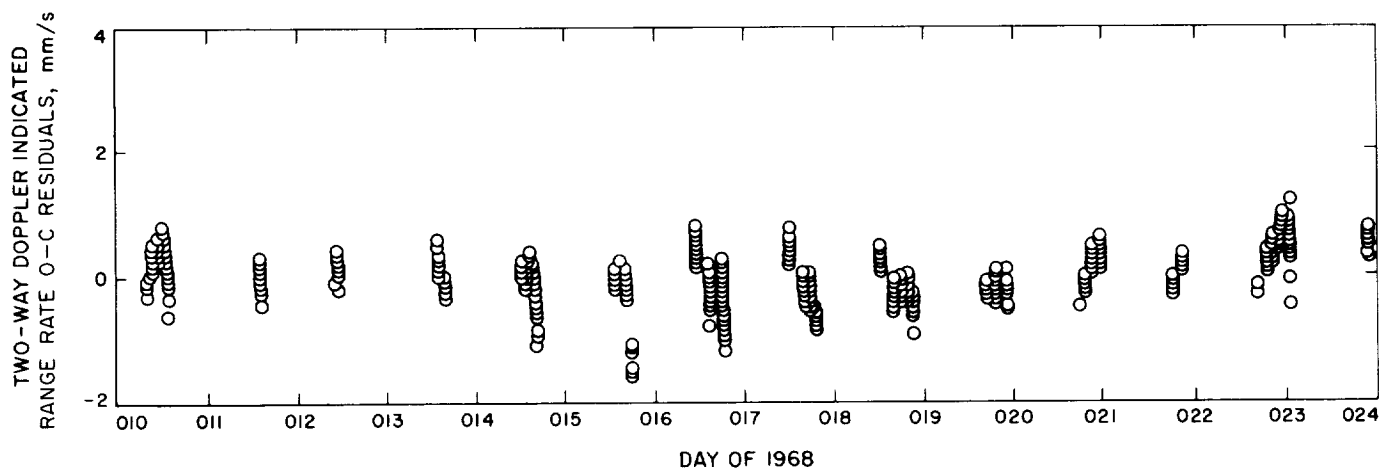
Fig. 14. Tidbinbilla DSS O − C residuals (using DE 29/LE 5) for Surveyor VII

LE 4 are more pronounced than those of LE 5, and can be seen in Figs. 13–15 using LE 5 and Figs. 16–18 using LE 4. The residual long-term trends associated with LE 5 have a 0.7 mm/s amplitude and demonstrate an approximate period of one lunar cycle (Fig. 15).

c. Diurnal periodicities. The diurnal signatures of the *Surveyor VII* O − C residuals (Figs. 19–21) are similar to those of *Surveyor I* (SPS 37-48, Vol. II, pp. 4–7), and *Surveyors III, V,* and *VI* (Ref. 4). However, the acquisition of low elevation *Surveyor VII* tracking data has provided a more complete picture of the daily nature of the residuals.

Recent investigations by A. Liu (SPS 37-50, Vol. II, pp. 93–97) and J. D. Mulholland (SPS 37-49, Vol. II, pp. 4–6) have identified and ordered the three diurnal errors presently incorporated into the SPODP residual sets:

(1) Tropospheric refraction [$\sim$33 mm/s/100 N at 0 deg elevation (max)].

(2) Suspected lunar ephemeris error functions [$\sim$1.0 mm/s (max)].

(3) Ionospheric charged particle effects [$\sim$0.5 mm/s (max)].
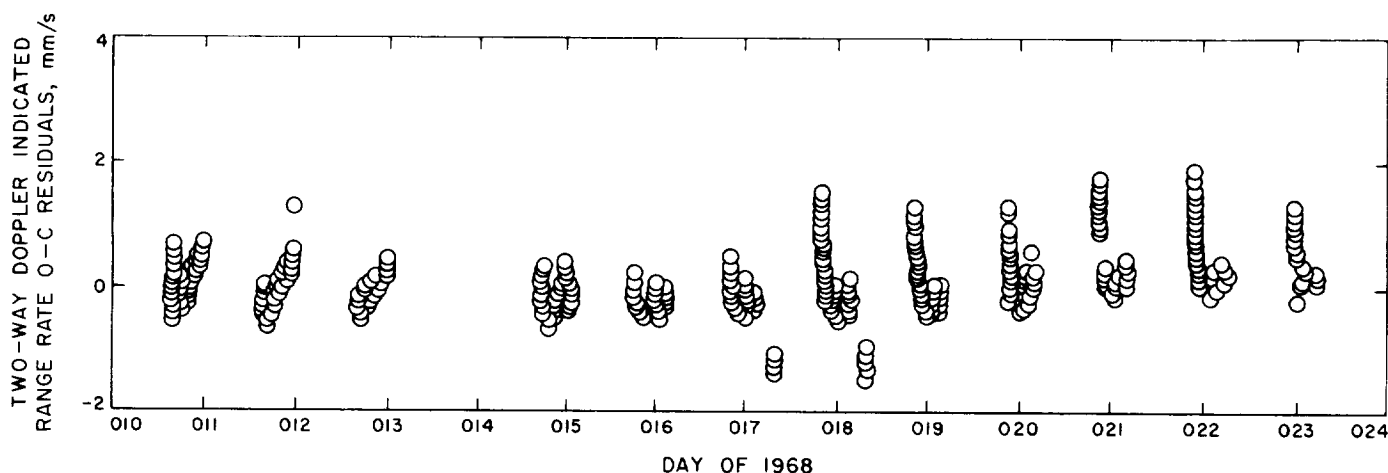
Fig. 15. Robledo DSS O − C residuals (using DE 29/LE 5) for *Surveyor VII*
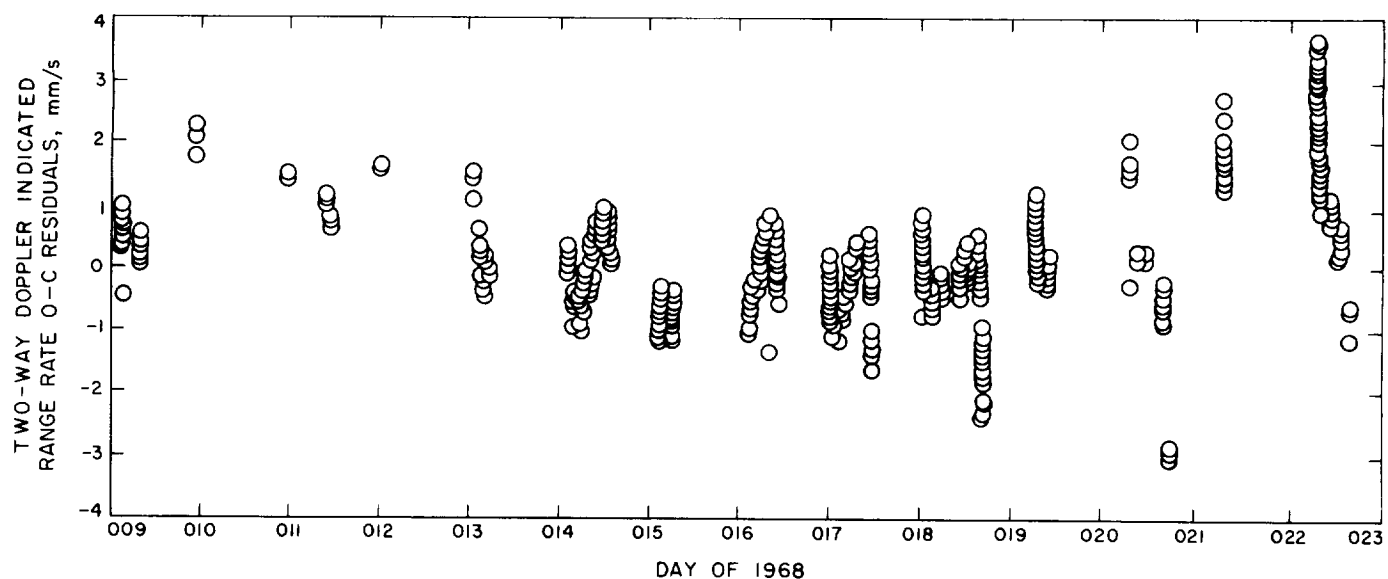
Fig. 16. Pioneer DSS O − C residuals (using DE 19/LE 4) for *Surveyor VII*
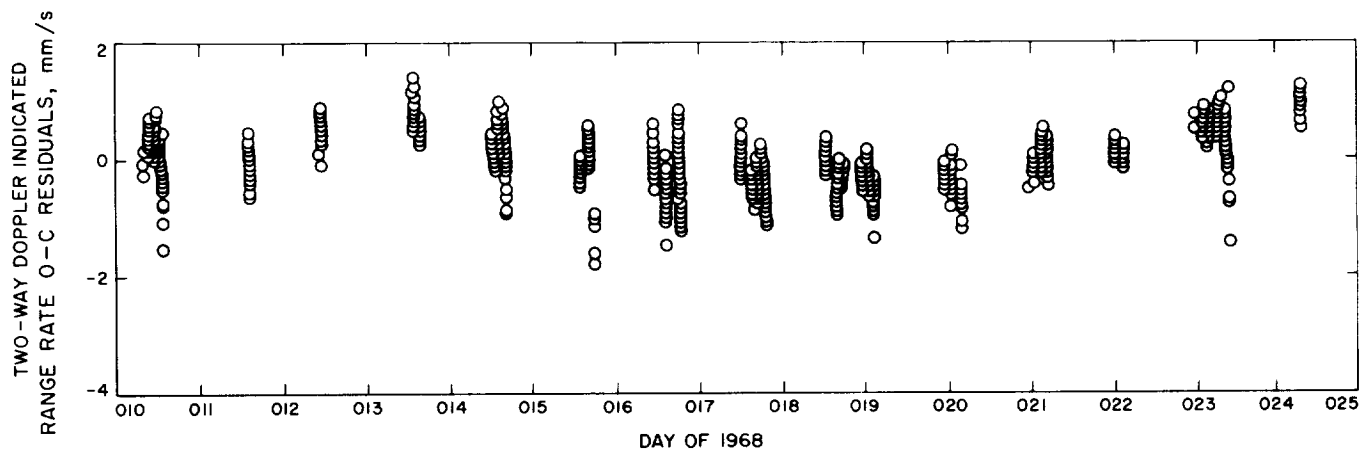
Fig. 17. Tidbinbilla DSS O — C residuals (using DE 19/LE 4) for *Surveyor VII*
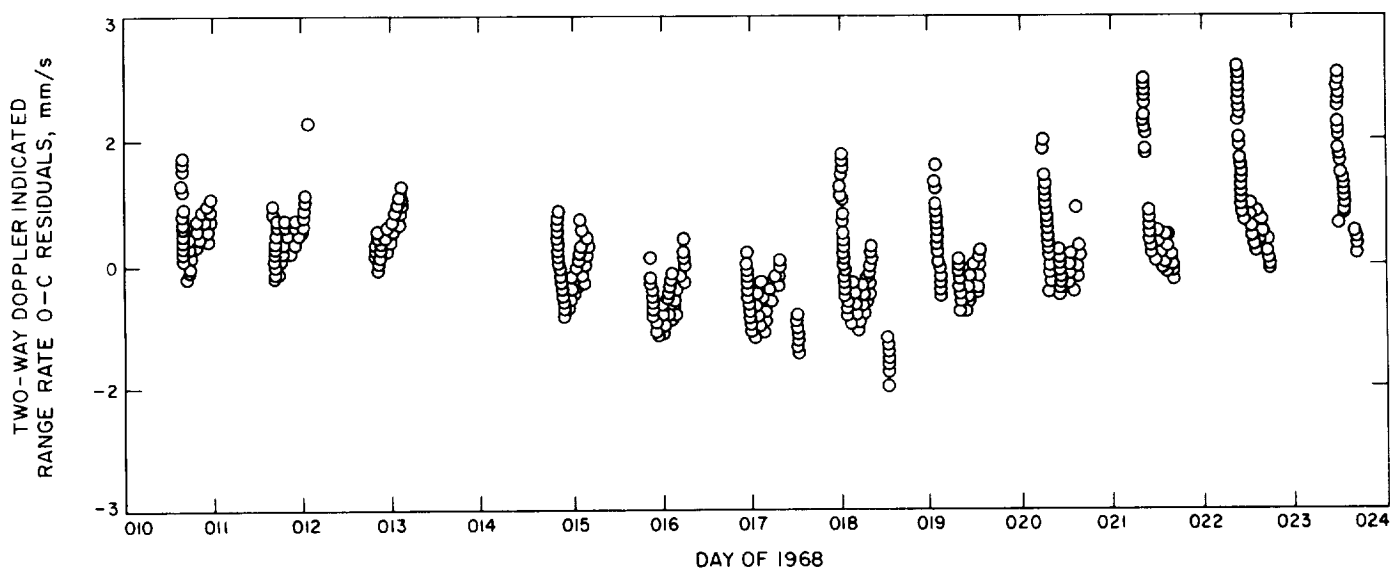
Fig. 18. Robledo DSS O — C residuals (using DE 19/LE 5) for *Surveyor VII*
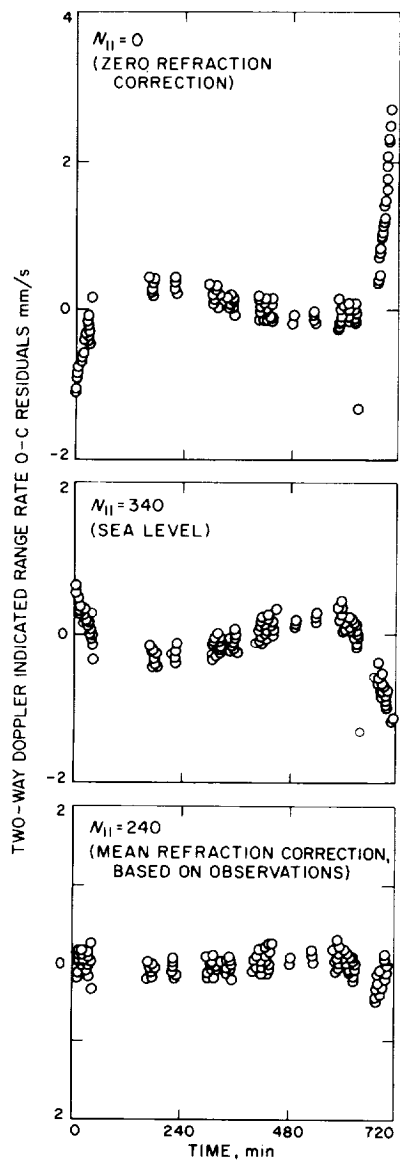
Fig. 19. Pioneer DSS pass 11/day 18
(using DE 29/LE 5)
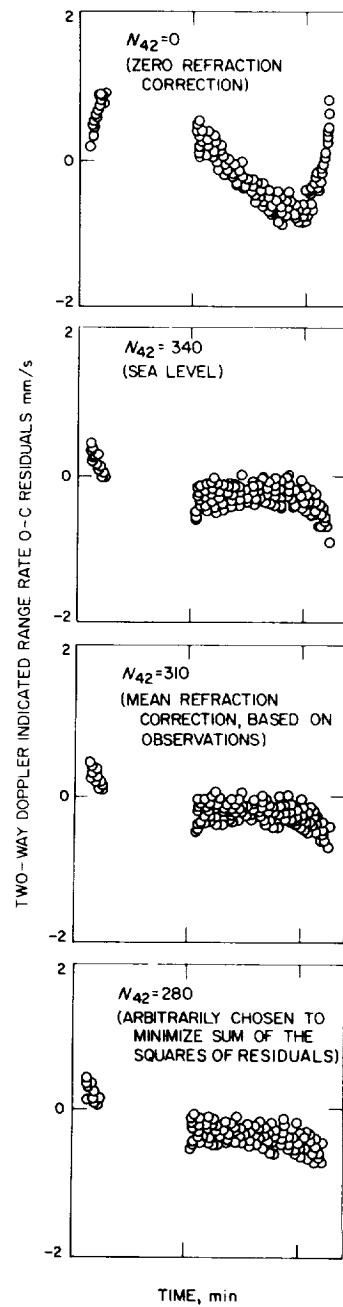
Fig. 20. Tidbinbilla DSS pass 11/day 18
(using DE 29/LE 5)
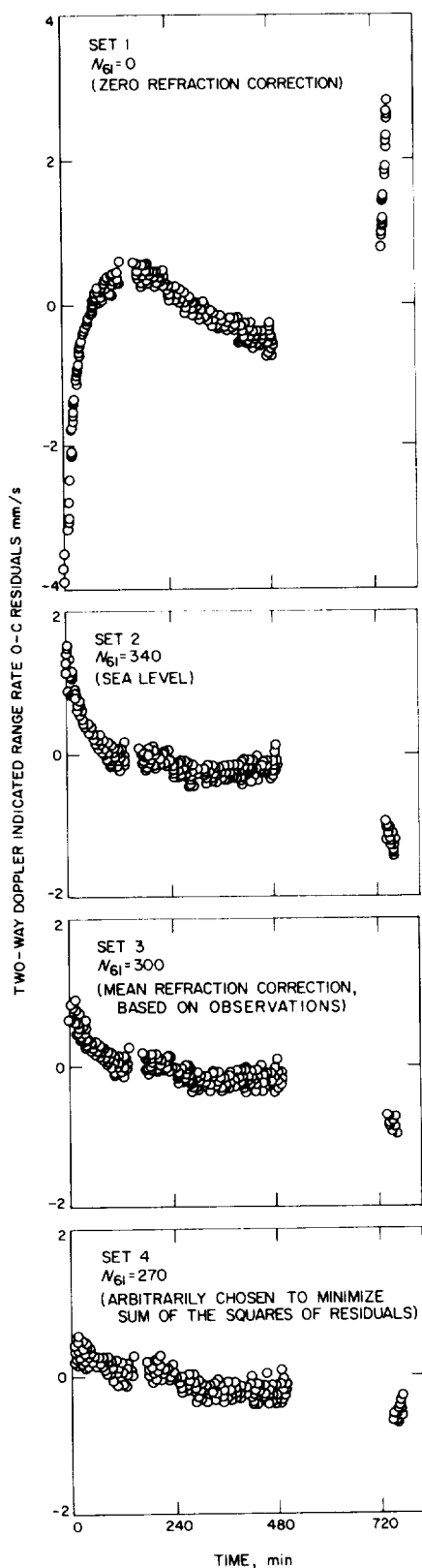
Fig. 21. Robledo DSS pass 11/day 18 (using DE 29/LE 5)

Tropospheric refraction. The refraction signature has been empirically determined and programmed into the SPODP (Ref. 1). The empirical refraction function is

$$\Delta r\dot{\rho} = \frac{C_1}{\tau}\left\{ \frac{1}{\left[\sin\left(\gamma + \frac{\dot{\gamma}\tau}{2}\right) + C_2 \right]^{C_3}} - \frac{1}{\left[\sin\left(\gamma - \frac{\dot{\gamma}\tau}{2}\right) + C_2 \right]^{C_3}} \right\} \frac{N}{340.0}$$

where C_1, C_2 and C_3 are empirically determined constants

$$C_1 = 0.0018958$$

$$C_2 = 0.06483$$

$$C_3 = 1.4$$

and

$\Delta r\dot{\rho}$ = refraction correction applied to the SPODP-calculated data types, Hz

τ = doppler count interval, s

γ = elevation angle

$\dot{\gamma}$ = rate of elevation angle change

N = refractivity index

The tropospheric refraction indices N employed in the SPODP solution for the Deep Space Stations (DSSs) are all set at $N = 340.0$. Recent research by A. Liu (SPS 37-50) has provided evidence that the following Ns are more precise:

$$\text{Pioneer DSS: } N_{11} = 240.0$$

$$\text{Tidbinbilla DSS: } N_{42} = 300.0$$

$$\text{Robledo DSS: } N_{61} = 310.0$$

The influence of tropospheric refraction is mainly a phase retardation coupled with a bending and consequential lengthening of the ray path. Utilizing Liu's formulation, an error of 100 units of N generates O − C residuals of 0.5 Hz (33 mm/s) for horizon range-rate observations. The refraction-induced O − C residual signature contained in SPS 37-50 greatly resembles the O − C residual characteristics of the *Surveyor VII* passes. Pioneer DSS, in comparison to the other stations, most frequently acquired low elevation tracking data. An examination of Fig. 19 (Pioneer DSS residuals, pass 11, using varying Ns) shows significant elevation-dependent

O – C residual biases which correlate remarkably well with the computed refraction error functions. Examination of Figs. 20 and 21, pertaining to Tidbinbilla and Robledo DSSs, reveals evidence of like influences.

Lunar ephemerides (diurnal O — C residual contribution). Although the troposphere is an acknowledged major, but unevaluated, error source that warrants the evaluation efforts under way, there are other model limitations such as the lunar ephemeris.

J. D. Mulholland (SPS 37-49) has provided tentative evidence of lunar ephemeris defects (to one significant place) which have an approximately daily period. A correlation study of Surveyor VII O — C residuals and the suspected error functions is inconclusive (Fig. 22). A new lunar ephemeris (LE 8), constructed incorporating these error functions, will be used in future analysis.

Ionospheric charged particle effects. To the present, ionospheric charged particle effects have been omitted from model consideration. The ionospheric influence on the CC3 O — C residuals is a function of effective electron density which is dependent on elevation angle, elevation rate of change, the sun's local hour angle, star activity, and transmitter frequency. The residual signature resulting from this model omission can be similar to

the tropospheric refraction error function signature; however, the ionospheric influence on tracking data is of a lesser magnitude. Accordingly, the ionospheric effect can be removed or diminished from the O — C residuals by a slightly erroneous N in the tropospheric model.

A history of ionospheric activity for the first lunar day of all Surveyors is being compiled by M. Davis (Stanford University Electronics Laboratories). Once this information is available, the correlation of the O — C residuals with tropospheric and ionospheric refraction will be investigated more fully.

d. A combinational parameter. The three diurnal components that comprise the diurnal signature are highly correlated. To utilize one "combinational parameter" as a means of fitting out of the O — C residual sets, the influences resulting from tropospheric refraction, ionospheric charged particle effects, and lunar ephemeris daily variations defects is the only available approach at this time.

The results from the employment of this procedure are most striking. The preponderance of the diurnal signature has been removed by the manipulation of the refraction indices. The O — C residuals emanating from the several SPODP Surveyor VII tracking data reductions are shown
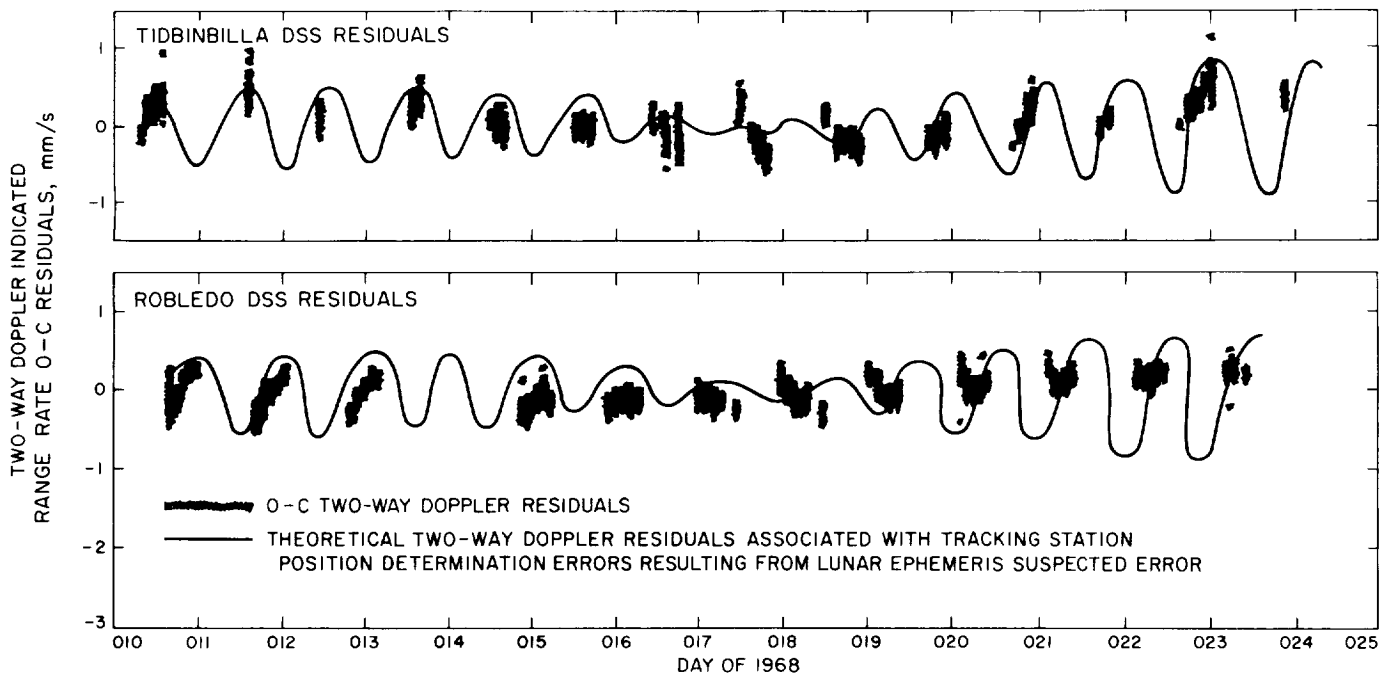
Fig. 22. Surveyor VII Tidbinbilla and Robledo DSSs two-way doppler O — C residuals vs suspected ephemeris-dependent tracking station position errors (using DE 29/LE 5 coupled with refraction refinement)

in Figs. 19–21. These data reductions were accomplished using the following refraction indices:

Set (1) $N_{11} = N_{42} = N_{61} = 0$ (no refraction correction)

Set (2) $N_{11} = N_{42} = N_{61} = 340.0$ (sea-level refraction correction)

Set (3) $N_{11} = 240$, $N_{42} = 310$, $N_{61} = 300$ (refraction correction based on observations of *Lunar Orbiter II* [Ref. 5])

Set (4) $N_{11} = 240$, $N_{42} = 280$, $N_{61} = 270$ (arbitrarily chosen to minimize the sum of the square of the residuals)

The influence of the combinational parameter on the parameter list is presented below.

e. Residual discontinuity. *Surveyor VII* O −C residuals from Madrid DSS exhibited a discontinuity of 0.2 mm/s during pass 8/day 14, pass 9/day 15, pass 10/day 16, and pass 11/day 17. The pass 11/day 17 O − C residuals presented in Fig. 20 illustrate this discontinuity. No explanation is available at this time.

f. Parameter vector solution. Table 3 is a tabulation of parameter determinations resulting from the SPODP data fits utilizing different ephemerides and the previously discussed combinational parameter. In all cases, one *Surveyor VII* tracking data sample was used.

The *Surveyor VII* selenocentric positions derived from the use of DE 29/LE 5 and DE 19/LE 4 are considerably displaced from each other. The relative metric displacements in selenocentric components are as follows:

3010 m, radial

3000 m, latitude

5550 m, longitude

This displacement is characteristic of the lunar ephemerides employed in the reduction. Tracking data reductions of *Surveyor I* (SPS 37-48, Vol. II, pp. 4–7) and *Surveyor VI* (Ref. 4), utilizing DE 29/LE 5 and DE 19/ LE 4, also exhibit large relative displacements.

The error ellipsoids resulting from these data reductions have, effectively, the same respective dimensions

Table 3. Parameter solution vectors[a]

LE[a]	N	DSS	r_s	σ_{r_s}	LO	σ_{LO}	RADS	σ_{RADS}	LATS	σ_{LATS}	LONS	σ_{LONS}
A Priori
—	—	Pioneer	5206.333	0.24	243.15070	0.005	1736.0	10.0	−41.1	5.0	348.56	5.0
—	—	Canberra	5205.348	0.24	148.98140	0.005						
—	—	Madrid	4862.601	0.24	355.75114	0.005						
Solutions
5	0	Pioneer	5206.349	0.002	243.15092	0.0001	1739.318	1.751	−40.926	0.050	348.512	0.024
	0	Canberra	5205.362	0.003	148.98182	0.0001						
	0	Madrid	4862.619	0.001	355.75136	0.0001						
5	340	Pioneer	5206.332	0.002	243.15114	0.0001	1741.695	1.752	−40.858	0.050	348.473	0.033
	340	Canberra	5205.344	0.003	148.98187	0.0001						
	340	Madrid	4862.603	0.001	355.75154	0.0001						
5	240	Pioneer	5206.337	0.002	243.15114	0.0001	1741.597	1.752	−40.857	0.050	348.472	0.033
	310	Canberra	5205.346	0.003	148.98187	0.0001						
	300	Madrid	4862.605	0.001	355.75155	0.0001						
5	240	Pioneer	5206.337	0.002	243.15110	0.0001	1741.486	1.752	−40.863	0.050	348.482	0.033
	280	Canberra	5205.387	0.003	148.98160	0.0001						
	270	Madrid	4862.607	0.001	355.75151	0.0001						
4	340	Pioneer	5206.339	0.002	243.15063	0.0001	1744.704	1.755	−40.757	0.049	348.658	0.033
	340	Canberra	5205.348	0.002	148.98135	0.0001						
	340	Madrid	4862.606	0.002	355.75103	0.0001						

[a]Column headings are defined as follows:
LE = Lunar Ephemeris
N = index of refraction
DSS = Deep Space Station
r_s = DSS spin-axis distance, km
LO = DSS longitude, deg
RADS = selenocentric probe distance, km
LATS = selenocentric latitude of probe, km
LONS = selenocentric longitude of probe, km

due to the use of one preliminary scrubbed tracking data sample in all parameter solutions. The relative displacement of the *Surveyor VII* selenocentric position error ellipses are graphically pictured in Fig. 23 with the *Surveyor VII* position determinations, using *Lunar*

Orbiter V photos (Ref. 5), and *Surveyor VII* cruise data fits (Ref. 6) for comparison.

g. Conclusion. Although substantial progress has been made in the analysis of the post-landing *Surveyor VII*

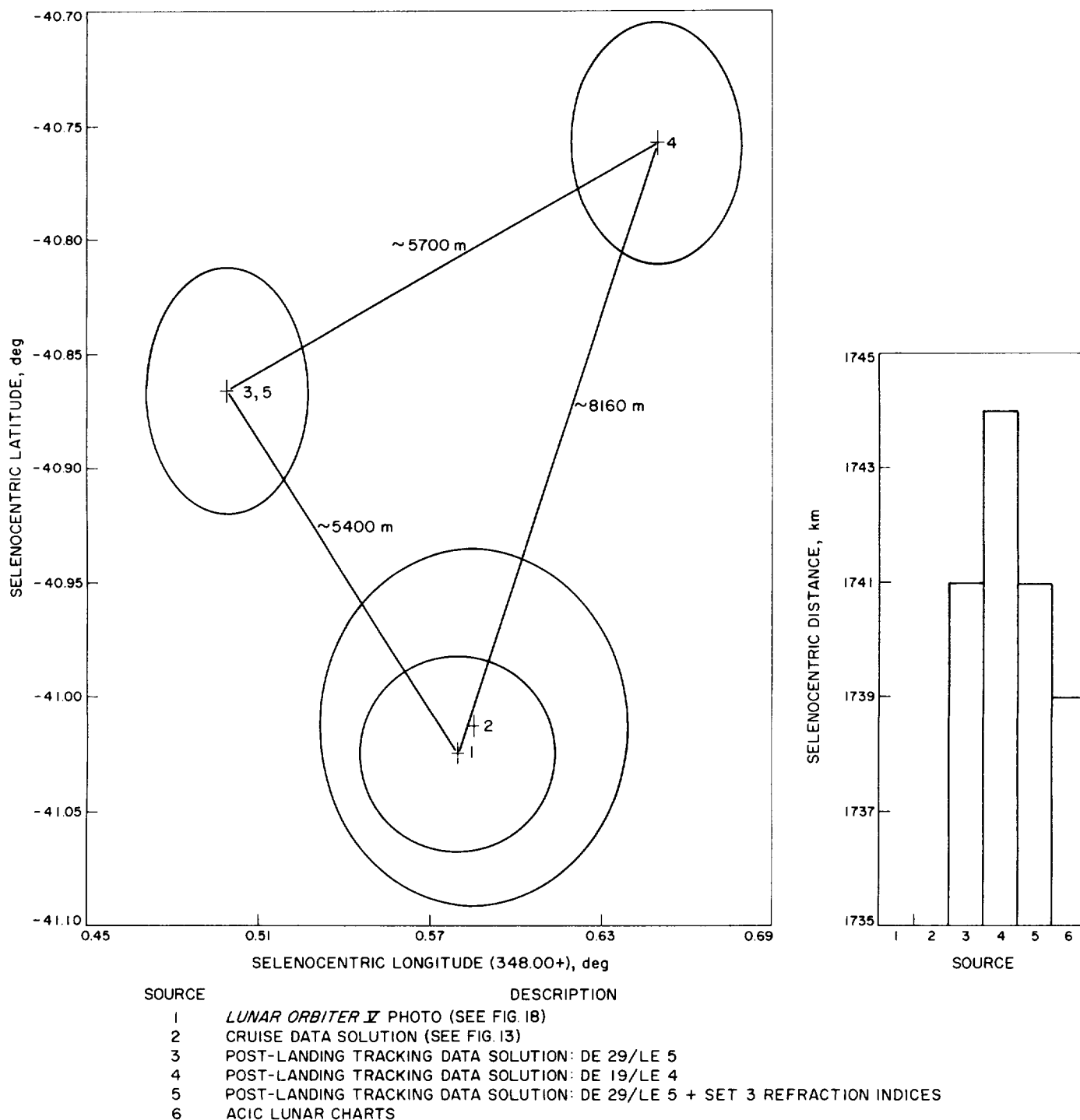| SOURCE	DESCRIPTION
1	*LUNAR ORBITER Ⅴ* PHOTO (SEE FIG. 18)
2	CRUISE DATA SOLUTION (SEE FIG. 13)
3	POST-LANDING TRACKING DATA SOLUTION: DE 29/LE 5
4	POST-LANDING TRACKING DATA SOLUTION: DE 19/LE 4
5	POST-LANDING TRACKING DATA SOLUTION: DE 29/LE 5 + SET 3 REFRACTION INDICES
6	ACIC LUNAR CHARTS

Fig. 23. Surveyor VII selenocentric error ellipses

tracking data, the investigation is incomplete. The disparity of the *Surveyor VII* position determinations is recognized and somewhat understood. With the advent of a more refined *Surveyor VII* data sample, and the removal of correlated parameters, the probe's position will be redetermined.

Much new information pertinent to model refinement has been realized from *Surveyor VII* analysis. This information includes the discovery of the following:

(1) The necessity for a more precise tropospheric refraction model.

(2) The inconclusive correlation between suspected lunar ephemeris defects and *Surveyor VII* O − C residuals.

(3) The deviation of LE 5 radial velocity component from observation.

References

1. Warner, M. R., and Nead, M. W., *SPODP—Single Precision Orbit Determination Program*, Technical Memorandum 33-204, Jet Propulsion Laboratory, Pasadena, Calif., Feb. 15, 1965.

2. Lawson, C. L., *Announcement of JPL Developmental Ephemeris No. 19*, Technical Memorandum 33-162, Jet Propulsion Laboratory, Pasadena, Calif., Apr. 13, 1967.

3. Mulholland, J. D., and Block, N., *JPL Lunar Ephemeris Number 4*, Technical Memorandum 33-346, Jet Propulsion Laboratory, Pasadena, Calif., Aug. 1, 1967.

4. Whitaker, E. A., "Television Observations from Surveyor VI," in *Surveyor VI Mission Report. Part II: Science Results*, Technical Report 32-1262, Jet Propulsion Laboratory, Pasadena, Calif., Jan. 10, 1968.

5. Winn, F. B., "Selenographic Location of Surveyor VI," in *Surveyor VI Mission Report. Part II: Science Results*, Technical Report 32-1262, Jet Propulsion Laboratory, Pasadena, Calif., Jan. 10, 1968.

6. *Surveyor VII Mission Report. Part I: Mission Description and Performance*, Technical Report (to be published), Jet Propulsion Laboratory, Pasadena, Calif.

5. Effects of IRS Gas Venting on Mariner Mars 1969 Encounter Two-Way Doppler, *J. E. Ball*

a. Introduction. The degradation of the *Mariner* Mars 1969 celestial mechanics experiment from infrared spectrometer (IRS) gas venting has been reported in two previous SPS articles (SPS 37-44, Vol. IV, pp. 4–8 and SPS 37-47, Vol. III, pp. 1–6). Recently, new information on the duration and magnitude of the force from IRS gas jetting became available informally through conversations with Dr. P. Gottlieb and T. Migliori of JPL.

Figure 24 presents this information in graphical form and represents a revision to the previous estimation of the force acting on the spacecraft from IRS gas jetting reported earlier.[6] Figure 24 shows the magnitude of the force in dynes acting on the spacecraft beginning from the start of IRS gas cool-down until all of the hydrogen and nitrogen gas in the system has been depleted.

The previous articles investigated the effects of the IRS gas jetting on the celestial mechanics experiment and, in particular, on the solution for the mass of Mars. It is the intent of this article to present the results of a cursory analysis to determine if the effects of IRS gas jetting on the spacecraft trajectory can be seen in the doppler residuals of the orbit determination program near the encounter phase. These results do show that the acceleration of the spacecraft due to IRS gas jetting can be seen in the two-way doppler residuals as indicated in Figs. 25 and 26.

b. IRS gas venting. During the IRS cool-down, which starts approximately 35 min prior to encounter, nitrogen and hydrogen are vented through a cryostat out through nozzles in the cone-axis mount on the scan platform. The venting occurs at a constant maximum rate and continues for approximately 52 min. At this point, the venting starts to gradually decay until all of the gas in the system has been depleted. The decay begins when the tank pressure drops below the regulator pressure (2700 psi for nitrogen and 1700 psi for hydrogen). The escaping gas exerts a thrust on the spacecraft, partly from the imbalance of the jet action and partly from the gas-cloud molecules striking the structural assembly and solar panels of the spacecraft. Since Migliori and Sproull (see footnote 6) state that the thrust resulting from the imbalance of the jet action can be kept to 50 dyn, or less, by using the proper techniques, the 50-dyn unbalanced force will be ignored in this analysis. The major thrust dealt with in this analysis is the force resulting from the gas cloud and is shown in Fig. 24 as a function of time.

The thrust shown in Fig. 24 remains constant at 400 dyn during the first 52 min and then begins to decay exponentially. The exponential function found to approximate the thrust during the decay period is

$$400 \exp \left[-\frac{1}{66} (t - 52) \right]$$

"Migliori, T. and Sproull, W., *Time Variation of Spacecraft Thrust From IRS Cooling Gas Venting for Mariner Mars 1969*, Sept. 13, 1967, (JPL internal document), Fig. 5.
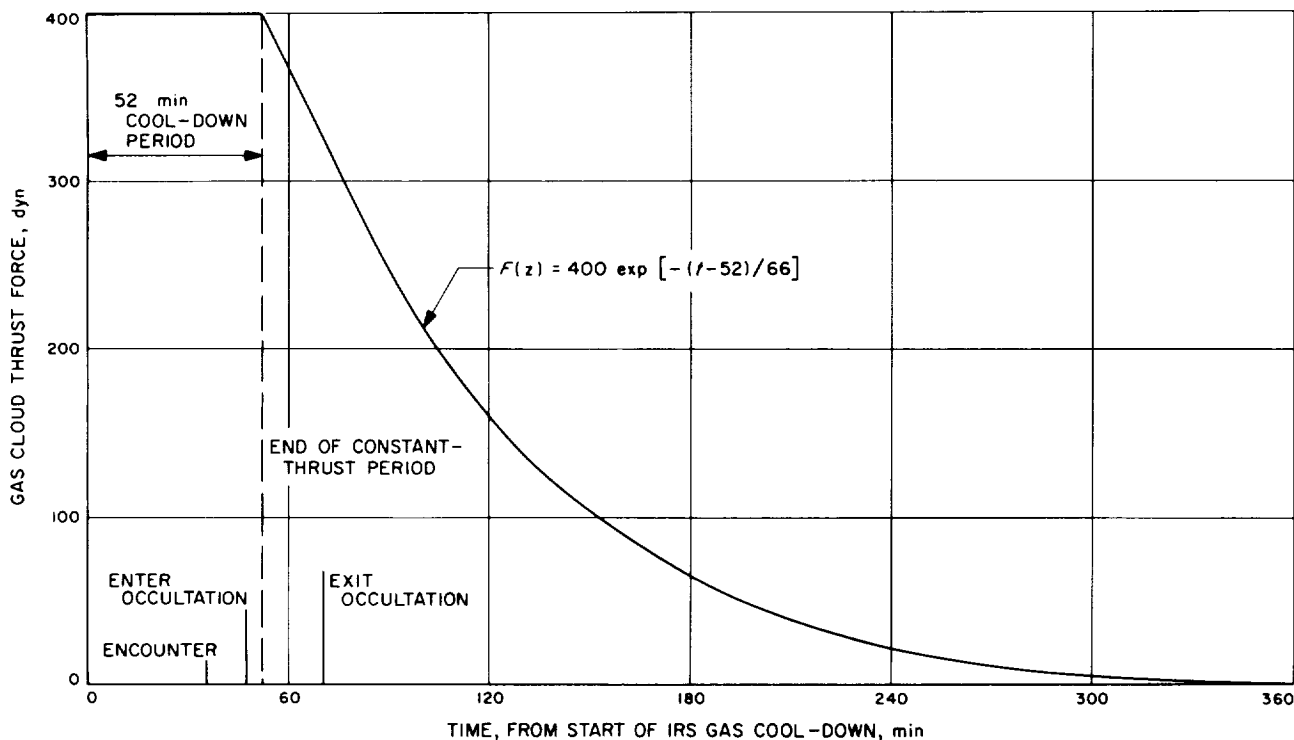
Fig. 24. IRS gas venting force in − Z direction (100% uncertainty)

where *t* is expressed in minutes. The direction of this force is in the −Z direction of the spacecraft-fixed coordinate system, equivalent to the direction of the vector from the spacecraft to the sun of a sun-stabilized spacecraft. The uncertainty of the magnitude of the force plotted in Fig. 24 was estimated by Dr. P. Gottlieb of Section 311 to be no more than a factor of 2, or 100%.

c. IRS venting effects. Based on this new information, the effects of the IRS gas jetting on the doppler residuals were estimated as follows:

The orbit determination program (ODP) computes the anticipated value of the range rate (doppler) and compares it to the actual observed values. The difference (residuals) between these values can be interpreted as an indication of how well the actual trajectory is behaving in relation to the anticipated trajectory. When IRS gas venting starts, the observed value of range rate will contain the venting effects. If the ODP does not contain a model for IRS gas venting, a difference will result when the observed values of range rate are compared to the computed values. This difference can be considered to be the effect of the IRS gas venting on the trajectory (assuming that the trajectory was known perfectly before IRS gas venting). Since the IRS gas venting will last 52 min, the residuals (referred to as the error in range rate) will in-

crease with time. As long as the error in the range rate values remains sufficiently below the level of the noise for the doppler data, IRS gas venting will not be a concern to orbit determination.

To get an estimate of the error in the range-rate values ($\Delta\rho_i$), the expression for the acceleration of the spacecraft from IRS gas jetting along the line-of-sight direction was integrated. The equation defining the error in the range-rate values is

$$
\Delta\dot{\rho_i} = \int_0^{52} \frac{400 \text{ dyn}}{M} \mathbf{U}_\odot \cdot \frac{\boldsymbol{\rho}}{|\boldsymbol{\rho}|} \, dt
$$
$$
+ \int_{52}^{t_i} \frac{400 \text{ dyn}}{M} \exp\left[-\frac{1}{66}(t - 52) \right] \mathbf{U}_\odot \cdot \frac{\boldsymbol{\rho}}{|\boldsymbol{\rho}|} \, dt
$$

$$(1)$$

where $\mathbf{U}_\odot$ is a unit vector directed along the vector from the spacecraft to the sun; the quantity $\mathbf{U}_\odot \cdot \boldsymbol{\rho}/|\boldsymbol{\rho}|$ is the cosine of the angle between the vector from the earth to the spacecraft and the vector from the spacecraft to the sun. The value can be taken from the coefficient in the first term of the expression

$$
\mathbf{U}_\oplus = 0.744\mathbf{U}_\odot + 0.021\mathbf{T} - 0.667\mathbf{N}
$$
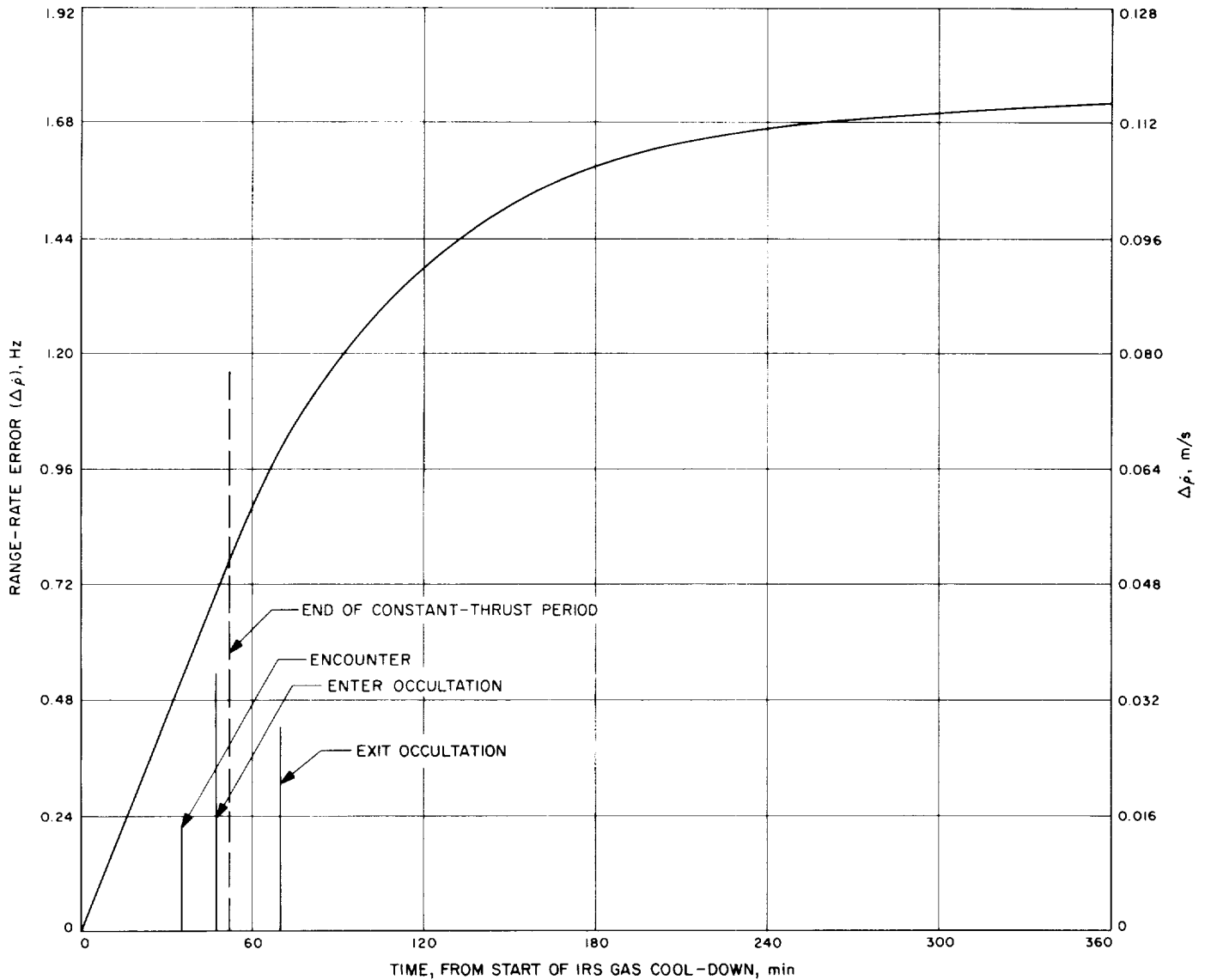
Fig. 25. Maximum range-rate error (no IRS gas-force model in ODP)

appearing in SPS 37-47, Vol. III, pp. 1-6. $U_\oplus$ is the unit vector from the earth to the spacecraft near encounter. This approximately defines the line-of-sight direction of the tracking station and is assumed constant over the time period of interest. M is the mass of the spacecraft and is taken to be 360 kg.

After 6 h, the gas can be considered essentially depleted since the contribution of the integral

$$\int_{360}^{\infty} \frac{400}{M} \exp\left[-\frac{1}{66}(t - 52) \right] dt$$

is negligible.

The values $\Delta\dot{\rho}_i$ resulting from Eq. (1) for an uncertainty of 100% in the magnitude of 400 dyn were plotted in Fig. 25 as a function of time. Figure 25 represents the maximum error in the range-rate values that would be seen in the residuals from IRS gas venting if no model for the venting is used in the orbit program. The uncertainty of the magnitude of the force plotted in Fig. 24 is 100%, therefore, the maximum range-rate error plotted in Fig. 25 is for the worst case.

d. Reduction of range rate error. The maximum range-rate error plotted in Fig. 25 could be reduced by modeling the IRS gas-venting force in the orbit program. The reduction of the range-rate error seen in the residuals will
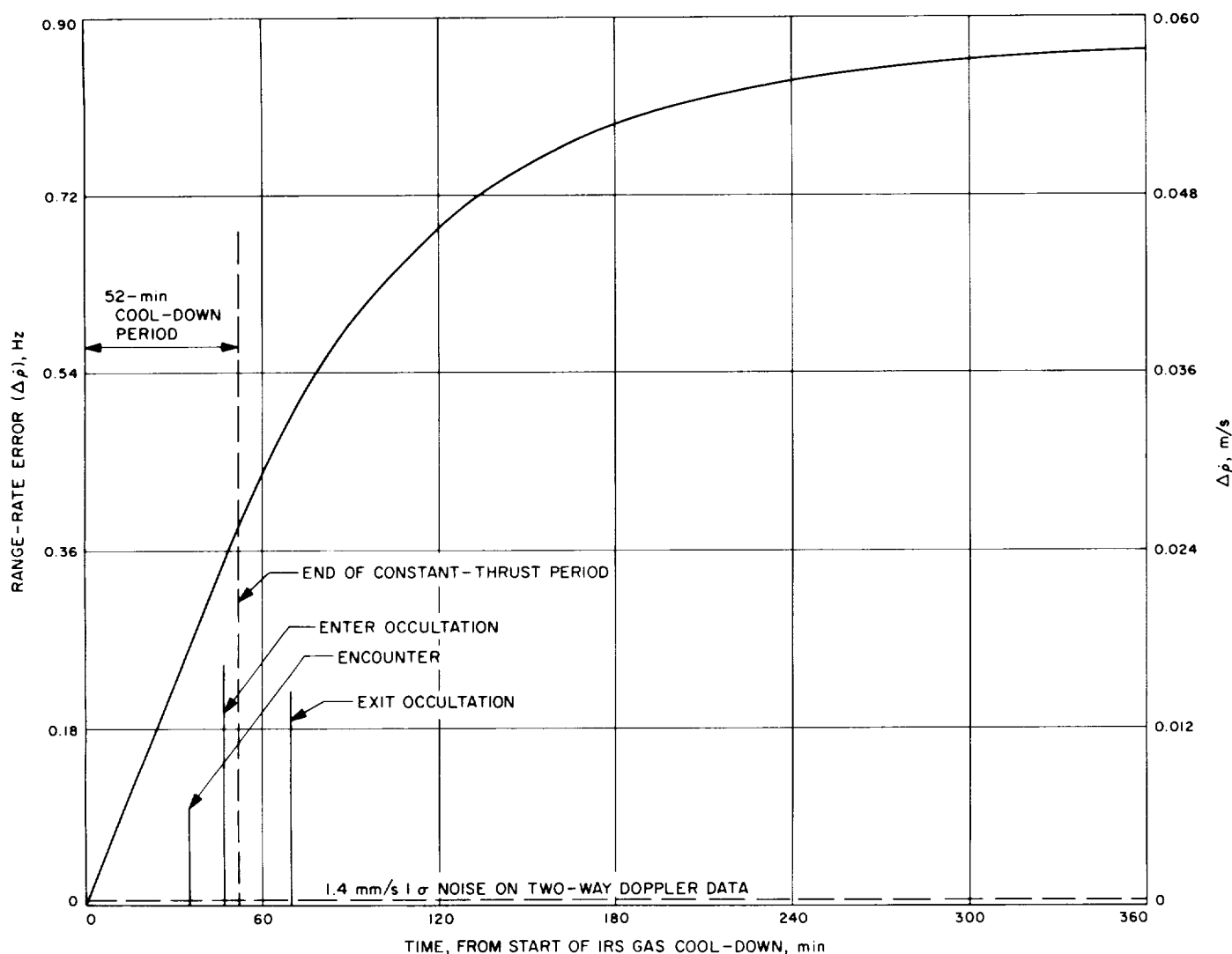
Fig. 26. Range-rate error with a priori IRS gas-force model in ODP

be proportional to the accuracy of the model used to represent the actual force from IRS gas venting. Since the model available for IRS gas venting is given in Fig. 24, Fig. 26, then, represents the error in range rate for the model given in Fig. 24. Figure 26 also shows the 1.4-mm/s level of the 1-σ noise for the 60-s samples of two-way doppler data. The noise is well below the range-rate error after the first few minutes of the IRS cool-down period. Therefore, the effect of the IRS gas jetting on the spacecraft will be clearly visible in the data. The value of using the model plotted in Fig. 24 in the orbit program to represent the force for IRS gas venting versus not using a model in the orbit program would be to reduce the level of the range-rate error by a factor of 2. However, if a more accurate model for the force from IRS gas venting were available, the range-rate error could be reduced proportionately.

Similarly, the range error could be computed by evaluating the double integral of Eq. (1) as a function of time. The result would be a set of curves corresponding to Figs. 25 and 26. Evaluating Eq. (1) for the range error after 6 h from the start of IRS cool-down, the error in range is approximately 0.170 km while the maximum error is 0.340 km.

The assumptions made in this analysis are as follows:

(1) The only non-gravitational force acting on the spacecraft from IRS gas venting is along the vector from the spacecraft to the sun (see Fig. 24).

(2) The uncertainty of the curve shown in Fig. 24 is 100%.

(3) The earth-probe-sun angle is equal to 42 deg and is constant over the 6-h time period.

(4) The earth–spacecraft vector is the same as the observer–spacecraft vector.

(5) The cone and clock angle of the scan platform remains constant.

e. Conclusions. Orbit determination results near encounter will be influenced by the gas jetting from the IRS equipment onboard the spacecraft. Figure 25 shows the maximum range-rate error when no model for the IRS gas-venting force is used in the orbit program. When a model for the IRS gas-venting force given in Fig. 24 is used in the orbit program, the range-rate error is shown in Fig. 26. In either case, orbit determination will be affected by the gas venting when trying to fit the range-rate data near encounter.

Information about the gravitational harmonics of Mars obtainable from the analysis of the encounter orbit will be masked by the IRS gas-venting force acting on the spacecraft. Particular examples of this masking effect are described in SPS 37-47, Vol. III, pp. 1–6 and SPS 37-44, Vol. IV, pp. 4–8. A check on the value for the oblateness coefficient of Mars from the natural satellite data to help better understand the relationship between the dynamical and optical flattening data would be of interest. However, this check will also be obscured due to the IRS gas venting.

The current model for the IRS gas-venting force will not satisfy the accuracy needed for the celestial mechanics experiment given in Ref. 1. In addition, the current ODP is not capable of handling the type of force model suggested by Fig. 24 for IRS gas venting without revising the program.

The following questions should be considered and answered in terms of the new information presented in this article:

(1) Does the IRS gas venting jeopardize the mission before encounter for pointing the scan platform or delivering the spacecraft to the aiming point?

(2) How much is the accuracy of the E + 15 day orbit determination results degraded?

(3) How much does it degrade the determination of certain physical constants which may be important to the celestial mechanics experiment?

(4) How are the determinations of such quantities as the ion-density, index of refraction, surface pressure, etc., of the S-band occultation experiment degraded?

Although the answer to the first question is "no" for the first arriving spacecraft, the effect of IRS gas venting upon the remaining three areas of concern may be important. Further investigations will be made to provide answers to the last three questions. This article indicates that the IRS gas-venting force may adversely influence the ability to determine the spacecraft orbit after encounter, as well as degrading certain results of the celestial mechanics experiment.

Reference

1. Anderson, J., *Effects of Range Data and IRS Gas Jet on MM '69 Celestial Mechanics Experiment*, TM 312-801, Jet Propulsion Laboratory, Pasadena, Calif., Mar. 1, 1967.

6. Estimation of the Cross-Coupling Coefficients,
S. R. McReynolds

a. Introduction. As part of the investigation of small, non-gravitational forces imparted to the *Mariner* spacecraft by the attitude control system (see SPS 37-47, Vol. II, pp. 21–27), it was observed that firing the attitude jets (which are nominally coupled about a single spacecraft axis) caused a significant transfer of angular momentum into the other (i.e., orthogonal) axes; e.g., jets that control motion about the pitch axis also cause motion about the yaw and roll axes. The ratio of the change of angular velocity about a cross axis to the change of angular velocity about the primary axis due to a particular jet depends only on the physical configuration of the spacecraft, and is independent of the absolute magnitude of the impulsive force. Hence, for any set of jets, it is possible to define a set of cross-coupling coefficients as

$$C_{ij} = \frac{\Delta\omega_i}{\Delta\omega_j} \tag{1}$$

where

$\Delta\omega =$ the change in angular velocity

$j =$ the primary axis

$i =$ the secondary axis

From the definition, it follows that

$$C_{ij} = 1, \qquad i = j$$

$$C_{ij} \leq 1, \qquad i \neq j$$

It was shown in SPS 37-47 that it is important to incorporate cross-coupling effects in order to estimate low-level torques on a spacecraft. Knowledge of the cross-coupling coefficients defined would permit this incorporation. In this paper, attitude data telemetered from *Mariner V* is used to obtain an estimate of its cross-coupling coefficients. In order to do this, a special curve-fitting program was written. This curve-fitting program estimates jumps in derivatives at given points and is based on an application of dynamic programming.

b. A fitting technique. In order to estimate the change in angular velocity about the primary axis, it is sufficient to fit attitude data on both sides of the impulse separately and compute the change in the slope at the time of impulse. However, since the change in angular velocity about a secondary axis is so small, a technique is required that fits the data on both sides of the impulse simultaneously. In order to do this, a sequential curve fitting program was written. The basic curve-fitting problem is formulated as an optimal control problem solved with dynamic programming.

The performance index is given by

$$J = \sum_{i=1}^{n} \frac{1}{2} [z(i) - x(i)]^2 \qquad (2)$$

where

$z(i)$ = angular measurement at the ith stage

$x(i)$ = value of fitted curve at the ith stage

The dynamics of the system between impulses are given by

$$x(i+1) = x(i) + v(i) + \frac{1}{2}a$$

$$\qquad (3)$$

$$v(i+1) = v(i) + a$$

where $v(i)$ is the slope of the curve and a is the constant acceleration. The time scale is chosen so that two consecutive measurements are a unit time apart. The above equations adequately model the attitude motion of a spacecraft for small angular velocities. At firings, it is assumed that only the angular velocities changed

$$v^+(i) = v^-(i) + C_{kj} I_j(i) \qquad (4)$$

where

k = axis being fitted

$I_j(i)$ = impulse delivered primarily about j-axis at the ith stage

The fitting problem is now to find the coefficients C_{kj} that minimize J, given by Eq. (2), subject to the constraints given by Eqs. (3) and (4). To solve this problem, dynamic programming is employed. A return function is introduced

$$V^p[x(p), v(p), a, C_{kj}] = \frac{1}{2} \sum_{i=p}^{N} [z(i) - x(i)]^2 \qquad (5)$$

V^p satisfies the following relations:

$$V^{N+1} = 0 \qquad (6)$$

$$V^p[x(p), v(p), a, C_{kj}] =$$
$$\frac{1}{2} [z(p) - x(p)]^2 + V^{p+1}[x(p) + v(p)$$
$$+ \frac{1}{2}a, v(p) + a, a, C_{kj}] \qquad (7)$$

$$V^p[x(p), v^-(p), a, C_{kj}] =$$
$$V^{p+}[x(p), v^-(p) + C_{kj} I_j(p), a, C_{kj}] \qquad (8)$$

These relations completely define V^p, $1 \leq p \leq N + 1$.

Next, it is necessary to show that V^p is a quadratic function of its arguments and deduces sequential relations for the coefficients

$$V^p[x(p), v(p), a, C_{kj}] =$$
$$V_0(p) + V_x(p) x(p) + V_v(p) v(p)$$
$$+ V_a(p) a + V_c(p) C_{kj}$$
$$+ \frac{1}{2} [V_{xx}(p) x^2(p) + 2V_{xv}(p) x(p) v(p)$$
$$+ 2V_{xa}(p) x(p) a + 2V_{xc}(p) x(p) C_{kj}$$
$$+ V_{vv}(p) v^2(p) + 2V_{va}(p) v(p) a$$
$$+ 2V_{vc}(p) v(p) C_{kj} + V_{aa}(p) a^2$$
$$+ 2V_{ac}(p) a C_{kj} + V_{cc}(p) C_{kj}^2] \qquad (9)$$

For simplicity, only one cross-coupling coefficient is included. It is deduced from Eq. (6) that the values of these coefficients are all zero when $p = N + 1$. Now, by applying Eq. (7), the following sequential relations are obtained:

$$V_z(p) = V_z(p + 1) - z(p)$$

$$V_v(p) = V_v(p + 1) + V_z(p + 1)$$

$$V_a(p) = V_a(p + 1) + \frac{1}{2} V_z(p + 1) + V_v(p + 1)$$

$$V_C(p) = V_C(p + 1)$$

$$V_{zz}(p) = V_{zz}(p + 1) + 1$$

$$V_{zv}(p) = V_{zv}(p + 1) + V_{zz}(p + 1)$$

$$V_{za}(p) = \frac{1}{2} V_{zz}(p + 1) + V_{zv}(p + 1) + V_{zc}(p + 1)$$

$$V_{zc}(p) = V_{zc}(p + 1)$$

$$V_{vv}(p) = V_{vv}(p + 1) + V_{zz}(p + 1) + 2V_{zv}(p + 1)$$

$$V_{va}(p) = \frac{1}{2} V_{zz}(p + 1) + \frac{3}{2} V_{zv}(p + 1)$$
$$+ V_{za}(p + 1) + V_{vv}(p + 1) + V_{va}(p + 1)$$

$$V_{vc}(p) = V_{vc}(p + 1) + V_{zc}(p + 1)$$

$$V_{aa}(p) = \frac{1}{4} V_{zz}(p + 1) + V_{vz}(p + 1) + V_{az}(p + 1)$$
$$+ V_{zv}(p + 1) + 2V_{va}(p + 1) + V_{aa}(p + 1)$$

$$V_{ac}(p) = \frac{1}{2} V_{zc}(p + 1) + V_{vc}(p + 1) + V_{ac}(p + 1)$$

$$V_{cc}(p) = V_{cc}(p + 1) \tag{10}$$

From Eq. (8), discontinuities are obtained at firing times:

$$V_c^-(p) = V_c^+(p) + V_v^+(p) I_j(p)$$

$$V_{zc}^-(p) = V_{zc}^+(p) + V_{zv}^+(p) I_j(p)$$

$$V_{vc}^-(p) = V_{vc}^+(p) + V_{vv}^+(p) I_j(p)$$

$$V_{cc}^-(p) = V_{cc}^+(p) + V_{vv}^+(p) I_j^2(p)$$
$$+ 2V_{vc}^+(p) I_j(p) \tag{11}$$

The optimal choice of C_{kj} is obtained from maximizing $V'[x(1), v(1), a, C_{kj}]$ with respect to its arguments. This

is equivalent to solving the simultaneous equation

$$0 = V_z(1) + V_{zz}(1)x(1) + V_{zv}(1)v(1)$$
$$+ V_{za}(i)a + V_{zc}(1)C_{kj}$$

$$0 = V_v(i) + V_{vz}(1)x(1) + V_{vv}(i)v(i)$$
$$+ V_{va}(1)a + V_{vc}(i)C_{kj}$$

$$0 = V_a(i) + V_{az}(1)x(1) + V_{av}(1)v(1)$$
$$+ V_{aa}(1)a + V_{ac}(1)C_{kj}$$

$$0 = V_c(1) + V_{cz}(1)x(1) + V_{cv}(1)v(1)$$
$$+ V_{ca}(1)a + V_{cc}(i)C_{kj} \tag{12}$$

c. Results. The above equations were coded by K. Thuleen of Section 311 and were applied to attitude data from *Mariner V*. The matrix of cross-coupling coefficients was computed to be

$$C = \begin{pmatrix} 1.000 & 0.097 & 0.000 \\ 0.113 & 1.000 & -0.004 \\ - & - & 1.00 \end{pmatrix} \tag{13}$$

The coordinate axes are defined by the pitch, yaw, and roll axes. Since roll data was contaminated with many large errors, it was not possible to estimate C_{31} and C_{32}. The standard deviation of these estimates is about 0.003.

B. Communications System Research

1. Frequency Generation and Control: Performance and Analysis of a 100-MHz VCXO, A. Sward

a. Introduction. A 100-MHz voltage-controlled crystal oscillator (VCXO) has been under development for the past several months. Preliminary data has been taken, and the final modules are now under construction.

These VCXOs will be used in conjunction with the hydrogen maser to produce an ultra-stable hydrogen maser frequency standard. The importance of developing a high frequency, low noise VCXO can be readily appreciated when one considers that, since the frequency of the VCXO is multiplied up to S band, the noise is also multiplied by the same factor. The higher the frequency of the VCXO, the less multiplication that is needed, and the lower the noise at S band.

This article is a continuation of one appearing in SPS 37-45, Vol. III, pp. 59–62, that uses the basic circuit design of existing VCXOs (SPS 37-15, Vol. III, pp. 34–36,

ALL RESISTANCE IN Ω UNLESS OTHERWISE SPECIFIED
ALL CAPACITANCE IN pf UNLESS OTHERWISE SPECIFIED

Fig. 27. 100-MHz VCXO

and SPS 37-34, Vol. III, pp. 48–54). A circuit analysis is provided for this oscillator to show the important parameters involved in its operation.

b. Performance. The complete VCXO that has been developed, and which is still under test, is shown in Fig. 27. Preliminary results indicate phase noise to be approximately 0.09 deg rms in a $2\beta_L = 5$-Hz loop. Several factors in the circuit that contribute to the phase noise, in varying degrees, are as follows:

(1) The drive level of the crystal.

(2) The loaded Q of the crystal.

(3) The noise generated by the transistor in the oscillator.

The drive level of the crystal was found to be quite critical, such that a 25% change could cause almost a 2 to 1 change in phase noise. A low drive level produced good long-term stability but poor short-term stability.

A high drive level caused poorer long-term stability, possibly due to the heating of the crystal.

The higher the loaded Q of the crystal, the lower the noise of the oscillator. Since the loaded Q of the crystal is proportional to the unloaded Q, a crystal with a high unloaded Q is desirable. However, there is a limitation in that the higher one goes in frequency, the more difficult it becomes to obtain high Qs in quartz crystals with low series resistance.

c. Circuit description. If one looks at an oscillator from the consideration of bandwidth, several conclusions can be drawn.

$$B_W = \frac{f_c}{Q_L}$$

Bandwidth varies as a function of the ratio of frequency to loaded Q. (See Table 4 for the definitions of the nomenclature used throughout this article.) Hence, to

Table 4. Nomenclature

A	voltage gain		L_e, C_e, R_e	parameters of equivalent series network
B_W	bandwidth		L_s, R_s	inductance and resistance of series inductor
C_b	equivalent input capacity of oscillator transistor		L_r, C_r, R_r	parameters of crystals
C_d	coil-to-case capacity of tuning coil in collector circuit		Q	quality factor
			Q_L	loaded Q of the crystal
C_{dg}	drain-gate capacity		Q_x	unloaded Q of the crystal
C_{gs}	gate-to-source capacity		R_b	equivalent input resistance of oscillator transistor
C_{in}	input capacity of field-effect transistor			
C_v, R_v	parameters of varicap		R_c	equivalent output resistance of oscillator transistor
C_1	base load capacity			
C_2, C_{22}	collector load capacity		R_F, C_F	equivalent base and end load
C_3	coupling capacity		R_p	equivalent π circuit resistance
C_4	input capacity to amplifier following oscillator		R_T, C_T	equivalent collector end load
			V_1, V_2	voltages at particular points
f_c	frequency		X_{cF}	impedance of C_F
G_L	circuit loop gain		X_{cT}	impedance of C_T
G_T	transistor gain		Z_l	load impedance
G_x	external circuit gain		β	current gain of transistor
g_m	transconductance of transistor		$2\beta_L$	noise bandwidth
j	$\sqrt{-1}$		ω	frequency of oscillator

obtain the same bandwidth in an oscillator at a frequency four times higher, the loaded Q of the circuit must also be four times greater. The previously noted limitation of the crystals now becomes an important factor. Several aspects of this 100-MHz VCXO that merit consideration are as follows:

(1) Capacitor tuning was used in the oscillator instead of inductive tuning because of the microphonic effects of the coil.

(2) The input was injected into a low impedance point (base of the transistor) for better oscillator stability.

(3) A field-effect transistor was used as a buffer amplifier to minimize power drain on the oscillator and to give good isolation from the load. The source-follower configuration was chosen to minimize variations of its input capacity due to the Miller effect, i.e., since input capacity is no longer a function of voltage gain, it remains constant, thereby causing no detuning in the oscillator circuit. The input capacity can be shown to be

$$C_{in} = C_{dg} + (1 - A) C_{gs} \cong C_{dg}$$
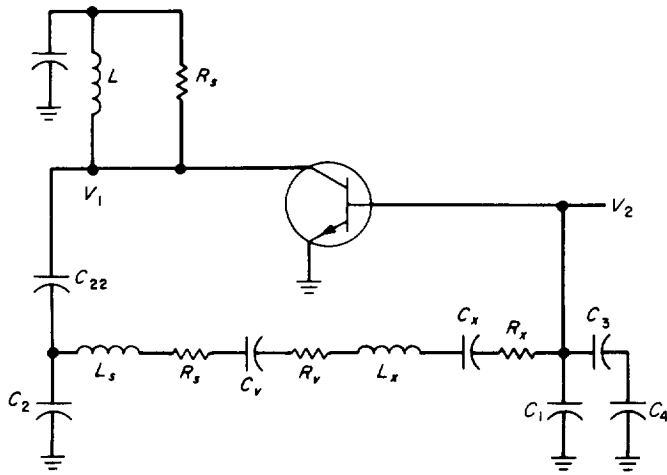
Fig. 28. RF circuitry of the VCXO
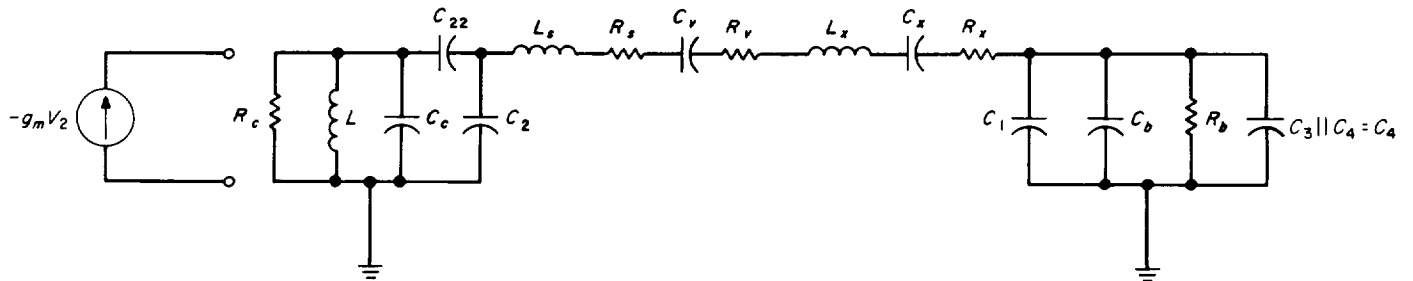
d. Circuit analysis. The RF circuitry of the oscillator is shown in Figs. 28–31. (See Table 4 for definitions of the terms used in these figures.) Stray capacities must be taken into account because of the high frequency involved. The following analysis, although detailed, is necessary for a complete understanding of the problems involved.

The quantities shown in Fig. 30 are as follows:

$$C_c' \cong \left(\frac{C_{22} + C_2}{C_{22}}\right)^3 \frac{1}{\omega^2 R_c^2 C_{22}} \tag{1}$$

$$C_b' = C_b + C_1 + C_4 \tag{2}$$

$$R_c' \cong \left(\frac{C_{22}}{C_2 + C_{22}}\right)^2 R_c \tag{3}$$

Finally, in Fig. 31, the equivalent end-loading circuits are shown by computing an equivalent series network for both ends.

$$C_F = \frac{1 + \omega^2 (C_b')^2 R_b^2}{\omega^2 R_b^2 C_b'} \cong C_b' \tag{4}$$

$$C_T = \frac{1 + (\omega R_c' C_c')^2}{(\omega R_c')^2 C_c'} \cong \frac{1}{(\omega R_c')^2 C_c'} \tag{5}$$

$$R_T = \frac{R_c'}{1 + (\omega R_c' C_c')^2} = \frac{R_c'}{1 + \frac{(R_c')^2}{X_{C_c'}^2}} \cong R_c' \tag{6}$$

$$R_F \cong \frac{X_{C_b'}^2}{R_b} \tag{7}$$

The equivalent circuit in Fig. 31 can now be used to calculate the loaded Q of the oscillator.

Fig. 29. Equivalent RF circuitry of the VCXO
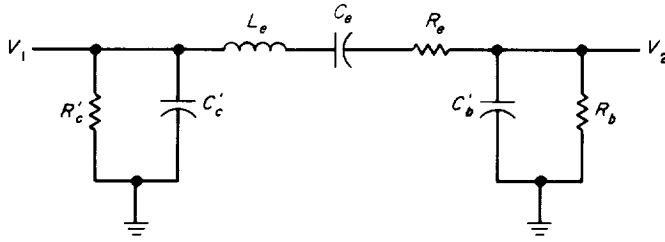
Fig. 30. Simplified equivalent RF circuitry of the VCXO
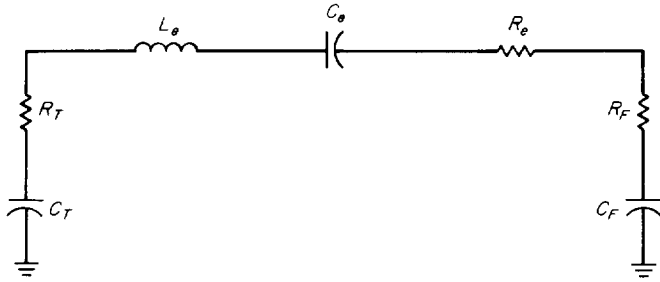
Fig. 31. Basic RF circuitry of the VCXO

In order to simplify the expressions for capacitances, some typical values must be known. For the 2N918 transistor, $C_b = 9$ pF, $C_c = 2$ pF, $R_b = 200\ \Omega$, $R_c = 2$ kΩ, and $g_m = 30$ millimhos. For the field-effect transistor used, $C_1 = 5$ pF. To minimize the variations of the transistor's capacities on the tuning of the circuit, the shunting capacities were chosen to be much greater than the transistor capacities. However, at this high frequency, the circuit will not oscillate if the external capacities are too high because of the low β. Thus, let

$$C_1 = 5C_b$$

$$C_2 // C_{22} \cong 10C_c$$

Hence,

$$C_b' \cong C_b + C_1$$

The loaded Q of the crystal can now be calculated and is

$$Q_L = \frac{\omega L_e}{R_F + R_T + R_e}$$

However, since

$$L_e \cong L_r$$

then

$$Q_L = \frac{\omega L_r}{R_F + R_T + R_e}$$

Hence,

$$Q_L = \frac{R_r Q_r}{R_F + R_T + R_s + R_v + R_r}$$

The loop gain of the oscillator is the product of gain in the external circuit times the gain of the transistor.

The gain of the transistor is

$$G_T = -g_m Z_l$$

The circuit transformations used to obtain Z_l are shown in Fig. 32.

At resonance, Z_l is

$$Z_l \cong \frac{R_c R_p}{R_c + R_p}$$

where

$R_c = $ (output resistance of transistor) $// R_s$

$$R_p = (R_E + R_F)\left(\frac{C_2 + C_{22}}{C_{22}}\right)^2$$

The gain of the transistor is

$$G_T = -g_m Z_l = \frac{-g_m R_c R_p}{R_c + R_p}$$
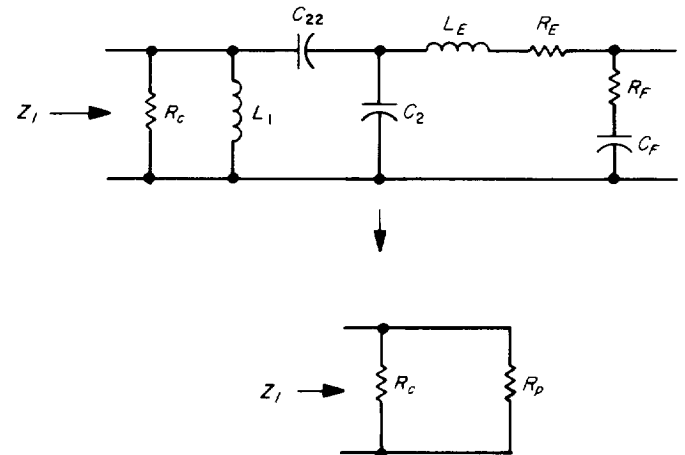
Fig. 32. Circuit transformations used to obtain Z_l

The gain of the external circuit is

$$G_X = \left(\frac{C_{22}}{C_2 + C_{22}}\right)\left(\frac{R_F - jX_{cF}}{R_F + R_E + jX_{cT}}\right)$$

Hence, the loop gain is

$$G_L = \left(\frac{g_m}{\omega C_b'}\right)\left(\frac{C_2 + C_{22}}{C_{22}}\right)\left(\frac{R_c}{R_c + R_p}\right)$$

For the values shown in the circuit in Fig. 27,

$$C_b + C_i = 55\,\text{pF}$$

$$R_s = 2.9\,\Omega$$

$$R_v = 3.2\,\Omega$$

$$R_r = 22.1\,\Omega$$

$$Q_r = 86,500$$

$$R_F = \frac{(29)^2}{200} = 4.2\,\Omega$$

$$R_c' = 900\left(\frac{30}{210}\right)^2 \cong 18.5$$

$$R_T \cong 18.5$$

$$g_m = 30\,\text{millimhos}$$

The loaded Q of the crystal is, then,

$$Q_L = \frac{(22.1)(86,500)}{4.2 + 18.5 + 2.9 + 3.2 + 22.1} \cong 38,000$$

The circuit loop gain (G_L) is

$$G_L = (0.03)(29)(7)\left(\frac{900}{900 + 1750}\right) \cong 2.1$$

The phase relationship for the oscillator is not included in the analysis because the long and tedious equations involved would only serve to obscure the important results obtained. It is sufficient to say that the tuned tank circuit on the output of the transistor accounts for a small part of the phase shift needed, while the π network in the feedback circuit gives the remainder.

e. Conclusion. There are two new oscillator circuits now in the design stage that might improve the phase

noise in VCXOs. One of these circuits, which utilizes a field-effect transistor with its high input and output impedance as the active device, will increase the loaded Q of the crystal and thereby produce a smaller bandwidth. The other circuit uses several transistors in the oscillator with a moderate amount of negative feedback.

2. Information Systems: Digitally Controlled Oscillator,
W. A. Lushbaugh

a. Introduction. The digitally controlled oscillator, another in the J-card series of computer compatible units, is designed to extend the capability of the Scientific Data Systems (SDS) 900 series computers. The card is capable of being commanded by the computer to generate an accurately spaced series of interrupts that can be used to provide real-time information to a program via the interrupt lines.

b. Functional description. Figure 33 shows the block diagram of the digitally controlled oscillator. The basic oscillator loop consists of a 20-bit primary counter and a hold register of equal length. The primary counter counts at a 2- or 1-MHz rate depending upon the input frequency standard available. If a 10-MHz reference is available, it is divided by 5 in the clock divider and distributed to the system; otherwise, a 1-MHz frequency is selected by the jumper on the board and distributed. When the primary counter reaches the value of all *ones*, a word detector sets the interrupt flip-flop, which also transfers the number held in the hold register into the primary counter. Thus, the primary counter will provide an interrupt to the computer at a rate dependent upon the value held in the hold register.

The value in the hold register can be changed by command of the computer. Upon receipt of EOM 37677,4 the EOM control unit sets a flip-flop and during the next parallel output (POT) 1 signal from the computer, it will transfer a new value from the computer C-register into the hold register.

Since an extra unit of time is used to transfer the hold register to the primary counter, the computer loads the *two's* complement of the desired period into the hold register.

The digitally controlled oscillator also has the capability of shifting the phase of interrupt output. The auxiliary counter is used for this purpose. After receipt of EOM 37577,4 the EOM unit loads the contents of the C-register into the auxiliary counter during the next POT 1
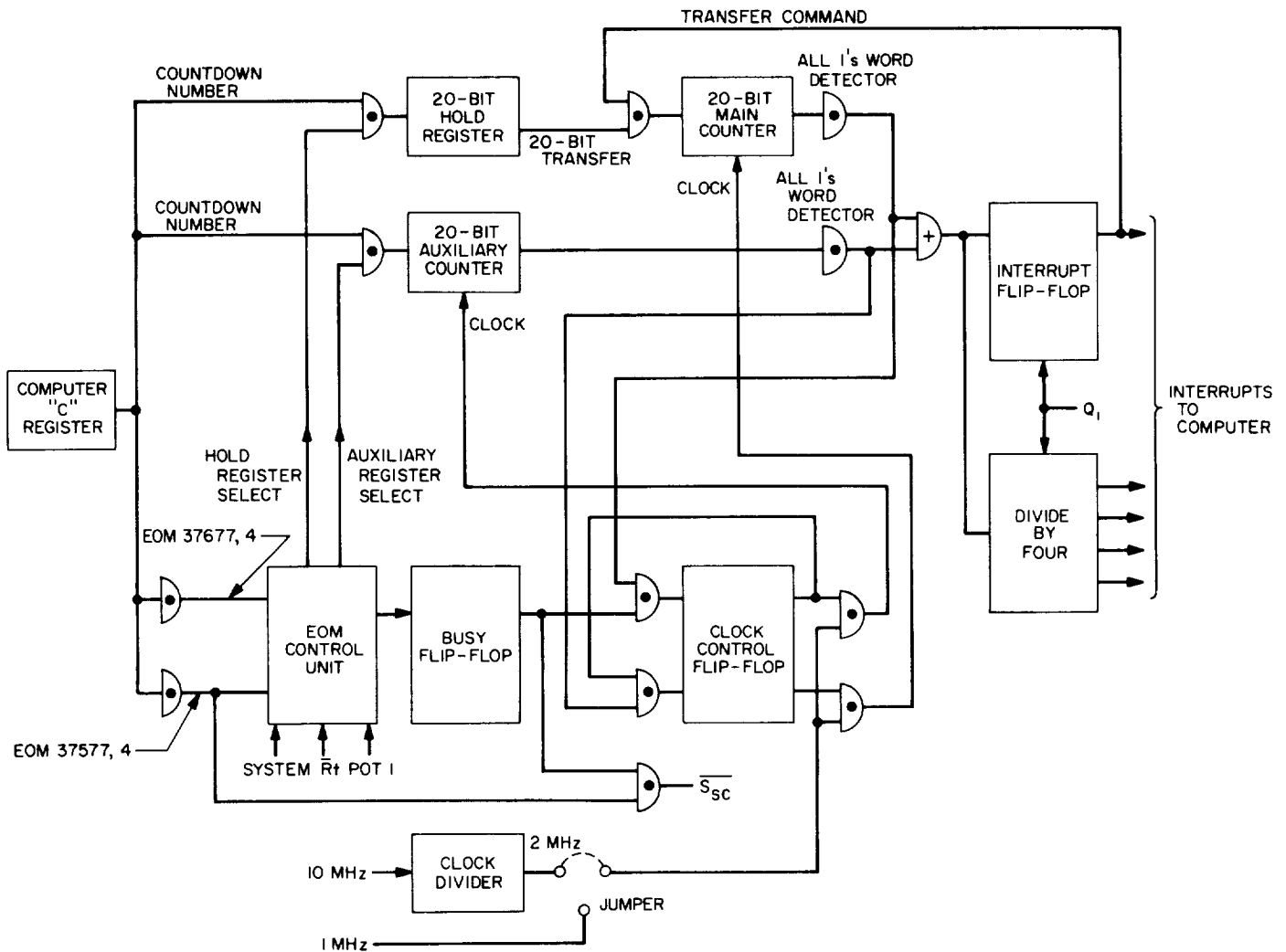
Fig. 33. Digitally controlled oscillator block diagram

signal and sets the busy flip-flop. This value is then held until the next time at which the primary counter develops an output. This output is used to turn over the clock control flip-flop and direct the counting pulses to the auxiliary counter. When the counter reaches the all *one's* state, it will generate the interrupt in the same manner as the primary counter and also reset the busy flip-flop and return the clock control flip-flop to its normal state.

The busy flip-flop also serves to provide an SKS[7] signal to the computer to allow it to check if the auxiliary register is free to be used.

Four quadrature interrupts are developed from the primary interrupt. These four interrupts occur in fixed sequence, once each for every four primary interrupts. This particular sequence permits the number-controlled

oscillator to be used as the timing control device of a bit synchronization and tracking loop.

c. Hardware. The digitally controlled oscillator was entirely constructed from microcircuits. The Amelco 361 was used to convert the 8-V computer signals at the input to microcircuit levels and Raytheon 210G was used at the interrupt outputs to restore the signal to 8 V. The remainder of the microcircuits was Signetics 8000 series, including a new 4-bit binary counter/hold register package type S8281. In all, there are sixty-two flat packs, packaged in eight stick modules, one TO-5 package, two discrete component gates and power supplies packaged on one standard SDS 6- × 4½-in. card. The completed system is shown in Fig. 34.

---

[7]SKS = skip if external signal not set.
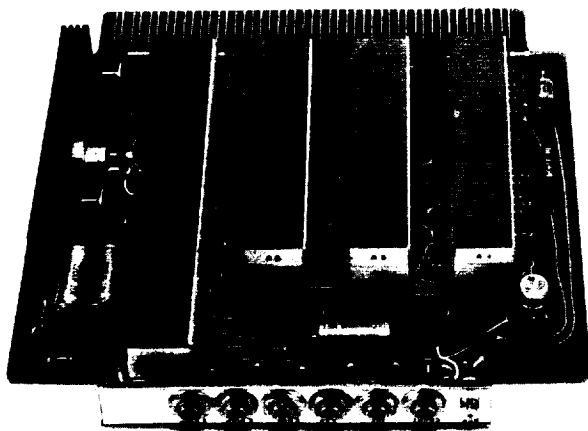
Fig. 34. Digitally controlled oscillator card

3. Information Systems: Improved Magnetic Tape Capability for the SDS Symbol Assembler, D. L. Rice

a. Introduction. The Scientific Data Systems (SDS) symbol assembler, SYMBOL, operating under the Monarch control system has been modified to provide a greater flexibility for magnetic tape input/output (I/O) operations. With the improvements described in this article, it is possible to make the assignment of magnetic tape unit numbers for symbolic input, symbolic intermediate scratch, binary output, and list output from the Monarch system at the time the SYMBOL system is called. In addition, requests can be made by means of Monarch parameters for an input intermediate scratch tape with typewriter, paper tape, or card symbolic input and for a diagnostic list output with only those output lines listed that begin with a non-blank diagnostic character. These modifications result in a system more consistent with the capabilities inherent in the Monarch control system.

b. Present SYMBOL system. The magnetic tape I/O subroutines used with the existing SYMBOL assembler were written so that particular unit numbers are assumed for each magnetic tape I/O function (i.e., if magnetic tape is specified as the symbolic input medium, the input data is assumed to be on tape unit 1; if a scratch tape is requested, the symbolic input is copied on unit 1 during pass 1; if binary output on magnetic tape is requested, it is written on unit 2; and, likewise, magnetic tape list output is written on unit 7). This system has the disadvantage that when the SYMBOL system is used in conjunction with other programs for manipulating data on magnetic tape it is often necessary to change the unit

selector switch on several of the physical tape units. This results in delays in processing due to the pause for operator intervention as well as possible confusion in remembering which physical tape unit contains a particular segment of data. One possible result of the latter difficulty is that of accidentally erasing magnetic tape 1 by requesting a scratch tape.

Requests for an intermediate scratch tape and for an output listing containing only diagnostic lines are made in the existing system by means of console switch settings, which also require operator intervention if these are to be changed during batch processing jobs.

c. Modifications. The Monarch control message processor has been modified so that two more parameters may be specified in the SYMBOL system call. This control message now has the form:

$$\Delta \text{SYMBOL} \quad P_1, P_2, P_3, P_4, P_5$$

Parameter P_1 specifies which mnemonic table is to be used during the assembly:

Parameter	Mnemonic table
910	910
920	920
9300	9300

Parameter P_2 is optional and specifies whether an intermediate scratch tape is written when the symbolic input is read from TY, PR, or CR:

Parameter	Function
SI	Scratch tape written on X1 if input is from TY, PR, or CR
S2	No scratch tape written. Two passes read from S1 device

If P_2 is not present, the value SI is assumed. Parameters P_3, P_4, and P_5 are also optional and specify the output data from the assembly:

Parameter	Type of output
BO	Binary output
LO	List output
D	Diagnostic listing

If both LO and D are present, a diagnostic listing is output. Magnetic tape unit assignments, including X1, are taken from unit assignment table (UAT) values established by the most recent ASSIGN control message.

d. Technical considerations. The contents of location 02 are used to communicate the presence of the various parameters to the SYMBOL loader according to the following format:

Old system	New system	Function
Bit 3 set	Bit 3 set	Read input from SI device
Bit 9 set	Bit 7 set	Binary output on BO device
Bit 15 set	Bit 11 set	List output on LO device
	Bit 15 set	Read pass 2 from X1 device
	Bit 19 set	List diagnostic listing only
Bits 22, 23	Bits 22, 23	0 = 920
		1 = 910
		2 = 9300

The 4 UAT entries for SI, BO, LO and X1 are accessed via addresses stored in locations 03 through 06. The unit assignment codes are used as in the old system to determine which I/O subroutines should be loaded. These codes are then merged with a table of I/O instructions (EOMs and SKSs) for each device and stored in the subroutines as they are loaded. All I/O instructions in the various subroutines have been changed to *execute* (EXU) instructions referring to the stored I/O instruction table.

The parameters for scratch tape request and diagnostic output request (location 02, bits 15 and 19) are used to set flags X1FLAG and DFLAG in the loader. The loader in turn stores X1FLAG in the input subroutine TSI–PSI or CSI, and DFLAG in any list output subroutine loaded (TLO, MLO, or LLO).

The I/O subroutines have been increased in length somewhat to accommodate the I/O instruction table and a short routine to modify the buffer instructions MIW and WIM to MIY and YIM, respectively, when Y buffer assignment is specified. This increase ranges from 15 locations in the subroutine PBO to 48 locations in the subroutine CSI. The total increase in system storage requirements is less than 130 locations for any I/O configuration.

4. Information Systems: Spacecraft Demonstration of Sequential Decoding Using *Lunar Orbiter V*, W. Hurd

a. Introduction. The performance of sequential decoding in deep space communications has previously been predicted analytically and experimentally. A series of experiments utilizing *Lunar Orbiter V* and the Echo DSS has recently demonstrated that the performance of a sequential decoder using data transmitted on a spacecraft link is comparable to that predicted and significantly superior to that of practical block codes. For example, an erasure probability of 10^{-4} can be attained using sequential decoding with 2 dB less signal-to-noise ratio than required for an error probability of 10^{-4} using a $k = 6$ biorthogonal code and maximum likelihood decoding.

b. Background on sequential decoding. Sequential decoding is useful for deep space communications because it enables communication at lower signal-to-noise ratios and with lower error probabilities than block codes of reasonable size. Practical sequential decoders can be mechanized to operate with negligible error probability at signal-to-noise ratios within 4 to 5 dB of channel capacity, i.e., with ratios of information bit energy to noise spectral density, E_B/N_0, of 2.4 to 3.4 dB. Jacobs (Ref. 1) presents a clear comparison of the theoretical performance of sequential decoding systems and block-coded systems, and an introduction to sequential decoding. Theoretical and laboratory experimental results for the decoder used in this experiment are given by Stanek.[8]

In a system using sequential decoding, the encoder is particularly simple, consisting of a binary shift register of about 24–36 stages, and several *exclusive or* gates. The data is encoded into long blocks, called *trees*, of length 500 to several thousand bits. For a rate R code, $1/R$ symbols are generated for each information bit, and, if one of the $1/R$ symbols is always equal to the information bit, the code is said to be a *systematic code*. The length of the shift register is known as the *constraint length*, because the encoded symbols for a data bit depend on this number of previous information bits.

The number of computations required to decode a tree of data is random, with statistics depending on the signal-to-noise ratio. For each system, there is a signal-to-noise ratio, $(E_B/N_0)_{comp}$, such that for this and all higher signal-to-noise ratios, the average number of computations per information bit is finite for all tree sizes.

The probability of having an undetected error using a sequential decoder can be made arbitrarily small at all

[8]Stanek, P., "A Digital Demonstration of Sequential Decoding and Comparison With Block-Coded Systems, SPS 37-51, Vol. III (to be published).

signal-to-noise ratios corresponding to rates below channel capacity. In particular, the bit error probability at $(E_B/N_0)_{comp}$ varies as 2^{-K} for nonsystematic codes (Ref. 2) and $2^{-K(1-R)}$ for systematic codes (SPS 37-50, Vol. III, pp. 241–248), where K is the constraint length. Thus, the error probability is reduced simply by increasing the constraint length.

Even though undetected errors can be made arbitrarily rare, erasures do occur more frequently. Erasures occur because of the random number of computations required to decode a tree. When the number of computations required to decode a particular tree exceeds the capability of the decoder, the tree cannot be decoded in real time and is "erased." The probability of erasure is small when the decoder speed advantage is high, i.e., when the decoder can make a large number of computations per bit time. It is important to note that data which is not decoded in real time is not irrevocably lost; it can be stored on tape and decoded off line. In fact, the probability of not decoding correctly can be reduced to the arbitrarily small undetected error probability, because a tree of finite length can always be decoded in a finite length of time.

Finally, even if one does not chose to decode "hard" trees off line, practical sequential decoders can be built which have lower *erasure* probabilities than the *error* probabilities of practical block codes for E_B/N_0 exceeding about 3 to 4 dB.

c. Description and performance of decoder used in the experiment. The code used in this experiment is a systematic rate one-third code with constraint length 25 and tree length 2048 bits, of which 32 are used for tree termination and synchronization. Eight-level quantization is used at the decoder input. With these parameters, $(E_B/N_0)_{comp} = 2.2$ dB, and the probability of an undetected bit error is small for all signal-to-noise ratios exceeding 2.2 dB. This error probability could have been made smaller by increasing the constraint length.

The decoding algorithm was implemented on an SDS 930 computer. Data symbols are entered into the computer through an interrupt routine. The decoder's first function is to obtain tree synchronization by performing a matched filtering operation on the known symbols included in every tree for this purpose. The program was written to achieve positive synchronization at information rates in excess of 1000 bits/sec, and requires typically three to six trees of data before synchronization is attained.

After obtaining tree synchronization, the computer decodes the data, printing the decoded data on the line printer. When an erasure occurs, special symbols are printed to indicate this event. When five successive trees contain erasures, the program assumes that tree synchronization has been lost, and returns to the synchronization mode. The reason for re-synchronization is that cycle slipping in the subcarrier phase-locked loop or in the symbol tracking loop could cause loss of tree synchronization, and five successive overflows are otherwise unlikely to occur at signal-to-noise ratios of interest.

Laboratory tests (see Footnote 8) were performed using pseudo-random noise to determine the erasure rates for the decoder as a function of signal-to-noise ratio and data rate. The results are shown in Fig. 35 for rates of 1000, 500, and 100 bits/s. As anticipated, the erasure rate increases with the data rate, because the computer can make fewer computations per bit time at higher data rates. The data rates of 1000, 500, and 100 bits/s correspond to speeds of approximately 5, 15 and 100 node examinations per information bit. The relationship is nonlinear because of computer "overhead" for input/output.
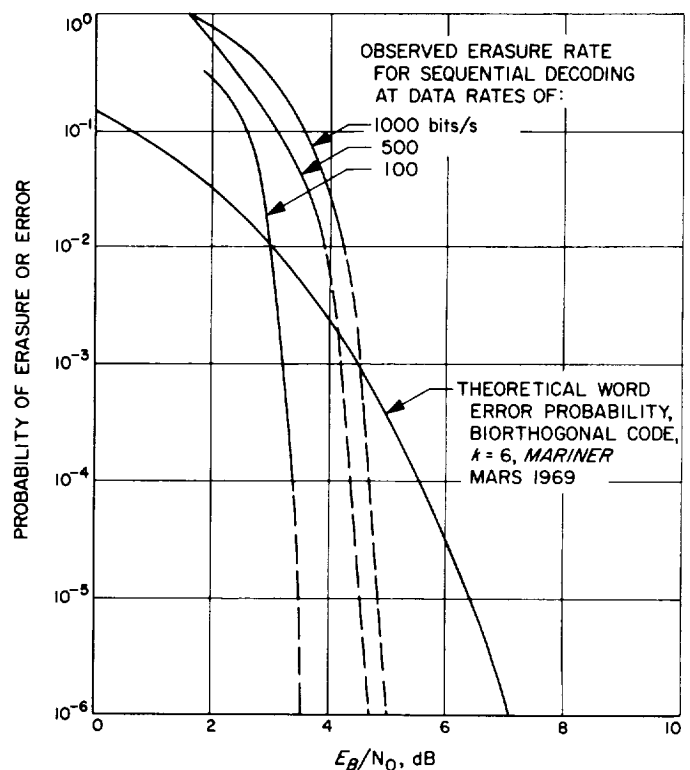
Fig. 35. Observed erasure probability for sequential decoding compared with error probability for biorthogonal code

At low data rates, erasures probably occurred more often due to the short buffer size (512 bits) than due to computation time. Decoders with larger buffers would thus make fewer erasures than this decoder at speed advantages of about 20–50 and higher. At 100 bits/s, the erasure probability is 10^{-3} at a signal-to-noise ratio of about 3.2 dB, or 1 dB above $(E_B/N_0)_{comp}$, and drops to 10^{-4} at about 3.4 dB. Throughout these experiments, no undetected errors occurred at any signal-to-noise ratios of $(E_B/N_0)_{comp}$ or higher.

Also shown in Fig. 35 is the theoretical word error probability for the *Mariner* Mars 1969 biorthogonal ($k = 6$) block code. For data rates of 100 bits/s, the erasure rate for the sequential decoder is lower than the error rate for the block code at all signal-to-noise ratios exceeding 3 dB, and the comparison is quite startling at higher signal-to-noise ratios. For example, to obtain an error probability of 10^{-4} with the block code, E_B/N_0 of about 5.5 dB is required, whereas the sequential decoder can obtain an erasure of 10^{-4} with about 2 dB less signal-to-noise ratio. This same energy-saving performance can be obtained at data rates as high or higher than the 16,200-bit/s *Mariner* Mars 1969 rate by using fairly inexpensive special-purpose sequential decoders.

d. Description and results of the Lunar Orbiter V experiment. The *Lunar Orbiter* V sequential decoding experiment used the decoder described above, together with the communication system shown in Fig. 36. Fifteen trees of data were encoded in advance and stored in an SDS 910 computer, and then read out repetitively during

the experiments. The data was modulated onto a subcarrier by a specially designed symbol and subcarrier generator, and then onto the ranging channel of the Echo DSS transmitter. The data was transmitted to *Lunar Orbiter* V, and transponded back to the Echo DSS, where it appeared at baseband on the receiver video output. Subcarrier and symbol synchronization and symbol detection were accomplished by a modified Elpac model 1020 signal conditioner, and the symbols were read into the SDS 930 computer through a 3-bit analog-to-digital converter. The computer acquired tree synchronization and decoded the data as described in the previous section.

After decoding, the binary data bits were converted to the SDS 6-bit alphanumeric code, and the corresponding characters were printed by the line printer. Each tree of data corresponded to 3 lines on the line printer output, and the 15 trees comprised a pattern corresponding to the JPL letterhead. Figure 37 shows this pattern as received over the spacecraft link. When erasures occurred, a special symbol was inserted at one or more places within

Fig. 36. Communication system block diagram for
Lunar Orbiter V sequential decoding experiment

Fig. 37. Message received from Lunar Orbiter V
with no erasures or errors

Fig. 38. Message received with erasures on first four trees of data

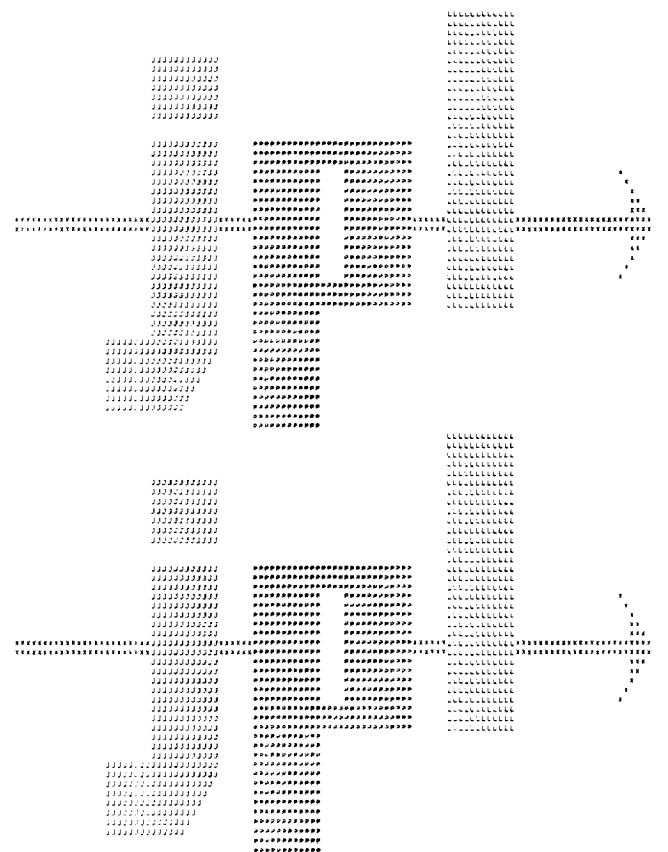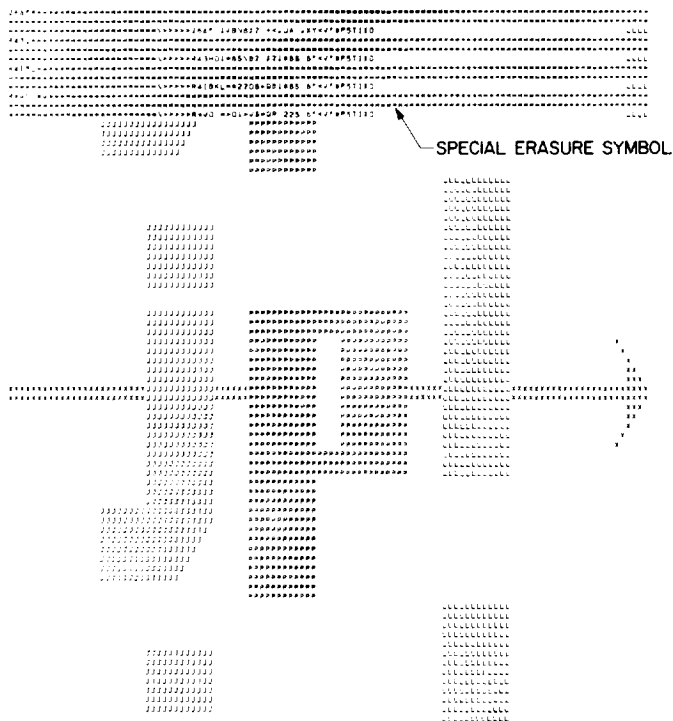the three lines corresponding to the tree erased. Figure 38 shows an example of erasures. In this particular case, the first line shown was the first line received after tree synchronization was attained. Four successive trees contained erasures, but then decoding proceeded erasure-free. If a fifth tree had been erased, the decoder would have returned to the synchronization mode.

In 3 days of testing, the system was operated at various data rates and signal-to-noise ratios. The signal-to-noise ratio at the decoder varied even at fixed data rates, mainly because the system noise temperature depended on the position of the tracking antenna relative to the moon. The maximum rate at which decoding was accomplished was 625 bits/s, but the signal-to-noise ratio was below $(E_B/N_0)_{comp}$, so that about half of the trees were erased. Fairly good performance was attained at $416\frac{2}{3}$ bits/s.

During the demonstration held on February 26, 1968, the system was operated at one data rate, 312.5 bits/s. By measuring the symbol error probability at the detector output, E_B/N_0 was estimated to be about 5 to 5.5 dB. Data was decoded for about an hour, or for about one million bits, without having any erasures or errors. To demonstrate the synchronization capability of the decoder, the data was momentarily disconnected from the

computer, causing erasures and loss of tree synchronization. Each time this was done, the decoder promptly reacquired tree synchronization.

To demonstrate performance at lower signal-to-noise ratios, the tracking antenna boresight was turned away from the spacecraft so that less signal power was received. Initially, E_B/N_0 was reduced to about 3.5 to 4 dB, at which level no errors or erasures were observed. When further reduced to about 2 to 2.5 dB, erasures became frequent and, after a few minutes, five successive erasures occurred, returning the decoder to the synchronization mode. Synchronization was successfully acquired, but only after several minutes. This type of performance is to be expected at such low signal-to-noise ratios, near $(E_B/N_0)_{comp}$.

Overall, the performance of the decoder with the spacecraft communication link was about the same as the laboratory performance shown in Fig. 35. Exact comparisons could not be made because of the varying signal-to-noise ratio and the difficulty in accurately measuring the signal-to-noise ratio. The error-free performance at 312.5 bits/s was attained with about 17 dB less energy per bit than the uncoded *Lunar Orbiter V* command channel, which operates at 50 bits/s with about 12 dB more signal power than the ranging channel used in this experiment.

References

1. Jacobs, I. M., "Sequential Decoding for Efficient Communication from Deep Space," *IEEE Trans. Commun. Technol.*, Vol. COM-15, No. 4, pp. 492–501, Aug. 1967.

2. Viterbi, A. J., "Error Bounds for Convolutional Codes and an Asymptotically Optimum Decoding Algorithm," *IEEE Trans. Inform. Theory*, Vol. IT-13, No. 2, pp. 260–269, Apr. 1967.

5. Digital Communications: Digitization and Recording of Analog Tape Recorded Data, G. A. Morris, Jr.

a. Introduction. A program has been written in the SDS symbol language to convert data recorded on analog magnetic tape to digital data recorded on computer digital magnetic tape. The program runs on the SDS 930 computer located at the Venus DSS. The program will run on any SDS 930 with 800-bit/in. tape units and interlace.

b. System. The block diagram of the system is shown in Fig. 39. One or more tracks of the analog magnetic tape is recorded with a signal plus a reference frequency which is used to control sampling of the signal. The reference frequency must be chosen to exceed the Nyquist sampling rate. The reference signal is recorded on the
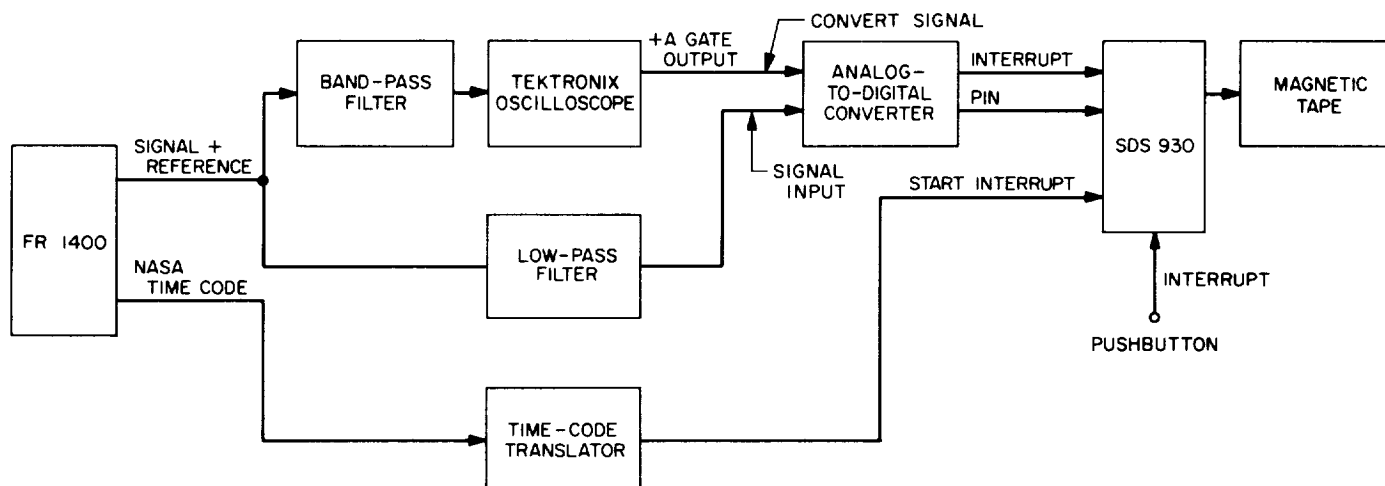
Fig. 39. System block diagram

same track as the data to reduce phase modulation caused by tape skew. The reference is removed from the signal before the analog-to-digital (A/D) converter by passing the signal through a low-pass filter.

This particular system was developed to digitize data taken during the *Mariner* Venus 67 occultation experiment. The bandwidth of the signal was 100 kHz and a reference frequency of 320 kHz was chosen. This reference frequency represents the fastest rate that can be processed onto magnetic tape by the computer when the analog tape playback is reduced in speed by a factor of 16. The limiting element in the system is the rate at which digital data can be written on magnetic tape. The reason for the entire system is that the signals of these bandwidths cannot be digitized and recorded on magnetic tape in real time, but by recording analog and playing back with a large speed reduction, it is possible to accomplish the same objective.

The reference frequency is removed from the signal by a bandpass filter. A standard oscilloscope is used as a zero-crossing detector and has proved to be quite acceptable in performance and is readily available. The output of the Tektronix oscilloscope +A gate output triggers the A/D converter sample and hold circuit, which in turn interrupts the computer when the signal has been converted and is ready to be accepted by the computer. The computer stores digitized samples until a block of 2048 samples (12 bits each) can be written on magnetic tape. The block length of 2048 (12-bit) words is chosen to be as large as possible so that the write speed on magnetic tape will be as high as possible without requiring too much memory in the computer which later processes the data. With this block length at 20-kHz sampling rate, the digital

tapes are averaging almost 55 in./s, where the maximum rate is 60 in./s.

The NASA time code is recorded on one track of the analog tape and can be converted by a time code translator to provide a 1-s pulse to automatically start processing data on the second. If the automatic start signal is not available, the program may be started manually by the pushbutton connected to interrupt 72.

It is desirable to put an integral number of seconds of real-time data on one digital magnetic tape. This maximum works out to be 28 s which is made up of 4375 records of 2048 words of 12 bits each. This technique provides for relatively easy timing of the digital information since no time information is needed, except for tape record counting.

c. Program. The program, when sampling at 20 kHz, must input a number from the A/D converter and output 12 bits (2 characters) to the magnetic tape every 50 μs and also have time available to set up the interlace output, detect errors, and control the data flow into and out of core storage.

A flow chart of the entire program is shown in Fig. 40. The "begin" interrupt may be from the time code translator or pushbutton interrupt 72. The "data" interrupt is from the A/D converter.

The data is read from the A/D converter into a 4096-word array. When the first half of the array is filled, it is written on magnetic tape while the second half of the array is being filled. When the second half of the array is filled, it is written on magnetic tape while the first half

Flow Chart

```
START
  │
ERASE FROM
LOAD POINT
  │
INITIALIZE
PROGRAM
  │
ARM BEGIN
INTERRUPT
  │
FIRST
HALF OF TABLE ──NO
FILLED?
  │ YES
CHANNEL ──NO──→ DISABLE
READY?              INTERRUPT
  │ YES             HALT
WRITE ──YES──→ RECORD
ERROR?              RECORD
  │ NO              NUMBER
WRITE
TAPE
  │
SECOND
HALF OF TABLE ──NO
FILLED?
  │ YES
CHANNEL ──NO──→ DISABLE
READY?              HALT
  │ YES
WRITE ──YES──→ RECORD
ERROR?              RECORD
  │ NO              NUMBER
WRITE
TAPE
  │
NO── 4375
     RECORDS?
  │ YES
TYPE WRITE
ERRORS
  │
HALT
```

```
BEGIN
INTERRUPT
  │
DISARM
BEGIN
  │
ARM DATA
INTERRUPT
```

```
DATA
INTERRUPT
  │
DATA
SUBROUTINE
```

Fig. 40. Program flow chart

is being filled again. This technique requires the tape write operation to be slightly faster than the input of data.

A test is made each time a magnetic tape write request is given to see if the tape unit is ready. If it is not ready, then the sampling rate is too high and the program dis-

ables the interrupts and halts. This is one error-detection feature built into the program. The other error detector in the program records the number of any record containing a write error. The total number of write errors and the record numbers are typed out at the end of the tape.

The subroutine used to collect data and store it in the table is shown below. This subroutine requires 13 memory cycles for 22.75 μs. During this time the interlace magnetic tape output requires one memory access for a total time of 26.25 μs out of every 50 μs. The remaining time is available for error testing and magnetic tape channel setup.

DATA	PZE		
	EOM	030006, 4	A/D INPUT
	PIN	TBL + 4096, 2	
	BRX	$ + 2	
	LDX	= −4096	
	BRU	*DATA	

6. Digital Communications: Iterative Sequential Digital Logic Machines for Generating Orthogonal and Biorthogonal Codes, T. O. Anderson

a. Introduction. In contrast to the popular cyclic codes, the orthogonal code is a highly structured code. Although cyclic codes are easier to generate, an orthogonal code was selected for the *Mariner* Mars 1969 high-rate channel because of the ease with which it may be decoded. The *Mariner* Mars 1969 decoder is an iterative sequential digital logic machine (SPS 37-17, Vol. IV, pp. 71–73, and SPS 37-39, Vol. IV, pp. 247–252). Because of its modularity, this type of machine has many obvious advantages over other special-purpose machines. It is the *Mariner* Mars 1969 decoder design that inspired the modular encoder design presented here. Besides requiring less hardware than other special-purpose encoders, the same advantages are claimed for this encoder as for the *Mariner* Mars 1969 decoder.

b. Structural property of the orthogonal code. The code dictionary is a square matrix whose elements are +1 and −1 and whose row vectors are mutually orthogonal. A matrix or dictionary H_n includes 2^n vectors and is defined by

$$H_n = H_{n-1} \otimes H_1$$

where $\otimes$ is the symbol for the Kronecker product and

$$H_1 = \begin{bmatrix} +1 & +1 \\ +1 & -1 \end{bmatrix}$$

which is also the dictionary for a single variable. The dictionary for two variables is

$$H_2 = \begin{bmatrix} H_1 & H_1 \\ H_1 & H_1 \end{bmatrix}$$

and for

$$H_n = \begin{bmatrix} H_{n-1} & H_{n-1} \\ H_{n-1} & \overline{H_{n-1}} \end{bmatrix}$$

The actual dictionaries for two and three variables are:

Two-variable dictionary

$$\begin{bmatrix} 1 & 1 & 1 & 1 \\ 1 & -1 & 1 & -1 \\ 1 & 1 & -1 & -1 \\ 1 & -1 & -1 & 1 \end{bmatrix}$$

Three-variable dictionary

$$\begin{bmatrix} 1 & 1 & 1 & 1 & 1 & 1 & 1 & 1 \\ 1 & -1 & 1 & -1 & 1 & -1 & 1 & -1 \\ 1 & 1 & -1 & -1 & 1 & 1 & -1 & -1 \\ 1 & -1 & -1 & 1 & 1 & -1 & -1 & 1 \\ 1 & 1 & 1 & 1 & -1 & -1 & -1 & -1 \\ 1 & -1 & 1 & -1 & -1 & 1 & -1 & 1 \\ 1 & 1 & -1 & -1 & -1 & -1 & 1 & 1 \\ 1 & -1 & -1 & 1 & -1 & 1 & 1 & -1 \end{bmatrix}$$

The partitions show the structural properties of the code. From this structure, it can be deduced that a code word can be generated symbol-by-symbol by a mod 2 mapping between the original information word and a binary sequence of the same number of variables.

One design of an encoder to generate this code is shown in Fig. 41. Each bit of a binary counter is *and*-ed with a
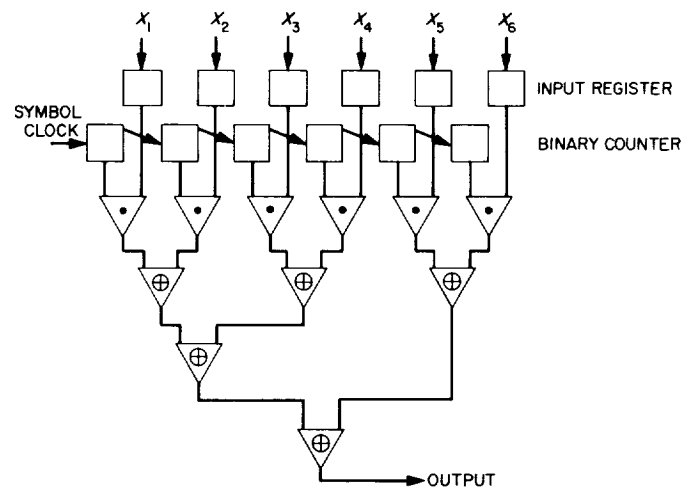
Fig. 41. Biorthogonal code encoder design concept

corresponding information bit. The mod 2 function between the output of the *and* gates is formed by cascading 2-term exclusive *or* gates.

The mod 2 function is equivalent to a parity function which indicates whether the number of *ones* in a vector is odd or even. This suggests the mechanization shown in Fig. 42 and described in detail in SPS 37-47, Vol. III, pp. 263–267. The information bits here are contained in a shift-around register. As the register is shifted around, the *ones* will trigger a flip-flop. The final state of the flip-flop will indicate whether the number of *ones* was odd or even. The binary mapping is accomplished by shifting the binary count around synchronously with the information bits and adding one binary count for each cycle. A single *and* gate selects only the appropriate information bits. In this design, the mod 2 function is then computed serially using six time units as opposed to the previous method computed in parallel using one time unit. A saving of hardware is then possible in the serial method as hardware is traded against operational time units.
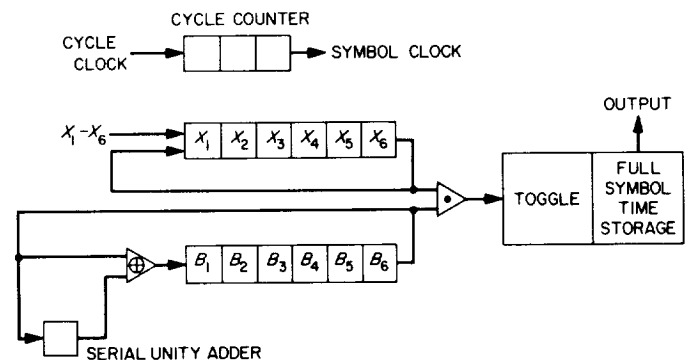
Fig. 42. Serial concept biorthogonal code encoder

c. Design of iterative sequential encoder.

c. Design of iterative sequential encoder. For the design introduced here, there are no known references. The description and explanation will therefore be meticulous.

This design is modular and each module operates in a continuous serial or cyclic mode. While previous serial designs use as many time units per symbol as there are information bits in the original data word, this design uses only one time unit per code symbol. Each module consists of a 2-bit shift register, a mod 2 gate, and a storage bit. The input to the register is a mod 2 function between its output and the holding bit.

Each higher order module is shifted around at one-fourth the rate of the lower order module. No other switching or control is required.

The design strategy is based on the following mod 2 algebraic expressions

$$X \oplus 0 = X$$

$$X \oplus X = 0$$

$$X \oplus X \oplus X = X$$

$$X \otimes X \oplus X \oplus X = 0$$
$$\vdots \qquad \vdots$$

That is,

$$\text{Odd number of } X = X$$

$$\text{Even number of } X = 0$$

This suggests that if a set of variables in a shift register is continuously shifted around and entered through a mod 2 function between the output of the register and another variable, each variable in the register will be mod 2-ed every other cycle with the entry variable. This then suggests the mod 2 mapping between the entered variables and a binary sequence that is sought. The block diagram shown in Fig. 43 and the truth table (Table 5)
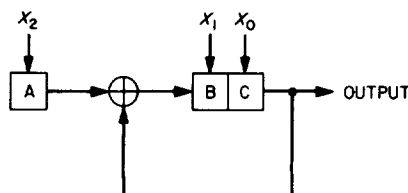
Fig. 43. Module diagram

Table 5. Truth table

Clock	A	B	C
1	X_2	X_1	X_0
2	X_2	$X_0 \oplus X_2$	X_1
3	X_2	$X_1 \oplus X_2$	$X_0 \oplus X_2$
4	X_2	X_0	$X_1 \oplus X_2$
5	X_2	X_1	X_0
·	·	·	·
·	·	·	·
·	·	·	·

Table 6. Truth table, where $X_0 = 0$

Clock	A	B	C
1	X_2	X_1	0
2	X_2	X_2	X_1
3	X_2	$X_1 \oplus X_2$	X_2
4	X_2	0	$X_1 \oplus X_2$
5	X_2	X_1	0

Table 7. 2-bit binary truth table

X_2	X_1
0	0
0	1
1	0
1	1
0	0
0	1
1	0
1	1

will clarify this point. The variables X_0, X_1, and X_2 are loaded into the module and a shift clock applied to the 2-bit recycling shift register. If $X_0 = 0$, the truth table will be as shown in Table 6. The output from C will then be a mod 2 mapping between the entered variables X_1 and X_2 and a 2-bit binary truth table (Table 7). If the output of a second identical module whose entries are 0, X_3, and X_4 is connected mod 2 to the output of the first module (Fig. 44), and if the second module is clocked once every fourth clock pulse, the combined output will be a mod 2 mapping between the entered variables X_1, X_2, X_3, and X_4 and a 4-bit binary truth table (Table 8).

For a larger number of variables, identical modules are similarly added as required and each new module is clocked at one-fourth the rate of the preceding module.

Table 8. 4-bit binary truth table

X₄	X₃	X₂	X₁
0	0	0	0
0	0	0	1
0	0	1	0
0	0	1	1
0	1	0	0
0	1	0	1
0	1	1	0
0	1	1	1
1	0	0	0
1	0	0	1
1	0	1	0
1	0	1	1
1	1	0	0
1	1	0	1
1	1	1	0
1	1	1	1

Fig. 45. Functional design of iterative sequential biorthogonal encoder

Fig. 44. Mod 2 output connection of two identical modules

The operation is continuous and no other switching or control is required.

Figure 45 is a functional block diagram of an encoder utilizing the design concept described. This encoder is equivalent to those shown in Figs. 41 and 42.

d. Encoder application of design for the Mariner Mars 1969 biorthogonal code. It is shown in SPS 37-47, Vol. III, pp. 263–267, that the Mariner Mars 1969 code can be generated by a mod 2 mapping between the original six information bits and a certain truth table (Table 2, p. 264, of SPS 37-47). Five bits of this truth table progress in a binary sequence and the sixth is simply the mod 2 function of the previous five bits.

A generator that maps, mod 2, a vector with a binary truth table has been described. It will now be shown

Fig. 46. Mariner Mars 1969 code generator implementation based on the iterative digital logic concept

how the same basic type of generator can be used to generate the actual mod 2 function of the binary truth table. This usage has application to the Mariner Mars 1969 biorthogonal code.

The output of such a generator is mapped with the sixth information bit in a simple and gate. The output from this and gate added mod 2 to the output of the first described generator will then produce the desired code.

The generator is initialized for each new data word. Figure 46 is a block diagram of an alternate arrangement for the *Mariner* Mars 1969 code generator. From the following truth table

$X_2 X_1$	M
0 0	0
0 1	1
1 0	1
1 1	0

it is evident that function M can be generated by a simple 2-bit shift register module (Fig. 47). Initially set to 0, 1 and with its false output fed back into its true input, this module will generate the sequence sought.
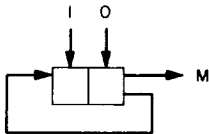
Fig. 47. Two-bit shift register module

In examining the mod 2 sequence for a 4-bit binary truth table, one finds that it consists of four 2-bit sequences inverted and not inverted in a pattern of the 2-bit sequence (Table 9).

Table 9. Mod 2 sequence for 4-bit binary truth table

Four-variable binary truth table	Mod 2 function = output from modules
0 0 0 0	0
0 0 0 1	1
0 0 1 0	1
0 0 1 1	0
0 1 0 0	1
0 1 0 1	0
0 1 1 0	0
0 1 1 1	1
1 0 0 0	1
1 0 0 1	0
1 0 1 0	0
1 0 1 1	1
1 1 0 0	0
1 1 0 1	1
1 1 1 0	1
1 1 1 1	0

It then follows that a generator for this sequence can be designed from two identical modules whose outputs are added mod 2 and with the clock for the second module being one-fourth of the first. From the general structure of the binary truth table, it follows that for a larger number of variables identical modules are added. The strong similarities between the two generators (Fig. 48) make it possible to use identical physical components.
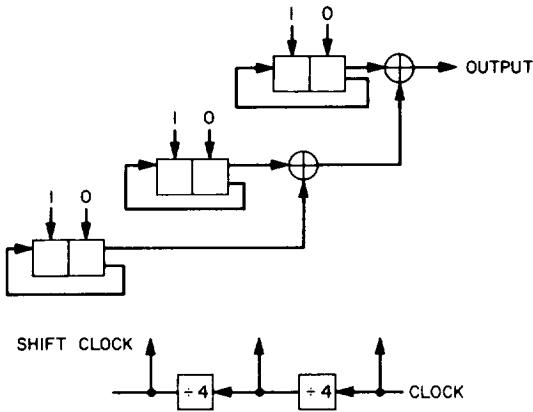
Fig. 48. Three 2-bit shift registers connected in series to two code generators with common shift clock

C. Tracking and Data Acquisition Elements Research

1. Low-Noise Receivers, Microwave Maser Development, Second Generation Maser, R. C. Clauss

a. Introduction. A balanced phase detector has been used with a microwave sweep oscillator to measure phase shift characteristics of the second generation maser. The frequency range of interest is 2270 to 2300 MHz, and the flat gain versus frequency response of the maser allows swept-frequency phase measurements to be made with available laboratory instrumentation. Information describing gain, bandwidth, noise temperature, and stability of the second generation maser has been reported previously (SPS 37-47, Vol. II, pp. 71–73, through SPS 37-50, Vol. II, pp. 34–36).

b. Maser delay time. The traveling wave maser slow wave circuit (comb structure) is necessary for high maser gain. The 30.4-cm physical length is multiplied by the slowing factor (130) in order to obtain the equivalent free space (electrical) length. A nondispersive network of equivalent length (39.5 m) represents a fixed delay time of 0.13 μs and causes an insertion phase shift which changes with frequency at the rate of 47 deg/MHz

between 2270 and 2300 MHz. Measurements of the maser phase shift versus frequency are made by comparison of a test signal through the maser to a reference signal which passes through a 0.13 μs delay line. Maser saturation is avoided by using a test signal level of −85 dBmW.

c. Instrumentation. The phase shift measurement block diagram is shown in Fig. 49. Equal path lengths for the reference and test signals are necessary when using the swept frequency technique. Reference and test signals of equal amplitude are combined in the 3-dB hybrid coupler prior to additional amplification and detection. Sensitivity to amplitude changes limits the usable range to a region between 2267 and 2308 MHz (flat gain region of maser response).

d. Results. Figures 50 and 51 are X-Y plots of phase detector output voltage as a function of sweep oscillator frequency. In Fig. 50, Traces 1 through 5 are each recorded after a calibrated phase change was added to the reference path. The extreme Traces, 1 and 5, occur at a phase angle change of ±90 deg. Traces 2 and 4 are the result of a ±30 deg change (with respect to Trace 3). In Fig. 51, Traces 2 and 3 are the result of a ±30 deg change in the reference path (with respect to Trace 1). Traces 4 and 5 were recorded after changing the maser field-shape current (±8 mA). The peak-to-peak variation in Trace 3 (15 deg between 2270 and 2300 MHz) represents the comparison of the maser delay time and the delay time in the reference path. The 15 deg "ripple" is caused by the maser.
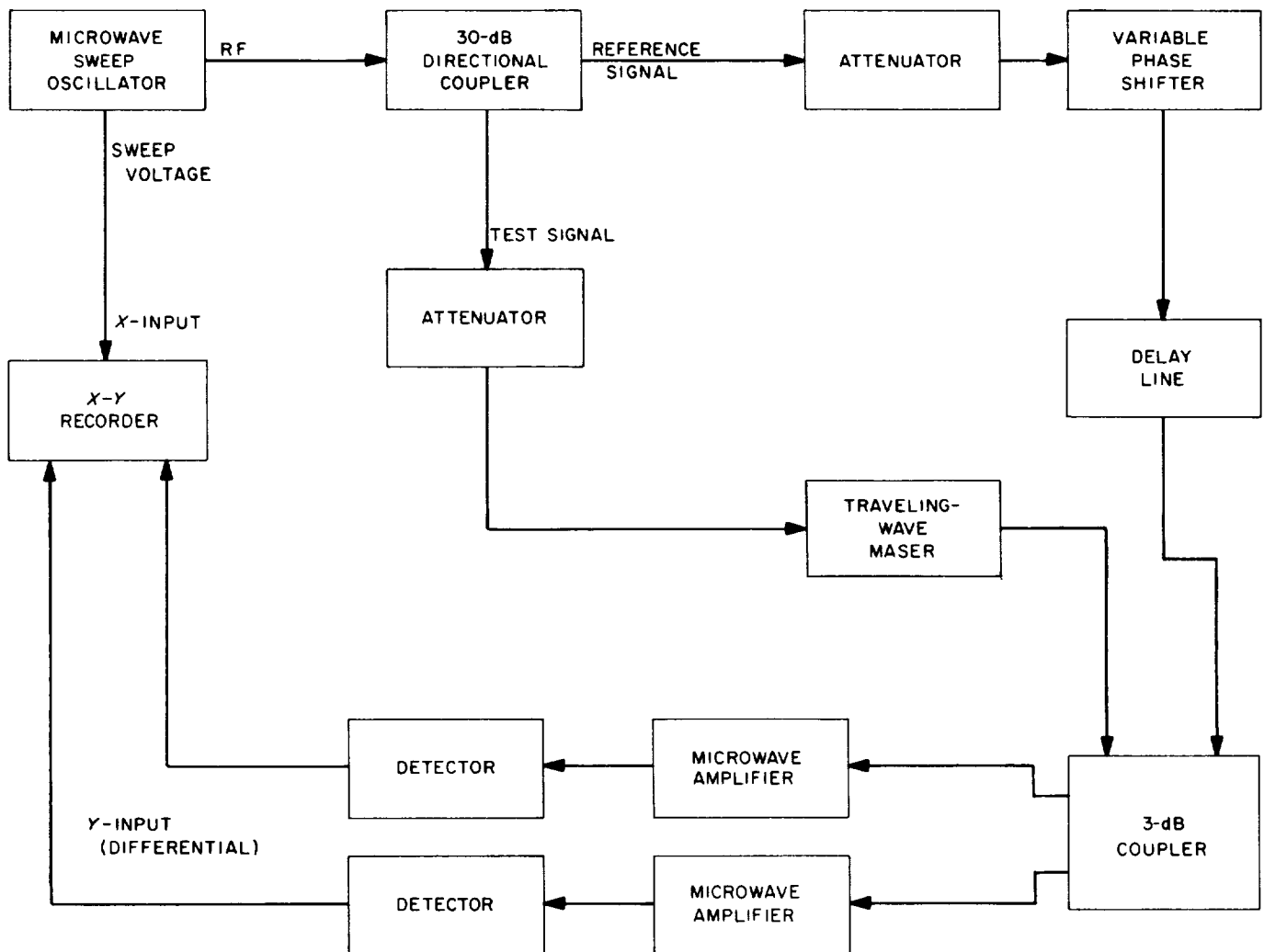
Fig. 49. Instrumentation for phase shift measurement
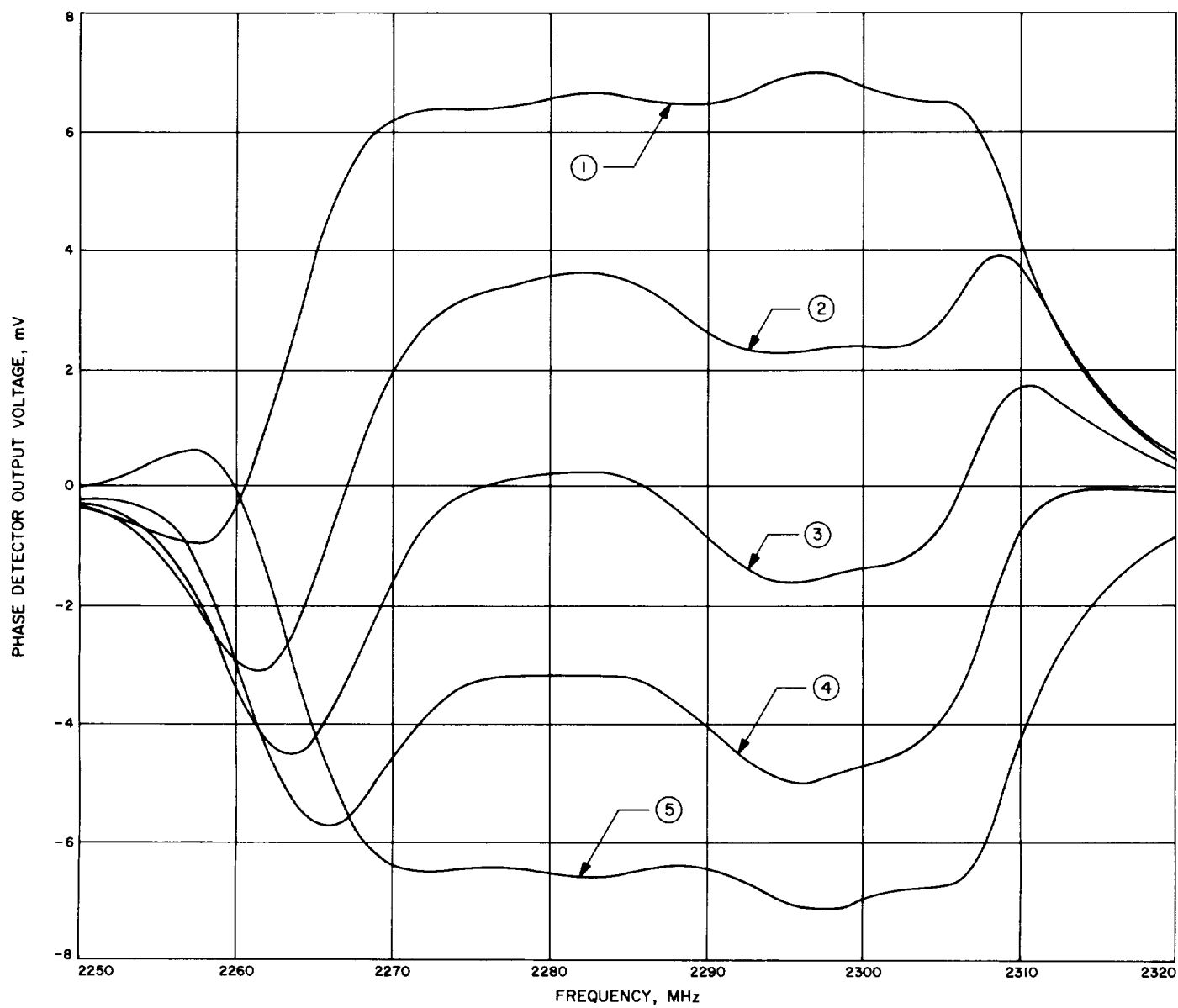
Fig. 50. Phase detector voltage versus frequency with calibrated phase shifts

Table 10. Effect of maser tuning changes on phase shift at various frequencies

Maser tuning change			Differential phase shift of maser for various frequencies, deg						
Function	Change	Percentage change	2270 MHz	2275 MHz	2280 MHz	2285 MHz	2290 MHz	2295 MHz	2300 MHz
Pump frequency	4 MHz	0.03%	6	7	8	9	10	10	8
Magnet[a] field strength trim current	4 mA	1.2%	18	10	9	7	7	12	14
Magnet field shape current	16 mA	22.0%	14	9	6	3	0	3	6

[a]A 4mA trim current change causes a 1-G change in the 2500-G magnetic field.
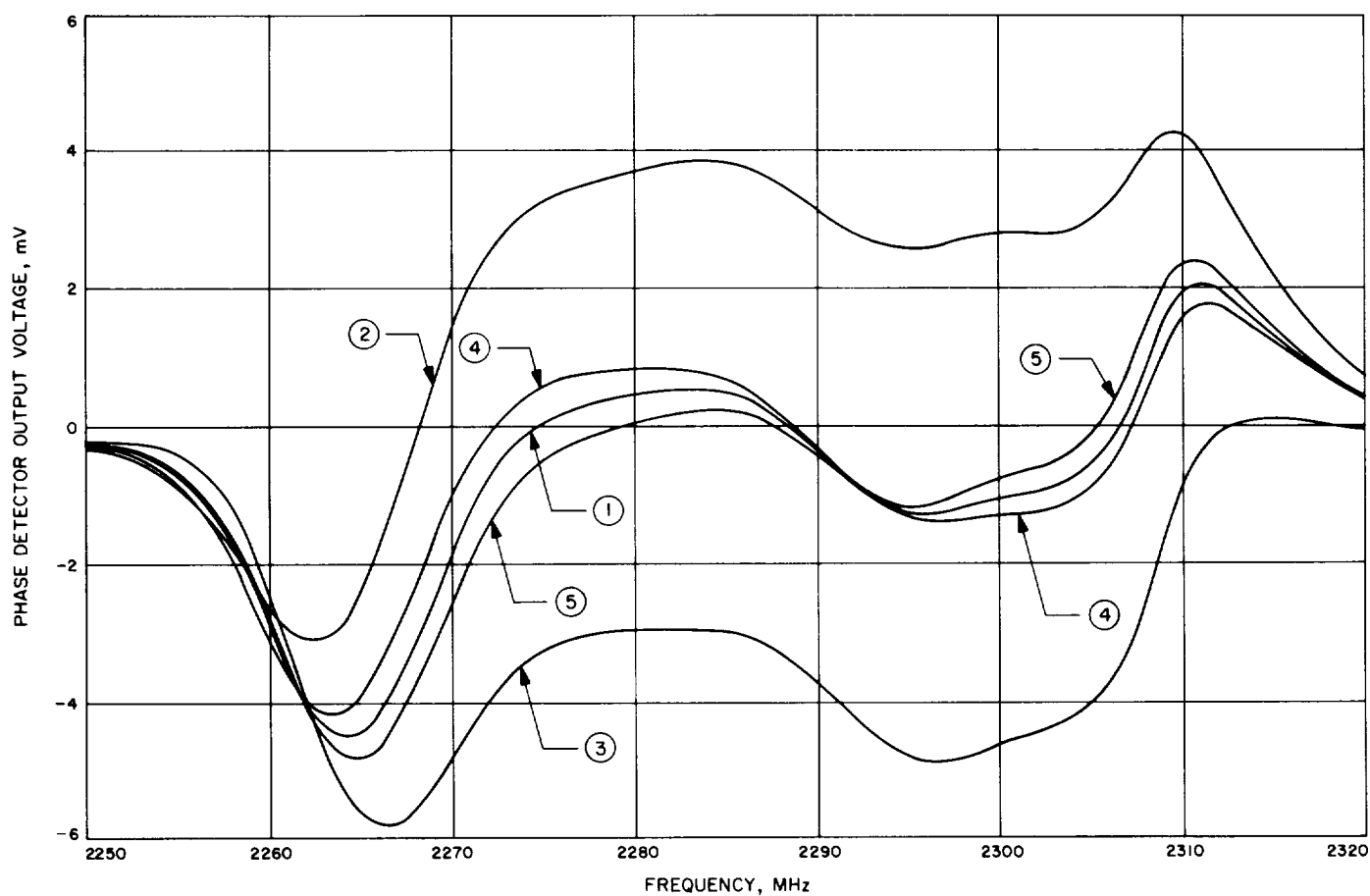
Fig. 51. Phase detector voltage versus frequency and magnetic field shape

Differential phase shifts caused by variations in pump frequency and magnetic field were measured. Figure 51 is typical of data obtained when variations in maser tuning adjustments are made. Results of the measurements are shown in Table 10.

2. Solid State and Superconducting Electronics,

R. W. Berwin

a. Introduction. Voltage output characteristics, as a function of magnetic field, of a superconducting interference bridge junction have been recorded for a 28-day period at a constant temperature of 4.4°K. The results of these measurements are reported here.

b. Experimental technique and results. A superconducting bridge junction which exhibited the desired quantum interference of the current through it was constructed by the solder droplet technique described in SPS 37-50, Vol. II, pp. 36–41. The junction was mounted in a closed-cycle refrigerator (Ref. 1) and maintained at a constant temperature of 4.4°K and in an absolute pressure of 2×10^{-8} to 10^{-7} Torr. The junction was mounted to the 4.4°K heat station by means of four ruby washers, the short dimensions of which were cut approximately 30 deg to the C-axis in order to provide good heat conduction with good electrical insulation. Since it is not known how much temperature increase occurs across these four washers, the actual temperature of the junction is uncertain. Therefore, the temperatures reported here are those of the heat station.

The experimental arrangement is shown in Fig. 52. The magnetic field was produced by a 10-turn solenoid with a coil constant of 1.95 G/A. The niobium wire formed a closed loop which surrounded the solenoid. The area of the loop was 12 cm².

An attempt was made to line the copper cavity in which the junction was mounted with high-purity lead in order to have a superconducting magnetic shield; however, on cooling, there were non-superconducting areas in the lead which devaluated the usefulness of such a shield. Therefore, the junction was unshielded to ambient magnetic fields. This was not serious, because a change in ambient field simply shifted the voltage presentation and this shift was found to be approximately 7×10^{-4} G in the 28-day period.

Figures 53 and 54 show the results of the measurements. On March 26, an accidental shifting of instrumentation near the refrigerator caused a large shift in the
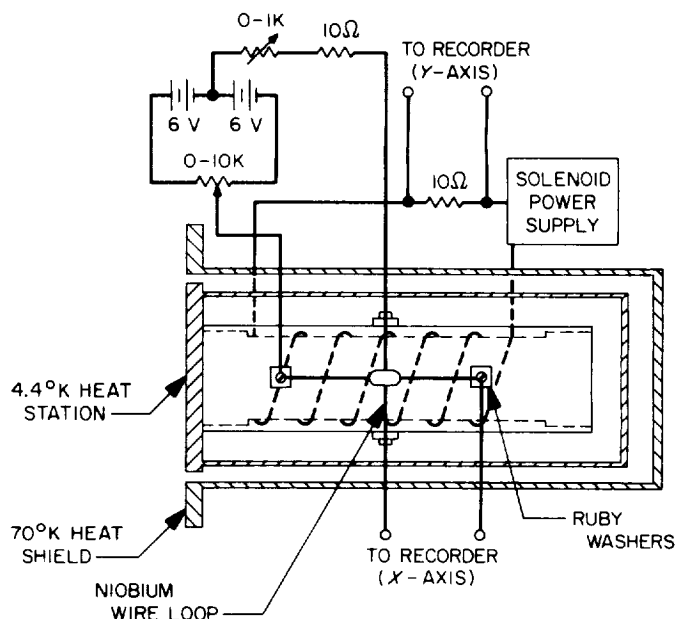
Fig. 52. Experimental arrangement showing junction mounted on tube with solenoid inside; the niobium wire forms a loop around the solenoid
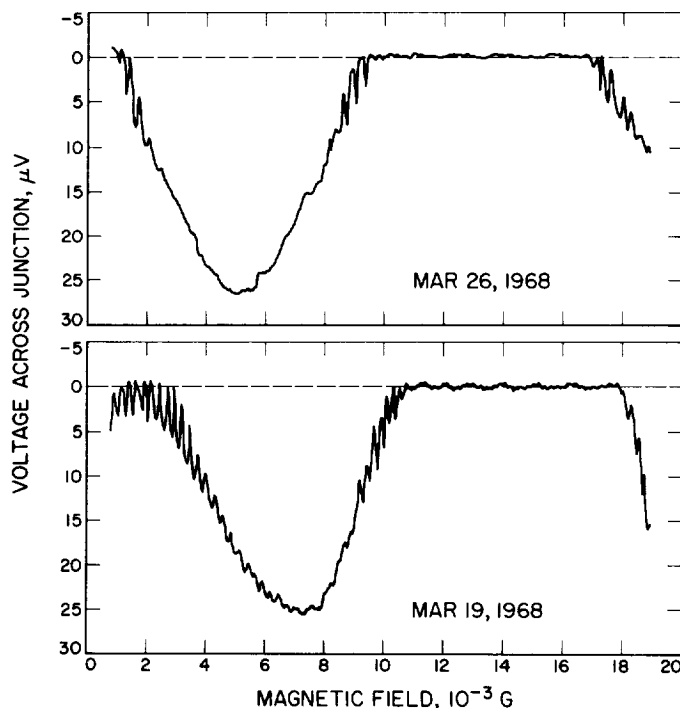
Fig. 53. Junction voltage as a function of magnetic field, March 19 to March 26
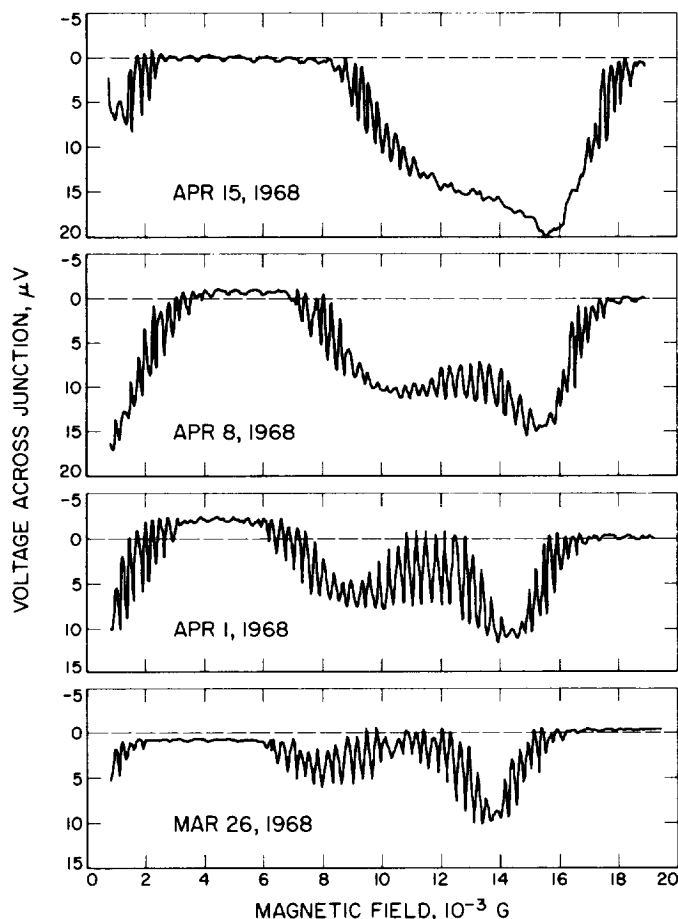
Fig. 54. Junction voltage as a function of magnetic field, March 26 to April 15

ambient magnetic field, thereby changing the presentation. However, the presentation as a function of time is to be noted. From March 19 to April 15 a gradual increase in the voltage amplitude of the gross structure occurred (excluding the change on March 26), but the period or the amplitude of the fine structure has no noticeable change. The increase in the voltage amplitude can be hypothesized as an increase in the Cooper pair current in the resistive-superconducting region of the voltage–current characteristic curve.

c. Conclusions. The long-term stability of the voltage output as a function of magnetic field shows promise as a device for detecting a field and controlling it to within 10^{-5} or 10^{-6} G by means of feedback control. More investigation is needed in order to carefully observe the long-term behavior of the voltage output while controlling various parameters such as the junction current to within 0.1 μA, the magnetic field to within 10^{-6} G, and the junction temperature to within $0.1°K$.

Reference

1. Higa, W. H., and Wiebe, E., "A Simplified Approach to Heat Exchanger Construction for Cryogenic Refrigerators," *Cryogenic Technology*, Vol. 3, No. 2, p. 15, Mar.-Apr. 1967.

3. Modified S-Band Cassegrain Ultra Cone (SCU SN1 Mod 1) Calibrations and Checkout, F. McCrea, B. Seidel, T. Otoshi, and C. Stelzried

a. Introduction. The S-band cassegrain ultracone (SCU) has been modified at JPL for polarization diversity (interior photograph, Fig. 55). This cone was installed at the Mars DSS on March 5, 1968. A block diagram of the cone receiving system with the Mars DSS instrumentation is shown in Fig. 56.

The following configuration codes have been adopted:

Code	Configuration
0	Maser 1, R&D receiver, 2295 MHz
1	Maser 1, DSIF receiver 1, 2295 MHz
2	Maser 1, DSIF receiver 2, 2295 MHz
3	Maser 1, R&D receiver, 2288 MHz
5	Maser 2, DSIF receiver 1, 2295 MHz
6	Maser 2, DSIF receiver 2, 2295 MHz

In addition to polarization changes, a standard diplexer (SCD) has been added (Fig. 57), which allows diplexed received signals to be amplified by a second maser located in the 3A module. Both masers are tunable over the 2270–2400 MHz frequency range.

A summary of possible operating modes includes:

(1) Maser 1 and 2 listen only.

(2) Diplexed operation of maser 2 with 2270–2400 MHz listen, and 2105–2120 MHz transmit.

(3) Transmit only at 2105–2120 MHz.

All of the above modes will allow a single selection of left-hand circular polarization (LCP), right-hand circular polarization (RCP), or rotating linear polarization. This contrasts with the SMF feedcone previously used at Mars DSS which allowed simultaneous LCP/RCP capability.

Although the polarization performance of the original SCU cone has been reported (SPS 37-46, Vol. III, p. 65), none of the changes made should materially degrade the original performance. The Telecommunications Building roof check-out system was used as a reflection-free vertical antenna range. Probes in the horn aperture were
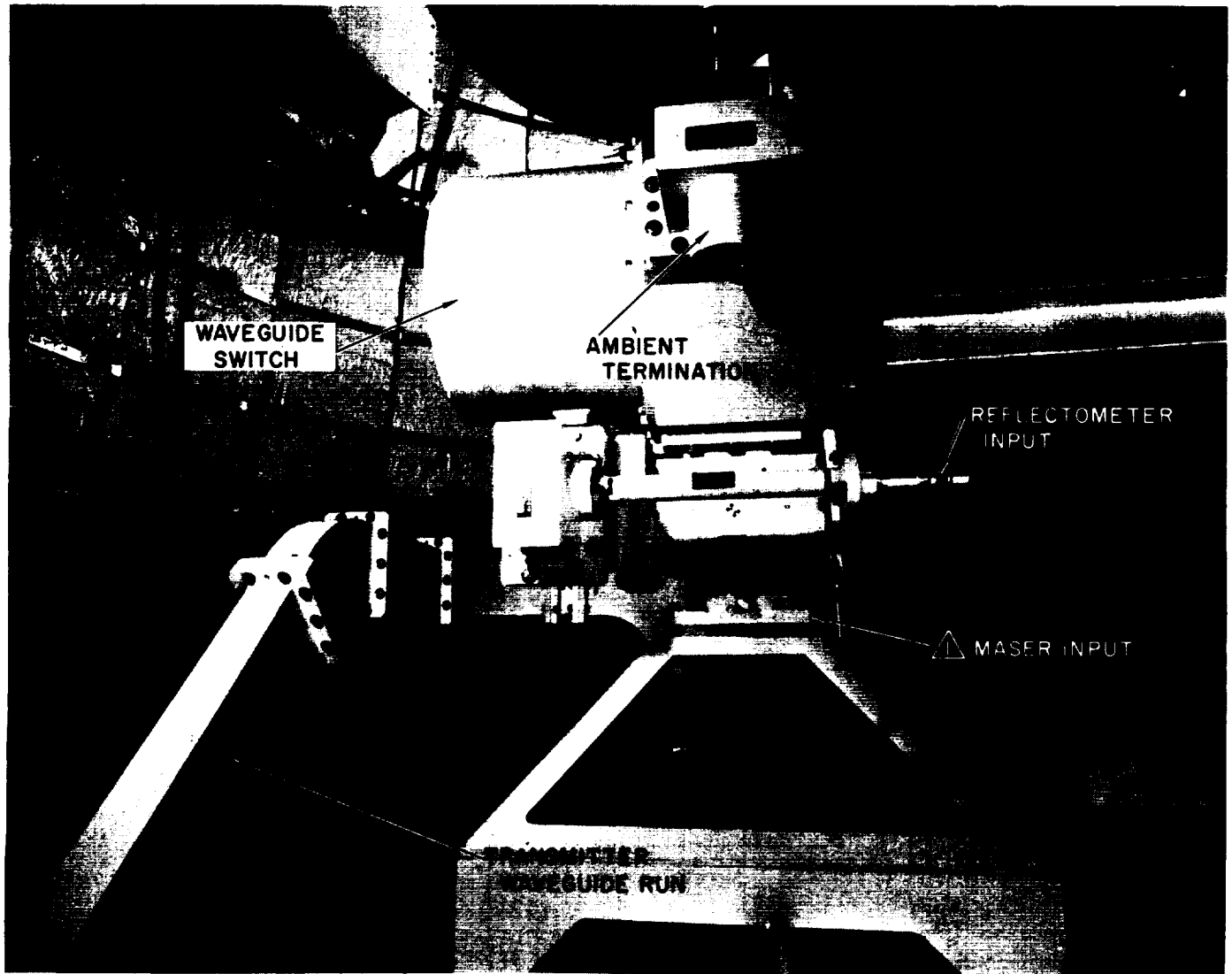
Fig. 55. Modified S-band cassegrain ultra cone interior
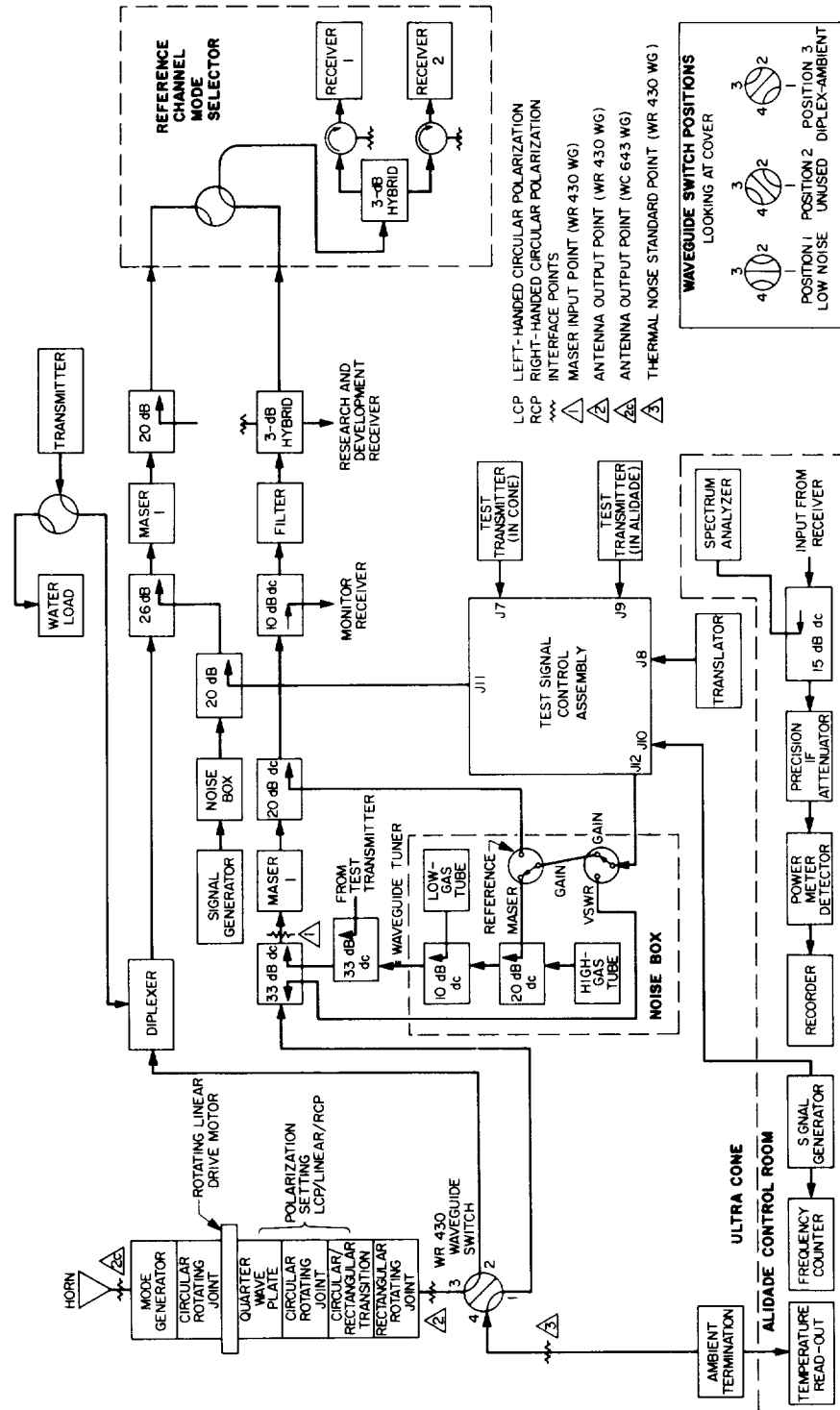
Fig. 56. Modified SCU cone (SN1 Mod 1) receiving system and Mars DSS instrumentation

Fig. 57. Standard diplexer in modified ultra cone

Fig. 58. Aperture ambient termination

used to verify the 0.15-dB ellipticity at 2295 MHz and the 0.30-dB ellipticity at 2388 MHz. In a rotating linear polarization test at 2295 MHz, an observed null depth of −50 ±5 dB was observed. It appears that the modified SCU feedcone has the potential of being a very high-quality polarimeter; further effort would be necessary to calibrate it.

The input of maser No. 2 in the 3A module cannot be switched between the horn and an ambient termination for daily system noise temperature measurements. The aperture ambient load (Fig. 58) can be used in a hand switched mode to provide system temperature verification (e.g., gas tube calibrations). A temperature probe is buried in the absorbing material.

b. Waveguide calibrations. Detailed insertion loss measurements of the modified ultra cone waveguide configuration were not performed. However, only two major system changes affect the original waveguide calibrations which are reported in SPS 37-48, Vol. II, pp. 51–54. These are:

(1) The change of components between points △2△ and △2c△ of Fig. 56.

(2) The replacement of the cryogenic load at point △3△ by the ambient reference load.

Since each individual component in the modified transmission line between points △2△ and △2c△ is well matched (typically less than 1.02 VSWR), it is permissible to add up the component losses to give the overall loss with only a small error due to mismatches. The errors due to mismatches are computed from equations for cascade-connected attenuators given by Beatty (Ref. 1). Insertion loss and voltage reflection coefficient data for individual components such as the circular/rectangular transition, rectangular rotary joint, and the circular rotary joints may be found in SPS 37-48, Vol. II, and in a JPL internal document.[9]

Measurements of system voltage reflection coefficients of the modified cone were performed at 2295 and 2388 MHz. These were made at the maser input point △1△ as seen looking into the ambient load and into the antenna in its various polarization configurations. In addition, the maser reflection coefficient was also remeasured. The results of voltage reflection coefficient measurements[10] are shown in Table 11.

[9]Otoshi, T., Stelzried, C., and Mullen, D., *Waveguide Rotary Joint Calibrations*, Sept. 22, 1967 (JPL internal document).

[10]D. Mullen performed these measurements.

Table 11. Measured voltage reflection coefficients for modified ultra cone waveguide system

Part A. Antenna noise source at point ⚠1				
Frequency, MHz	**Operating configuration**			**Voltage reflection coefficient[a]**
	Description of feed termination	**Polarization mode**	**Feed rotation angle, deg.**	
2295	Free space	RCP	220	0.0195 ±0.0002
			340	0.0216 ±0.0003
		Linear	100	0.0162 ±0.0002
			260	0.0216 ±0.0003
		LCP		0.0209 ±0.0003
2388	Free space	RCP	130	0.0525 ±0.0004
			310	0.0684 ±0.0005
		Linear	70	0.0447 ±0.0004
			250	0.0543 ±0.0004
		LCP		0.0556 ±0.0004
2295	Aperture ambient load	RCP	0	0.0240 ±0.0004
			280	0.0160 ±0.0004
		Linear	60	0.0367 ±0.0004
			350	0.0389 ±0.0004
2388	Aperture ambient load	RCP	60	0.0501 ±0.0006
			320	0.0692 ±0.0006
		Linear	40	0.0733 ±0.0006
			280	0.0902 ±0.0006

Part B. Ambient load noise source at point ⚠2		
2295	Point ⚠2 terminated by WR 430 ambient load thermal noise standard	0.0005 ±0.0002
2388	Point ⚠2 terminated by WR 430 ambient load thermal noise standard	0.1161 ±0.0008

Part C. Maser assembly at point ⚠1		
2295	Maser pump power turned on; maser is peaked at 2295 MHz	0.1175 ±0.0008
	Maser pump power is turned off; maser is peaked at 2295 MHz	0.0716 ±0.0005
2388	Maser pump power is turned on; maser is peaked at 2388 MHz	0.1109 ±0.0007

[a] All tolerances shown are probable errors which include errors due to imperfect reflectometer tuning, imperfect sliding load, and imperfect reflectometer attenuation standard. Measurement dispersion errors are not included.

c. Noise temperature calibrations and system checkouts.

The rectangular rotary joint with 0.013 dB dissipative loss[8] was the single largest contributor to an increase of system temperature of approximately 1°K at 2295 MHz. However, this increase in system temperature was largely offset by an improvement in the maser input structure of approximately 0.5°K to a predicted 4.1°K maser temperature (SPS 37-46, Vol. II, p. 69).
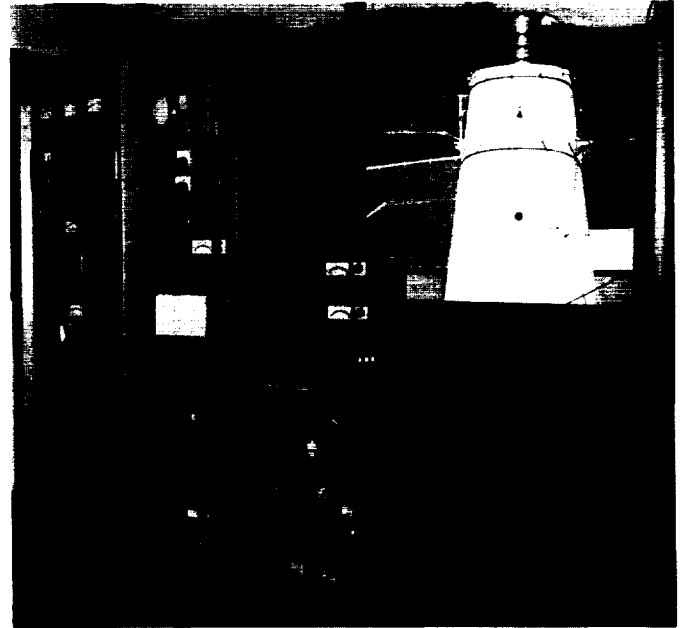
Fig. 59. Modified SCU cone (SN1 Mod 1)/control racks undergoing checkout tests on JPL Telecommunications Building roof

A photograph of the ultra cone on the roof of the Telecommunications Building (control racks in adjacent room), undergoing system tests, is shown in Fig. 59. A summary of the twelve system temperature measurements (CTS20B program) taken between February 29 and March 1, 1968 (local time) is shown in Fig. 60. The total system temperature at zenith, on the ground with clear weather is slightly below 13°K.

The system temperature on the antenna under similar conditions is expected to be under 17°K. Figure 61 shows a system linearity verification.

Receiver and gas tube noise temperature calibrations were made with a WR 430 waveguide liquid nitrogen bucket termination (which replaces the normal ambient load for these tests) and the antenna aperture termination. Although the liquid nitrogen termination will be more accurately calibrated in the future, preliminary calibrations were performed at JPL to provide system checks. These calibrations resulted in a measured high gas tube noise temperature of $(7.4 \pm 0.5, 3\sigma)°K$ and a maser temperature of $(4.7 \pm 1.5, 3\sigma)°K$ defined at the maser input.

Reference

1. Beatty, R. W., "Cascaded-Connected Attenuators," *Proceedings IRE*, Vol. 38, No. 10, p. 1190, Oct. 1950.
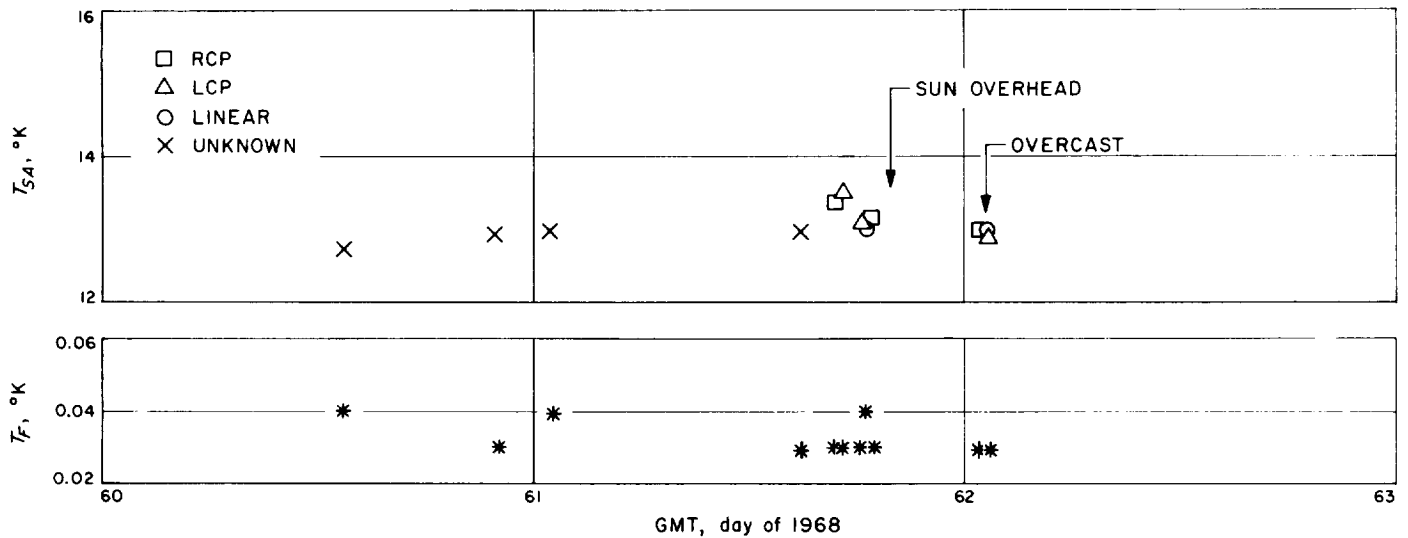
Fig. 60. Modified ultra cone system temperature measurements taken on roof of Telecommunications Building
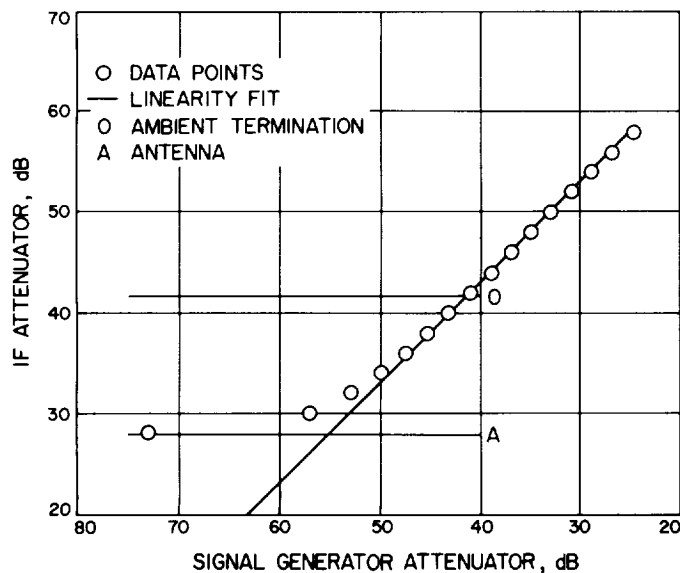
Fig. 61. Verification of 2295-MHz ultra cone system linearity

4. Modified Ultra Cone (SCU SN1 Mod 1) Operational Performance Evaluation at the Mars DSS, R. E. Cormack

Using the performance of the S-band multifrequency feedcone (SMF) as a basis for comparison, predictions were prepared prior to installation to provide early check-out of SCU SN1 Mod 1 operational performance. Detailed knowledge of SMF losses (SPS 37-38, Vol. IV, p. 185) and of SCU (unmodified) losses (SPS 37-48, Vol. II, p. 53) coupled with losses of additional components comprising

the modification allowed calculations of loss ratios as follows:

$$\frac{\text{SCU SN1 Mod 1}}{\text{SMF (low loss path)}} = 0.9746 \text{ for low loss arm}$$

$$\frac{\text{SCU SN1 Mod 1}}{\text{SMF (low loss path)}} = 0.9975 \text{ for diplexer arm}$$

Note that the additional component losses include a measured 0.013 dB for the waveguide rotary point,[11] a nominal 0.078 dB for the diplexer (SPS 37-30, Vol. III, p. 29), and 0.023 dB (estimated) for the standard WR-430 transmission line.

Applying these loss ratios to 3C123 source temperature data using the SMF at the Mars DSS, the two predicted SCU SN1 Mod 1 performance curves of 3C123 source temperature versus elevation angle depicted by Curves A and B in Fig. 62 were derived. These data were collected during scheduled DSN system development star tracks initiated in December 1967. For comparison, Curve C of Fig. 62 shows the same parameters as actually measured immediately after installation. It should be noted that only the low-loss arm performance has been confirmed according to this scheme; the diplexer arm comparison which is yet to be made depends upon an accurate gas tube standard calibration currently in progress, since the ambient load standard used in establishing Y-factors with the low-loss arm is not accessible to the second maser of the diplexer arm.

[11]Otoshi, T., Stelzried, C., and Mullen, D., Waveguide Rotary Joint Calibrations, Sept. 22, 1967 (JPL internal document).
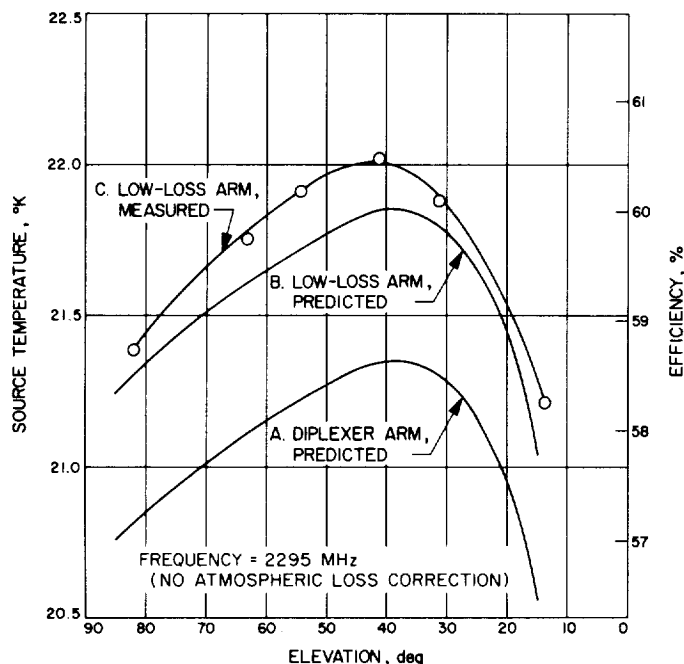
Fig. 62. Predicted and actual 3C123 source
temperature versus elevation angle

5. PIN Modulator Test Results, H. G. Nishimura

A need has arisen for an electronically controlled atten-
uator with minimal phase shift to simulate operational
conditions during testing at the DSIF facilities. The PIN
Modulator, a relatively new device, is being considered
for use in this application. Tests have been conducted to
investigate the attenuation and phase shift of the PIN
Modulator at various temperature extremes.

The PIN Modulator is a current-controlled absorption
type attenuator having PIN diodes mounted as shunt
elements between the RF transmission path and ground.
Each modulator unit includes a low-pass filter, two high-
pass filters, a number of PIN diodes, and a 50-Ω strip
transmission line (Fig. 63).
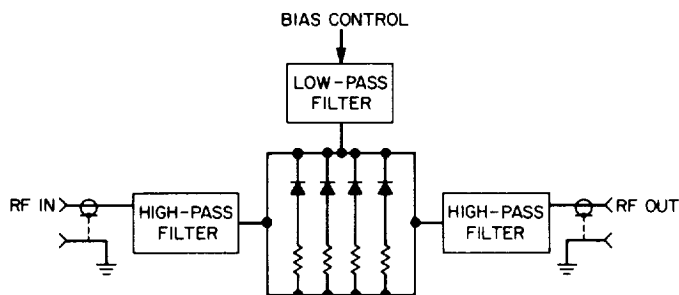
Fig. 63. PIN modulator simplified block diagram

The PIN diode is a silicon junction diode and derives
its name due to its P and N trace regions which are sep-
arated by a layer of intrinsic (I) silicon semiconductor. At
frequencies above 100 MHz, the diode ceases to behave
as a rectifier. Due to stored charge in the intrinsic layer,
it acts like a resistance dependent upon the applied bias.
When the diodes are forward-biased, the equivalent diode
resistance is about 30 Ω and most of the RF energy is
absorbed by the diodes. However, when the diodes are
reverse-biased, the equivalent resistance is on the order of
thousands of ohms and the RF energy continues through
the modulator with negligible absorption.

Two units of the Hewlett-Packard PIN Modulator,
Model 8732B, were tested to examine their attenuation
and phase shift characteristics at frequencies of 2113 and
2295 MHz. These frequencies represent the DSIF trans-
mit and receive frequencies, respectively. This report
describes the unit which exhibited the larger changes.
Testing was performed in two parts as follows:

a. Attenuation characteristics. The attenuation char-
acteristics were determined as a function of the forward
bias current and voltage. The curves in Figs. 64 and 65
show the negative bias current and voltage required to
obtain various levels of attenuation. As a function of cur-
rent, the attenuation is linear to within ±1.5 dB between
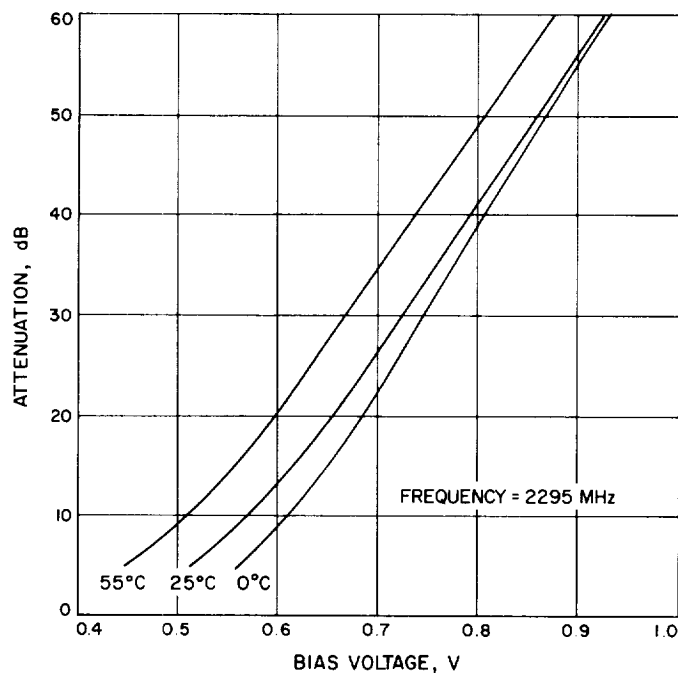
Fig. 64. PIN modulator attenuation as a function of
bias voltage at various ambient temperatures
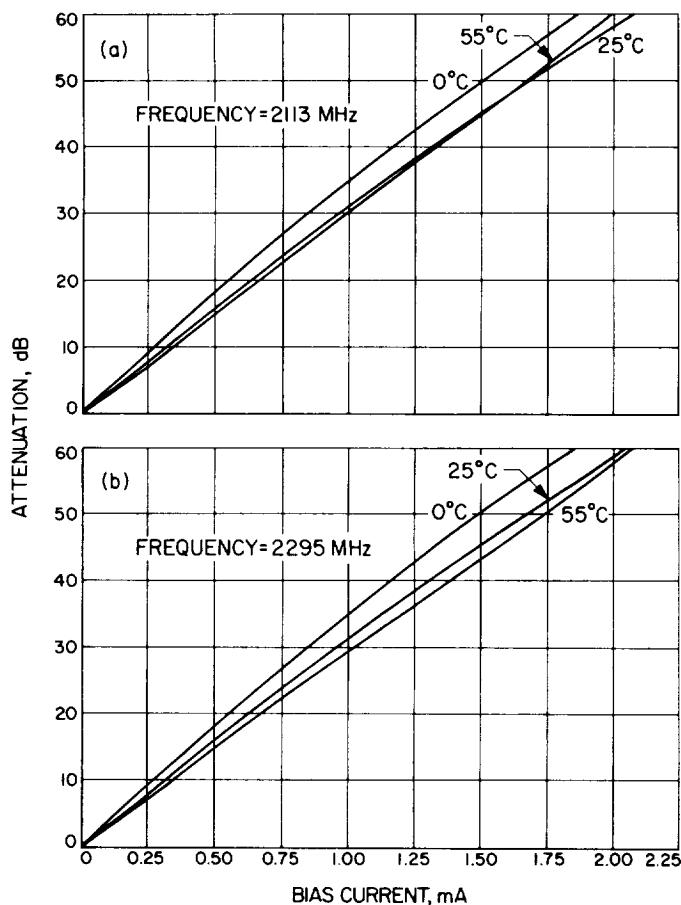
Fig. 65. PIN modulator attenuation as a function of
bias current at various ambient temperatures

Fig. 66. PIN modulator attenuation as a function
of phase shift at various ambient
temperatures

0 and 60 dB. As a function of bias voltage, it is linear from 20 to 60 dB. Below 20 dB, the linearity deviation is about 6 dB. In practice this deviation can be minimized by using a bias supply voltage much higher than the required bias voltage, such as 20 or 30 V, dc. With a large series voltage dropping resistance, R, the modulator attenuation becomes essentially linear as a function of the supply voltage.

Data for these curves was obtained at three different temperatures, -25, 0, and $55°C$. The device temperatures were permitted to stabilize for 1 h prior to the start of readings. In every case, the drift was more pronounced between 0 and 25°C. As a function of current, Fig. 65 clearly indicates an increase in the attenuator sensitivity at 0°C as evidenced by the steeper slopes. At lower values of attenuation, the effects of varying the ambient temperature appear to have little effect on the diode characteristics. However, at 60 dB, the drift was on the order of 5 dB.

b. Phase shift characteristics. Data was obtained at room temperature for phase variations between the input and output of the attenuator at various levels of attenuation. These readings were also taken at temperatures of 0 and 55°C and are shown in Fig. 66. The phase shift was more pronounced at 2113 MHz. At any specified temperature, the total phase shift was about 27 deg.

In summary, the PIN Modulator attenuators were sensitive to frequency changes. Note the data differences at 2113 and 2295 MHz. Temperature variations also affected the attenuation and phase shift characteristics. These were confirmed by the device manufacturer. The characteristics of the two units tested were not uniform. While the device exhibited a considerable amount of phase shift, it is not considered detrimental to the intended purpose. The results of these tests and the poor aging characteristics of semiconductors seem to point out that this device should not be considered for use as a calibrated attenuator. However, these units can be used for spacecraft compatibility tests.

D. Supporting Research and Technology

1. FORTRAN IV Language Extension: Interval Arithmetic,
H. L. Smith

a. Introduction. This article describes an extension to the FORTRAN IV language facilitating the use of interval data. (An interval is a pair of real numbers $[a,b]$, with $a \leq b$ [Ref. 1].) Definitions of arithmetic operations, a more complete treatment of interval arithmetic, and a description of a set of FORTRAN-callable subroutines to perform interval arithmetic were given by R. J. Hanson in an earlier article (SPS 37-50, Vol. III, pp. 66–69). The subroutines discussed in that article provide a straightforward, but tedious, means of performing interval arithmetic. With the FORTRAN language extensions described here, the use of interval arithmetic is greatly simplified. An example of a FORTRAN program using the interval arithmetic language extensions is given in *Paragraph c.*

The following considerations influenced the design of the language extension:

(1) The language extension should not conflict with existing language features. The extended FORTRAN IV must not introduce any new restrictions for the user not using interval arithmetic. The use of any other language feature must not be precluded by the use of interval arithmetic.

(2) The language extension should itself be logically extendable. The interval data type was extended to interval double precision and interval complex. The definition of interval arithmetic was extended to complex numbers.

(3) The style should be consistent with that of FORTRAN IV.

(4) The initial implementation would be as an extension to FORTRAN IV for the IBM 7094 computer (Ref. 2).

b. Description

Constants. Three additional types of constants are as follows:

(1) *Interval constants.* An interval constant consists of an ordered pair of signed or unsigned real constants separated by a comma and enclosed in dollar signs, e.g.,

$5.,21.0E3$; $0.,5.0E - 3$; $ - 0.203,3.14159$. The first real constant represents the left end point of the interval; the second represents the right end point. The dollar signs are required regardless of the context in which the interval constant appears. The left end point of the interval must be algebraically less than, or equal to, the right end point.

(2) *Interval double-precision constants.* An interval double-precision constant consists of an ordered pair of signed or unsigned double-precision constants separated by a comma and enclosed in dollar signs, e.g., $ - 5.0D0,21.0D3$; $0.0D0,3.14159265358979$. The features of the interval double-precision constant are the same as those of the interval constant.

(3) *Interval complex constants.* An interval complex constant consists of an ordered pair of unsigned interval constants separated by a comma and enclosed in parentheses, e.g., ($1.0,2.0$,$ - 2.0, - 1.0$). The first interval constant, $1.0,2.0$, represents the left and right end-points of the real part of the interval complex number; the second interval constant, $ - 2.0, - 1.0$, represents the left and right end-points of the imaginary part of the interval complex number. The parentheses are required regardless of the context in which the interval complex constant appears.

Variables. In addition to the five types of variables previously defined for FORTRAN IV (integer, real, double-precision, complex, and logical), three new types are defined. They are interval, interval double-precision, and interval complex. Hereafter "interval" will be used to refer to these three data types. Interval variables must have their type specified by a type statement. Type statements are discussed separately later in this article.

The type of interval function name appearing in a FUNCTION statement is specified by that FUNCTION statement. A symbol is implicitly typed if it is used as a function reference and is the same name as that of a built-in or standard library function. Table 12 shows the mathematical subroutines to be added to the standard library functions. Table 13 shows the built-in functions to be added to those available to the FORTRAN programmer.

Subscripts. Interval variables may be made to represent elements of arrays in the same manner as other FORTRAN variable types. The rules for subscripted interval variables are the same as for other types of subscripted variables.

Table 12. Mathematical subroutines

Function	Entry name	Definition	No. of arguments	Type[a] Arguments	Type[a] Function
Exponential	VEXP	e^{arg}	1	Interval	Interval
	VDEXP	e^{arg}	1	Interval * 2	Interval * 2
	VCEXP	e^{arg}	1	Interval * C	Interval * C
Natural logarithm	VLOG	ln(arg)	1	Interval	Interval
	VDLOG	ln(arg)	1	Interval * 2	Interval * 2
	VCLOG	ln(arg)	1	Interval * C	Interval * C
Common logarithm	VLOG10	$\log_{10}$(arg)	1	Interval	Interval
	VDLOG1	$\log_{10}$(arg)	1	Interval * 2	Interval * 2
Arcsine	VASIN	arcsin (arg)	1	Interval	Interval
Arccosine	VACOS	arccos (arg)	1	Interval	Interval
Arctangent	VATAN	arctan (arg)	1	Interval	Interval
	VDATAN	arctan (arg)	1	Interval * 2	Interval * 2
Sine	VSIN	sin (arg)	1	Interval	Interval
	VDSIN	sin (arg)	1	Interval * 2	Interval * 2
	VCSIN	sin (arg)	1	Interval * C	Interval * C
Cosine	VCOS	cos (arg)	1	Interval	Interval
	VDCOS	cos (arg)	1	Interval * 2	Interval * 2
	VCCOS	cos (arg)	1	Interval * C	Interval * C
Tangent	VTAN	tan (arg)	1	Interval	Interval
Cotangent	VCTAN	cotan (arg)	1	Interval	Interval
Square root	VSQRT	$arg^{\frac{1}{2}}$	1	Interval	Interval
	VDSQRT	$arg^{\frac{1}{2}}$	1	Interval * 2	Interval * 2
	VCSQRT	$arg^{\frac{1}{2}}$	1	Interval * C	Interval * C
Hyperbolic cosine	VCOSH	cosh (arg)	1	Interval	Interval
Error function	VERF	$\frac{2}{(\pi)^{\frac{1}{2}}} \int_{0}^{z} e^{-u^2} du$	1	Interval	Interval
Gamma	VGAMMA	$\int_{0}^{\infty} u^{x-1} e^{-u} du$	1	Interval	Interval
Log-gamma	VALGAM	$\log_e \Gamma(x)$	1	Interval	Interval

[a]Interval * 2 indicates interval double precision.
Interval * C indicates interval complex.

Arrays are stored in column order in increasing storage locations with the first of their subscripts varying most rapidly and the last varying least rapidly. The storage location of the real part of a complex number (including interval complex) precedes the storage location of the imaginary part. The left end point of an interval precedes the right end point in storage. Table 14 is an example of storage for a one-dimensional array of various data types.

Arithmetic expressions. Interval variables may be combined with other interval variables and with some other types of variables to form arithmetic expressions. The rules for constructing arithmetic expressions are unchanged from those for non-interval arithmetic. Tables 15 and 16 indicate which constants, variables, and functions may be combined by the arithmetic operators to form arithmetic expressions. Table 10 gives the data type resulting from valid combinations with respect to the arithmetic operators $+$, $-$, $*$, and $/$.

Table 16 gives the valid combinations with respect to exponentiation. The type of the result of the arithmetic operator denoting exponentiation (i.e., $**$) is the same as the type of the base.

Table 13. Built-in functions

Function	Entry name	No. of arguments	Type[a] Arguments	Type[a] Function		Function	Entry name	No. of arguments	Type[a] Arguments	Type[a] Function
Absolute value[b]	VABS	1	Interval	Interval		Obtaining most significant part of an Interval * 2 argument correctly rounded	VSNGL	1	Interval * 2	Interval
	VDABS	1	Interval * 2	Interval * 2						
	VCABS	1	Interval * C	Interval						
Truncate[c]	VINT	1	Interval	Interval						
Molular arithmetic[d]	VMOD	2	Interval	Interval		Express an Interval argument in Interval * 2 form	VDBLE	1	Interval	Interval * 2
Sign transfer[e]	VSIGN	2	Interval	Interval						
	VDSIGN	2	Interval * 2	Interval * 2						
Express two scalar arguments in interval form	VAL	2	Real	Interval		Obtain real part of a complex interval	VREAL	1	Interval * C	Interval
	VALD	2	Real * 2	Interval * 2						
	VALC	2	Complex	Interval * C		Obtain imaginary part of complex interval	VIMAG	1	Interval * C	Interval
Obtain part of an interval (1 for left end point; 2 for right end point)	RVP1	1	Interval	Real						
	RVP2	1	Interval	Real		Express two intervals in interval complex form[f]	VCMPLX	2	Interval	Interval * C
	DVP1	1	Interval * 2	Real * 2						
	DVP2	1	Interval * 2	Real * 2						
	CVP1	1	Interval * C	Complex		Obtain conjugate of complex interval argument[g]	VCONJG	1	Interval * C	Interval * C
	CVP2	1	Interval * C	Complex						
Obtain midpoint of an interval	RVPM	1	Interval	Real						
	DVPM	1	Interval * 2	Real * 2		Status of an interval relative to zero[h]	ISGNV	1	Interval	Integer
	CVPM	1	Interval * C	Complex			ISGNVD	1	Interval * 2	Integer

[a] Real * 2 indicates double precision.
Interval * 2 indicates interval double precision.
Interval * C indicates interval complex.

[b] Given the interval $V = [v_1, v_2]$ the absolute value of V is defined as

$$\text{for } v_1 \leq v_2 \leq 0 \qquad |V| = [\,|v_2|, \,|v_1|\,]$$
$$\text{for } v_1 < 0 < v_2 \qquad |V| = [0, \max (|v_1|, \,|v_2|)]$$
$$\text{for } 0 \leq v_1 \leq v_2 \qquad |V| = [v_1, v_2]$$

When V is an interval complex consisting of real interval V_R and imaginary interval V_i, then the absolute value of V is defined as the interval $[(V_R)^2 + (V_i)^2]^{1/2}$.

[c] The truncation of an interval $V = [v_1, v_2]$, is computed as

$[v_1], \{v_2\}$	when	$0 \leq v_1 \leq v_2$
$-\{|v_1|\}, [v_2]$	when	$v_1 \leq v_2 \leq 0$
$-\{|v_1|\}, \{v_2\}$	when	$v_1 < 0 < v_2$

where $[x]$ is defined as the largest integer not exceeding x and $\{x\}$ is defined as x when x is an integer and as $[x] + 1$ when x is not an integer.

[d] Given two intervals, V_1 and V_2, then VMOD (V_1, V_2) is computed as
$$V_1 - \text{VINT} \times (V_1/V_2) * V_2.$$

[e] Given two real intervals, $A = [a_1, a_2]$ and $B = [b_1, b_2]$, the transfer of sign function, VSIGN (A, B), is computed as follows:

	B		
A	$0 \leq b_1 \leq b_2$	$b_1 < 0 < b_2$	$b_1 \leq b \leq 0$
$0 \leq a_1 \leq a_2$	A	undefined	$-A$
$a_1 < 0 < a_2$	$|A|$	undefined	$-|A|$
$a_1 \leq a_2 \leq 0$	$-A$	undefined	A

[f] $V = arg_1 + i \ arg_2$.

[g] $V = X - iY$ for $arg = X + iY$.

[h] The status value (M) of an interval $V = [v_1, v_2]$ is defined as

$$M = 1 \text{ if } v_1 \leq v_2 < 0$$
$$M = 2 \text{ if } v_1 < 0 < v_2$$
$$M = 3 \text{ if } v_1 < 0 = v_2$$
$$M = 4 \text{ if } 0 = v_1 < v_2$$
$$M = 5 \text{ if } 0 = v_1 = v_2$$
$$M = 6 \text{ if } 0 < v_1 \leq v_2$$

Table 14. Storage arrangement for one-dimensional arrays

Word	Real	Double precision[a]	Complex[b]	Interval[c]	Interval double precision[d]	Interval complex[c]
1	A(1)	D(1)M	C(1)R	V(1)LV	VD(1)LVM	VC(1)RLV
2	A(2)	D(1)L	C(1)I	V(1)RV	VD(1)LVL	VC(1)RRV
3	A(3)	D(2)M	C(2)R	V(2)LV	VD(1)RVM	VC(1)ILV
4	A(4)	D(2)L	C(2)I	V(2)RV	VD(1)RVL	VC(1)IRV
5	A(5)	D(3)M	C(3)R	V(3)LV	VD(2)LVM	VC(2)RLV
6	A(6)	D(3)L	C(3)I	V(3)RV	VD(2)LVL	VC(2)RRV
7	A(7)	D(4)M	C(4)R	V(4)LV	VD(2)RVM	VC(2)ILV
8	A(8)	D(4)L	C(4)I	V(4)RV	VD(2)RVL	VC(2)IRV
.	.	.	.	.	.	.
.	.	.	.	.	.	.
.	.	.	.	.	.	.

[a]M = most significant
L = least significant
[b]R = real part
I = imaginary part
[c]LV = left half of interval
RV = right half of interval

[d]LVM = left half of interval — most significant
LVL = left half of interval — least significant
RVM = right half of interval — most significant
RVL = right half of interval — least significant
[c]RLV = real part of interval — left half
RRV = real part of interval — right half
ILV = imaginary part of interval — left half
IRV = imaginary part of interval — right half

Table 15. Type of the result of +, —, *, / operations

+, —, *, /	Integer	Complex	Real	Real * 2	Interval	Interval * 2	Interval * C
Integer	Integer	—	—	—	—	—	—
Complex	—	Complex	Complex	—	—	—	Interval * C
Real	—	Complex	Real	Real * 2	Interval	Interval * 2	Interval * C
Real * 2	—	—	Real * 2	Real * 2	Interval * 2	Interval * 2	—
Interval	—	—	Interval	Interval * 2	Interval	Interval * 2	Interval * C
Interval * 2	—	—	Interval * 2	Interval * 2	Interval * 2	Interval * 2	—
Interval * C	—	Interval * C	Interval * C	—	Interval * C	—	Interval * C

Note: Real * 2 indicates double precision.
Interval * 2 indicates interval double precision.
Interval * C indicates interval complex.
— indicates an invalid combination.

Table 16. Valid combinations with the arithmetic operator * *

Base		Exponent
Integer Complex Interval complex	} ** {	Integer
Real Double precision Interval double precision	} ** {	Integer Real Double precision

Logical expressions. The relational operators may not be used with interval arithmetic expressions. This rule is similar to the rule that complex quantities may never appear in logical expressions.

Arithmetic statement. A FORTRAN arithmetic statement is of the form $a = b$ where a is a subscripted or non-subscripted variable, and b is an expression. Table 17 indicates which type expressions may be equated to which type of variable in an arithmetic statement.

Arithmetic IF statement. The type of the arithmetic expression tested in the arithmetic IF statement may not be interval, interval double precision or interval complex.

Input/output of interval quantities. Since an interval quantity consists of at least two separate and independent numbers (four in the case of interval complex), the format statement that transmits the interval data must be specified accordingly. The following three formats could be used to transmit one data quantity of each of the types indicated:

(1) FORMAT (2E20.7), interval.

Table 17. Valid forms of the arithmetic statement

Variable (left side of equal sign)	Expression (right side of equal sign)						
	Integer	Complex	Real	Double precision	Interval	Interval double precision	Interval complex
Integer	Y	N	Y	Y	N	N	N
Complex	N	Y	Y	N	N	N	N
Real	Y	N	Y	Y	N	N	N
Double precision	Y	N	Y	Y	N	N	N
Interval	Y	N	Y	Y	Y	Y	N
Interval double precision	Y	N	Y	Y	Y	Y	N
Interval complex	N	Y	Y	N	Y	N	Y

Note: The symbol Y indicates a valid statement; the symbol N indicates an invalid statement.

(2) FORMAT (2D25.15), interval double precision.

(3) FORMAT (4F15.6), interval complex.

This requirement is similar to, and consistent with, formatted input/output of complex quantities.

Interval FUNCTION subprograms. Interval FUNCTION subprograms are defined by a special FORTRAN source language program. Additional forms of the FUNCTION statement are as follows:

(1) INTERVAL FUNCTION name $(a_1, a_2, \cdots, a_n)$.

(2) INTERVAL DOUBLE PRECISION FUNCTION name $(a_1, a_2, \cdots, a_n)$.

(3) INTERVAL COMPLEX FUNCTION name $(a_1, a_2, \cdots, a_n)$.

where the name is the symbolic name of a single-valued function, the arguments $a_1, a_2, \cdots, a_n$ (of which there must be at least one) are nonsubscripted variable names or the dummy name of a SUBROUTINE or FUNCTION subprogram, and the function type is explicitly stated preceding the word "FUNCTION." The additional forms follow the same usage rules as other types of FUNCTION subprogram statements.

Type statements. The type of an interval variable must be specified by one of the following three new type statements:

(1) INTERVAL $a(i_1)$, $b(i_2)$, $c(i_3)$, $\cdots$.

(2) INTERVAL DOUBLE PRECISION $a(i_1)$, $b(i_2)$, $c(i_3)$, $\cdots$.

(3) INTERVAL COMPLEX $a(i_1)$, $b(i_2)$, $c(i_3)$, $\cdots$.

where $a, b, c, \cdots$ are variable, array, or function names appearing within the program and $(i_1), (i_2), (i_3), \cdots$ are optional and give dimension information for arrays. Each i_n is composed of from one to seven unsigned integer con-

stants, separated by commas, representing the maximum value of each subscript in the array. Each i_n may be an unsigned integer variable only when the type statement in which it appears is in a subprogram. The other rules concerning the usage of type statements in FORTRAN IV also apply to the interval type statements.

Other specification statements. Interval type variable names may appear in dimension, common, equivalence, and namelist statements. Interval type variables, array element names, or array names may appear in data statements. The data value may only be of the corresponding interval constant type.

c. Example. The following is part of a program to compute the real roots of the quadratic equation $X^2 + bX + c = 0$ where the numbers b and c are interval numbers. Using the tedious subroutine calls (SPS 37-50, Vol. III, pp. 66–69) to perform interval arithmetic results in:

```
      REAL  B(2),C(2),T(2),S(2),X1(2),X2(2)
      CALL  ISQR (B,S)
      CALL  ISMITC (C,4.0,T)
      CALL  ISUB (S,T,S)
      CALL  INMAG (S,T)
      CALL  IINTST (S,T,T,I)
      IF (I .EQ. 0) GO TO 1
      CALL  INSSRT (T,T)
      CALL  ISUB (T,B,X2)
      CALL  IADD (T,B,X1)
      CALL  ISSCH (X1,X1)
      CALL  ISDIOC (X1,2.0,X1)
      CALL  ISDIOC (X2,2.0,X2)
C     ROOTS ARE IN X1 AND X2
      •
      •
      •
C     NO REAL ROOTS
 1    CONTINUE
```

More simply, using the extended FORTRAN IV language to perform interval arithmetic:

```
        INTERVAL  B,C,S,T,X1,X2
        S = (B * * 2) - (4.0 * C)
        CALL IINTST (S,VABS(S),T,I)
        IF (I .EQ. 0) GO TO 1
        X1 = (VSQRT(T) - B)/2.0
        X2 = -(VSQRT(T) + B)/2.0
   C    ROOTS ARE IN X1 AND X2
          .
          .
          .
   C    NO REAL ROOTS
   1    CONTINUE
```

d. Status. This extension of the FORTRAN IV language to simplify the use of interval arithmetic is in the process of being implemented on the IBM 7094. The mechanism for making the extension is a program called the JPL FORTRAN Language with Intervals Preprocessor (JFLIP) which is written as a preprocessor to the IBM 7094 FORTRAN IV compiler.

References

1. Moore, R. E., *Interval Analysis*, Prentice Hall, Englewood Cliffs, N. J., 1966.

2. *IBM 7090/7094 IBSYS Operating System Version 13 FORTRAN IV Language, Form C28-6390*, International Business Machines Corp., White Plains, New York, Nov. 1966.

IV. Development and Implementation

A. SFOF Development

1. The Mission-Independent Software of the SFOF Data Processing System, C. A. Seafeldt

a. Introduction. This article reports on the data processing system that is used in the Space Flight Operations Facility (SFOF) at JPL to support all missions.

The basic data processing unit (Fig. 1) is termed a "string" and consists of an IBM 7044 computer connected to an IBM 7094-II computer by a shared disk and a direct data connection. There are currently two such strings in the SFOF. The IBM 7044 is termed the input/output processor. It is a 65K machine with tape, drum, disk, and data communication input/output channels. The data communication channel (IBM 7288) provides the interface with the external world. This includes the communication net to the deep space stations (teletype and high-speed lines) and the SFOF user areas (remote terminals containing printers, plotters, card readers, message composers, etc.). The IBM 7094-II with tape and disk input/output channels is termed the central processor. The IBM 7094-II communicates with the external world through the IBM 7044 by use of the shared disk and the direct data connection and produces bulk output for off-line processing on IBM 7040s and an S/C 4020.

The mission-independent software system resides in both the IBM 7044 and 7094-II computers. It includes the real-time multiprogramming system to support two missions simultaneously in one string and the programs that handle all input/output (peripheral storage, remote terminals, and the communication net). In addition, it provides a clean interface for any of the mission-dependent program modules which are required for a particular project. In the IBM 7044, these mission-dependent modules typically consist of programs necessary to decommutate and alarm telemetry data. In the IBM 7094-II, they consist of commonly termed "user programs" used for orbit determination, detailed telemetry analysis, etc.

The mission-independent software system has undergone continuous modification and development since its inception. This has been necessary because of new hardware development and new functional requirements. The purpose of this article is to report on the major new developments being implemented during the first half of 1968.

b. ADSS compatibility. In May 1967, the DSN office approved a new configuration of the ground communications facility for *Mariner* Mars 1969 operations support.
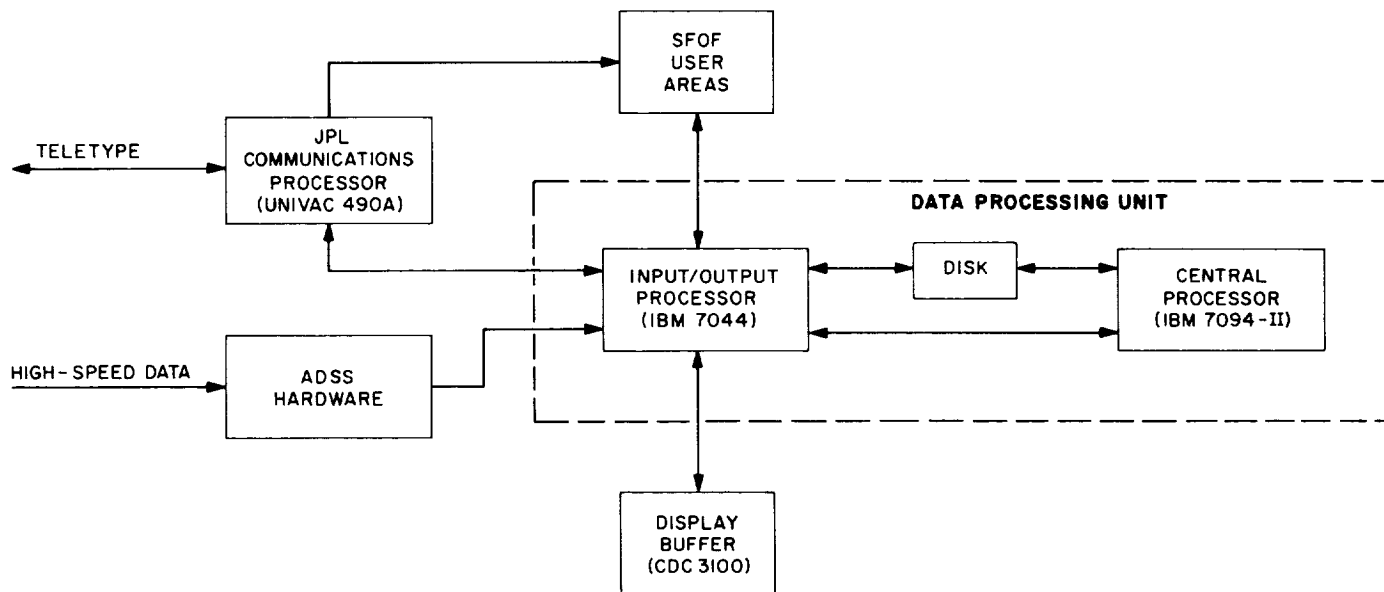
Fig. 1. SFOF data processing system

This configuration would use the NASCOM automatic data switching system (ADSS) for high-speed data transmission from the deep space stations to the data processing system in the SFOF. It would include the multiplexing of several data streams onto one high-speed data circuit.

The mission-independent software for the data processing system will be completed on May 1, 1968 to correspond with the delivery of the ADSS hardware (encoder/decoder and synchronizer) that will interface the high-speed data with the IBM 7044 data communication channel.

The implementation requires a new program to accept and process ADSS data and modifications to existing message input and trap processing programs.

c. IBM 7094-II Fortran IV and JPTRAJ compatibility. In October 1967, a proposal was made that Fortran IV compatibilities be provided in the data processing system. It was proposed that this compatibility be implemented by modifying JPTRAJ (the JPL trajectory monitor). The justification was the desire to write new *Mariner* Mars 1969 user programs in Fortran IV because of its extended capabilities over Fortran II and its easier conversion to a third-generation computer facility.

The software is scheduled to be complete on May 1, 1968 in order to provide a system for *Mariner* Mars 1969 user program testing.

The implementation requires a major rewrite of portions of the IBM system and of the SFOF library routines.

d. DSN monitoring. The first automated display of DSN monitoring data is being implemented and is scheduled for completion on July 1, 1968. Monitoring data from the deep space stations and the ground communication facility are being transmitted to the IBM 7044. A subset of this data will be displayed by the IBM 7044, and the entire stream, along with IBM 7044 generated monitor data, will be routed to a CDC 3100 computer for display throughout the SFOF facility.

e. Psuedo-residual modifications. In addition to the new functional capabilities discussed above, several existing features have been expanded. One major effort is a modification to the psuedo-residual program. This is a real-time IBM 7044 program which calculates and displays statistics concerning the differences between predicted values of observables and the actual tracking data. The current modifications being implemented provide a multi-mission capability, increased accuracy, and automatic processing that requires manual intervention only in case of nonstandard conditions.

2. Use of the Simulation System as a Data Source for Software Development, Integration, and Verification, *E. L. Dunbar*

a. Introduction. Integration and validation of the DSN data system is accomplished by individual subsystem

checkout followed by an end-to-end (antenna to final display device) flow of data of known format and content. The tool which provides this checkout data for the telemetry data system is a software package residing in the simulation data conversion center (SDCC) in the Space Flight Operations Facility (SFOF) at JPL. For the *Mariner* Mars 1969 project, this package provides: (1) teletype outputs to test the JPL communications processor, (2) two spacecraft data streams for recording of data to be utilized for on-site testing, and (3) either serial or parallel high-speed data outputs to test the communications system and the SFOF data processing system.

For the past reporting period, SDCC activity has consisted of code check, integration, and validation of this software package. Since this program has essentially four operating modes directed towards different system users, acceptance has proceeded in stages based on which user would first be ready to utilize the test data output for code checks. Accordingly, the parallel high-speed data output mode was validated first to support the SFOF software redesign and is now in use for mission-independent and mission-dependent code checking and integration. Validation and integration of the serial spacecraft and high-speed test data output is still in progress. Validation of all modes of the test data software package is projected for completion in late April 1968.

The program provides spacecraft commutators for engineering and science data with the exception of the 16.2-kbit science stream. All data channels may be displayed and varied under operator control with the exception of the two science playback streams. Spacecraft mode and bit rate are also under operator control.

b. High-speed data output. The program outputs blocks of data conforming to the automatic data switching system (ADSS) format.

All the data in the overhead (headers and trailers) may be varied or masked under operator control. Five types of high-speed data blocks may be selected for output to include both spacecraft data and the data relative to the ground-station operation and receiver status. Ground-station data blocks are output as a function of time selected by operator input. Spacecraft blocks are output when 168 bits of engineering data or 240 bits of science data have been commutated and are thus output as a function of the bit rate. Blocks may be output containing either 564 or 600 bits. If the error detector encoder decoder (EDED) is utilized, 564 bit blocks are output. The EDED adds a 36-bit error detection code to

be decoded by the receiving EDED. If errors are detected by the receiving EDED, it flags the data as failing the error test. Because the simulation software package preceded the installation of the EDEDs, a 600-bit output was provided in the simulation software package to allow SFOF telemetry program development to proceed in parallel with the EDED development.

c. Teletype output. The teletype output consists of five separate formats which are automatically selected by the program depending upon the type or condition of the data output from the spacecraft commutator. Header input which designates transmitting station, routing indicators, and data type can be input by the operator.

d. Program checkout and validation

Parallel high-speed data mode. Validation of the parallel output high-speed data mode has been simplified by the existence of an established interface to the SFOF data system and a standard SFOF computer data logging program. Data was transferred through this interface to the SFOF computers and logged on magnetic tape, then dumped on a line printer. While the data was being transferred, the simulation computer logged its own output buffer transmissions on a line printer. Successful comparison of the two printouts with the known program inputs constituted the validation of data transmission in this mode. Data control and display and teletype outputs were then exercised and verified.

Serial high-speed data mode. The serial high-speed data mode is utilized when a representative output of a Deep Space Instrumentation Facility (DSIF) is desired to test the communications and data processing hardware. In this mode, the SDCC outputs data serially into a 205 modem which is received by another 205 modem, passes through an EDED, then into an ADSS synchonizer which converts the serial data to 36-bit parallel data for transfer to the SFOF data system. Because the EDED and ADSS synchronizers were not scheduled to be available to meet the date that the simulation program would be ready for checkout, it was not possible to use the SFOF computer system delog capability. Therefore, a software package to accept and log this serial data was generated for the telemetry processing station (TPS) computers so that the SDCC verification could proceed. Since a never-ending series of software packages to check out software packages can result from this approach, the logging program was kept as simple as possible. A hardware decommutator is used as the interface to the TPS computer to generate an interrupt when it recognizes a sync word. The program files all data following the sync

interrupt in 24-bit blocks on magnetic tape until it receives another sync interrupt. Time of sync word reception is also recorded. Breakout of the data is somewhat tedious, but the program simplicity facilitated its checkout. The TPS program is now utilized in the final checks of the SDCC program to verify SDCC output.

Spacecraft operating mode. In this mode, two serial data streams are produced and output non-return-to-zero from two separate pulse-code-modulated transmitters. The validation of this data output is again a process of logging the data in the same program in the TPS computer which is used to verify the serial high-speed data output. One stream at a time is fed into the TPS computer, then delogged, and the delog is compared with the known program input and the SDCC line printer record.

e. Conclusions. Implementation of a communications package which will permit transfer of the SDCC data to the DSIF is underway. This will provide a powerful tool for system integration by routing controlled data patterns through the complete system with the system data input and output controlled and compared at a single location.

3. Communications Processor/IBM 7044 Redesign System Test Series, *R. G. Polansky*

a. Introduction. This is the second in a series of articles (see SPS 37-50, Vol. II, pp. 150–151) describing tests being conducted to determine the functional characteristics of the communications processor (CP)/IBM 7044 redesign system under various conditions. The second test has been completed at this time. The objectives of this test and the results obtained are presented in this article.

b. Description of second test. The second test was run using a mode 2 SFOF hardware system (IBM 7044–disk–IBM 7094 combination) and the *Surveyor G* programming system. As in the first test, the CP used the mode 2 version of the communications processor program. High-speed data at all *Surveyor* bit rates from 17 to 4400 bits/s were input to the 7044 from the telemetry processing station. During another portion of the test, *Surveyor* TTY data was input to the 7044 from a deep space station via the JPL CP. The objectives of the test were:

(1) To determine and document the effects of increasing the number of TTY readout display devices being driven by the CP/7044 system. (This determination included the effects of the "data sleeving" function in the mission-independent 7044 programming.)

(2) To determine the effects of 7094 program activities on the CP and 7044 delay characteristics.

(3) To determine the effects of mode 2 and mode 3 predict transmission on the CP and 7044 delay characteristics.

(4) To determine the delays attributable to the JPL CP, of TTY telemetry data being routed through the CP, to the 7044 and to a readout display device.

The satisfying of these objectives gave us baseline information on the performance of the *Surveyor* system as opposed to the information obtained for the *Mariner* system in the first test.

c. Results of second test. The results of the second test consist of delays experienced in selected portions of the 7044 system and in the CP under controlled loading conditions. They also include statistics gathered in the CP during the test. As in the first test, the characteristics determined agree well with the functional characteristics of the CP/7044 system as originally specified.

Delays experienced. As in the first test, no measurable delays in 100-word/min teleprinter responses were noted as a result of running 7094 programs.

The delay between the time the CP took the data from the 7044 to the time it displayed it on a 100-word/min teleprinter averaged 9.1 s. High values of 19 and low values of 3 s were noted. There appeared to be no correlation in these delays to the incoming data source (TTY or high-speed) or to the number of teleprinters being used; however, Table 1 shows that the delay did build up from a 7.5-s average at the lower data rates to a 9.5-s average at the higher rates. This may be a result of the sleeving function in the 7044 and the increased CP loading. Tabular information on all system delays is shown in Table 1.

The delay between the time the data was available to the CP and the time it was accepted was a function of the order in which the format requests were originally entered. The first three machines for which output was requested experienced delays averaging 10 ms. The fourth machine experienced delays averaging 45 ms; the fifth, sixth, and seventh machines experienced delays averaging 90, 140, and 190 ms, respectively. [The explanation for this is that formats are generated sequentially by the 7044 *in the order requested.* Each *Surveyor* format takes about 80 ms to generate (*Mariner* formats take about 160 ms to generate). Message segments to the CP from

Table 1. Tabular information on system delay times averaged for all TTY outputs

Data source	Time-tag-to-7044-output delay, sec			CP-in-to-CP-out delay, sec			Time-tag-to-CP-out delay, sec		
	Av	High	Low	Av	High	Low	Av	High	Low
TTY CP	136	187	100	7.5	13	4	143	196	105
17-bit/s high-speed	135	144	123	8.3	10	6	146	154	134
137-bit/s high-speed	16.6	21	11	9.8	18	3	25.9	35	15
550-bit/s high-speed	5.3	7	4	9.1	13	3	14.2	20	7
1100-bit/s high-speed	4.5	7	3	9.3	17	4	14.0	22	7
4400-bit/s high-speed	4.9	6	4	9.5	19	5	14.8	25	9
				9.1 Av					

the 7044 are not allowed to be transmitted any closer than 100 ms apart due to the action of a built-in hardware delay. This delay causes formats requested later to be back-buffered in the 7044 until the CP/7044 interface will accept them. The only deviation from this occurred at the 4400-bit/s data rate. Here, the formats took an average of 95 ms to compute, and the last TTY output device only backed up about 80 ms.]

Transmission of NASCOM headers to the CP caused up to 1.5-s delay, while transmission of predicts to two TTYs again caused up to 7.9 s of delay. It appears now that the 7.9-s figure is a worst-case condition that occurs when predicts completely saturate the CP output buffers in the 7044.

Inbound TTY data was played through the CP to a TTY machine and to the 7044. The CP delayed this semi-continuous data by an average of 18 s to the TTY machine and 14 s to the 7044. NASCOM headers were delayed by an average of 26 s to the TTY machine.

The normal processing time in the 7044 for quick-look data for TTY output is 4 s, once the input data buffer has been trapped (filled). The worst-case 7044 throughput time occurs when a telemetry frame just overlaps from one input buffer to its alternate. The best throughput time occurs when the last word of the frame occupies the last word of the input buffer. These are intuitive statements and are borne out by the tests.

The worst and best times just discussed can be calculated for the 7044s as follows:

$$\text{Best throughput time} = \left(4 + \frac{\text{seconds}}{\text{frame}}\right)$$

$$\text{Worst throughput time} = 4 + \frac{\left(\dfrac{\text{words}}{\text{frame}} + 128\right)}{\left(\dfrac{\text{words}}{\text{second}}\right)}$$

Seconds/frame, words/frame, and words/second all reference data at the 7044 input interface.

For the mode 2 computer configuration, it was possible to transmit predicts to the CP at all *Surveyor* bit rates. The time for transmission to the CP varied in an almost linear manner with the incoming data rate, as can be seen in Fig. 2.

For the mode 3 computer configuration, it was possible to reliably transmit predicts to the CP at input data rates up to about 750 bits/s (70 words/s). Predict tape search became erratic at higher data rates. Below 300 bits/s (27 words/s) the predict tape searched at its maximum rate, indicating that the tape search routine could run whenever it desired at these incoming data rates.

Statistics gathered in the CP. Pack areas stay dedicated to output TTY devices until the output message (or data) is complete (figure shift, H, letter shift sequence received by the CP). The maximum number of pack areas used is equal to the number of output machines being exercised plus the number of possible simultaneous input messages to these machines received by the CP. The maximum of 20 pack areas was used.

A minimum of three timer list entries are needed for the CP in its idle condition. An additional entry is required for each input and each output requiring a pack area. The maximum of 20 timer list entries was used.
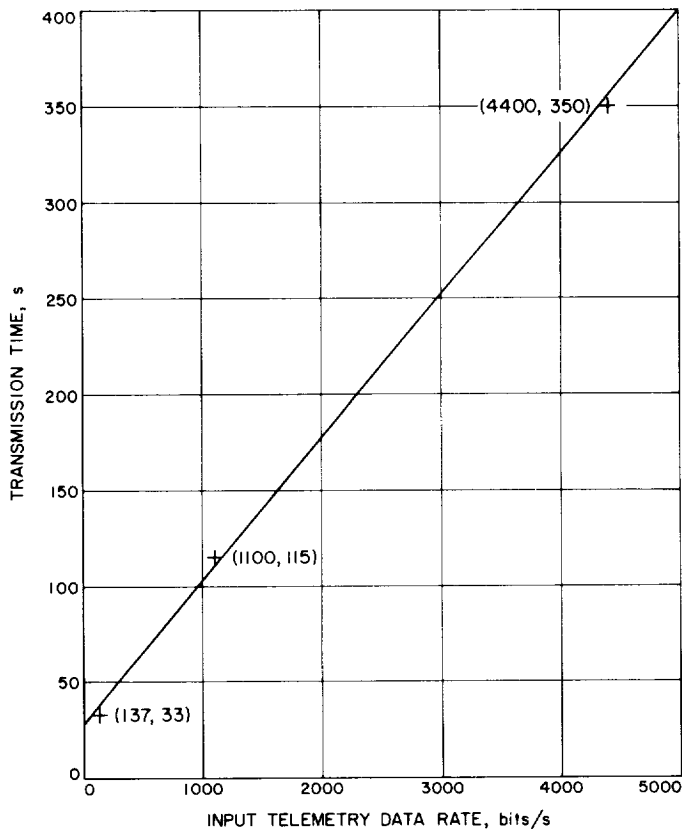
Fig. 2. Transmission time of predicts to communication processor

The maximum of 15 simultaneous drum input/output requests and 6 simultaneous validation queue entries was made.

The average "busy rate" of the CP during idle time was 11.6%. During high activity periods, the busy rate averaged 50%. The maximum busy rate of 81% was observed when predicts were going to two TTY machines and 4400-bit/s data were being output to all seven 100-word/min data printers. Busy rates as defined here are averaged over 1-s periods as opposed to the 5-min period normally used.

When the incoming data rate to the 7044 was sufficiently high, data were output to the teleprinters at approximately 10-s intervals. When the data rate was slower than 1 frame each 10 s, it was output once per frame. This indicates that sleeving in the 7044 mission-independent program is functioning as designed.

d. Test 3. Test 3 using a dual-mission *Mariner/Surveyor* system in the 7044 has recently been completed. The CP program for test 3 was modified so insight could be gained

into where the CP time delays were occurring. One of the major objectives of test 3 was to exercise recovery actions in all systems (CP and 7044). The results of test 3 will be presented in a future SPS, Vol. II.

B. GCF Development

1. Circuit Configuration Status, *F. E. Bond, Jr.*

Figure 3 illustrates the configuration and capabilities of the GCF as of April 1, 1968. The interconnecting circuits reflect the circuit reduction that resulted from the full implementation of the JPL communications processor as well as the circuit reduction that was realized by the removal of those circuits previously required for the support of the *Lunar Orbiter, Surveyor,* and *Mariner* Venus 67 Projects. Prior to the scheduled *Pioneer* 9 launch and continuing through the *Mariner* Mars 1969 launches, additional circuits will be required in order that the total ground communications requirement of these projects as well as those of the *Mariner* extended mission operations may be met. After the *Mariner* Mars 1969 launches, these additional circuits will be removed.

2. SFOF/GCF Implementation, *F. E. Bond, Jr.*

As a direct result of the full implementation of the JPL communications processor at the SFOF, the manual switching equipment previously used for teletype switching at the SFOF was removed from service on April 1, 1968. All switching of teletype traffic at the SFOF will hereafter be automatically accomplished by the communications processor except in those cases where the back-up facilities are used.

Installation of an automatic voice/data switching center at the SFOF terminal of the GCF is proceeding according to schedule and should be operational prior to the *Pioneer* launch. Upon completion and acceptance of this new facility, all switching of voice and data circuits to and from, as well as within, the SFOF can be done rapidly and efficiently.

The proposed concept of designating the GCF communications center at the SFOF as a NASCOM switching center for those NASCOM communications terminals geographically located closer to JPL than to NASCOM at Greenbelt, Maryland has progressed to the point where the necessary installation of teletype switching equipment at JPL is scheduled for mid-1968. Approximately 18 NASCOM teletype circuits connected from NASCOM to various terminations, ranging from Guaymas, Mexico
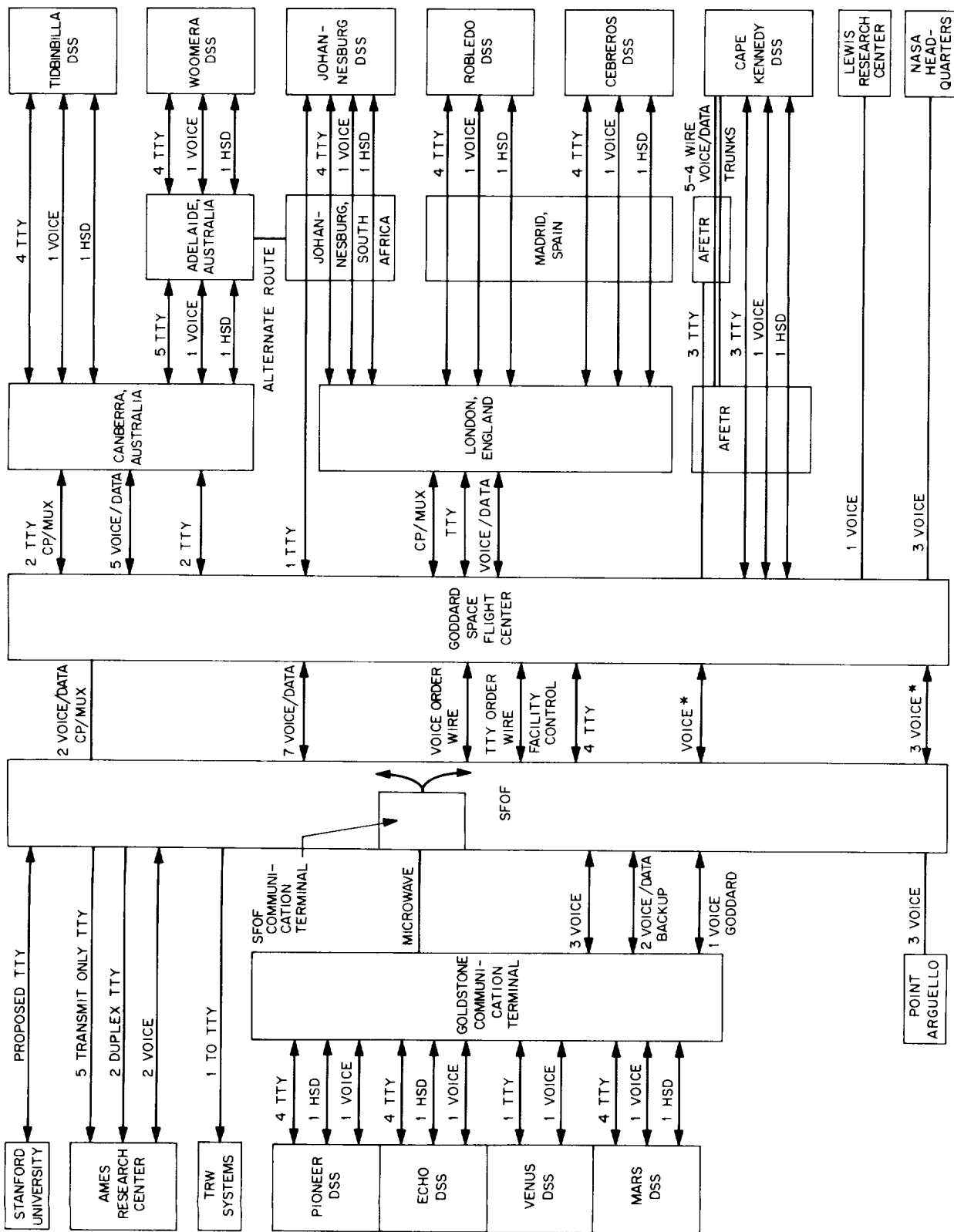
Fig. 3. GCF configuration

to Vandenberg, California, are planned to be reterminated at the SFOF and multiplexed to NASCOM over two audio circuits installed for that purpose between NASCOM and the SFOF.

3. DSIF/GCF Implementation, E. L. Yinger

a. Communications Center at Goldstone DSCC. All Goldstone DSCC communications terminal equipment has been relocated to the new addition to building G-33 at Goldstone. This was done to provide for more efficient operation and maintenance of equipment. The new Goldstone DSCC communications center now houses the following equipment:

(1) Dial telephone central office (SPS 37-50, Vol. II, p. 196).

(2) Western Union microwave terminal. This terminal, except for wideband equipment, was moved during the month of April. The wideband equipment used during the *Ranger, Surveyor,* and *Lunar Orbiter* Projects was removed. The five California Interstate Telephone circuits normally used to provide a backup for Western Union equipment were used for all operations while the microwave terminal was being moved.

(3) Intersite microwave terminal. This terminal consists of the DSCC communications center end of the following microwave links: DSCC–Pioneer DSS, consisting of six wideband channels; DSCC–Venus DSS, consisting of six wideband channels; and DSCC–Mars DSS, consisting of five wideband channels and twelve voice frequency channels. The Echo DSS, due to its close proximity to the DSCC communications center, is served by coaxial cable only.

(4) Communications control group (CCG) teletype terminal. This equipment, which has been operating for several months, was moved from another area of building G-33.

(5) The CCG voice data terminal. This terminal is a new unit and replaced existing voice data terminal equipment.

(6) Teletype machines. These machines will continue to provide the patch and monitor function for each of the Goldstone DSSs until each DSS has its own communications center established and ready for use.

b. Communications junction module. The communications junction module (CJM) was developed to provide a flexible but standard interface point between the GCF and the DSIF within each DSS. The total capabilities of all GCF and DSIF equipment enter the CJM on connectors. Interconnections are made in the CJM as required. The actual GCF/DSIF interface is at the connectors where the GCF equipment cables are plugged into the CJM. The CJMs will be installed at each DSS at the same time the new GCF equipment (CCG, high-speed data, DSIF/GCF interface computer) is installed. The CJMs are currently being fabricated, and orders are being placed for the interconnecting cables.

c. Standardized TTY configuration. A standard configuration is presently being developed to provide teletype equipment to each DSS in accordance with the functions that station performs in order to standardize the function and number of machines and their assignment to TTY circuits. Efforts are also being made to standardize the equipment arrangement in the communications rooms at each station to improve operator efficiency. Each machine will be cabled into the CCG/TTY terminal via a TTY junction box and the CJM.

4. DSIF/GCF Interface Assembly, E. A. Garcia

a. Introduction. A previous SPS article (SPS 37-50, Vol. II, pp. 168–172) presented, in general, the functional requirements, implementation plans, and theory of operation of the DSIF/GCF interface (DGI) assembly. This article will present additional information on the hardware.

The DGI assembly consists of one Scientific Data Systems (SDS) 910 computer and a communications buffer assembly.

Previous SPS articles on the digital instrumentation subsystem (DIS), telemetry and command processor (TCP), and antenna pointing subsystem (APS) have presented descriptions of the SDS 910/920 computers, their capabilities, and peripheral hardware. Thus, this article will not provide a description of the SDS 910 computer, but rather will present a description of the communications buffer assembly.

b. DGI communications buffer assembly. The DGI communications buffer assembly will consist of the following subassemblies, housed in a standard DSIF cabinet (Fig. 4):

(1) Power supply drawer (Phases I and II).

FRONT

POWER SUPPLY
POWER SUPPLY *
ADSS RECEIVE/SEND 1
ADSS RECEIVE/SEND 2 *
DECODER/CONTROL
DSS RECEIVE/SEND (DIS)
DSS RECEIVE/SEND (TCP-a)*
DSS RECEIVE/SEND (TCP-β)*
DSS RECEIVE/SEND (TDH)*
SIMULATION A
SIMULATION B
PATCH PANEL*
POWER PANEL

REAR

DGI BYPASS (PHASE I ONLY)
INTERFACE JUNCTION PANEL
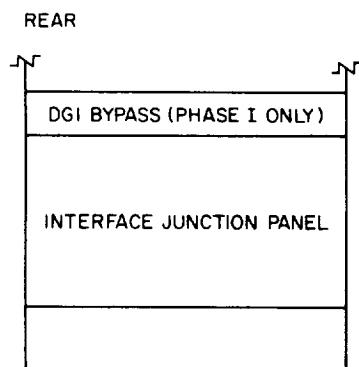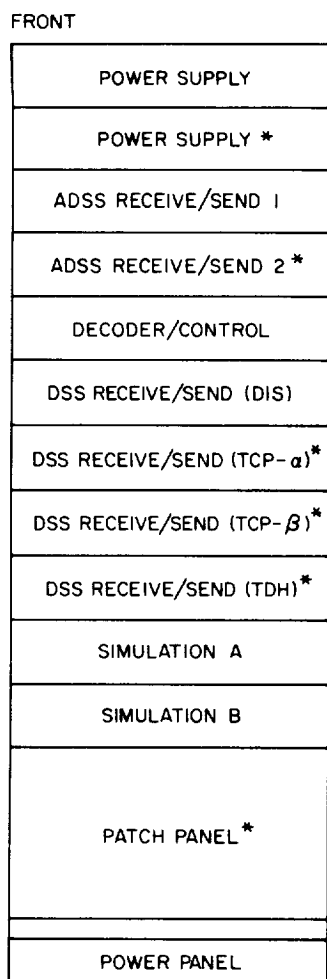
*PHASE II IMPLEMENTATION ADDITIONS

Fig. 4. DGI communications buffer assembly

(2) Power supply drawer (Phase II).

(3) ADSS[1] receive/send drawer (Modem 1, Phases I and II).

(4) ADSS receive/send drawer (Modem 2, Phase II).

(5) Decoder/control drawer (Phases I and II).

(6) DSS receive/send drawer (DIS, Phases I and II).

(7) DSS receive/send drawer (TCP-α, Phase II).

(8) DSS receive/send drawer (TCP-β, Phase II).

(9) DSS receive/send drawer (TDH-II, Phase II).[2]

(10) Simulation A drawer (Phases I and II).

(11) Simulation B drawer (Phases I and II).

(12) Interface junction panel (Phases I and II).

(13) DGI interface patch panel (Phase II only).

(14) DGI by-pass panel (Phase I only).

(15) Cabinet power panel (Phases I and II).

c. *Power supply drawer.* The two power supply drawers are identical and contain three Lambda Electronics modular power supplies (LM-D12). The supplies are connected to distribute +12 and −12 Vdc bias voltages required to power the logic circuits housed in the other drawer assemblies.

d. *ADSS receive/send drawer.* The two ADSS receive/send drawers are identical and contain the logic and signal conditioning elements required to interface the GCF's ADSS to the DGI computer, and vice versa. The basic functions performed within this drawer are:

(1) Conversion of serial input data to the 24-bit parallel output required by the computer (receive channel register).

(2) Conversion of the computer's 24-bit parallel output to a serial bit stream required by the ADSS (send channel register).

(3) Sync detection for the DGI computer of the start of an incoming ADSS data block. (The sync detector circuitry provides the capability of allowing up to three random errors in a sync word by a manual switch located in the decoder/control drawer.)

---

[1]ADSS = automatic data switching system.
[2]TDH = tracking data handling.

The logic elements required to perform the above basic functions are assembled into three plug-in sub-assemblies: two are 24-bit shift registers (parallel in-serial out and serial in-parallel out) and the third is the receive/send control logic, which operates on both registers and interface.

e. Decoder/control drawer. The decoder/control drawer contains all the logic and signal conditioning circuits required to interface the DGI computer to the various DGI buffer receive/send and simulation drawers. The circuitry in this drawer provides the following functions:

(1) 24 Line drivers to interface the clocked outputs of all ADSS and DSS receive shift registers (receive channel registers) to the computers.

(2) Power amplification to distribute the computer's 24-bit parallel output to all clocked inputs of the ADSS, DSS, and simulation *send* shift registers (*send* channel registers) and to the decoder portion of this drawer.

(3) Decoding of the computer's 24-bit output lines and generation of discrete codes (under computer control) as shown in Table 2.

(4) Generation of visual and audible alarms resulting from mutual DGI buffer/computer alarm monitors and tests (see Table 3 for buffer status word to the computer).

(5) Time sequencing for the input/output operations of all DSS receive/send circuits to prevent simultaneous interrupts to the computer.

(6) Manual control switching for setting of the allowable ADSS sync word error magnitude, DGI-buffer master reset, and audible alarm disable.

The above functions are contained in three plug-in subassemblies, two of which are identical decoder/buffer subassemblies, except for external wiring. The third subassembly is the decoder/sequencer subassembly.

The decoder/buffer subassemblies provide the 24-bit parallel input/output signal conditioning and first-level decoding. The decoder/sequencer subassembly provides the second-level decoding, sequencing, and alarm monitoring. The decoder/control drawer front panel houses all manual operator controls and indicators.

Table 2. EOM address assignments[a]

Function	EOM address (octal)	Comments
Input		
Energize input of hardware status word	33701	Followed by pin instruction
Energize input from HSD 1 (RCV)[b]	33702	
Energize input from HSD 2 (RCV)[b, c]	33703	
Energize input from DIS[c]	33704	
Energize input from TCP-α[c]	33705	
Energize input from TCP-β[c]	33706	
Energize input from TDH-II[c]	33707	
Return HSD-1 input logic to search mode	33772	Set or reset hardware logic
Return HSD-2 input logic to search mode[c]	33773	
Output		
Energize output to simulation A	33710	Followed by pot instruction
Energize output to simulation B	33711	
Energize output to HSD 1 (trans)[c]	33712	
Energize output to HSD 2 (trans)[c, d]	33713	
Energize output to DIS	33714	
Energize output to TCP-α[c]	33715	
Energize output to TCP-β[c]	33716	
Energize output to TDH-II[c]	33717	
Energize last output to HSD 1[c]	33752	
Energize last output to HSD 2[c]	33753	
Energize last output to DIS	33754	
Energize last output to TCP-α[c]	33755	
Energize last output to TCP-β[c]	33756	
Energize last output to TDH-II[c]	33757	
Set internal clock A to 8⅓ bits/s	33720	Set or reset hardware logic
Set internal clock A to 33⅓ bits/s	33721	
Set internal clock A to 66⅔ bits/s	33722	
Set internal clock A to 270 bits/s	33723	
Select internal clock for simulation A	33724	
Select external clock for simulation A	33725	
Start simulation data stream A	33726	
Set internal clock B to 8⅓ bits/s	33730	
Set internal clock B to 33⅓ bits/s	33731	
Set internal clock B to 66⅔ bits/s	33732	
Set internal clock B to 270 bits/s	33733	
Select internal clock for simulation B	33734	
Select external clock for simulation B	33735	
Start simulation data stream B	33736	
Enable multiplexer inputs[c]	33775	
Inhibit multiplexer inputs[c]	33776	
Reset hardware timer	33777	

[a]EOM = energize computer output/input instruction.

[b]RCV = receive.

[c]Indicates Phase II implementation.

[d]TRANS = transmit.

f. DSS receive/send drawers. The DSS receive/send drawers are mechanized in the same manner as the

Table 3. Status word format

Bit	Source	Indication[c]
0 1	Allowed error set for sync detection	00 → no error 10 → 2-bit error 01 → 1-bit error 11 → 3-bit error
2 3	HSD-1 CF line[a] HSD-2 CF line[a, b]	0 → block with perfect sync is being sent to the DGI
4 5	HSD-1 input register HSD-2 input register[b]	1 → sync has been recognized and a block is being received
6 7 8 9	DIS input register[b] TCP-α input register[b] TCP-β input register[b] TDH-II input register[b]	1 → register is currently receiving a block of data
10 11 12 13 14 15	HSD-1 output register[b] HSD-2 output register[b] DIS output register TCP-α output register[b] TCP-β output register[b] TDH-II output register[b]	0 → register is available for the start of a new block of data
16 17	Simulation clock A Simulation clock B	0 → internal, 1 → external
18 19	Simulation output A Simulation output B	1 → output enabled
20 21 22 23	Selected internal Clock rate A Selected internal Clock rate B	00 → 8⅓ bits/s 10 → 33⅓ bits/s 01 → 66⅔ bits/s 11 → 270 bits/s

[a] CF = a DSS block sync detection line.

[b] Indicates Phase II implementation.

[c] Ones and zeros refer to computer memory content.

ADSS receive/send drawers, except that the wiring is modified to accept the DSS's HSD[3] interface rather than the GCF's ADSS. In addition, the input/output of these drawers are under computer control via the decoder/control drawer sequencer. The plug-in chassis contained in these drawers is the same as for the ADSS drawers.

g. Simulation A/B drawers. The simulation A and simulation B drawers provide the required circuitry to produce two independent serial bit streams, at any one of four, computer programmed, basic clock rates (8⅓, 33⅓, 66⅔, and 270 bits/s) or external clocks. The serial bit streams are derived from the DGI computer processing of incoming simulation ADSS data blocks.

---

[3] HSD = high-speed data.

The first three clock frequencies are derived from a countdown chain using the station's frequency and timing subsystem 10-kHz signal. The 270-Hz clock is generated by a crystal oscillator within the drawer.

Each drawer contains two plug-in subassemblies: one is a 24-bit parallel-in/serial-out shift register (the same assembly used in the receive/send drawers) and the other contains the shift register control circuitry, clock selection control, and clock generator countdown chains.

h. Interface junction panel. The interface junction panel is the point where all drawers interface with each other, the computer, and the external subsystems. The panel consists of interface connectors and terminal boards and accommodates all DGI interface requirements for Phase I and II implementation plans.

i. DGI-by-pass panel. This panel is temporary in nature and is used for Phase I implementation only. Its purpose is to by-pass the DGI in case of failure and connect the GCF's ADSS directly to the DSS–DIS subsystem.

j. DGI interface patch panel. This panel will take the place of the DGI-by-pass panel as part of the Phase II implementation plan and will provide for the following functions:

(1) Patch any of the two ADSS HSD modems to any one of the DGI ADSS receive/send drawers, or directly to any one of the DSS subsystems (DIS, TCP-α, TCP-β, and TDH-II).

(2) Patch any of the DSS subsystems to any of the DGI DSS receive/send drawers.

k. Cabinet power panel. The cabinet power panel is a standard DSIF panel containing primary power circuit breakers and monitors.

C. DSIF Development

1. Instrument Tower Position Control for 210-ft Antenna, W. M. Peterschmidt

a. Introduction. The angular reference of the 210-ft antenna at the Mars DSS is provided by the Master Equatorial, which is mounted on the top of the instrument tower as shown in Fig. 5. In order to fully utilize the accuracy of the Master Equatorial, it is desirable to limit the angular movement of the instrument tower top to a value approximately equal to the error of the Master Equatorial. As described in SPS 37-50, Vol. II, pp. 151–158, the angular movement of the instrument tower could be approximated at 12.7 arc sec. The above-referenced article suggests as one solution a servo system using heating of the tower to hold the tower in the proper position. The design and testing of such a servo system is the subject of this article.

The configuration of this servo system is shown in Fig. 5. The levels are located inside the Master Equatorial base and provide the error signals to the amplifiers in the floor below. These amplifiers provide the driving signals to the power stage which provides power to the heater strips. The heat deflects the tower until signals from the levels turn off the heater strips.

b. Selection of type of power stage. Two types of power stages were considered for this servo system. They are proportional power amplifiers and discontinuous or relay-switching power stages.
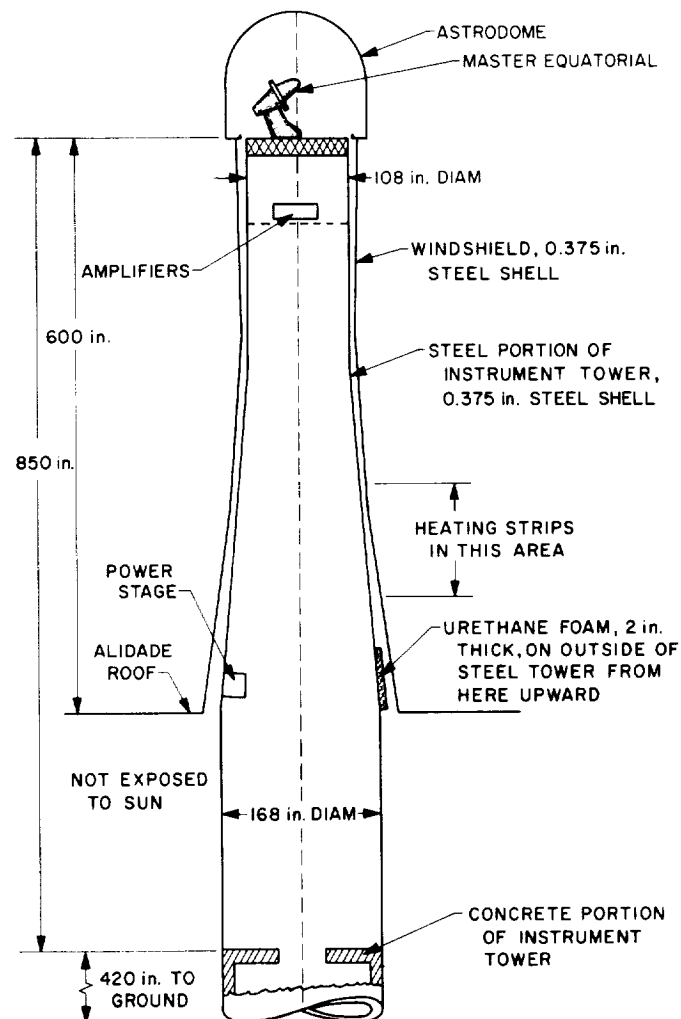
Fig. 5. Instrument tower configuration

The proportional power amplifiers have the advantages of less static error, which is inversely proportional to gain, and reliability in that they are completely solid state. However, for this power level, it would require a silicon controlled rectifier (SCR) type amplifier which implies possible radio frequency interference problems.

A discontinuous power stage has the advantages of low cost and short lead time. Its error is also inversely proportional to gain, but the gain is proportional to switching rate. The switching rate is important because its affects the lifetime of the relays.

Because of its advantages, the error versus switching rate trade-off was studied for the discontinuous control. Since the differential equations describing the tower tilt are also discontinuous, it was decided to construct an analog computer simulation of this control system.

c. Analog simulation. The relation between the rate of change of temperature of the tower and the electrical power input is derived in the following equations, assuming that all the heat loss is due to radiation:

$$\dot{T}(t) = \frac{\beta}{C_p W} P - \frac{\sigma F_a F_\varepsilon}{C_p W} \lambda \, [T^2 + T_0^2 \,]$$
$$\times [T + T_0] [T(t) - T_0] \qquad (1)$$

where

$T(t)$ = the tower temperature in the heated area

T_0 = the ambient temperature

β = 0.057 Btu/min

C_p = the specific heat = 0.1138

W = the weight of steel heated = 460 lb

P = the electrical power input in watts

λ = the area heated = 52.5 ft^2

F_a = a geometrical factor = 1.0

F_ε = an emissivity factor = 0.818

σ = the Stefan–Boltzmann constant = 0.288 $\times$ 10^{-10} Btu/min ft^2 °R^4

The relationship between tower tilt angle and temperature is assumed to be

$$\theta(t) - \theta_0 = \alpha[T(t) - T_0] \qquad (2)$$

where $\dot{\theta}(t)$ is the instantaneous tower position, θ_0 is the original tower position due to ambient temperature T_0, and α is a constant of proportionality, experimentally determined to be 0.365°/°R.

Combining Eqs. (1) and (2) gives

$$\dot{\theta}(t) = - \frac{\sigma F_a F_\varepsilon}{C_p W} \lambda \gamma [\theta(t) - \theta_0] + \frac{\beta \lambda}{C_p W} P \qquad (3)$$

where

$\gamma = (T^2 + T_0^2)$, $(T + T_0)$ is assumed to be constant

= 0.067 $\times$ 10^{-10} °R^3

Substituting values for the constants gives

$$\dot{\theta}(t) = -0.0159[\theta(t) - \theta_0] + 3.98 \times 10^{-4} P \qquad (4)$$

Selecting scale factors for the computer, time scaling by 100 and converting to seconds of time gives:

$$\dot{\theta}(\tau) = - \frac{0.0159}{K_1} \frac{100}{60} K_1[\theta(\tau) - \theta_0]$$
$$+ 3.98 \times 10^{-4} \times \frac{100}{60} K_2 P$$
$$= -0.0264 \, [\theta(\tau) - \theta_0] + 0.0221 \times 0.03P \qquad (5)$$

where

$$K_1 = \frac{100v}{100 \, s} = 1 \, v/s$$

$$K_2 = \frac{100v}{2880_\omega} = 0.0347 \, v/\omega \simeq 0.03 \, v/\omega$$

Due to the vibrations present in the tower, an averaging filter was added to the control system to reduce the possibility of noise turning on the power stage. The computer scaled equations for the 10-sec filter are:

$$\theta_1(\tau) = \frac{1}{T} [K \, \theta(t) - \theta_1(\tau)]$$
$$= 100\theta(\tau) - 10\theta_1(\tau) \qquad (6)$$

The completed computer diagram is shown in Fig. 6. The gain of Amplifier 55 was adjusted to switch power on when the tower tilt was greater than 1 arc sec.

Figure 7 shows the response of the control system to an initial error of 10 arc sec for two values of power input. The limit cycle characteristic has a cycle time of 4 s/cycle $\times$ 100/60 s/min = 6.67 min/cycle for 1728 W input. At this switching rate, a relay with a life expectancy of 10^5 operations would last more than a year. This life expectancy seemed to be long enough to justify a field test of the control system.

d. Field tests. Two Ideal Aerosmith precision levels were placed in the base of the Master Equatorial so that one of them measured rotation about a north-south axis and the other an east-west axis.

Four sets of Electrofilm strip heaters were glued to the inside of the tower wall in the region shown in Fig. 5. The four sets were spaced 90 deg apart, and each set formed a rectangular pattern approximately 72 in. high by 48 in. wide.
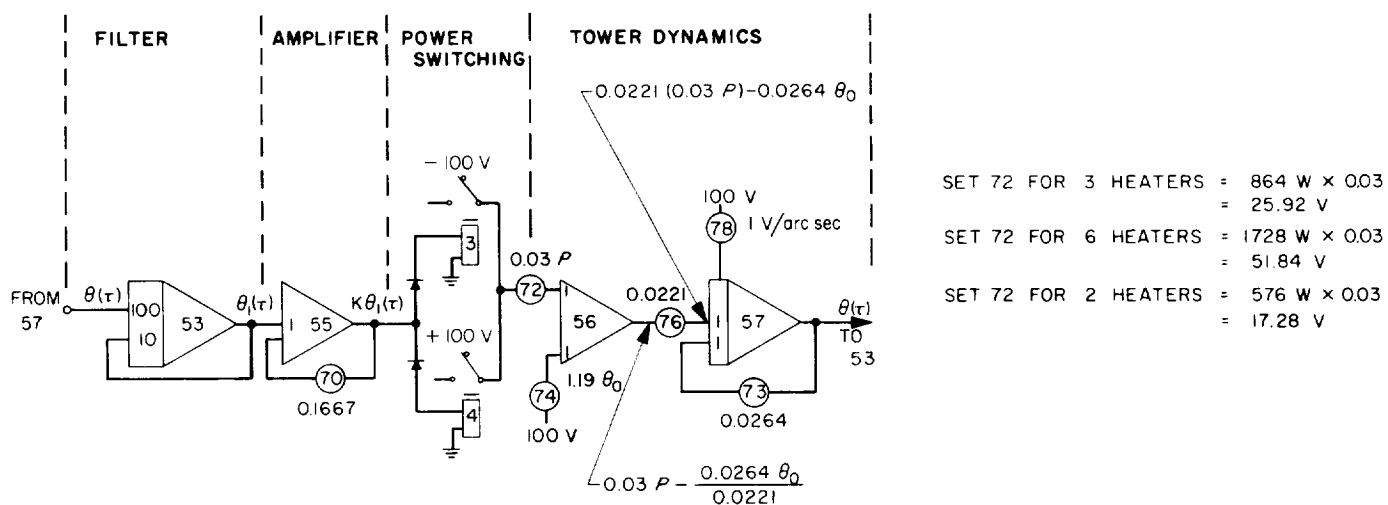
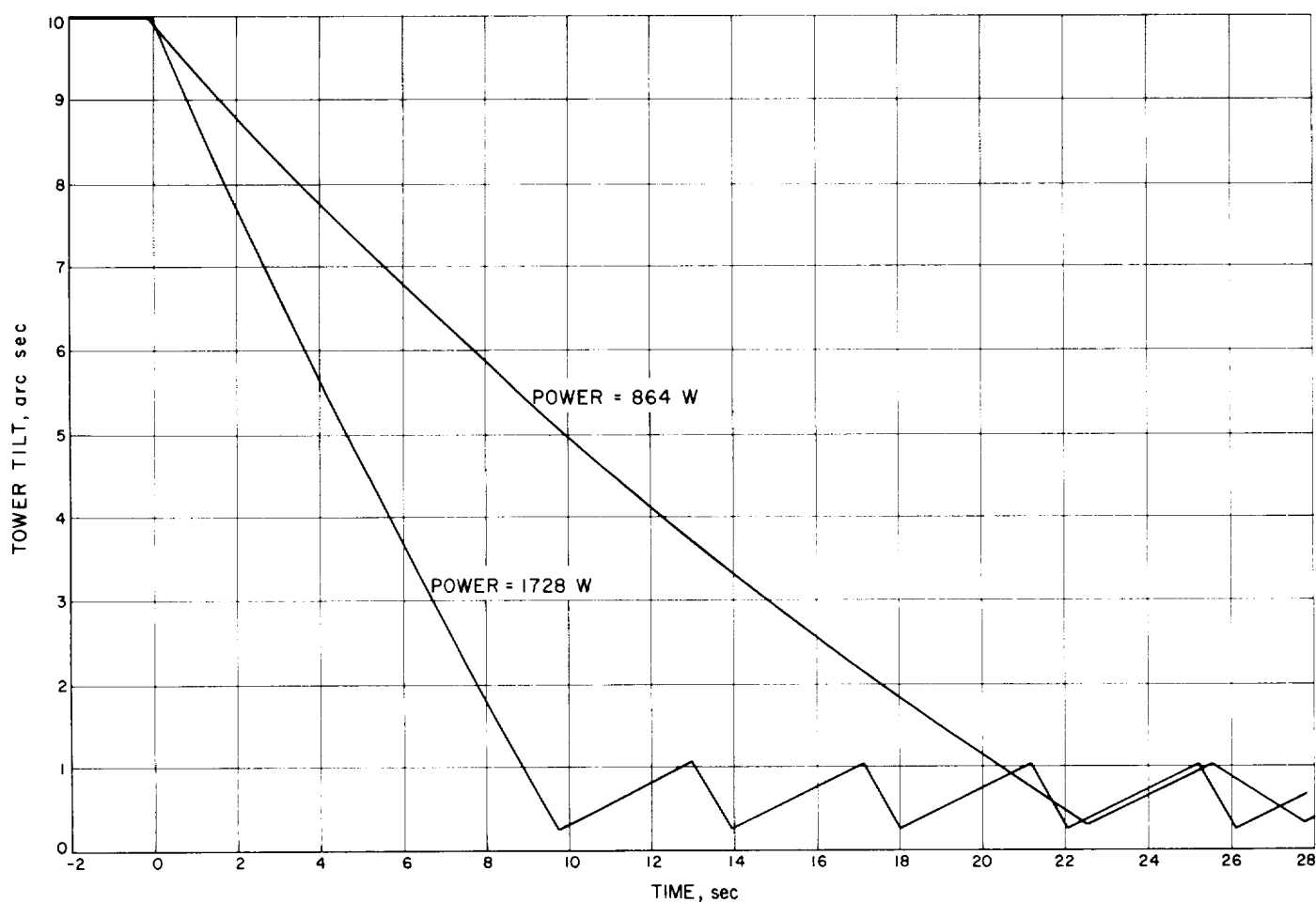**Fig. 6. Analog computer simulation of power control system**

Fig. 7. Power control system response, analog simulation

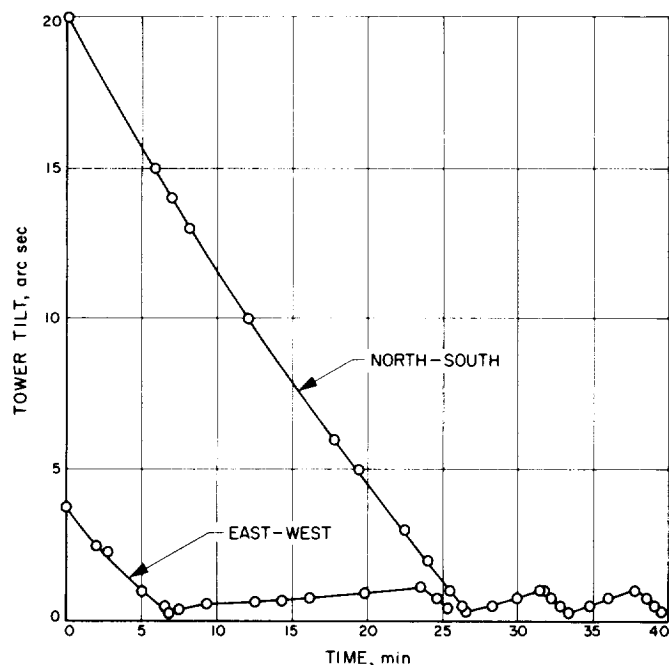When the control system was turned on, the north-south axis had an initial error of over 20 arc sec and the east-west axis had an initial error of 3.72 arc sec. Figure 8 shows the response of the tower to the control system. The detail of the north-south limit cycle is shown in Fig. 9. Its cycling time is approximately 6.5 min/cycle.

During the field testing when a 10 to 15 mph wind started, it was noticed that the control system changed its characteristic limit-cycling and turned on one set of heaters for a long time period. As the tower had been stable at a position for hours before this wind started, it was suspected that the levels were affected by the wind-induced vibration. Two $\pm$ 0.1-g accelerometers were placed at the top of the tower to determine vibration levels and frequency so that the levels could be tested under controlled conditions. The accelerometers detected a maximum acceleration of less than 1 mg at frequencies from 2 to 4 Hz. The predominant frequencies were at 3.5 to 3.8 Hz and 2.5 to 3.0 Hz.

A platform, as shown in Fig. 10, was constructed that allowed the levels to be vibrated horizontally without inducing angular tilt. The platform was excited at various frequencies by a linear solenoid, and the average level signal was recorded. This data, shown in Table 4, demonstrated that these levels were unsuitable for the vibration environment experienced as the tilt angle changed with vibration frequency.
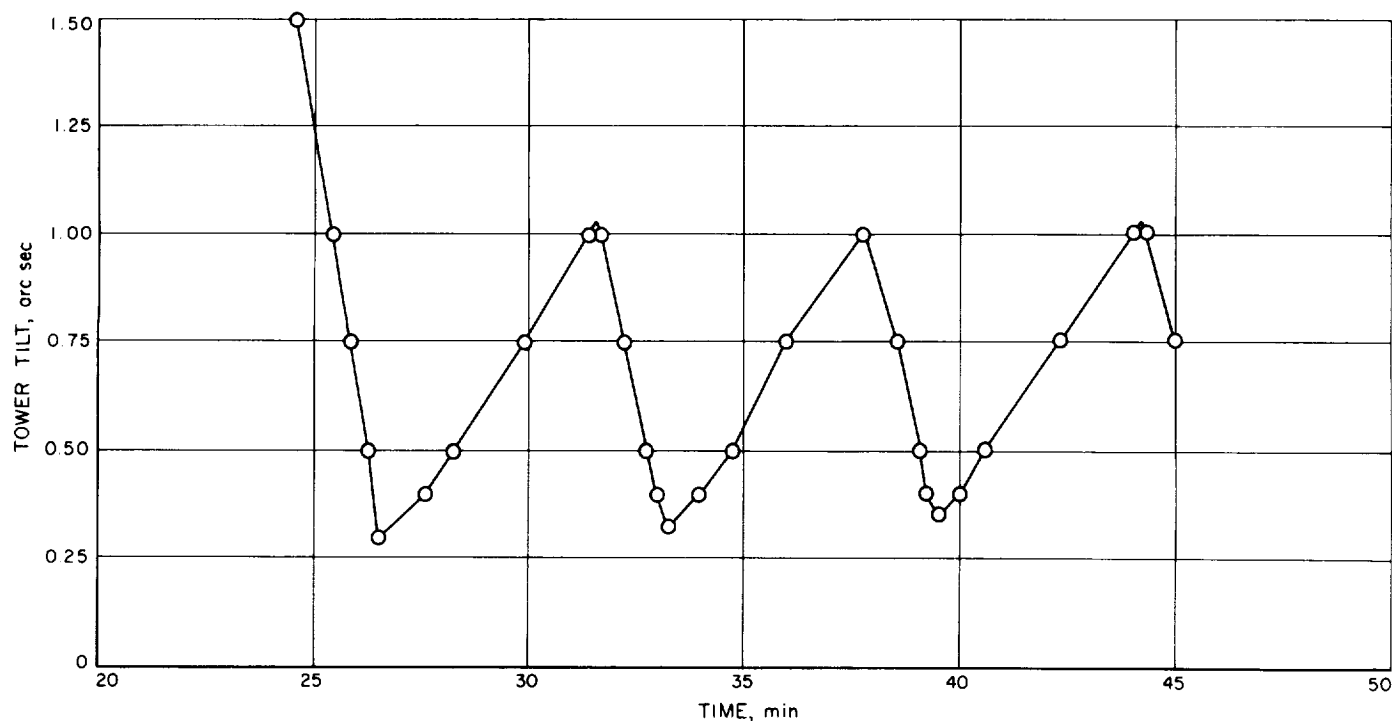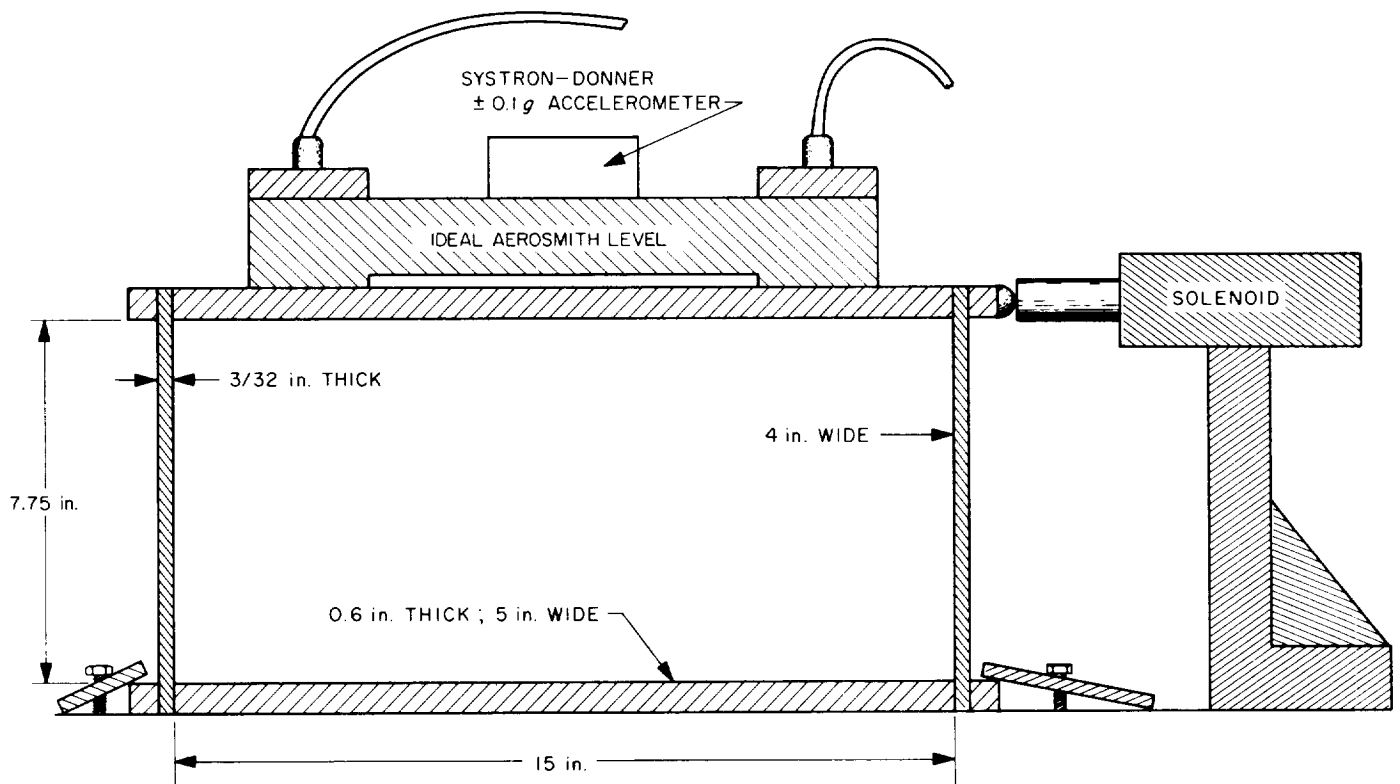

Fig. 8. Response of tower to control system

Fig. 9. Detail of north-south cycling

Fig. 10. Vibration test platform

Table 4. Level vibration tests

Vibration frequency, Hz	Level output, arc sec	Accelerometer, Milli-g
0	−1.7	0
2.0	−1.7	0.54
2.4	−1.7	0.59
2.5	+1.5	0.48
2.6	−6.0	0.59
2.8	−1.7	0.54
3.2	−1.7	0.59
3.6	−1.7	0.54
0	−1.7	0
4.0	−1.7	1.08
4.4	−1.7	1.24
4.8	−1.7	1.67
5.2	−1.7	1.89
5.6	−1.7	1.83
0	−1.7	0
6.0	−1.7	2.21
6.4	−0.8	2.27
6.48	+3.0	2.05
6.6	−10.0	2.16
6.8	−2.5	2.27
7.2	−1.7	2.32
0	−1.7	0
7.6	−1.7	2.70
8.0	−1.7	2.97
9.2	−1.7	3.24
9.26	−1.0	3.51
9.3	0	3.51
9.32	−1.3	3.51
9.34	−1.7	3.51
9.58	−7.5	3.78
9.60	−5.0	3.51
9.64	−9.0	3.51
9.7	−15.0	3.78
9.72	−13.0	3.78
9.74	−11.0	3.78
9.78	−9.0	3.78
9.8	−8.0	3.78
9.86	−6.0	3.78
9.98	−4.0	3.78
10.4	−2.5	4.32
0	−2.0[b]	
11.44[a]	+6.0[b]	
12.0[a]	+0.5[b]	
0	−2.0[b]	0

[a]Resonance of platform accelerometer saturated.
[b]Zero shift of −0.3 arc sec.

e. Conclusion. The basic result of this test is that a servo-controlled tower is a practical means of achieving the desired accuracy for the instrument tower if a suitable tilt sensor can be found.

2. Arc Detector for 450-kW Transmitter System, R. E. Arnold

a. Introduction. In parallel with the development of the 450-kW S-Band Transmitter System (SPS 37-49, Vol. II, pp. 84–88), a new arc detector was designed and built for use in that system. The arc detector (AD) was designed at JPL, and a prototype was built at a contractor's facility. This report discusses waveguide arcs, functions of an AD, and specific design features and tests performed on the prototype unit.

b. Waveguide arcs. A high-power radio-frequency (RF) arc in the output waveguide can cause catastrophic failure of a klystron's output RF window. An arc in a waveguide produces a sonic shock wave that can easily break a klystron waveguide window; high power klystron windows are generally made of beryllium oxide or ceramic, substances known for their mechanical brittleness as well as for their excellent dielectric characteristics at RF frequencies. Assuming a waveguide arc occurs, damage to the klystron can be prevented if the output RF power can be turned off before the resulting sonic shock wave obtains enough energy to damage the klystron window.

c. Functions of an AD. An AD's function is to detect a waveguide arc and to turn off the output RF power before damage can occur. The output RF power is turned off by actuating a switch in the RF drive line (input to the klystron). Figure 11 is a block diagram showing an AD. Although the figure shows many functions having dual-channel operation, single-channel operation should be assumed for a basic AD in this discussion. Waveguide arcs are detected in two ways; (1) light sensors, and (2) reflected power sensors, as follows:

Light sensor. A light sensor is attached to the waveguide near the klystron. The light sensor "looks" at the klystron window through a small hole in the waveguide. An arc in the dark waveguide causes a bright flash, and the light sensor is actuated. This, in turn, sends a signal to the crystal switch driver which turns off the crystal switch in the drive line. The klystron output RF is also turned off, and the arc is extinguished.

Reflected power sensor. Arcs occurring far from the klystron window may not be sensed by the light sensor because of light attenuation caused by waveguide bends. These arcs can be detected by the resulting waveguide mismatch occurring at the arc and the resultant very high voltage standing-wave ratio (VSWR). The reflected power of the VSWR is monitored by a directional coupler
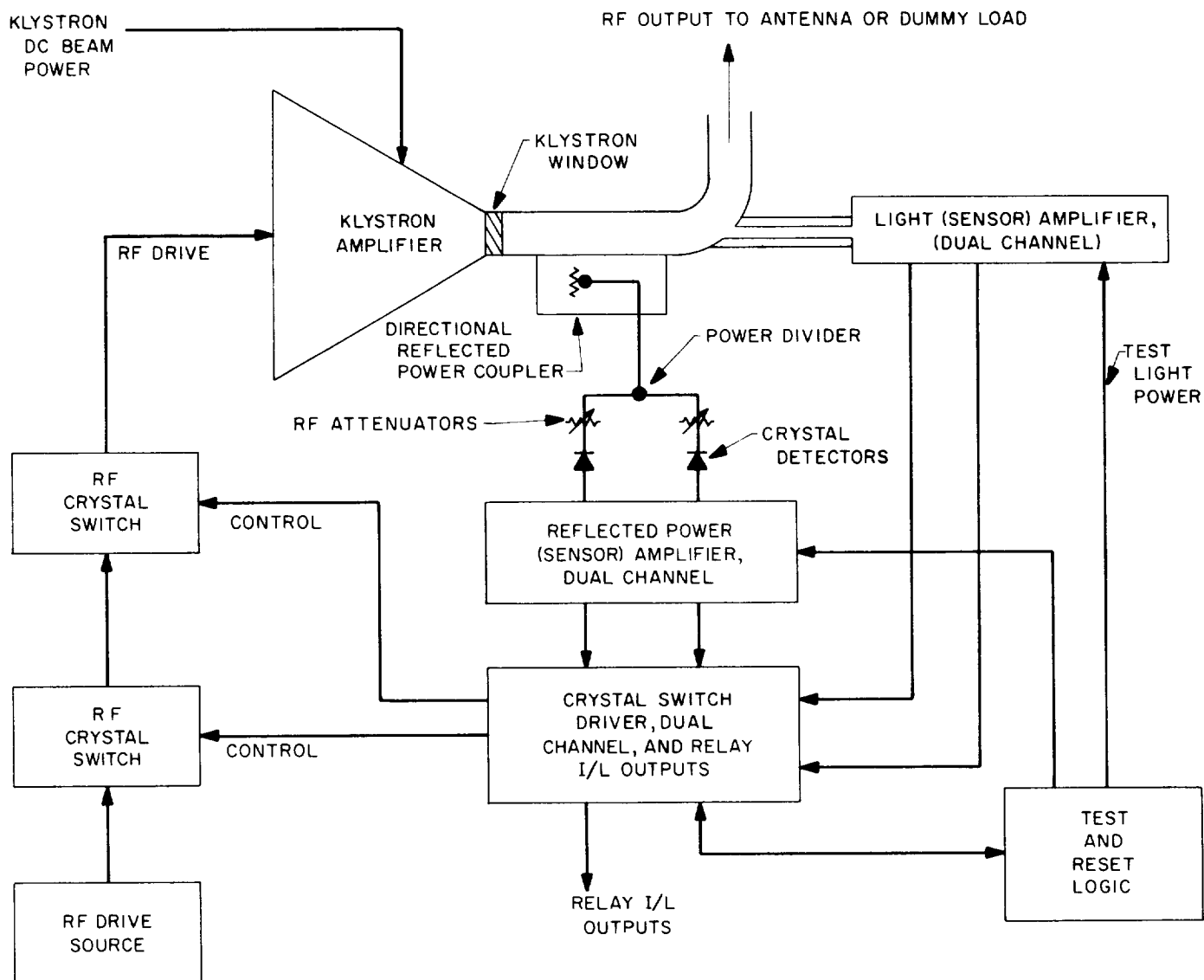
Fig. 11. Arc-detector block diagram, 450-kW transmitter

installed near the klystron. The directional coupler's output is rectified by a crystal detector, and the output dc voltage is sensed by a reflected power amplifier (a voltage comparator). If the reflected power exceeds a predetermined value, the reflected power amplifier sends a signal to the switch driver that turns off the crystal switch. The output RF power is turned off, and the arc is extinguished.

Power supply interlocks. As an added safety device, a slower-acting relay interlock circuit in the crystal switch driver is used to remove the klystron beam power through the associated klystron power supply equipment.

Test and reset logic. In addition to the sensing and control functions of an AD, it is desirable to have a self-testing circuit to ensure that the AD is operative before dc power is applied to the klystron. Malfunction of the AD could mean a loss of an expensive klystron.

Response times. The time duration between the initiation of an arc and the turn-off of the RF drive is referred to as "response time." The maximum allowable response time of an AD is specified by the klystron manufacturer; in general, response times diminish as power levels increase and as waveguide sizes get smaller. The S- and L-band 10-kW klystrons may require response times in the order of a millisecond, while some 100-kW to 250-kW X-band klystrons may have requirements of a few microseconds. Response times, as specified by the manufacturers, can be considered conservative since the manufacturers are reluctant to perform destructive testing to determine the absolute maximum allowable response time. The 450-kW klystron has a maximum response time requirement of 1 ms, unusual for a klystron of such high power rating.

d. Design features. In order to provide fail-safe operation, the 450-kW transmitter AD provides redundant operation through dual-channel operations where failure of a single channel could otherwise jeopardize the safety of the klystron. The AD provides two independent channels of reflective power monitoring, two channels of light sensing, and two crystal switch outputs for driving two cascaded crystal switches.

The portion of the AD mounted in the instrumentation cabinet of the transmitter cabinet consists of two separate chassis, described as follows:

Power supply chassis (PSC). The PSC (see Fig. 12) contains two regulated 50 V dc, 0.6 A power supplies.
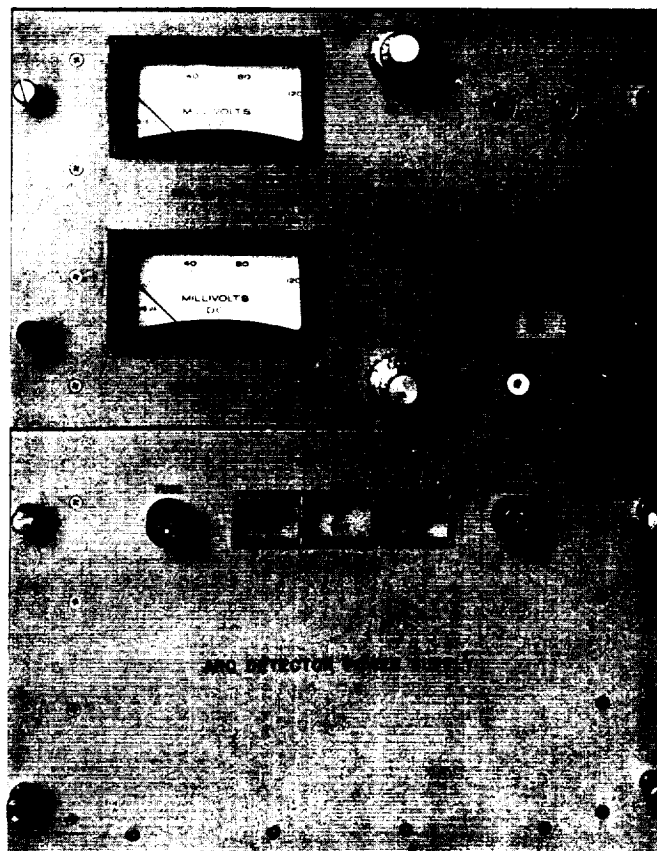
Fig. 12. Arc detector control and power supply chassis

These supply ±50 V to all control circuits, amplifiers, and indicator lights in the PSC and the control chassis.

Control chassis (CC). The CC (see Fig. 12) houses the following components:

(1) RF power divider.

(2) Two RF level set attenuators.

(3) 55°C oven housing two HP 420A RF crystal detectors.

(4) Dual-channel reflective power amplifier.

(5) Dual crystal switch driver.

(6) Test and reset logic circuit.

Reflective power components. Items (1) through (4), listed above, are part of the reflective power-sensing circuit (see Fig. 13). The RF attenuators, adjustable from the front of the CC, determine at which reflected power level the unit will be actuated. The RF crystal detectors, mounted inside a constant temperature oven, provide a dc output level for the reflected power amplifier; the detectors are mounted in a 55°C oven to improve temperature stability of the detector outputs.
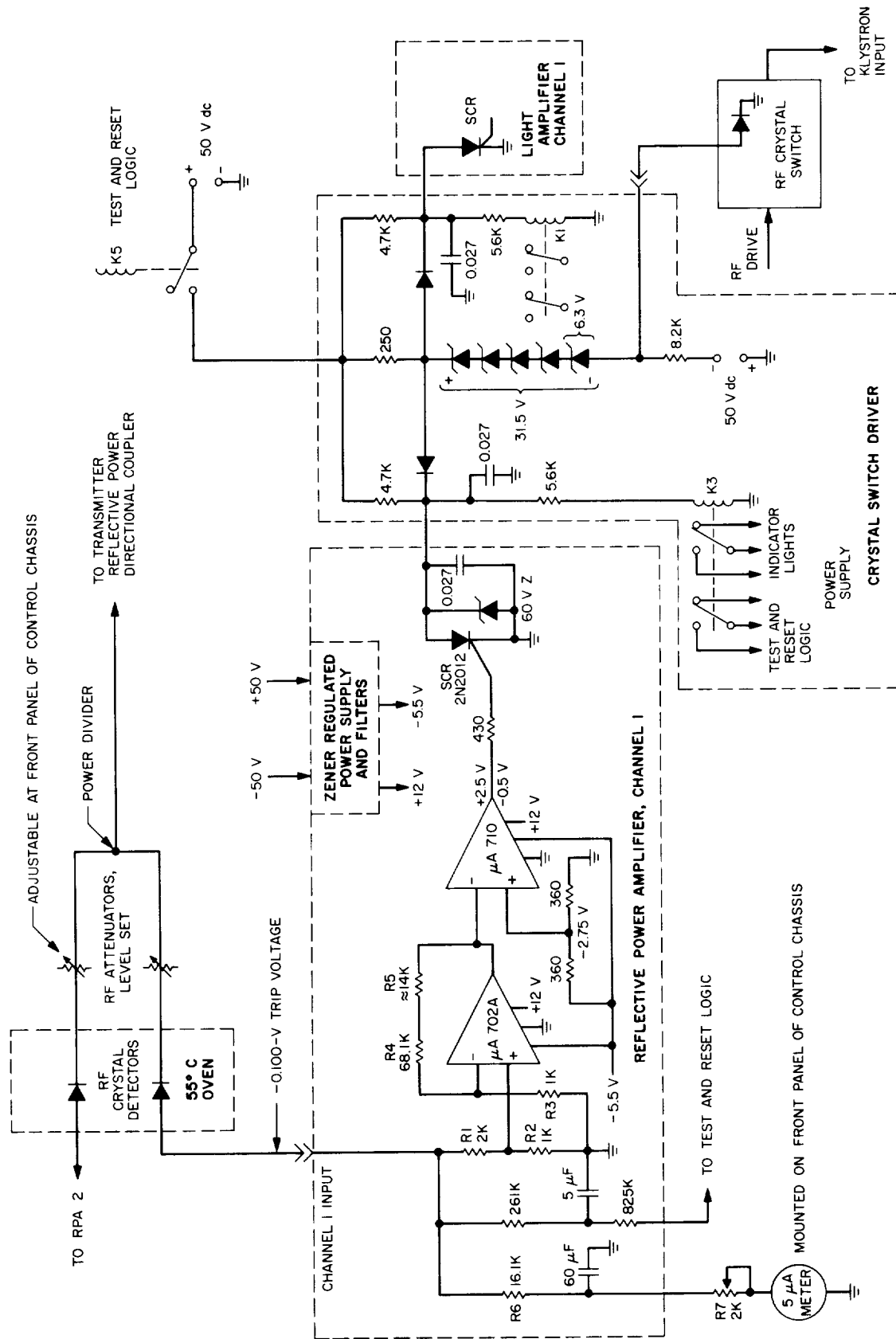
Fig. 13. RPA and switch driver

Reflective power amplifier module. Each channel of the dual-channel reflective power amplifier (RPA) module utilizes a μA702A operational amplifier microcircuit, a μA710 voltage comparator and a 2N2012 SCR. Circuit operation is as follows: The negative output of the crystal detector is amplified by a non-inverting amplifier formed by the μA702A and R1 through R5. When the μA710's inverting input goes more negative than the −2.75 V reference at the non-inverting input (equivalent to 0.100 V out of the RF crystal detector), the output of the μA710 changes from a saturated −0.5 V to a saturated +2.5 V. The silicon controlled rectifier (SCR) is thus triggered into conduction, the switch driver is actuated, and the RF drive to the klystron is turned off. The RPA circuit uses two 5 μA meters on the CC to monitor both RPA channel crystal detector voltages.

RPA temperature tests. The prototype RPA module was temperature-cycled from 130 to 0°F and from 160 to 0°F in an environmental chamber. A variable voltage source was used at the input of each channel to "fire" the SCR. The relative firing voltage versus temperature is shown in Fig. 14. The specific cause of the non-tracking of the curves is not known—probably a permanent change in a component at 160°F. Firing voltages did not vary more than ±3% over the entire 160°F range.

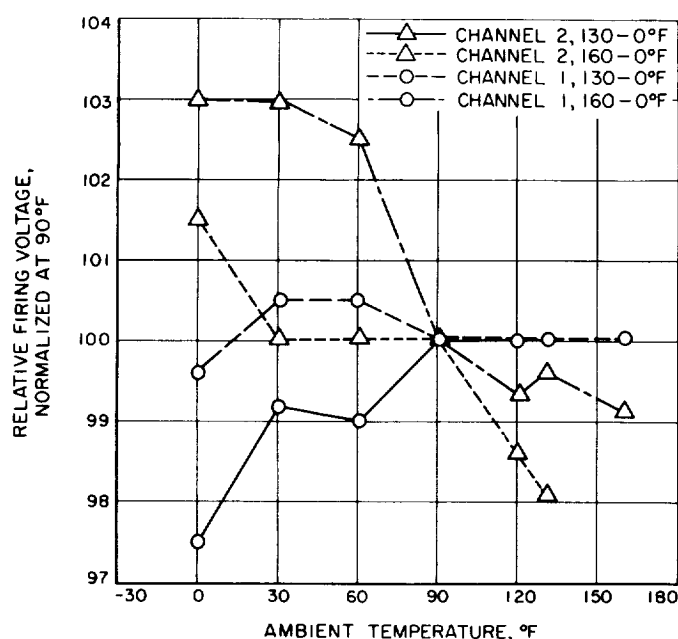*RPA response time.* The response time of the RPA is defined as the time interval between a step voltage at the input and the 10% point of the decay of the SCR cathode-anode voltage. The listing below shows the response time of the prototype RPA as a function of overdrive. A pulse generator with a 10K-Ω output impedance was used for the test. Response time has arbitrarily been defined at 110% of the dc threshold voltage since response time is a function of overdrive for any voltage comparator device. The response times are listed below:

RPA Firing voltages, % of threshold (0.100 V)	Response time, μs	
	Channel 1	Channel 2
105	4.0	2.4
110	3.5	1.8
120	3.3	1.7

Crystal switch driver (see Fig. 13): The AD contains two crystal switch drivers, one for each RF crystal switch. Each driver is actuated by a diode *or* circuit, either from an RPA channel SCR or a light amplifier channel SCR. During normal transmitter operation, all the SCR's are nonconductive, and the RF crystal switch is biased *on* at about +50 mA by constant current source formed by the 250-Ω resistor and 31.5-V zener chain. When an arc occurs, one or both of the SCR's are fired, the positive (+) end of the zener chain is grounded, and the RF crystal switch is biased *off* at −31.5 V. The *on* and *off* biases can be altered by changing the values of the 250-Ω resistor and zener voltages.

In addition to supplying bias voltages to the RF crystal switch, the device also senses when a particular SCR has been fired by the dc energization of a relay (e.g., K3). The relay provides outputs for the klystron power supply interlocks and outputs for the test and reset logic, discussed later.

Test and reset logic. The test and reset logic (TRL) ensures that the AD is functioning normally. Before the start of every transmitter run, and after any channel fires during a transmitter run, the TRL must be activated before dc power can be applied to the klystron. The TRL (see Fig. 15) performs the following sequential operations to ensure proper operation and safety of the klystrons:

(1) Reset (momentarily remove all voltages from all channels' SCRs) all SCRs that may have been fired.

(2) Send test voltages (−50 V) to both channels of the reflected power amplifier and to a test lamp in

Fig. 14. RPA firing voltage versus temperature
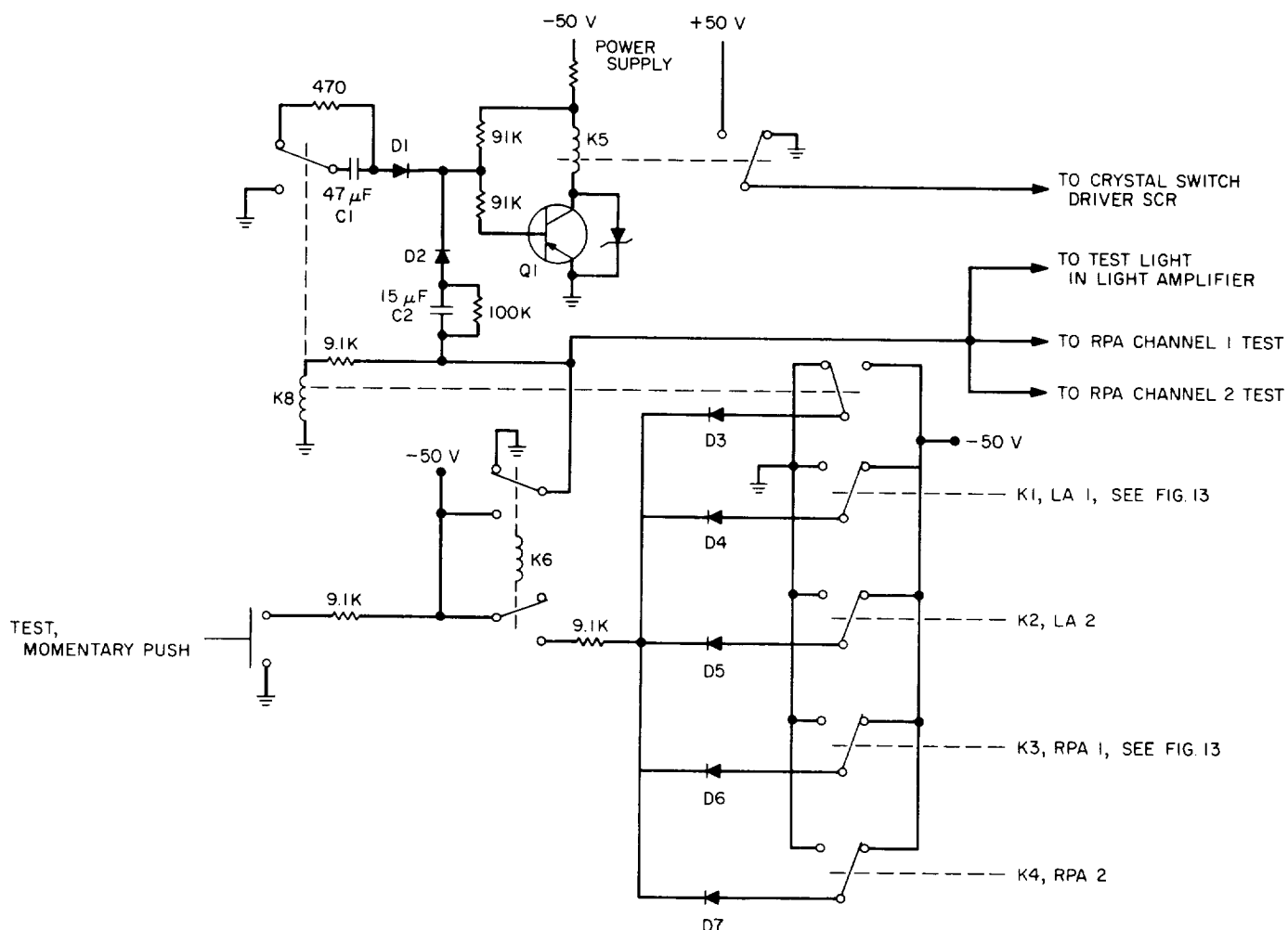
Fig. 15. Test and reset logic simplified

the light amplifier. The test voltages will fire all channels of a properly functioning AD.

(3) Perform a logic *and* operation to ensure that all channels have fired.

(4) Reset all SCRs and restore the AD to a ready state if, and only if, Step (3) was successfully performed. Otherwise, the test cycle will stop and the AD will not reset.

Light sensor. The light sensor presently being used on the 450-kW transmitter is a unit that was formerly used on a 100-kW S-band klystron transmitter; the light sensor was modified to make it compatible with the subject AD. Although it has protected the klystron, it is subject to false firing due to thermal drift and electrical transients. A new dual-channel light sensor using microcircuits is under development and will be discussed in a later report.

Over-all response time. The over-all response time of the RPA monitor circuit is defined as the time interval between an RF step input into the RF power divider and the point at which 90% of the negative voltage (-31.5 V) is reached at the output of the crystal switch driver. The over-all response times are listed below:

Amplitude of RF step impulse relative to threshold firing amplitude, %	Response time, μs	
	Channel 1	Channel 2
105	11.0	10.0
110	10.5	9.5
120	10.0	9.0

Thermal drift. The entire AD unit (excluding light sensor amplifier) was cycled through a 0° to 130°F

temperature range with constant temperature oven operating. The RF power level required to actuate the unit versus temperature is shown in Fig. 16. The RF attenuators were so adjusted that a nominal 10 mW of RF power was required at the power divider input to fire the RPA channels.

Fail-safe power supply operation. The AD provides fail-safe operation in case of power supply failure. Loss of the +50 V dc power supply de-energizes K1 and K3 (see Fig. 13), which actuate the interlock that turns off the klystron beam power supply. Failure of the −50 V dc power supply de-energizes K5 (see Figs. 13 and 15) which, in turn, de-energizes K1 and K3.
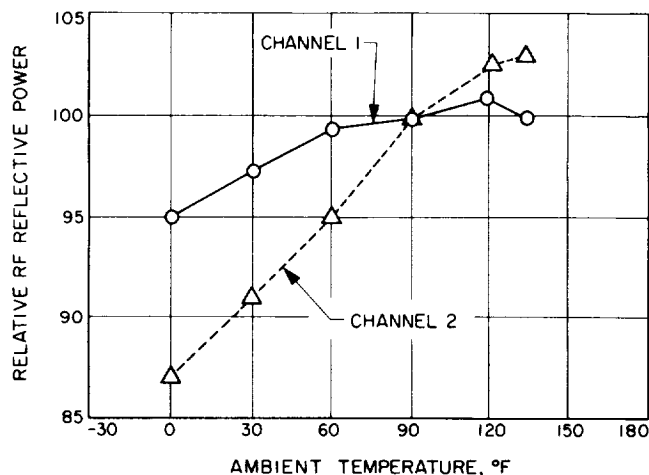

Fig. 16. Thermal drift of arc detector reflective power circuit

3. Characteristics of 20-kW Klystron, *R. C. Chernoff*

The bandwidth and saturated gain of the 5K70SG klystron have been measured for both 10 kW and 20 kW RF output. This klystron is used in the dual 20-kW transmitter subsystem in which it serves as the final amplifier for both DSN and MSFN missions. The klystron power output required for MSFN missions is 20 kW (a 10-kW carrier is radiated and another 10 kW is lost in the hybrid load), while the maximum output power presently specified for DSN missions is 10 kW. The specified bandwidth is 2100 to 2110 MHz for MSFN operation and 2110 to 2118 MHz for DSN. It was known from previous measurements that the saturated 1.0-dB bandwidth of the 5K70SG is greater than 18.0 MHz at 18.0 kV (corresponding to 20-kW output at band center), but there was some question, due to the different power levels required, whether the 5K70SG could adequately

cover the MSFN band plus the DSN band, i.e., 2100 to 2118 MHz, without retuning. While frequency agility is not a specified requirement of the transmitter subsystem at present, it is obviously desirable to elminate the necessity for retuning the klystron whenever the system is switched from DSN to MSFN status and vice versa. The measurements described in this article show that retuning is unnecessary when the 5K70SG klystron is correctly tuned, provided that certain assumptions as to UHF buffer amplifier characteristics and klystron input circuit losses are fulfilled.

The klystron was tuned according to the standard procedure.[1] In order, however, to emphasize the upper (DSN) part of the 2100- to 2118-MHz band, the band center was set at 2112.5 MHz instead of the normal 2110 MHz; i.e., the cavity settings prescribed in the standard procedure were each raised 2.5 MHz to give the following set of cavity resonant frequencies:

Cavity No.	Resonant frequency, MHz
1	2108.0
2	2108.0
3	2121.0
4	2137.5
5	2112.5

The output and saturation drive power were then measured at each point bandpass, again using the standard procedure. The measurement was made, without any change in klystron tuning, at both 20- and 10-kW levels. This point-by-point method, while more laborious than the swept-frequency bandpass measurement, is necessary in order to measure the variation of saturated gain over the bandpass. The resulting bandwidth, which is always larger than the swept-frequency bandwidth, is more realistic from the point of view of most DSIF operations since the transmitter drive power can be adjusted for saturation at the particular DSN or MSFN transmit frequency of interest.

The 10- and 20-kW bandpasses are shown in Fig. 17. These curves show: (1) that the 1.0-dB 20-kW bandpass covers both the MSFN and DSN bands (2100 to 2118 MHz) with 1.0 W maximum drive power, and (2) that the 1.0-dB 10-kW bandpass covers the DSN band (2110 to 2118 MHz) with 0.70 W maximum drive power.

---

[1]*Transmitter Subsystem Technical Manual,* TM-00204, Para. 5–9 (JPL internal document).
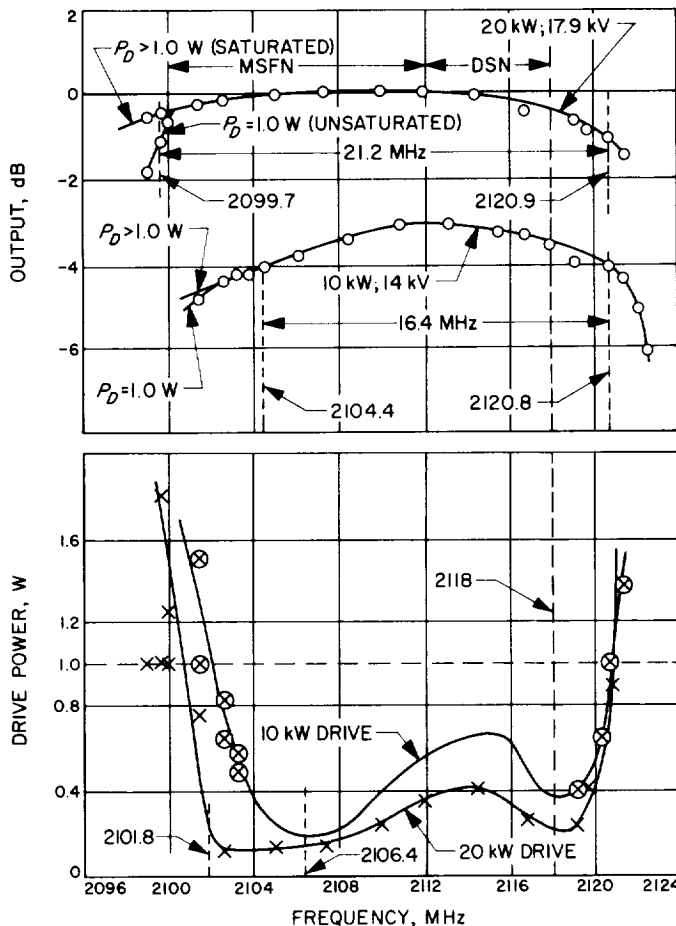
Fig. 17. Output and drive power, 5K70SG klystron

The curves also show that the average saturation drive for the 10-kW output is considerably higher than that for the 20-kW output. It appears that the Block IIIC version of the UHF buffer amplifier should be capable of saturating the klystron at either power level. This conclusion should, however, be checked by measurements at all stations at which the Block IIIC has been installed, since the drive power actually delivered to the klystron varies widely due to non-uniformity in transmission line and other losses between the UHF buffer amplifier and the klystron input.

The bandpass in Fig. 17 is adequate for transmission of at least the upper (2106.4 MHz) MSFN carrier. However, the lower MSFN carrier (2101.8 MHz) falls in a region where the saturated gain is changing rapidly. Whether this would adversely affect system performance is not clear at this time. If so, the bandpass could be translated approximately 2.0 MHz lower to place the 2101.8 MHz carrier in a "flat" part of the drive curve. Since the upper edge of the 10-kW bandpass curve in

Fig. 17 is at 2120.8 MHz, the downward-shifted band-pass should still cover the DSN band up to 2118 MHz.

4. A 10-MHz IF Distribution Amplifier, *J. H. Wilcher*

a. Introduction. A new 10-MHz IF distribution amplifier was developed to provide the receiver/exciter subsystem with the capability of operating with up to four multiple mission telemetry subcarrier demodulator assemblies. The new distribution amplifier design incorporates the additional required outputs. It also has a greater dynamic operating range and lower noise figure than the existing distribution amplifier design.

b. Performance requirements. Performance specifications established for the 10-MHz IF signal distribution amplifier are:

Center frequency:	10MHz (nominal)
Noise figure:	< 6 dB
Gain:	15.0 ±0.5 dB
3-dB bandwidth:	±5.5 MHz (minimum)
Gain linearity:	±0.5 dB for output levels between −15 and +10 dBmW
Input and output impedance:	$50 \pm 20 + j_o \pm 20 \ \Omega$

c. Circuit description. The 10-MHz IF signal distribution amplifier consists of four transistor stages, as shown in Fig. 18. A 10-MHz input signal, applied to connector J1, is coupled to linear amplifier Q1 through transformer T1. The amplifier provides a signal gain of approximately 28 dB. Transformer T1 provides an impedance transformation from the required 50-Ω input to the Q1 input impedance. The amplified signal is applied through emitter–follower Q2 to the output driver stage consisting of Q3 and Q4. The output driver is coupled through transformer T2 and the 3-dB attenuator section to the eight-way power divider to the output connectors J2 through J9. Transformer T2 and the 3-dB attenuator section are to transform the output impedance of the driver section to 50 Ω and maintain a relatively flat resistive output impedance over the 3-dB bandwidth. The eight-way power divider (a magnetic hybrid unit) provides a minimum of 30-dB isolation between outputs with a loss of 7 dB and phase difference between outputs of less than 3 deg over a temperature range of 0 to 49°C.
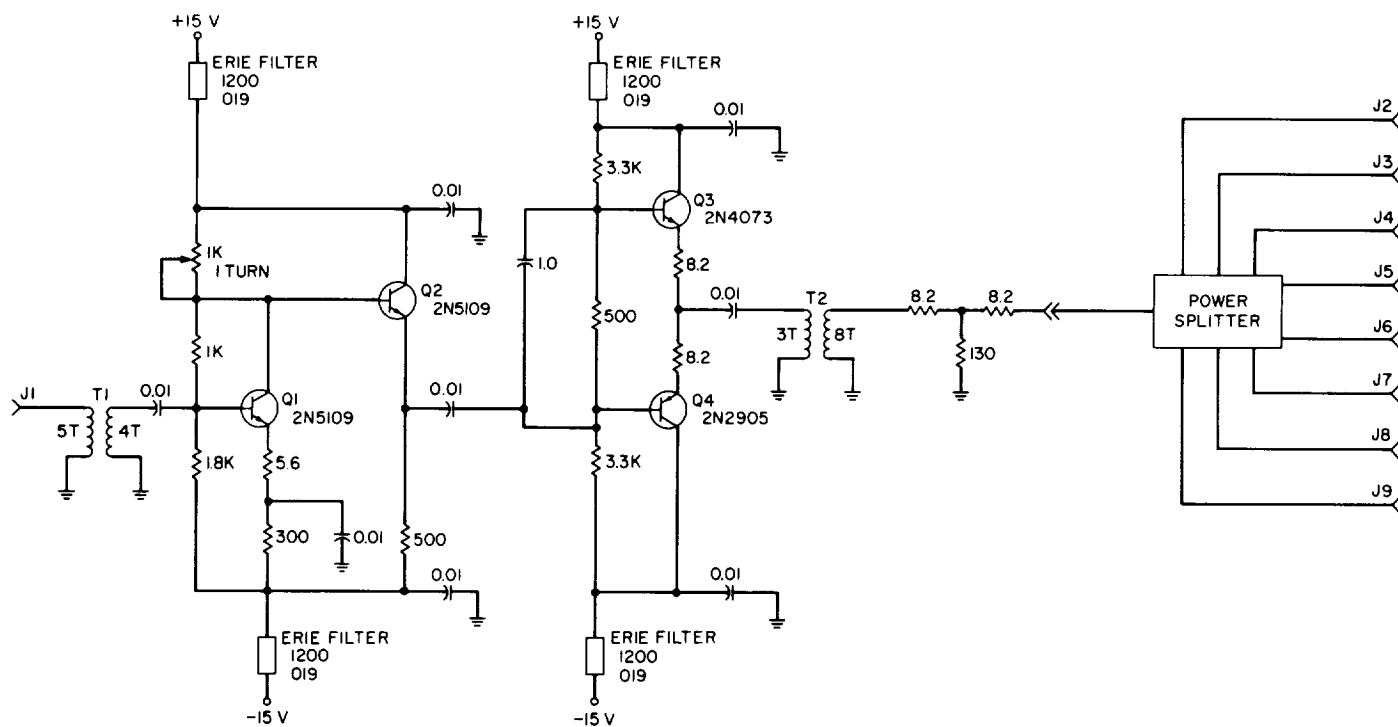
Fig. 18. Schematic diagram of 10-MHz IF distribution amplifier
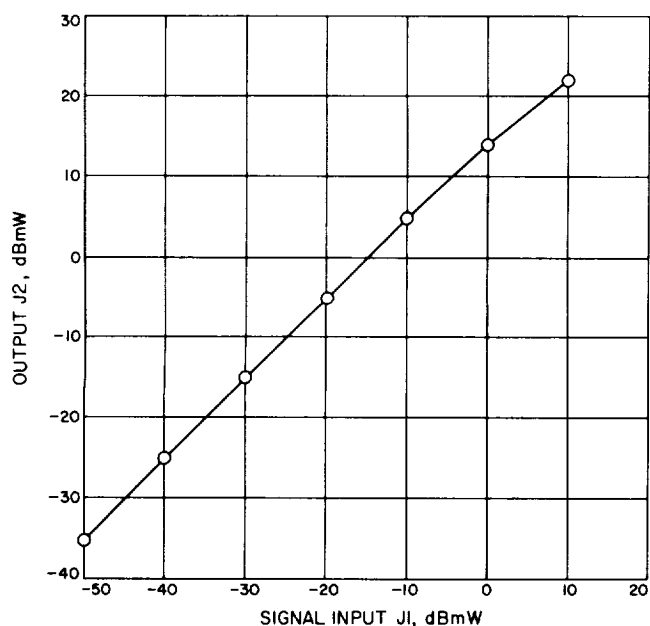
d. Test results. The results of tests conducted on the engineering prototype are compiled in Tables 5 and 6 and Fig. 19.

Fig. 19. Test results of 10-MHz IF signal distribution amplifier

Table 5. Performance as a function of temperature, J1–J2

Performance factor	0°C	25°C	49°C
Gain, dB	15.0	15.0	15.0
Phase shift, deg	101.0	99.8	100.0
Noise figure, dB	4.3	4.0	4.1

Table 6. Phase shift and isolation between indicated outputs

Performance factor	J2–J3	J3–J4	J4–J5	J5–J6	J6–J7	J7–J8	J8–J9
Phase shift, deg	−0.5	0	+0.1	−0.2	0	+0.3	+0.2
Isolation, dB	35.0	36.0	35.0	35.5	36.0	37.0	36.5

5. Signal Level Tracking Function and Receiving System Noise Temperature Calibration at Compatibility Test Area, N. C. Ham and R. W. Burt

a. Introduction. Two basic DSIF system configurations exist within the DSN that support a flight project. One configuration is used for tracking, data acquisition, and command purposes; the other is used for verifying compatibility of the flight telecommunication systems with the DSIF systems prior to the actual flight. Compatibility Test Area 21 (CTA 21) located at JPL is typical of the latter configuration.

Both configurations must necessarily have similar DSIF system functions characteristics, e.g., the telemetry, command, doppler, ranging, and signal level tracking functions. A series of engineering test descriptions has been devised to verify that each system function performs within specified limits as dictated by theoretical model studies. The method used for the DSIF system high-rate telemetry function test is presented in SPS 37-49, Vol. II, pp. 123–126. This article presents another system test by describing the method and results of the tests performed on the signal level tracking function and system noise temperature calibration at CTA 21.

b. Technique for testing signal level tracking function and receiving system noise temperature. The signal level tracking function and receiving system noise temperature calibration at CTA 21 was performed using a prototype signal level/system noise temperature measurement assembly. The theory, development, and use of this equipment have been reported in SPS 37-35, Vol. III, pp. 58–62, SPS 37-48, Vol. II, pp. 54–57, and Ref. 1.

The test technique for accurate signal level calibration consists of three steps. First, the system noise temperature is measured using the Y-factor technique in the usual manner employed in the DSIF. Next, the DSIF receiver automatic gain control (AGC) curve (signal level versus AGC voltage) is obtained using a calibrated test signal source, again in the usual manner. Finally, three or four signal levels are accurately measured using the Y-factor technique; the average of these is used to determine a correction factor for the AGC curve.

The Y-factor technique basically consists of accurate measurements of the signal-to-noise ratio (SNR) at three or four signal levels. The accurately known value for the system noise temperature is used to determine noise power in a known bandwidth from the relationship $P_N = kT_sB$ and to compute the signal power from the

SNR. A discussion of the errors involved is included at the end of this article.

c. Methods of measurement. Using the equipment configuration shown in Fig. 20, system noise temperature and signal level are measured as follows:

System noise temperature T_N is the sum of the ambient load temperature, RF component noise temperature, and receiver noise temperature, referenced to the receiver input. The receiver noise temperature contribution T_R referenced to the receiver input may be determined by (1) alternately connecting two well-matched temperature sources T_N (nitrogen RF load) and T_O (ambient RF load) to the preamplifier input, and (2) measuring the additional attenuation (Y-factor) that must be introduced with the precision attenuator A2 to obtain the same power indication with the hotter source as with the colder source. Since the system noise temperature is also referenced to the receiver input,

$$T_N = T_0 + T_R \tag{1}$$

where

$$T_R = \frac{T_0 - T_N Y_{on}}{Y_{on} - 1}$$

with Y_{on} representing the measured system noise temperature Y-factor.

This technique for determining the system noise temperature is the standard procedure used within the DSIF, where the preamplifier utilizes a traveling-wave maser (TWM) and the known temperature sources are greater than the TWM temperature. The situation is different at CTA 21, where a transistor preamplifier is used and the known temperature sources are lower than the preamplifier's temperature, resulting in a low Y-factor value as can be seen by examining the above equation. Speculation arose as to whether this technique would produce valid and repeatable determination of the system noise temperature. The results have borne out that this technique is valid and has application within the DSIF for accurately determining the system noise temperature for operational purposes.

Various received power levels P_{si} (referenced to the receiver input) are first injected into the receiving subsystem and the resultant AGC voltage is tabulated using a calibrated test signal source, from strong signal levels to a level approaching threshold. The accuracy of this
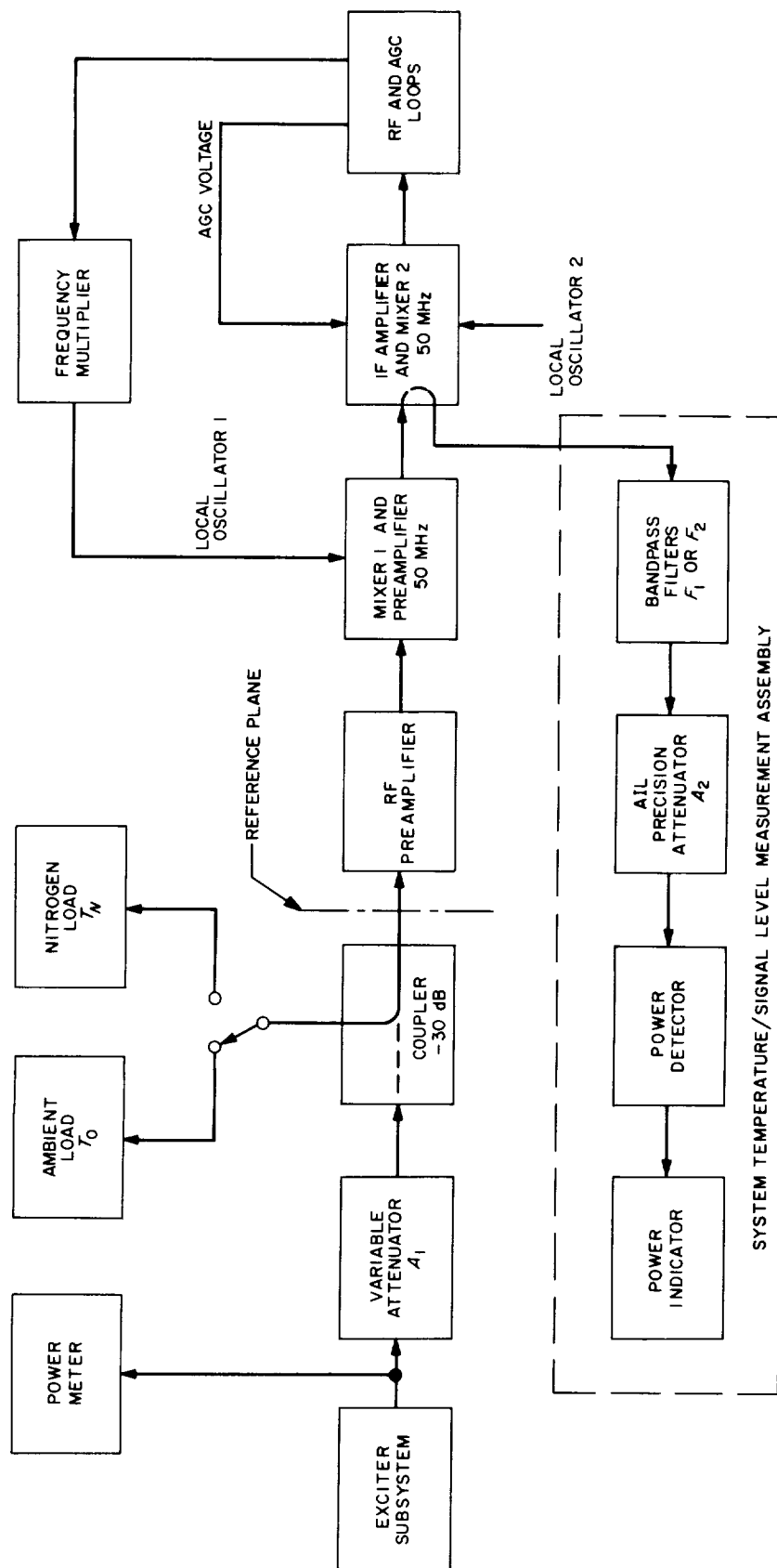
Fig. 20. System noise temperature and signal level measurement equipment configuration

calibration method is dependent upon the accuracy of the insertion loss between the RF attenuator A1 and the receiver input reference point, the accuracy of the attenuator A1, and the accuracy of the power level measurement of the test signal source. However, to improve the overall accuracy, the absolute value of the received power is calibrated directly at the reference plane by the Y-factor method, which does not depend on the insertion loss and power level measurement or on the RF attenuator calibration. The measured quantity is, instead, the additional attenuation that must be removed with the precision attenuator when the test signal is injected to obtain the same power indication as when the measured receiver power is from the ambient load only. This Y-factor measurement may be expressed by

$$P_{si}^* = (Y_{oc} - 1) kT_s F \qquad (2)$$

where

P_{si}^* = mean calibrated signal level (calibrated RF signal power referenced to the receiver input)

Y_{oc} = Y-factor measured for signal level calibration

F = filter bandwidth within which the Y-factor is measured

The range of received signal level for which this measurement may be performed is limited by receiver linearity at strong signals, loss of signal in the noise at low signal levels, the system noise temperature, and noise bandwidth of the filter F2. Thus, P_{si}^* is measured at three or four signal levels (or SNR), and the results are used to correct the curve of P_{si} versus AGC voltage.

d. Obtained results. System noise temperature and corrected AGC curves, measured at CTA 21 on 16 different days during January and February 1968, provided the measurement from which the data contained in Table 7 were derived. The average system noise temperature is $T_s = 1128.3°K$.

The Y-factors given were measured for three nominal signal levels. Table 8 gives the mean calibrated signal levels computed for each nominal signal level. Calibrated signal levels were found for each Y-factor from Eq. (2) and the mean and probable error ($\simeq 0.67\ \sigma$) found at each nominal signal level. The average correction factor from Table 8 is -1.18 dB.

Table 7. System noise temperatures and AGC Y-factors determined for the Compatibility Test Area

| Date, 1968 | T_s, °K | AGC Y-factors, dB | | |
| | | P_{si}, dBmW | | |
		−114.68	−119.44	−124.19
Feb 27	1162	12.32	8.06	4.45
Feb 23	1083	13.02	8.71	4.92
Feb 21	1094	12.55	8.28	4.58
Feb 16	1078	12.55	8.30	4.61
Feb 15	1088	12.56	7.95	4.41
Feb 13	1113	12.18	8.31	4.64
Feb 8	1118	12.69	7.54	4.13
Feb 6	1113	11.92	8.45	4.76
Feb 1	1162	11.79	7.50	3.99
Jan 31	1130	12.80	8.45	4.80
Jan 30	1123	12.43	8.06	4.52
Jan 29	1176	12.95	8.52	4.87
Jan 26	1176	12.67	8.33	4.49
Jan 25	1162	12.95	8.80	4.91
Jan 24	1162	12.95	8.49	4.83
Jan 22	1113	12.26	7.94	4.47

Table 8. Nominal and calibrated signal levels

Nominal signal level P_{si}, dBmW	Mean calibrated signal level P_{si}^*, dBmW	Correction factor, dB	Probable error, dB
−114.68	−115.84	−1.16	0.28
−119.44	−120.61	−1.17	0.30
−124.19	−125.41	−1.22	0.28

e. Error analysis. The accuracy of the mean calibrated signal levels given in Table 8 are estimated from an investigation of Eq. (2). Random and systematic errors involved are considered separately.

Random errors. The random errors consist of the stability of P_{si}^* and T_s, and the resettability of the power detector. The probable errors given in Table 8 will be assumed to adequately estimate these random errors, giving a worst-case random error of 1.5 dB (peak error is $\simeq 5$ times probable error).

Systematic errors. Systematic errors are introduced by the calibration of the attenuator A2 and filter bandwidth, and by the measurement of the system noise temperature.

The value of F, which is the average of four band-width measurements taken at CTA 21 using the method given in Ref. 1, was 9.867 kHz. Using this method, the peak error in F is $\simeq 0.045$ dB.

Attenuator A1 has an accuracy as given by the manufacturer of ± 0.05 dB per 10 dB. Since only a 10-dB range was used for the measurements, the worst-case error due to A1 will be taken as ± 0.05 dB.

System noise temperature is given by Eq. (1). Nitrogen temperature is given by

$$T_N = \frac{T'_N}{\alpha} + \left(\frac{\alpha - 1}{\alpha}\right) T_0 \qquad (3)$$

where

T'_N = manufacturer's specified value for the nitrogen load temperature

α = insertion loss from the jack into which the nitrogen termination is connected to the output jack of the 30-dB directional coupler just preceding the preamplifier (Fig. 20)

This insertion loss was measured at 0.25 ± 0.05 dB. The manufacturer's temperature of the nitrogen termination is listed as 80 $\pm 2°$K. Thus, for an ambient temperature of 290°K, $T_N = 91.8 \pm 4.2°$K; while for an ambient temperature of 300°K, $T_N = 92.3 \pm 4.3°$K.

The systematic error in T_S may now be found from

$$T_S(\pm \beta) = T_0(\pm \gamma) + \frac{T_0(\pm \gamma) - T_N(\pm \delta) Y_{on}(\pm \Delta)}{Y_{on}(\pm \Delta) - 1}$$

$$(4)$$

using $\delta = \pm 4.3°$K, $\Delta = \pm 1.015$, and assuming the value of T_0 used may have been in error by as much as 5°K. The systematic error in T_S could be as large as $\simeq \pm 0.5$ dB. Adding the random and systematic errors gives a total probable error of 0.42 dB. This value appears to be somewhat pessimistic in view of the results obtained.

Reference

1. Stelzried, C. T., and Reid, M. S., *Precision Power Measurements of Spacecraft CW Signal Level With Microwave Noise Standards*, Technical Report 32-1070. Jet Propulsion Laboratory, Pasadena, Calif. (Reprinted from *IEEE Trans. Instrum. Meas.*, Vol. IM-15, No. 4, pp. 318–324, Dec. 1966.)

6. Venus DSS Activities, E. B. Jackson, J. D. Campbell, M. A. Gregg, and A. L. Price

a. Experimentation. During the period February 16 through April 15, 1968, the 30-ft antenna at the Venus DSS continued to be used for transmission of time synchronization signals at 8.45 GHz and for radiometric observations of the planet Venus and other objects at 23 GHz. The 85-ft antenna, still undergoing modifications, was not in tracking status during this period.

The time synchronization transmissions are again being received by all three stations: the National Bureau of Standards (Boulder, Colo.), the Pioneer DSS, and the Tidbinbilla DSS. The system is working well, and the network is being extended to other DSN stations.

The monostatic planetary radar experiment (SPS 37-49, Vol. II, pp. 132–133) operating on the Mars 210-ft antenna was terminated on March 5 with the installation of the ultra cone on the 210-ft antenna. This cone does not have a 2388-MHz transmitting capability, although reception at this frequency can be accomplished. Prior to termination, the one-way range to Venus had increased to 216×10^6 km on March 5.

The 23-GHz observations of Venus, made with a dual-horn radiometer (SPS 37-48, Vol. II, pp. 150–154), are being made in an effort to detect and measure the water vapor content in the Venusian atmosphere.

b. System performance

Receiving systems. During this period the 8448- to 30-MHz converter was used intermittently as an output and modulation monitor for the time synchronization transmitter.

R&D transmitter (450 kW) system. This system has been used for testing the modified feed (SPS 37-50, Vol. II, pp. 165–166). Evaluation and modification for installation in the new antenna-mounted electronics room has continued.

X-band transmitter system. This system has operated for 26 time synchronization experiments.

c. System improvements

Receiving systems. The receiver module testing program is proceeding as time allows. Performance of one of the X-band receiver 455-kHz IF amplifiers was found

to be out of the specification limits. Upon visual examination of the internal components, a fungus-like substance was found on and around several electrical parts. Also, the module gold plating in the area of these components was found to be pitted and lifting from the base metal (Fig. 21). Tests are underway to determine the cause of this corrosion and its effect on module operation.

The Venus DSS 2388- to 30-MHz converter has been removed from the feed cone for performance measurement prior to the cone being installed on the 85-ft antenna.

A control panel for the X-band transmitter antenna/water load waveguide switch has been completed. This control panel enables this waveguide switch to be operated independently from the station waveguide switch controller with appropriate drive power interlocking being provided by the new control panel.

Transmitting systems. The following hardware installations and modifications were performed:

(1) A new pump controller was installed at the 1.2-MW heat exchanger to mate with the new transmitter control system.

(2) The new crowbar cabinet, with new cabinet interface junction box and high-voltage ignitron, was installed.

(3) The new cables to the control room, required by the new transmitter control system, were installed. Replacement and additional cables, including the new, very flexible, high-voltage (75-kV) cable, were installed in the antenna cable wrap-up. A redesigned, high-voltage junction box was installed in the antenna pedestal "teepee."
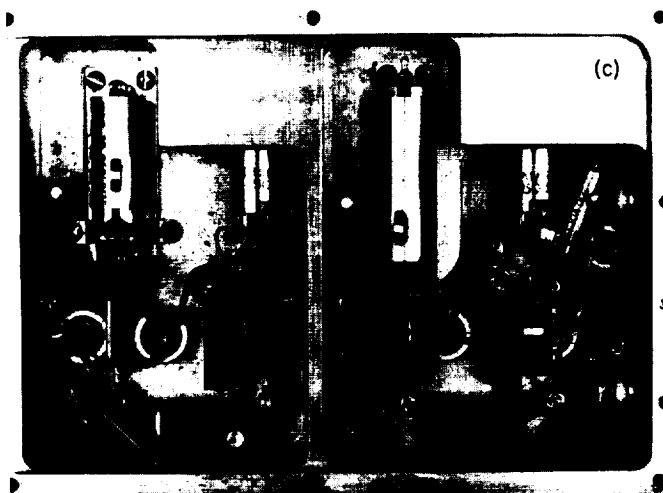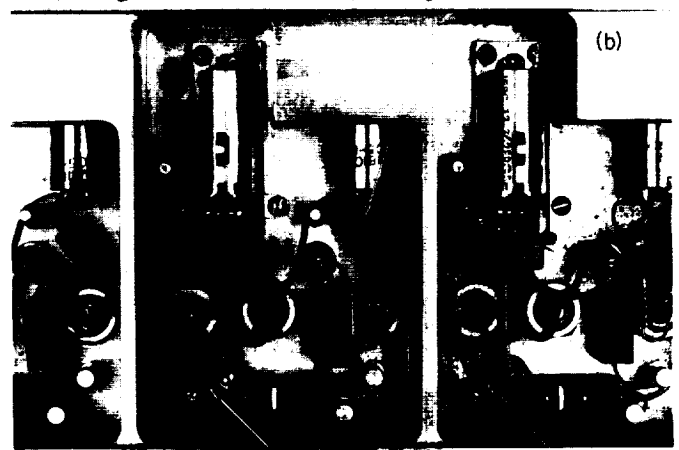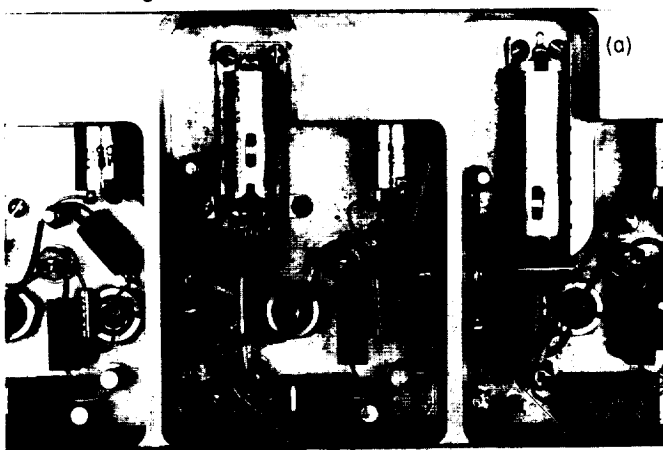

Fig. 21. Fungus growth and plating damage
in IF amplifier

(4) A new waveguide feedthrough for the transmitter cabinet was installed to mate with the new waveguide switch to be mounted in the antenna-mounted electronics room. This feedthrough will permit easier removal of the high-power waveguide coupler.

(5) The new series-resistor and modulating-anode cabinet was installed in the antenna-mounted electronics room.

(6) A new water load mounting panel and associated water plumbing has been installed in the electronics room.

(7) The transmitter's water plumbing was modified to permit easier access to the water fittings at the bottom of the 450-kW transmitter cabinet.

Fig. 22. 450-kW transmitter cabinet in place in electronics room, 85-ft antenna

(8) A new 500-kW motor–generator and associated controls were installed at the 30-ft antenna. This additional power system will enable higher (250-kW) X-band transmitter power.

Tests were run on the 450-kW transmitter to ensure that no harmful X-radiation was present at the klystron cabinet. Maximum X-ray levels measured were 5 mR/h. The transmitter was installed in the antenna room, and measurements were made of the deflection of the window of the klystron as the antenna moved in elevation. (Figure 22 illustrates the technique used for installation.)

Servo systems. The final surface panel alignment on the 85-ft az–el antenna is currently being done at night. Painting of the new electronics room and antenna structure is being done during the day. The modified azimuth "torque tube" has been replaced, and the azimuth angle indicating system is ready for alignment. Two new platforms have been added to the alidade structure athwart the elevation bearings. These platforms will support portions of the water-cooling system and permit easier maintenance on the elevation angle system. All antenna modifications, alignment, and equipment installation are expected to be completed in late April 1968. Approximately 1 wk will be required for servo response tests before scheduled operation can resume.

7. DSIF Station Control and Data Equipment, *E. Bonn, R. Flanders, A. Burke, J. Woo, D. Hersey, and P. Harrison*

a. Antenna pointing subsystem, Phase I. The antenna pointing subsystem, phase I (APS I), equipment is being installed in the DSSs to provide the capability of positioning the station antenna by computer control. Current activity includes the installation of APS I equipment at the Echo DSS concurrent with the station upgrade now under way. Installation of APS I involves (1) a retrofit of the SDS 910 computer previously used for the interim APS, (2) integration of the SDS 910 computer to the new APS interface rack, (3) performance of acceptance tests to ensure that equipment is operating correctly, (4) integration of the APS I into the station subsystem configuration, and (5) performance of the APS I system tests to ensure that APS I is functioning correctly with other subsystems.

Steps 1, 2, and 3 have been essentially completed, and installation is expected to be completed in early May 1968.

b. Digital instrumentation subsystem, Phase II. The digital instrumentation subsystem, Phase II (DIS II),

performs the function of system performance and status monitoring for each deep space station within the DSIF. The DIS II provides for the recording, display, and communication of configuration, status, and performance parameters, and the detection of nonstandard operating conditions for alarm generation.

The DIS II retrofit implementation progress is as follows:

(1) The first of six DIS II retrofit kits has been received at the Echo DSS and installation is currently in progress. Completion of this effort is expected in late April 1968. Receipt of subsequent retrofit kits is scheduled at approximately 3-wk intervals.

(2) The prototype DIS II has been assembled and is being used for checkout of the individual retrofit kits by the supplier.

(3) A preliminary acceptance test plan has been prepared and will be verified during final acceptance of the first retrofit kit installation.

Station line printers for all DIS II installations have been received; units required at overseas stations have been checked out and shipped. Delivery of system and subsystem cables is planned to coincide with the installation of the DIS II retrofit kit at each respective site.

The DSIF monitor system, Phase I, computer program is being prepared (SPS 37-50, Vol. II, pp. 181–185), with checkout scheduled to follow completion of the subsystem installation activities.

c. Telemetry and command processor, Phase II. The telemetry and command processor, Phase II (TCP II), provides the DSIF with a mission-independent telemetry and command processing capability for real-time operation. The TCP II is in the process of expansion (TCP II-C) to increase the telemetry data processing capability to support the DSIF multiple-mission telemetry system.

The installation of the TCP II-C equipment is proceeding at the various DSSs and at JPL Compatibility Test Area 21. The TCP II at the Pioneer DSS has been removed and the computers and magnetic tape units are being transferred to the Johannesburg DSS. Memory units on these computers have been expanded from an 8000- to a 16,000-word capacity. The TCP II-C provides the DSIF with the required capability to meet *Mariner* Mars 1969 requirements.

d. Station monitor and control console, Phase II. The Phase II station monitor and control console (SMCC) is an essential part of the DSIF Phase I monitor function. The Phase II SMCC has a countdown clock, an X–Y recorder, and the program alarm and control panel in addition to the existing displays in the Phase I SMCC.

These additions in conjunction with DIS II greatly enhance the monitoring capability of the SMCC. This article presents a description of the Phase II SMCC program alarm and control panel with its associated logic.

The purpose of the program alarm and control panel is to notify the console operator of DSN and DSIF alarms, and to display the subsystem that created the alarm. In addition, the program alarm and control panel has provisions for allowing the console operator to request printouts of parameters (monitored by the DIS) on the line printer and to indicate his concurrence or nonconcurrence with the panel indications.

To perform these functions, the program alarm system uses the standard DSIF digital logic modules, indicator lights, an audible alarm, and switches as shown in Fig. 23.

The DIS supplies to this logic two negative (true) signals when an out-of-tolerance condition is detected in one of the DSS subsystems. One of these, titled ALARM SET, causes the SYSTEM FAIL light to flash and the horn to sound repeatedly (1 s *on*, 1 s *off*). This alarm state is maintained until flip-flop A is reset by the operator using the ALARM RESET pushbutton on the control panel.

The other signal generated at the time of the DIS alarm signal causes one of the ten subsystem condition indicators to change from green to red. These indicators are illuminated green (good) with a zero-level signal supplied by the DIS and red (bad) with a negative (true) signal supplied by the DIS. These indicators are independent of the system fail logic and will at all times indicate whether the subsystem parameters are in or out of tolerance.

The program alarm and control panel contains a three-position toggle switch (CONCUR/NONCONCUR) with which the operator may cause a NONCONCUR signal to be sent to the DIS. The NONCONCUR signal is sustained if the switch is left in the *up* position and is present for 1 s if the switch is momentarily depressed. The presence of a positive (true) level at the output of *nand* gate G3C indicates to the DIS that the operator does not concur with one or more of the indications on the control panel. CONCUR and NONCONCUR lights are provided

Fig. 23. Program alarm and control logic
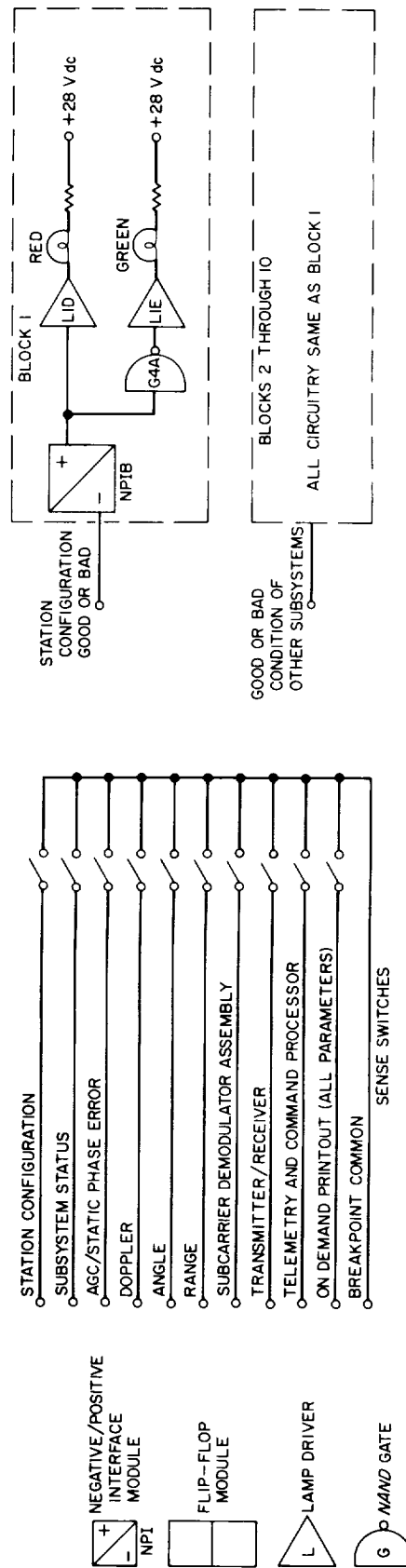
on the control panel to prevent the operator from inadvertently leaving the CONCUR/NONCONCUR switch in an unintended position and to allow verification that the NONCONCUR signals were generated by the logic circuits.

The console operator notifies the DIS that he wishes all parameters of one or more subsystems to be displayed on the line printer by closing one or more of the ten sense switches on the control panel. The DIS samples the position of these switches once each second and services the request on a priority basis.

e. Frequency and timing subsystem. The frequency and timing subsystem prototype construction has been completed. The evaluation is approximately 90% complete with results indicating the subsystem will fulfill all the requirements.

Contract negotiations are under way for the production of the five units required for *Mariner* Mars 1969. These will be prepared as modification kits, which are scheduled to be installed and be operational not later than September 1, 1968.

Frequency and timing subsystem, Phase II, is slated for design review during April 1968.

8. DSIF Monitor System Doppler Data, R. M. Thomas

a. Introduction. This article provides an expansion of the doppler-data discussion contained in SPS 37-50, Vol. II, p. 184, which states that proper analysis of doppler data requires detrending, blunder point detection, generation of a least-squares approximation, and mean and standard deviation computations.

A constant 1-min time interval between each sampling of doppler data is assumed. This sampling interval lends itself to the development of a sequence, namely, a doppler data sequence that is developed chronologically and can be put into one-to-one correspondence with time $(t_i$, where $i = 1, 2, \cdots, N)$. This actual doppler sequence in question would be written as

$$X_i \equiv X(t_i), \qquad i = 1, 2, \cdots, N$$

One must now develop a model for X_i. This model can then be compared to the sampled doppler sequence. The doppler model chosen to approximate X_i is defined as follows:

$$X_i = P_i + R_i, \qquad i = 1, 2, \cdots, N$$

where $P_i = P(t_i)$ is the mean value function evaluated at $t = t_i$ (in this case, the value of a least-squares polynomial fit to the data); P_i is sometimes called the *trend* of X_i and R_i is the fluctuation or residual series about the trend.

b. Detrending. Detrending refers to subtracting an estimated mean value sequence P_i from the actual (observed) doppler sequence X_i. It is necessary to estimate the trend and then eliminate the trend in a way so that the noise or residual series R_i can be estimated. The procedure for trend estimation and obtaining estimates of doppler noise consists of the following steps:

(1) Testing for blunder points and removal (or replacement) of same. (Bad data as indicated by the data condition code is handled the same as a blunder point.)

(2) Least-squares polynomial approximation of the doppler residuals R_i to estimate the trend. The approximating polynomial $Q(t)$ is the trend or mean value function of $R(t)$.

(3) Obtaining each noise estimate R'_i by subtracting the value of the polynomial $Q(i)$ (that approximates R_i) from R_i, i.e., $R'_i = R_i - Q(i)$.

It becomes clear that blunder points are removed and then the predicted doppler values are subtracted from the corresponding actual doppler values. This yields what is termed the residual R_i. It should be noted that R_i still contains some noise along with the error made in estimating the doppler value(s). Development of a blunder point detection table using J consecutive doppler residuals (usually $J = 5$) and consisting of the first J points of a noise estimate table is outlined in *Paragraphs d* and *e*. A least-squares polynomial approximation $P(t)$ is generated for the J doppler residuals. The first J points of the noise estimate table have been generated as noted above. However, there will be M points in the noise estimate table (M is normally 21).

Using the process outlined in *Paragraph e* (blunder point test and construction of noise estimate and blunder point tables), M points will be generated. A least-squares polynomial approximation $Q(t)$ is generated for these M points. Then the noise estimates R'_{i+j} are defined as

$$R'_{i+j} = R_{i+j} - Q_{i+j}, \qquad j = 0, 1, \cdots, M - 1 \quad (1)$$

The mean μ, detrended mean μ', and the standard deviation of the noise estimates σ' are computed as

$$\mu = \frac{1}{M} \sum_{j=0}^{M-1} R_{i+j} \qquad (2)$$

$$\mu' = \frac{1}{M} \sum_{j=0}^{M-1} R'_{i+j} \qquad (3)$$

$$\sigma' = \left[\frac{1}{M} \sum_{j=0}^{M-1} (R'_{i+j-M'})^2 \right]^{1/2} \qquad (4)$$

The total process is continuously repeated until the track (mission in question) is terminated.

c. Choice of parameters. Examination of *Paragraph d* (blunder point detection and noise estimation) reveals that six parameters govern the process of obtaining noise estimates and statistical data. These are:

J = number of points in the blunder point detection table

σ = input rejection sigma (what you estimate the noise superimposed on the doppler should be)

K = input (nominally set to 3)

M = number of points in the noise estimate table (maximum number)

N_1 = degree of the polynomial $P(t)$

N_2 = degree of the polynomial $Q(t)$

In practice, the choice of $J = 5$, $M = 21$, $N_1 = 1$, and $N_2 = 2$ yields optimum results.

d. Blunder point detection and noise estimations. Blunder point detection is defined as detecting an invalid doppler data sample and replacing it with an estimated value. For blunder point detection, use is made of J consecutive doppler residuals,

$$R_i, R_{i+1}, \cdots, R_{i+j-1} \qquad (5)$$

corresponding to the times $t_i, t_{i+1}, \cdots, t_{i+j-1}$. The Set of Points (5) is designated as a "blunder point detection table" and also consists of the first J points of a "noise estimate table." The definitions of these tables will be made clear in what follows.

e. Blunder point test and construction of noise estimate and blunder point tables

Step 1. A least-squares polynomial approximation is formed $P(t)$ to the set of J observed doppler residuals given by Set of Points (1), which are currently in the blunder point table. The value of $P(t)$ at $t = t_{i+j}$ is termed the predicted value of R at $t = t_{i+j}$.

Step 2. For given parameters K and σ if

$$| R_{i+j} - P_{i+j} | \leq K\sigma$$

R_i is replaced by R_{i+j} in the blunder point table and R_{i+j} is added to the noise estimate table. Otherwise,

$$| R_{i+j} - P_{i+j} | > K\sigma$$

so R_i is replaced by P_{i+j} in the blunder point table and P_{i+j} is added to the noise estimate table. (Detection of blunder points is indicated.)

Step 3. Steps 1 and 2 are repeated until the noise estimate table consists of M points, where M is a given integer assumed to be $> J$. The noise estimate table now consists of the M points (denoted by R_i).

$$R_i, R_{i+1}, \cdots, R_{i+M-1}, \qquad M > J \qquad (6)$$

Step 4. A least-squares polynomial approximation $Q(t)$ is formed to the set of M residuals given by Set of Points (6) that are currently in the noise estimate table. Noise estimates R'_{i+j} are obtained from Eq. (1). The "detrended" residuals R'_i are to be used for doppler noise estimates. The mean μ, detrended mean μ', and the standard deviation of the estimates R'_i are computed from Eqs. (2), (3), and (4), respectively. Steps 1 through 4 are then repeated.

D. DSN Project and System Development: High-Rate Telemetry Project

1. Introduction, R. C. Tausworthe

This article presents a report on the program of the high-rate telemetry (HRT) project for processing the *Mariner* Mars 1969 pictures. Tests made on Lab Set A in the demonstration verification laboratory, and subsequent tests and procedures in the compatibility test area (where interfacing with the spacecraft breadboard, proof-test model, and flight systems taken place) are described. Also presented are analyses of the effects of coherent subcarrier and symbol waveforms on the lock-in characteristic
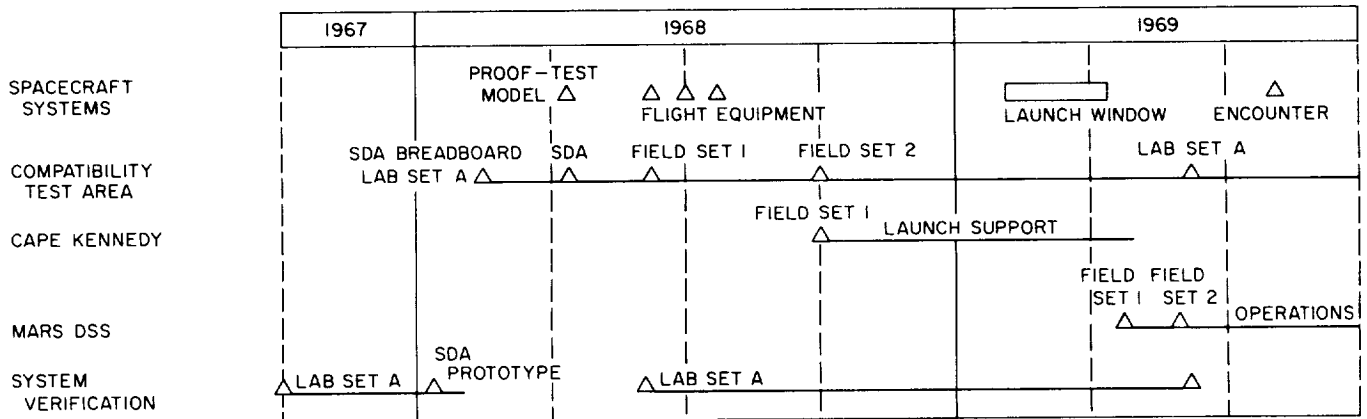
Fig. 24. High-rate telemetry project schedule

of the subcarrier demodulator assembly (SDA) and two different types of analyses of the symbol-tracking loop: one as the true sampled-data system that it is, and the other based on a continuous-time-parameter system which it closely approximates. Reports on the software development, cross-correlator, and test-code generator are also included.

This article shows that (1) the Lab Set and breadboard SDA perform as prescribed in their design within 0.1 dB, (2) schedules are being met for the cross-correlator field sets and GSDS SDAs, and (3) the software development is progressing accordingly. The schedule (Fig. 24) shows the deployment of the two field sets and Lab Set A to support spacecraft interfacing, launch, and encounter. The Compatibility Test Area has continuous support capability through encounter.

2. Demonstration System Verification Tests,

J. C. Springett and F. L. Larson

a. Introduction. As reported in SPS 37-48, Vol. II, p. 114, the primary object of this effort is to perform continuous tests on the high data rate (HDR) system, or portions of the system, as it evolves, in order to establish system performance relative to the parameters to be used in design control tables.

The prototype high-rate detector (Lab Set A) was available for testing by mid-October 1967. Somewhat prior to this time, the major portions of the demonstration system software had been delivered and were modified with respect to the SDS 930 computer[2] system. In addition, subroutines necessary to perform the experimental

[2]The system verification tests use the SDS 930 computer rather than the SDS 920 computer planned for operational use.

evaluation were written and incorporated into the demonstration software. By early November the detector and software were working sufficiently well so that preliminary testing could be started. These tests were conducted with all syncs and RF references hard-wired and noise-free. The results of initial testing showed that some minor problems existed in the software, as well as in the experimental signal and noise setup procedure. The greater portions of November and December were devoted to solving these problems.

The experimental data herein presented were gathered during the first three weeks of January 1968. Although the data should be considered preliminary, it is indicative of the performances of each of the major system elements prior to transfer of the equipment to the Compatibility Test Area. In particular, the results have shown that the detector itself, with all syncs hard-wired, performed as expected, while the performance of the symbol-tracking loop and subcarrier demodulation assembly (SDA) was

Table 9. Subsystem performance loss

Component	Loss (measured as departure from ideal), dB				
	ST_H/N_0				
	0.5	1.5	3.0	3.5	4.5
Lab Set A, hard-wired	0.1	0.15	0.1	0.0	0.1
Subcarrier demodulation assembly (phase DATA)	0.0	0.1	0.2	0.2	0.2
Symbol tracking loop (Lab Set A and SDS 930)	0.7	0.55	0.5	0.5	0.2
Sum of 1, 2, and 3	0.8	0.8	0.8	0.7	0.5
Measured degradation, total system	0.8	0.85	0.8	0.6	0.3

below nominal expectations. The latter initiated a few changes in these components during installation at the Compatibility Test Area.

b. Test summary. Preliminary testing of components of the HDR telemetry system was performed in four steps: (1) detector only, symbol sync hard-wired, (2) detector, symbol sync hard-wired, plus SDA, medium bandwidth, (3) detector plus symbol tracking loop, no SDA, and (4) the complete system. The performance loss attributed to each subsystem is summarized in Table 9, as well as the measured loss for the entire system.

The actual test data values are listed in Table 10. Plots of the data in Table 10 appear in Figs. 25, 26, and 27. The only major discrepancy in the measured data appears in lines 4 and 5 of Table 9, for high ST_B/N_0, wherein the number of data words per run was not high enough (due to available test time) to yield accurate results at $ST_B/N_0 = 4.5$ dB.

c. Test procedure.

Test calibration. Prior to performing the tests on the HDR components the signal-to-noise ratio produced by the radio-frequency test console (RFTC) was calibrated using a SNORE[3] computer program (SPS 37-27, Vol. IV, pp. 169–184). Also, a supplementary program was used

to remove the effect of ambient system noise, which was about 24 dB lower than the signal power actually registered by Lab Set A. The results of the calibration are
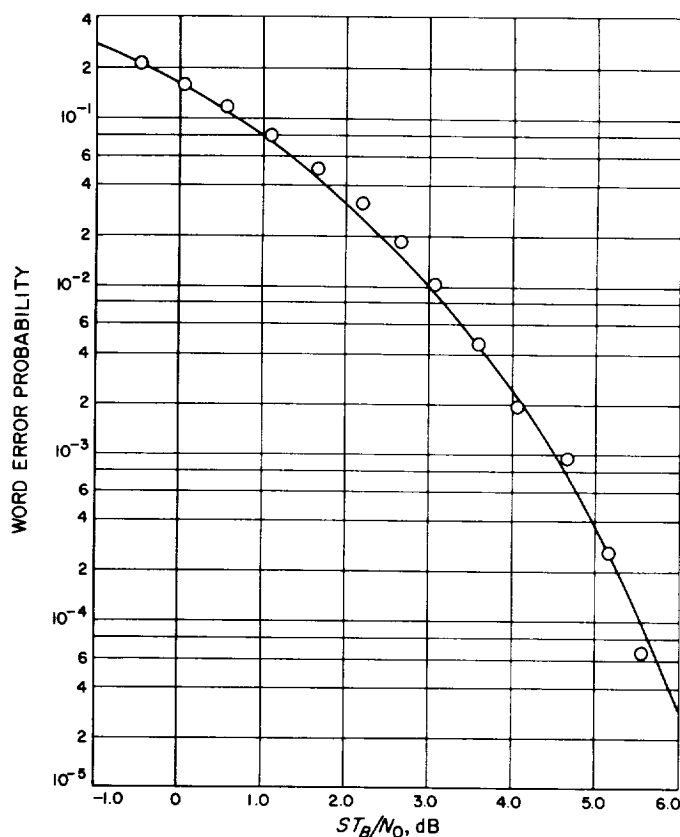
---

[3]Signal-to-noise-ratio estimator.

Fig. 25. Detector, symbol sync hard-wired

Table 10. Word error probability measurements

Nominal ST_B/N_0, dB	Detector only	Detector plus SDA, phase DATA	Detector plus SDA, phase DATA	Detector plus symbol loop	Complete system	Word-error probability
−0.5	2.10	2.04	2.45	—	3.20	$\times 10^{-1}$
0.0	1.60	1.60	1.95	—	2.57	$\times 10^{-1}$
0.5	1.18	1.22	1.52	1.88	1.94	$\times 10^{-1}$
1.0	8.13	8.79	11.14	—	14.6	$\times 10^{-2}$
1.5	5.23	5.89	7.92	9.32	10.1	$\times 10^{-2}$
2.0	3.28	3.79	5.34	—	6.93	$\times 10^{-2}$
2.5	1.88	2.31	3.43	3.59	4.61	$\times 10^{-2}$
3.0	1.02	1.29	2.06	—	2.61	$\times 10^{-2}$
3.5	4.74	6.48	11.1	9.90	11.4	$\times 10^{-3}$
4.0	1.99	3.05	5.69	—	4.63	$\times 10^{-3}$
4.5	8.41	12.28	24.0	19.2	17.2	$\times 10^{-4}$
5.0	2.62	5.13	11.2	—	7.3	$\times 10^{-4}$
5.5	6.6	10.0	24.7	16.4	16.2	$\times 10^{-5}$
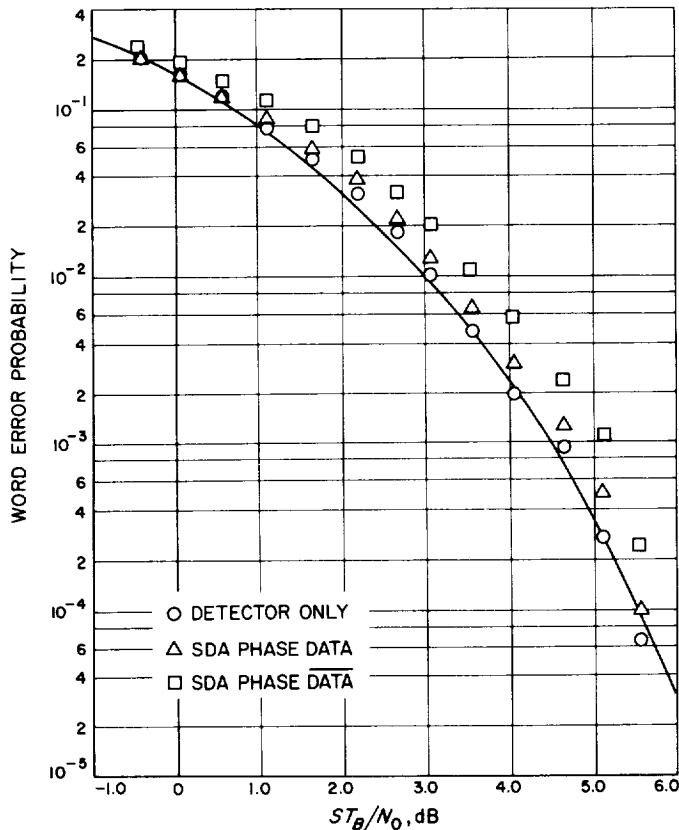
Fig. 26. Detector, symbol sync hard-wired, plus SDA
at medium-loop bandwidth

Fig. 27. Detector plus symbol tracking loop

listed in Table 11. The corrected SNORE reading is within
0.2 dB of the nominal ST_B/N_0 set by the RFTC signal
and noise attenuators.

Detector performance. Using the calibration discussed
above, a series of word-error runs was made using the
test setup of Fig. 28. The RFTC used the incoming sym-
bol stream to phase-modulate a 50-MHz subcarrier, sup-
pressing the carrier 3.0 dB. Gaussian noise was added,
and the resulting waveform was demodulated, yielding
a noisy baseband symbol stream which was filtered and
input to Lab Set A. The symbol sync for Lab Set A was
derived directly from the coder. The decoder packed
data word was input to the computer and was compared
to the true packed data word from the coder. The result-
ing number of word errors for a given run was then
displayed for recording.

A series of runs at 0.5-dB steps was performed using
the configuration of Fig. 28. The resulting measured per-
formance is plotted in Fig. 25. The average 0.1-dB degra-
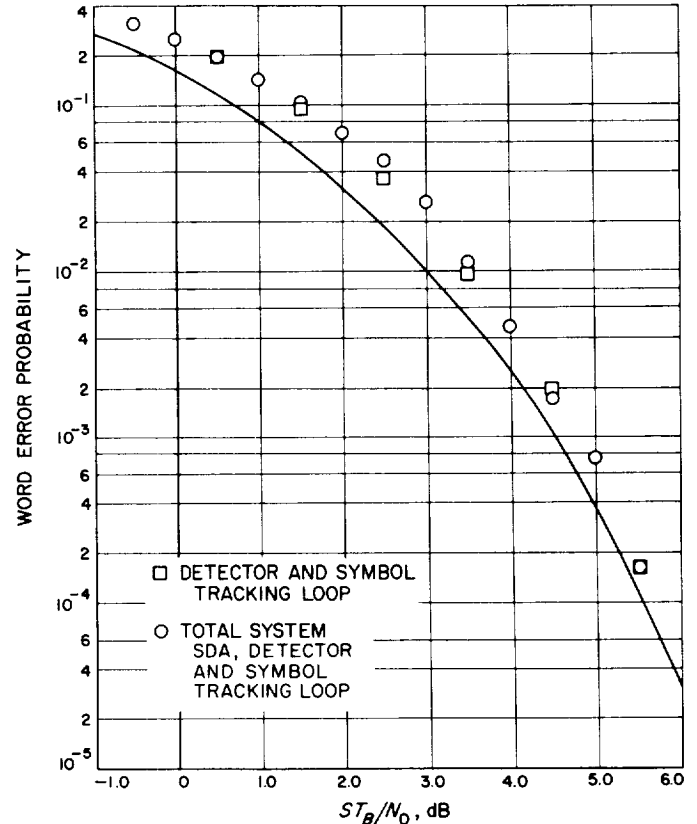dation from the ideal performance is attributed to Lab
Set A.

Table 11. High-rate baseband SNORE tests

| Nominal set-up ST_B/N_0 = 3.0 dB |
| Signal attenuation = 29.8 dB |
| Noise attenuation = 37.8 dB |
| Noiseless SNORE = 24.33 dB |

Noise attenuation	Nominal ST_B/N_0	SNORE ST_B/N_0	Corrected SNORE
40.3	5.5	5.51	5.57
39.8	5.0	5.08	5.13
39.3	4.5	4.60	4.65
38.8	4.0	4.00	4.04
38.3	3.5	3.53	3.57
37.8	3.0	3.03	3.06
37.3	2.5	2.64	2.67
36.8	2.0	2.16	2.19
36.3	1.5	1.63	1.65
35.8	1.0	1.08	1.10
35.3	0.5	0.55	0.57
34.8	0.0	0.05	0.07
34.3	−0.5	−0.46	−0.45

D DATA 16.2 kHz   **N** GAUSSIAN NOISE

D̂ DECODED DATA   **S** SYMBOLS, 86.4 kHz
ESTIMATE, 16.2 kHz

                            SS SYMBOL SYNC, 86.4 kHz
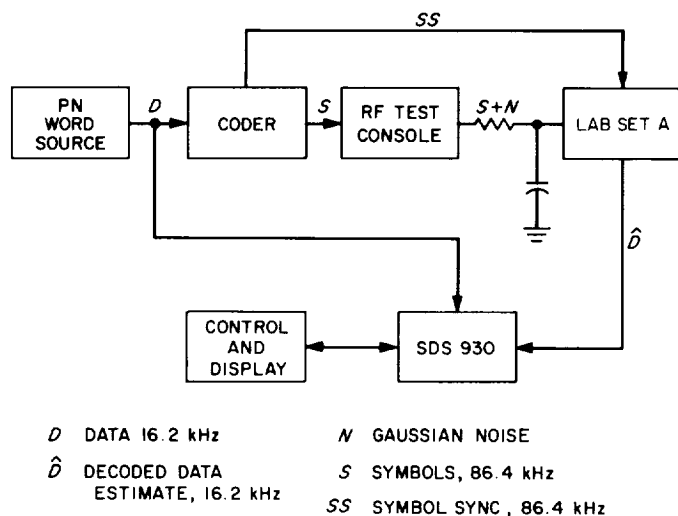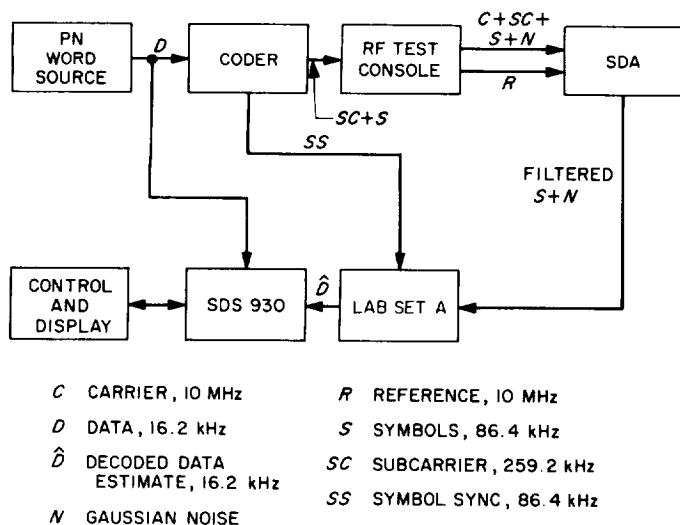
**Fig. 28. Test setup for measuring word-error
performance of the detector, Lab Set A,
with symbol sync hard-wired**

This basic word-error performance curve was used as a calibration check for the subsequent tests.

Subcarrier demodulation assembly. The next series of tests measured the performance of the subcarrier demodulation assembly. The test setup is indicated in Fig. 29. The results of these tests are illustrated in Fig. 26. Three sets of points are plotted. The first (indicated by zeros) is the baseband calibration check, using the setup of Fig. 28, run prior to the other tests. These points agree with the points plotted on Fig. 25.

C CARRIER, 10 MHz   **R** REFERENCE, 10 MHz

D DATA, 16.2 kHz   **S** SYMBOLS, 86.4 kHz

D̂ DECODED DATA   **SC** SUBCARRIER, 259.2 kHz
ESTIMATE, 16.2 kHz

                            SS SYMBOL SYNC, 86.4 kHz
N GAUSSIAN NOISE

**Fig. 29. Test setup for measuring word error
performance of the SDA**

Also plotted on Fig. 26 are two other sets of data, one indicated by triangles, and the other by squares. These two sets represent the performance of the system of Fig. 29 for the two possible subcarrier phases acquired by the SDA, arbitrarily termed "phase DATA" and "phase $\overline{\text{DATA}}$." As indicated in Fig. 26, the performance for the two phases differed by approximately 0.5 dB. Time did not permit a complete evaluation of this anomaly.

Both tests on the SDA were made at the SDA medium-loop bandwidth.

Symbol tracking loop. A series of runs was made to measure any degradation introduced by the noisy symbol reference in Lab Set A. The test setup of Fig. 28 was used, with the exception that the symbol tracking was done in closed loop between Lab Set A and the computer. The latest version of computer software as of January 20, 1968 was used for these tests. Also, the wideband filter constants rather than the nominal narrowband filter constants were used. (The symbol loop at that time was observed not to retain lock in the presence of noise when the narrow-band filter constants were used. Also, the loop exhibited very poor symbol acquisition, often requiring many program restarts before lock was acquired, for ST_R/N_0 below 3 dB).

The results of the symbol loop test at baseband (no subcarrier used) are plotted as squares on Fig. 27. The points fall approximately 0.5 dB from theory at $ST_R/N_0 = 3.0$ dB, and approximately 0.8 dB for lower SNR. Compared to the hard-wired case of Fig. 25 this represents a loss of from 0.5 to 0.7 dB due to the noisy symbol reference alone for ST_R/N_0 lower than 3.5 dB. Above 3.5 dB the points converge toward the ideal curve.

Total system. A total system test was conducted using a setup as shown in Fig. 29 except that the symbol loop was closed as in the symbol tracking loop tests above. Also, SDA phase DATA was used. The results of these tests are plotted as circles on Fig. 27. There was a close correspondence between the total system performance and that of the symbol tracking loop. Based on our tests, we concluded that the symbol loop at that time was the weak component in the system both with respect to acquisition and to tracking, and should be improved.

Also, steps should be taken to understand and correct the performance of the SDA for phase $\overline{\text{DATA}}$.

d. Laboratory breadboard. As previously reported (SPS 37-48, Vol. II, p. 123), a problem seemed to exist in the

laboratory breadboard when random data words were used. For the one SNR tested ($ST_B/N_0 = 5.0$ dB) the breadboard performed 0.37 dB better for a fixed data word than for random data words.

We have, in fact, discovered a marginal logic component which would tend to degrade the breadboard performance for random data. Since the data of Fig. 31 of SPS 37-48, Vol. II, p. 123 were obtained using random words, the curve can be considered pessimistic by an estimated 0.3 dB. However, the breadboard still performed worse than Lab Set A (Fig. 25, this article). No further effort is being made on the breadboard performance evaluation.

3. DSIF System Verification Tests, R. W. Burt

a. Introduction. The goal of this test was to demonstrate the performance characteristics of the DSIF high-rate telemetry function. The word error rate of the demodulated telemetry as a function of the RF input signal-to-noise ratio is used as the measure of performance. The measurement technique has been discussed previously (SPS 37-49, Vol. II, pp. 123–126). This report further details the test method and gives results obtained during installation and checkout of the prototype at the Compatibility Test Area. These results show that the design goal of less than 0.44-dB degradation at $ST_B/N_0 = 3$ dB was met during the tests. Also, it is shown that ST_B/N_0 may be set up with a worst-case error of 0.17 dB.

To exercise the entire high-rate telemetry function, the test signal is introduced at the S-band carrier frequency. The carrier is then converted to an intermediate frequency of 10 MHz by the receiver and is further processed by the telemetry demodulator assembly. The sideband modulation index of the S-band test signal is first adjusted for a specific sideband-to-carrier ratio. Then a

signal-to-noise energy per bit is determined which will produce a desired word error rate in the demodulated data. Next, the carrier-to-noise ratio is set to give the required sideband-to-noise energy ratio when modulation is applied. Finally, modulation is applied, and the performance of the high-rate telemetry function is judged by the word error rate of the output bit stream. The importance of accurately establishing signal-to-noise ratio and modulation index is discussed in the following paragraphs.

b. Bit error degradation. The output demodulated data error rate depends on four fundamental parameters which become evident when the simplified block diagram of the receiving system (Fig. 30) is examined. The general equation for effective sideband signal-to-noise ratio is

$$R = \frac{ST_B}{N_o} (l) (m) (n) (p) \qquad (1)$$

where

R = effective sideband signal-to-noise energy ratio per bit.

$\dfrac{ST_B}{N_0}$ = input sideband signal-to-noise energy ratio per bit required for the test.

l = degradation caused by inaccuracy in setting the carrier-to-noise energy ratio.

m = degradation caused by inaccuracy in setting the subcarrier modulation index.

n = degradation caused by the IF reference error.

p = degradation caused by phase errors in the telemetry demodulation assembly, including subcarrier reference error, bit synchronization error, and bit detection errors.
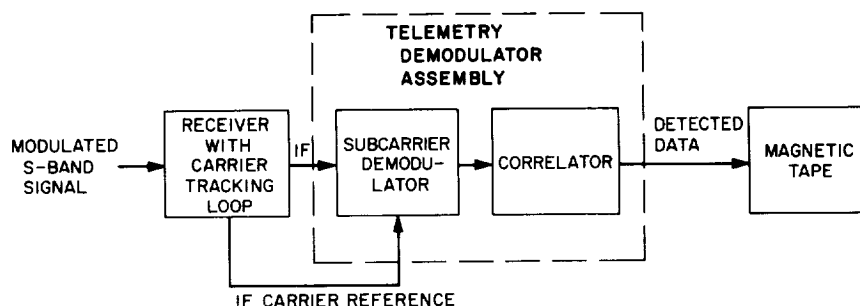

Fig. 30. DSIF high data rate telemetry system

The parameter p is determined during subsystem testing and has a design goal of 0.2 dB; n, a function of signal level and modulation index, is the result of signal processing between S-band and the telemetry demodulator assembly and has a design goal of 0.1 dB. A test accuracy goal has been established for each of the other two parameters. This goal is 0.1-dB maximum degradation when the probability of word error for the output bit stream is 0.01.

c. Test setup. Figure 31 is a block diagram of the test setup used at the Compatibility Test Area. The high-rate telemetry test set provides the telemetry subcarrier modulated with data. This is used to modulate a test translator. Attenuator A1 controls the subcarrier modulation index, and attenuator A2 controls the signal-to-noise ratio. The resulting S-band test signal is applied to the receiver and detector in the high-rate telemetry demodulator where the data error rate is measured. The S-band input signal-to-noise ratio is established at the receiver input by monitoring the heterodyne signal at 50 MHz using the system temperature/signal level measurement assembly. The use of this equipment in CW power calibration is described in Ref. 1. For the high-rate telemetry project, this equipment has been further developed to provide the means for precision signal-to-noise calibration at the Mars and Cape Kennedy DSSs and the Compatibility Test Area. The modulation index is set by observing the carrier suppression by using the HP 302 wave analyzer and the HP 355C attenuator, but the conventional method has been improved by substituting the attenuator accuracy for the wave analyzer dial calibration.

d. SNR measurement method. The technique used consists of accurately measuring the ratio of carrier-plus-noise power to noise power. First, the carrier-to-noise ratio necessary to give the required sideband-to-noise energy, when the carrier is modulated, is determined. Next, power indicator M1 is adjusted for full-scale deflection with the RF signal source off. Then, the desired ratio, or Y factor, less the dB bandwidth F is inserted in the precision attenuator A3, and, with the unmodulated signal source turned on, A2 is adjusted until the power level at M1 is returned to the same value. The measurement is expressed by

$$\frac{P_T \, G(f_0) + k \, T_0 \, F \, G(f_0)}{k \, T_0 \, F \, G(f_0)} = Y \tag{2}$$

Or

$$\frac{P_T}{k T_0 F} = Y - 1$$

where

$$P_T = \text{total RF power}$$

$$kT_0F = \text{noise power at the receiver input in the bandwidth } F$$

and

$$F = \int_0^\infty g(f) \, dB \tag{3}$$

where

$$g(f) = \frac{G(f)}{G(f_0)}$$

$$= \text{normalized gain response}$$

The accuracy of this measurement established the parameter l in Eq. (1) and is determined by the calibration accuracy of A3 and F, the stability of P_T and T_0, and the resettability of meter M1, assuming that response from S-band to the receiver 50-MHz output is flat across F so that $g(f)$ is only a function of the filter F.

e. Modulation index. Modulation index is adjusted by carrier suppression. With the receiver in manual gain control (MGC) and phase-locked to the incoming carrier at strong signal, a convenient level is set on the HP 302 wave analyzer. Attenuation equal to the desired carrier suppression is inserted in attenuator A4, and a reference level measured on the meter. A4 is then returned to its original setting, and modulation is applied until the reference level is again measured.

Figure 32 illustrates the manner in which the HP 302 wave analyzer records only the carrier. The 3-Hz bandpass filter excludes the modulated sidebands and all but a negligible amount of noise. Noise contribution to the error is negligible, however, since the carrier-to-noise power in this bandwidth is purposely set high during this measurement. The accuracy of this measurement established m in Eq. (1) and is determined by the calibration accuracy of A4, the resettability of the HP 302 and receiver linearity over the 8-dB measurement range.

f. Error investigation. The error in the measurement method can be established from an examination of Eq. (2). Modifying this equation slightly to account for modulation index gives

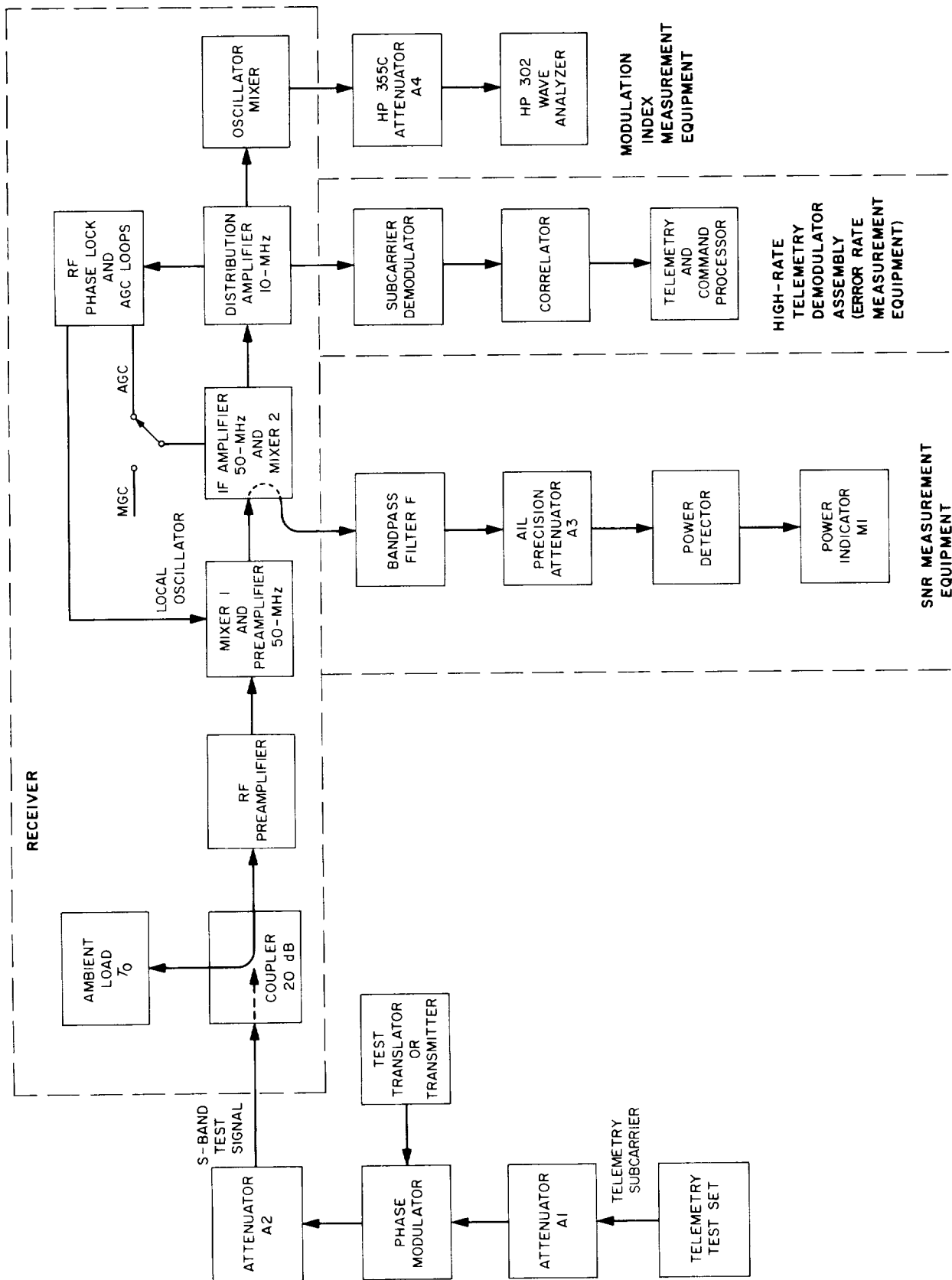$$\frac{M \, P_T(t)}{N_0} = (Y - 1) \, F \tag{4}$$

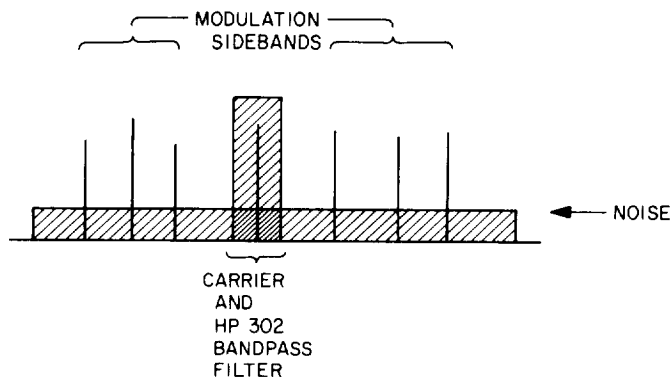Fig. 31. Block diagram of system verification test setup

Fig. 32. Wave analyzer observation of carrier

where

M = modulation correction factor

$P_T(t)$ = time variations in the RF power level

and

$$N_0 = k\,T_0$$

The errors in Eq. (4) are now considered individually:

Y Errors. The attenuator accuracy is ±0.05 dB per 10 dB. The meter resettability error is estimated as ±0.02 dB. This is based on repeatability observed in practice. Thus, the worst case error in Y is ±0.07 dB.

F Errors. The average of four bandwidth measurements taken at the Compatibility Test Area, using the method given in Ref. 1, was 9.867 kHz. Using this method, the peak error in F is ~0.05 dB.

M Errors. The error introduced due to receiver linearity over measurement range was measured and found to be negligible. Meter resettability is here assumed to introduce negligible error, since the measurement is performed at strong signal. Thus, the maximum error is due solely to the accuracy of attenuator A4, which is ±0.1 dB. The resulting worst-case error in sideband power is ±0.02 dB.

$P_T(t)$ Errors. To measure this, the equipment was set up as shown in Fig. 31 and, for a typical Y, the signal level at the output of meter M1 was monitored for 12 h with a chart recorder. The measured drift was no more than 0.03 dB in an hour, the approximate time required to run a bit error rate curve. Note that this includes exciter and receiver gain instabilities as well as instrumentation and temperature drifts.

The deviation due to l plus m in Eq. (1) is, therefore, 0.17 dB when the above errors are summed. Measured data indicates that this is a very pessimistic estimate.

Example: as an example of the method, consider the following: Suppose the test requirement is to set up a signal-to-noise ratio yielding a 1% word error rate. For this case

$$\frac{ST_B}{N_0} = 2$$

so that for

$$1/T_B = 16.2 \text{ kilobits}$$

$$\frac{S}{N_0} = 45.105 \text{ dB}$$

Also, assume square wave modulation with carrier suppression, given by

$$\frac{P_c}{P_T} = -8 \text{ dB}$$

where

P_c = carrier power at the receiver input

P_T = total signal power at the receiver input

and with modulation index specified by

$$\frac{S}{P_T} = -0.75 \text{ dB}$$

Note that the numbers closely approximate *Mariner* Mars 1969 requirements. Then, since

$$\frac{P_T}{P_n} = \frac{S/P_n}{S/P_T} = 45.855 \text{ dB}$$

the ratio required in the noise bandwidth F, for $F = 9.867$ kHz is 5.915 dB. Thus, the difference between signal-plus-noise and noise only to be set up with attenuator A3 is 6.89 dB. In practice, it is extremely difficult to set up ST_B/N_0 to some exact value. Instead, Y is set up to nearly the required value and measured several times to reduce resettability error. Then ST_B/N_0 is determined for the average Y measured. A computer program was written, giving ST_B/N_0 to the nearest 0.01 dB, and the results are used during the testing. A portion of the print-out is shown in Table 12.

Table 12. Y as a function of $\frac{ST_B}{N_0}$

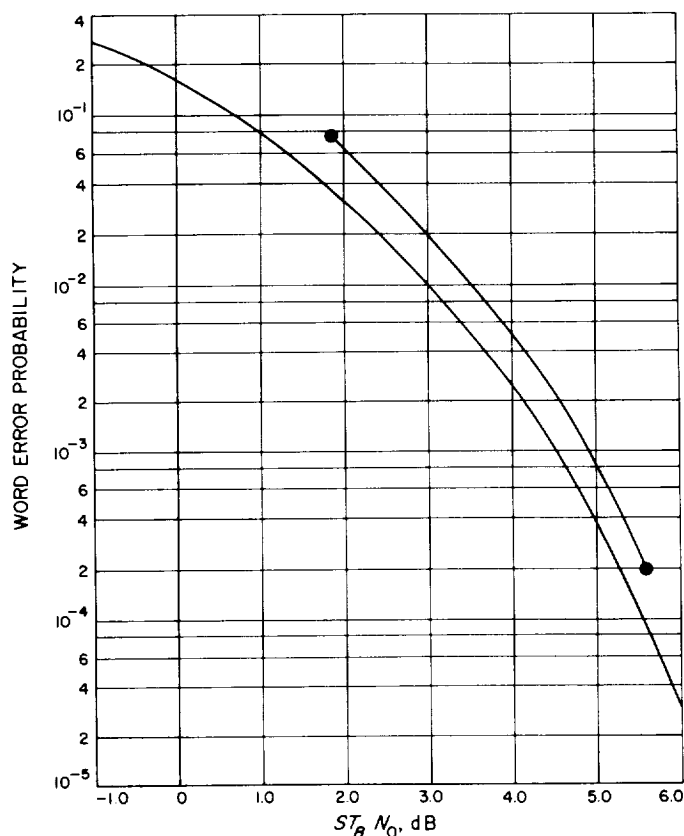| $\frac{ST_B}{N_0}$, dB	Y, dB									
	0.00	0.01	0.02	0.03	0.04	0.05	0.06	0.07	0.08	0.09
0.00	4.69	4.70	4.71	4.71	4.72	4.73	4.73	4.74	4.75	4.75
0.10	4.76	4.77	4.77	4.78	4.79	4.79	4.80	4.81	4.81	4.82
0.20	4.83	4.83	4.84	4.85	4.85	4.86	4.87	4.87	4.88	4.89
0.30	4.90	4.90	4.91	4.92	4.92	4.93	4.94	4.94	4.95	4.96
0.40	4.96	4.97	4.98	4.98	4.99	5.00	5.00	5.01	5.02	5.02
0.50	5.03	5.04	5.05	5.05	5.06	5.07	5.07	5.08	5.09	5.09
0.60	5.10	5.11	5.11	5.12	5.13	5.14	5.14	5.15	5.16	5.16
0.70	5.17	5.18	5.18	5.19	5.20	5.20	5.21	5.22	5.23	5.23
0.80	5.24	5.25	5.25	5.26	5.27	5.27	5.28	5.29	5.30	5.30
0.90	5.31	5.32	5.32	5.33	5.34	5.35	5.35	5.36	5.37	5.37
1.00	5.38	5.39	5.40	5.40	5.41	5.42	5.42	5.43	5.44	5.45

Rate: 16,200 bits/s
Frequency: 9.867 kHz

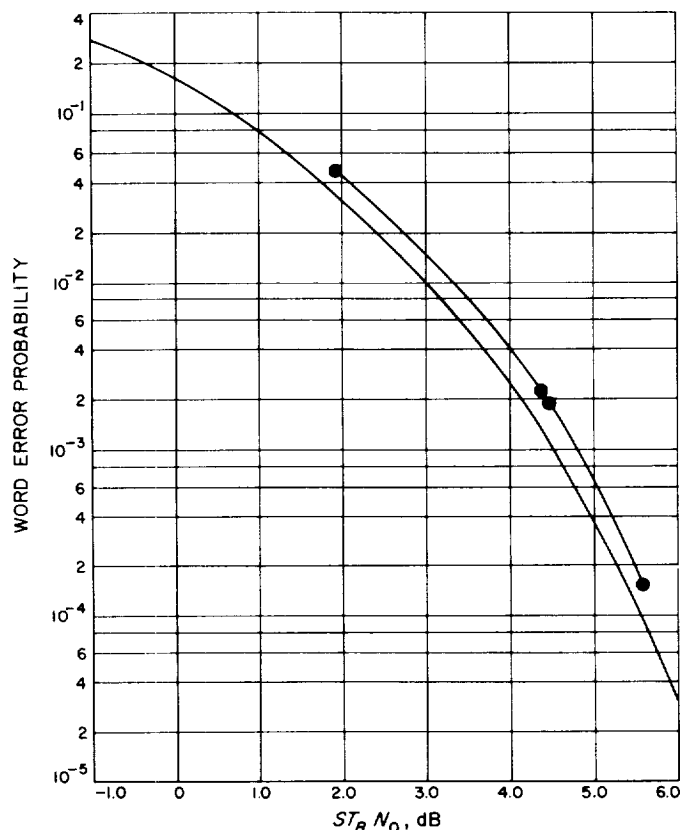**Fig. 34. HRT system test results, SDA time constant optimum**

Fig. 33. HRT system test results, SDA time constant nonoptimum

g. Results. High-rate telemetry system tests were run at the Compatibility Test Area on February 17, 19, and 20, 1968. Typical results are shown in Figs. 33 and 34. Test results for Fig. 33 were obtained using a nonoptimum time constant in the subcarrier demodulator, while the optimum $(T = T_{sym}/6)$ was used for the test reported in Fig. 34. For the optimum filter, the system design goal of less than 0.44-dB degradation at $ST_B/N_0 = 3$ dB was met (Fig. 34). Also notable is smoothness of the measured data curves. This is due in part to the excellent repeatability obtainable in setting up ST_B/N_0.

Reference

1. Stelzried, C. T., and Reid, M. S., *Precision Power Measurements of Spacecraft CW Signal Level With Microwave Noise Standard*, Technical Report 32-1070, Jet Propulsion Laboratory, Pasadena, Calif., (reprinted from *IEEE Trans. on Instrum. Meas.*, Vol. 1M-15, No. 4, pp. 318–324, December 1966).

4. Analysis of Coherent Subcarrier Demodulation,

R. W. Burt

a. Introduction. An analysis of the high-rate telemetry (HRT) coherent subcarrier demodulation was motivated

by the need to determine the loop filter time constant required to give zero static phase error. An exact expression for the expected value of the error voltage as a function of loop phase delay is developed and solved by computer for various loop filter time constants and signal-to-noise ratios. It is shown that the desired time constant yields zero phase offset at strong signal and minimum phase offset at minimum operating conditions. The signal suppression factors for the exact expression and the approximate model developed by Brockman (SPS 37-46, Vol. III, p. 197, Fig. 16) are then compared.
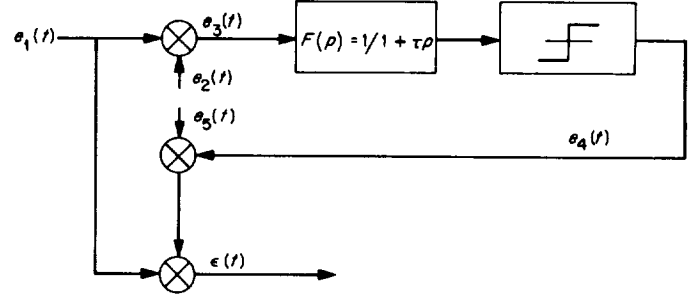
b. Analysis. A block diagram of the HRT subcarrier demodulation function is shown in Fig. 35. The input signal $e_1(t)$ is a square wave subcarrier at frequency ω_{sc}, biphase-modulated with data $(D(t))$:

$$e_1(t) = A\, D(t)\, \text{Cos}\, \omega_{sc}t + n(t) \tag{1}$$

where

$$D(t) = \pm 1$$

$n(t)$ = demodulator input noise waveform which is assumed gaussian with 0 mean, and a one-sided spectral density of N_0.

Fig. 35. HRT subcarrier demodulator functional block diagram

The input signal is multiplied by an in-phase subcarrier $e_2(t)$:

$$e_2(t) = \text{Cos}\,[\omega_{sc}t + \phi(t)] \tag{2}$$

where $\phi(t)$ = phase difference between the input signal and the loop estimate.

Multiplying the input signal by the subcarrier estimate gives $e_3(t)$.

$$e_3(t) = A\, D(t)\, \text{Cos}\, \omega_{sc}t\, \text{Cos}\,[\omega_{sc}t + \phi(t)] + n(t)\, \text{Cos}\,[\omega_{sc}t + \phi(t)] \tag{3}$$

After filtering and limiting, $e_3(t)$ becomes the data estimate $e_4(t)$.

$$e_4(t) = \hat{D}(t) = \text{sgn}\, \{F(p)[A\, D(t)\, \text{Cos}\, \omega_{sc}t\, \text{Cos}\,[\omega_{sc}t + \phi(t)] + n(t)\, \text{Cos}\,[\omega_{sc}t + \phi(t)]]\} \tag{4}$$

where sgn { • } designates the algebraic sign of the limiter output. The data estimate $e_4(t)$ is multiplied by the subcarrier shifted 90 deg, and subsequently by the input signal to yield the error voltage $\epsilon(t)$.

$$\epsilon(t) = A\, \text{sgn}\, \left\{ F(p) \left[D(t)\, \text{Cos}\, \omega_{sc}t\, \text{Cos}[\omega_{sc}t + \phi(t)\,] + \frac{n(t)}{A}\, \text{Cos}\,[\omega_{sc}t + \phi(t)] \right] \right\}$$

$$\times \left\{ D(t)\, \text{Cos}\, \omega_{sc}t\, \text{Sin}\,[\omega_{sc}t + \phi(t)] + \frac{n(t)}{A}\, \text{Sin}\,[\omega_{sc}t + \phi(t)] \right\} \tag{5}$$

Greenhall (SPS 37-44, Vol. IV, pp. 303–313) has shown for a stationary signal process $S(t)$, plus a stationary gaussian process $n(t)$, that the conditional expectation of the hard limiter output is

$$E\,\{\text{sgn}\,[S(t) + n(t)] \mid S(t)\} = \frac{2}{\pi^{1/2}} \int_0^{\frac{S(t)}{(2\sigma)^{1/2}}} \exp^{-t^2}\, dt = \text{erf}\left(\frac{S(t)}{(2\sigma)^{1/2}} \right) \tag{6}$$

where $E(n^2) = \sigma^2$.

The expected value of $\epsilon(t)$ using the result of Eq. (6) is given by

$$\overline{\epsilon(t)} = A\left\{ \mathrm{erf}\left[F(p) \frac{D(t)\,\mathsf{Cos}\,\omega_{sc}t\,\mathsf{Cos}\,[\omega_{sc}t + \phi(t)]}{2^{1/2}\left(\frac{N_0\,B_f}{A^2}\right)^{1/2}} \right]\right\}$$

$$\times \{D(t)\,\mathsf{Cos}\,\omega_{sc}t\,\mathsf{Sin}\,[\omega_{sc}t + \phi(t)]\}$$

(7)

where

$$\sigma = (N_0\,B_f)^{1/2}$$

N_0 = the one-sided noise spectral density of $n(t)$

B_f = the noise bandwidth of the filter represented by $F(p)$

Note that the expected value of $n(t)\,\mathsf{Sin}\,\omega_{sc}t$ is zero, since $n(t)$ and $\mathsf{Sin}\,\omega_{Rc}t$ are independent.

---

c. Strong signal considerations. The loop filter time delay T_c, which gives zero static phase offset for the ·strong signal case, is determined in this paragraph. Figure 36 shows the waveforms at several points in the subcarrier demodulator for a data bit of length T_{sym} beginning with a transition. The incoming signal (Fig. 36a) is mixed with a perfect subcarrier reference, filtered and hard-limited to give the data estimate, $\widehat{D}(t)$ (Fig. 36b). The solid line in Fig. 36b shows $\widehat{D}(t)$ for $T_c = T_{sym}/8$, while the dashed line shows $\widehat{D}(t)$ for $T_c = T_{sym}/6$. For the ideal case shown, $\widehat{D}(t)$ is a perfect estimate of $\widehat{D}(t)$ except for the delay T_c. Then $\widehat{D}(t)$ is mixed with the subcarrier at 90 deg (Fig. 36c), and the result is shown in Fig. 36d. This is then mixed with the incoming signal to provide the error signal $\epsilon(t)$, shown in Fig. 36e. To main-

tain in-phase and quadrature subcarrier estimates, $\phi(t)$ should be zero to make $\overline{\epsilon(t)}$ zero. To achieve this, Fig. 36e indicates that
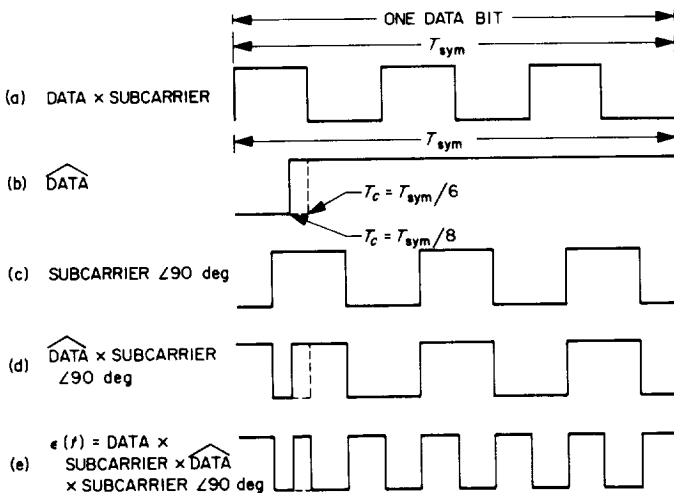
$$T_c = \frac{T_{sym}}{6}$$

$$\frac{1}{1 + p\tau}\,x = y$$

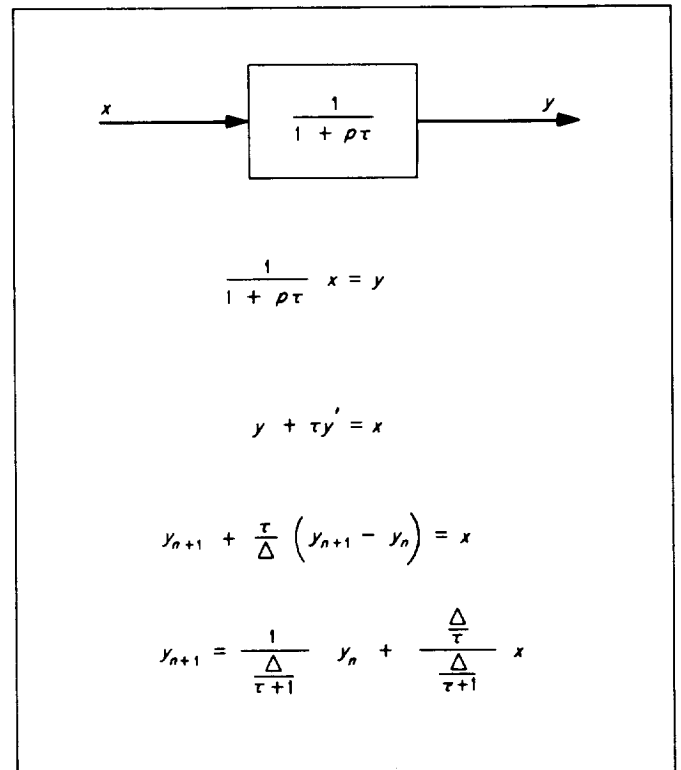$$y + \tau y' = x$$

$$y_{n+1} + \frac{\tau}{\Delta}\left(y_{n+1} - y_n\right) = x$$

$$y_{n+1} = \frac{1}{\frac{\Delta}{\tau}+1}\,y_n + \frac{\frac{\Delta}{\tau}}{\frac{\Delta}{\tau}+1}\,x$$

Fig. 37. Loop filter model

Fig. 36. Strong signal considerations

Note that a bias is introduced for $T_c = T_{sym}/8$. T_c is definable in terms of the filter time constant (τ) of the low pass filter $F(p)$. That is

$$1 - e^{-T_c/\tau} = 0.5$$

or

$$\frac{T_c}{\tau} = 0.693$$

d. $\overline{\epsilon(t)}$ Computer solution

Method. $\overline{\epsilon(t)}$ as given in Eq. (7) was programmed numerically on a computer as a function of the phase

delay for various filter time constants and signal-to-noise ratios. A pseudorandom gaussian number sequence was used to simulate gaussian noise. Fifty data words were averaged to establish value of $\overline{\epsilon(t)}$ for each value of ϕ. The model of the loop filter simulated is shown in Fig. 37.

Results. Plots of $\overline{\epsilon(t)}$ versus ϕ for various T_c at $ST_B/N_0 = 2$ (the minimum operating condition) and at $ST_B/N_0 = 0.817$ (the design point) are shown in Figs. 38 and 39, respectively. The time constants and signal-to-noise ratios involved are listed in Table 13, and the relationship used in defining signal-to-noise ratio is

$$\frac{A^2}{N_0 B_f} = \frac{3}{4}\left(\frac{ST_B}{N_0}\right)\frac{\tau}{T_{sym}}$$

Note that the loop phase error ϕ is a minimum for $T_{sym}/6$.
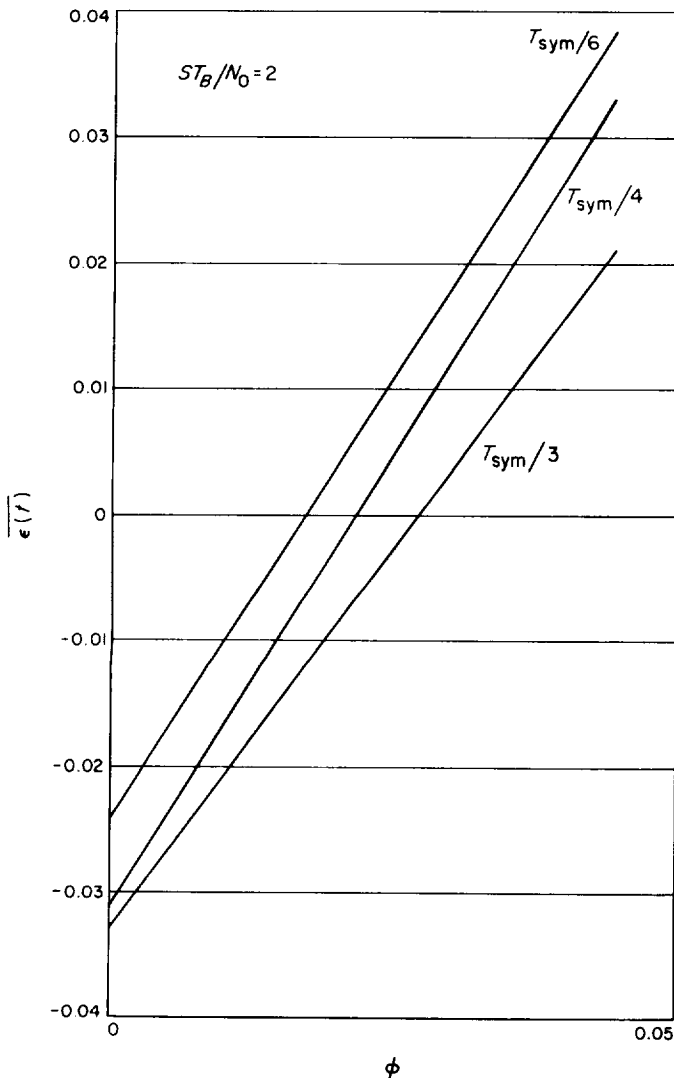

Fig. 38. $\overline{\epsilon(t)}$ versus ϕ at $\dfrac{ST_B}{N_0} = 2$ for various T_c
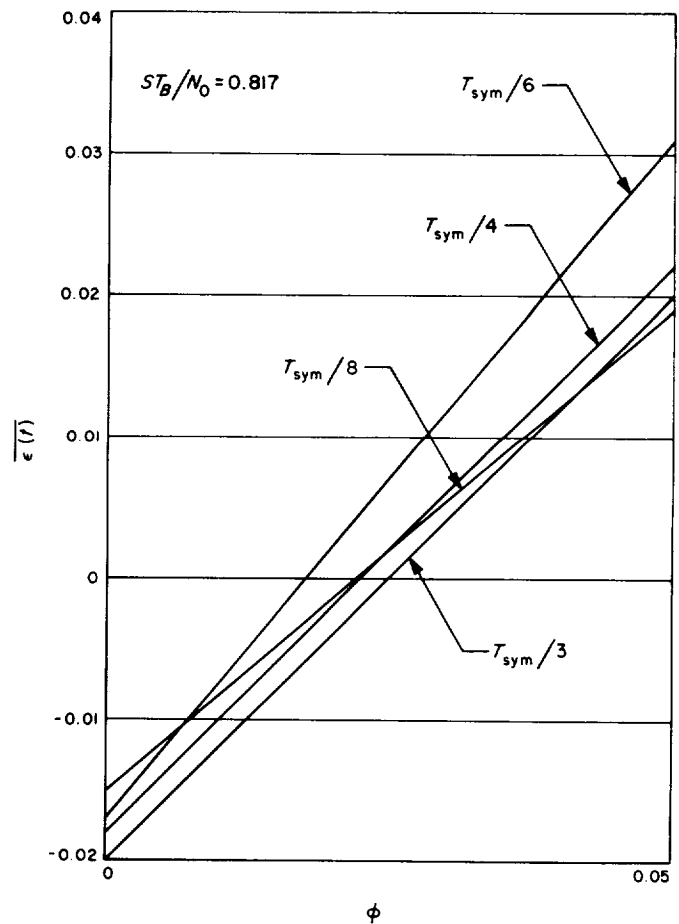

Fig. 39. $\overline{\epsilon(t)}$ versus ϕ at $\dfrac{ST_B}{N_0} = 0.817$ for various T_c

Table 13. Time constants and SNR's for Figs. 38 and 39

Filter bandwidth $B_f = \dfrac{1}{4\tau}$, Hz	Filter time constant τ, sec	Filter strong-signal time-delay T_c, sec	Filter input SNR $\dfrac{A^2}{N_0 B_f}$	
			$\dfrac{ST_B}{N_0} = 2$	$\dfrac{ST_B}{N_0} = 0.817$
0.520	0.481 T_{sym}	$\dfrac{1}{3} T_{sym}$	0.721	0.295
0.693	0.361 T_{sym}	$\dfrac{1}{4} T_{sym}$	0.531	0.221
1.040	0.241 T_{sym}	$\dfrac{1}{6} T_{sym}$	0.362	0.148
1.385	0.1805 T_{sym}	$\dfrac{1}{8} T_{sym}$	0.271	0.111

Full cycles of the subcarrier demodulator S-curve for $T_c = T_{sym}/6$ at various signal-to-noise ratios are shown in Fig. 40. As signal-to-noise increases (from design point to strong signal), the phase offset at $\overline{\epsilon(t)} = 0$ approaches zero. Figs. 38, 39 and 40, therefore, indicate that $T_c = T_{sym}/6$ is close to the optimum design value.

Suppression factor α was computed from the slip curves shown in Fig. 40. The result is given in Fig. 41 and compared with Brockman's result. The difference between curves results from the Brockman assumption of incoherence between data and subcarrier as well as the assumption of many subcarrier cycles per symbol. These assumptions, of course, are not valid for the high-rate case, but, as is evident from Fig. 40, the effect on signal suppression factor is slight.
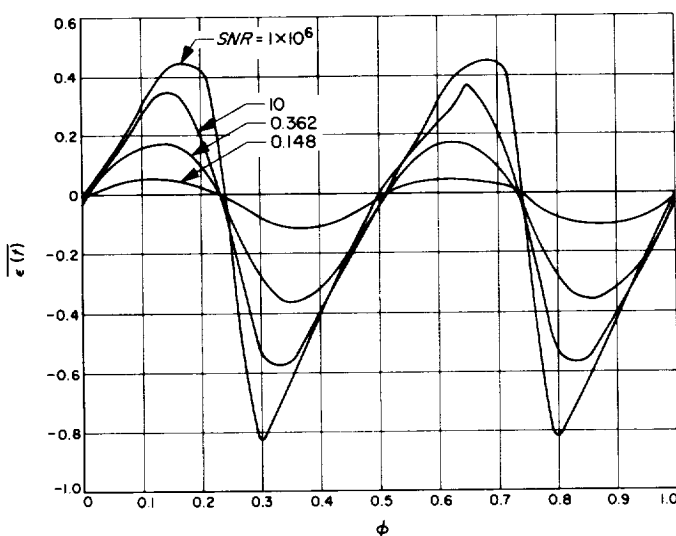

Fig. 40. $\overline{\epsilon(t)}$ versus ϕ for $T_c = T_{sym}/6$ at various SNR
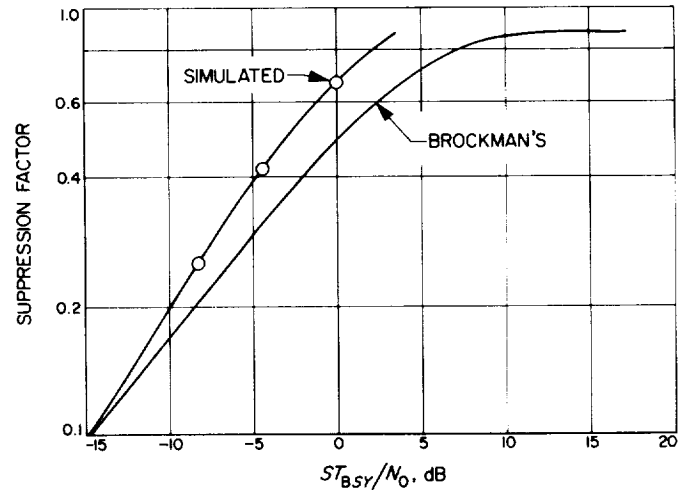

Fig. 41. Signal suppression factors

5. Symbol Timing Loop Sampled-Data Analysis,
R. Winkelstein

An analysis was made of the symbol timing loop as a sampled-data system for the purpose of defining the system parameters and investigating loop stability versus drift in these parameters. Only the noise-free case is considered here. Reference is made to SPS 37-48 and 37-49, Vol. II, which contain explanations of the loop operation. Those components that directly contribute to terms in the sampled-data equations are shown in Fig. 42. Fig. 43 shows the corresponding sampled-data block diagram.

a. Loop operation. The digital dump samples the integral of the received signal at the midpoint of each symbol time. These samples, together with the transition information from the cross-correlation detector, produce a number proportional to the displacement of the mid-symbol sync from the actual center of the symbol period. After 128 symbol periods, the accumulated error number goes to the computer where it is digitally filtered. The computer feeds the analog-to-digital converter which, in turn, provides a control voltage to the voltage-controlled oscillator (VCO). The midsymbol sync pulses are shaped directly from the output of the VCO. Loop action forces the digital dump error number to an average value of zero, and hence the timing of the midsymbol sync pulses is in coincidence with the midpoint of the symbol period.

b. Digital dump. The accumulation of integrals of the input signal from the midpoint of one symbol to the midpoint of the following symbol is monitored by the transition information from the cross-correlator
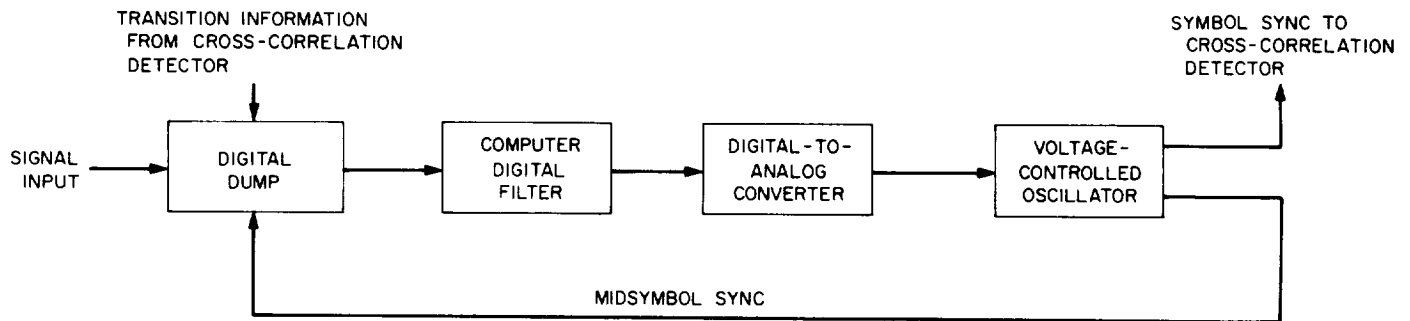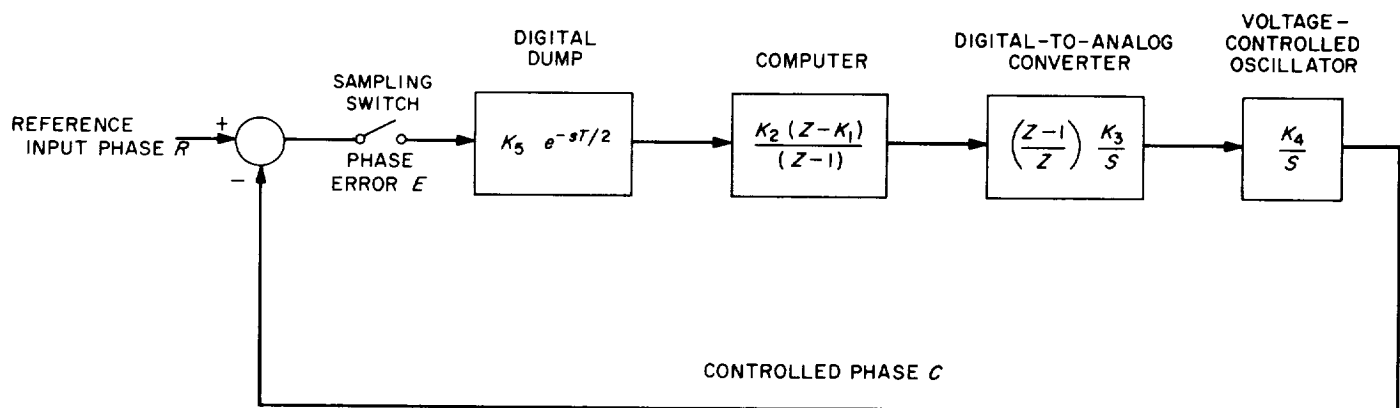
Fig. 42. Symbol timing loop

Fig. 43. Equivalent sampled-data block diagram
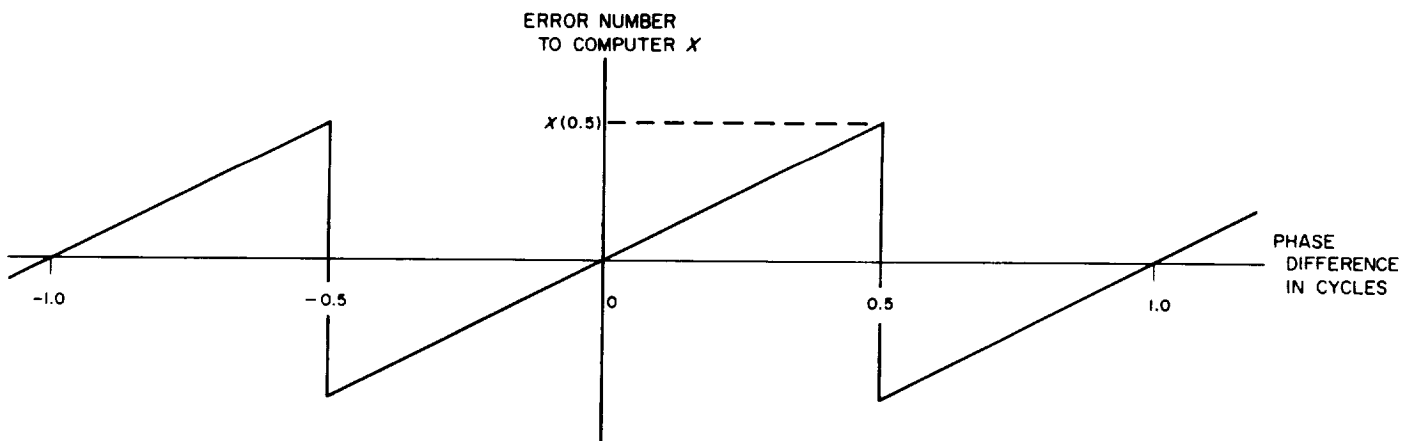
Fig. 44. Phase error characteristic

detector so as to allow accumulation of only those integrals which span a pair of symbols of opposite values. In addition, the transition information complements the integral of negative transitions so that all transitions are treated as positive, i.e., the first half of the integral is negative, and the second half is positive. At true midsymbol sampling, the generated error number is zero. As the midsymbol sync deviates from the symbol center, an error curve is generated, as shown in Fig. 44. The horizontal axis is phase shift in cycles where zero is

exact coincidence between the midsymbol sync and symbol center. The vertical axis is the number presented to the computer.

K_5, the digital dump gain constant shown in Fig. 43, is equal to the slope of the linear portion of the curve in Fig. 44. This slope is determined by estimating the limit of the computer number, $x(0.5)$, when the phase difference approaches 0.5 cycle from the left. In this case the individual integrals are timed from the beginning to end of a single symbol rather than from the midpoint of one symbol to the midpoint of the next $x(0.5)$ is found from

$$x(0.5) = (\Delta E) (A/D) (SF_1) (N) \qquad (1)$$

where ΔE is the expected voltage integral for one symbol given in volts per symbol, A/D is the conversion gain of the analog-to-digital converter given in converter bits per volt, SF_1 is the scale factor of the computer number given in CU^4/converter bit, and N is the number of symbol integrals accumulated.

Since the signal input comes from an imperfect integrator, i.e., a low-pass RC filter, the digital dump calculates

$$\Delta E = E_n - E_{n-1} + 2^{-3}E_{n-1} \qquad (2)$$

where E_n is the current sample, and E_{n-1} is the previous sample (SPS 37-48, Vol. II, p. 111). In the actual equipment, the signal gain is set by applying to the filter a DC level representing an infinite string of like polarity symbols. The output of the filter is a DC voltage known as the infinite bit voltage (E_∞). For this condition the terms in Eq. (2) become

$$E_n = E_{n-1} = E_\infty$$

and

$$\Delta E = 2^{-3}E_\infty$$

E_∞ is nominally set to 2 V, and hence ΔE is 2^{-2} V/symbol.

The analog-to-digital converter within the digital dump contains 13 bits plus a sign bit. Voltages in the range of -5 to $+5$ V may be converted. Therefore

$$A/D = 2^{13}/5 \text{ converter bits/V}$$

---

[1]CU = computer unit.

Bit 19 in the computer register word is filled from the least significant analog-to-digital converter bit. The more significant converter bits fill the lower numbered computer bits. Since the computer number or unit is assumed to have the binary point to the right of bit 0, the scale factor is

$$SF_1 = 2^{-19} \text{ computer units/converter bit}$$

Symbol integrals are accumulated for 128 symbol times. On the average, half of these integrals will involve transitions. Therefore N is equal to 64 symbols. Substituting the above values into Eq. (1) gives

$$\begin{aligned} x(0.5) &= (2^{-2} \text{ V/symbol}) (2^{13}/5 \text{ converter bits/V}) (2^{-19} \\ &\quad \text{computer units/converter bit}) (64 \text{ symbols}) \\ &= 0.05 \text{ computer units} \end{aligned}$$

The digital dump constant

$$K_5 = \frac{x(0.5)}{0.5 \text{ cycle}} = 0.1 \text{ computer units/cycle}$$

A new error number x is fed to the computer every 128 symbol times. Since this number is the result of accumulating single integral values throughout the previous 128 symbol times, x is the average phase error during the past period. With the input frequency constant and the voltage to the VCO constant during a sample time, the phase difference, if not zero, is some linear function of time during the sample period. The average value of a linear function between two times is the actual value of the function midway between those times. Therefore, x is the phase error at the midpoint of the previous sampling period. This is equivalent to having a pure delay of half a sampling period within the digital dump, and is represented in Fig. 43 by the term $e^{-sT/2}$ where e is the base of the natural logarithm, s is the complex Laplace frequency, and T is the sampling period. T is 128 symbols divided by the symbol frequency of 86.4 kHz giving T equal to 1.48 ms.

It is significant to note that K_5, and consequently the loop gain, is proportional to the input signal level as represented by the term ΔE in Eq. (1).

c. Computer digital filter. The implemented computer equation for digitally filtering the input numbers x is

$$y_n = y_{n-1} + K_2(x_n - K_1 x_{n-1}) \qquad (3)$$

where x_n is the current input error number, x_{n-1} is the previous error number, y_n is the output number to the digital-to-analog converter, y_{n-1} is the previous output number, and K_1 and K_2 are dimensionless constants (SPS 37-48, Vol. II, p. 94). Taking the Z transform of Eq. (3) gives

$$Y = Z^{-1}Y + K_2(X - K_1 Z^{-1} X)$$

where Z is equal to e^{sT}. By algebraic manipulation the transfer characteristic of the digital filter is found to be

$$\frac{Y}{X} = \frac{K_2(Z - K_1)}{(Z - 1)}$$

The constants, K_1 and K_2, are calculated after the loop equations are derived.

d. Digital-to-analog converter. The digital-to-analog (D/A) converter is equivalent to the well-known zero-order hold circuit discussed in basic texts on sampled-data systems (Ref. 1). The Laplace transfer function of the zero-order hold circuit is given by

$$G_{zoh} = \left(\frac{Z - 1}{Z}\right)\left(\frac{1}{s}\right)$$

The conversion constant is found from

$$K_3 = (D/A)(SF_2)$$

where D/A is the voltage change for a change in the most significant converter bit, and SF_2 is the computer scale factor. The converter output covers a range of 10 V with the most significant bit producing a change of 5 V.

Therefore

$$D/A = 5\text{ V/most significant D/A bit}$$

This most significant D/A bit is controlled by computer bit 6 with the lesser significant D/A bits being controlled by the higher numbered computer bits. Since the value of one computer unit is 2^6 times the value of bit 6, the scale factor is given by

$$SF_2 = 2^6 \text{ most significant D/A bits/computer unit}$$

Therefore

$$K_3 = (5\text{ V/most significant D/A bit})$$
$$\times (2^6 \text{ most significant D/A bits/computer unit})$$
$$= 320\text{ V/computer unit}$$

e. Voltage-controlled oscillator. The voltage-controlled oscillator (VCO) is an integral part of a frequency synthesizer and is normally switched into a selected decade of the synthesizer. When the VCO is switched into the tens decade, the variation of synthesizer output frequency is 100 Hz for a control voltage range of 10 V. Accordingly

$$K_4 = \frac{100\text{ Hz}}{10\text{ V}} = 10\text{ Hz/V}$$

The controlled output of the VCO is considered to be a phase function, i.e., the integral of frequency. Fig. 43 shows the block diagram of the VCO containing the term $1/s$, since this term is the Laplace transform of the integral operation.

f. Loop gain. The system open loop gain is found from Fig. 43 to be

$$G_{sol} = K_2 K_3 K_4 K_5 \left(\frac{Z - K_1}{Z}\right)\left(\frac{e^{-sT/2}}{s^2}\right)$$

G_{Zol}, the Z transform of G_{sol}, is found by taking the modified Z transform of $1/s^2$ and substituting $(1 - T/2)$ for the interpolating variable m. The result, when multiplied by $K_2 K_3 K_4 K_5(Z - K_1)/Z$, gives

$$G_{Zol} = K\frac{(Z - K_1)(Z + 1)}{Z(Z - 1)^2}$$

where

$$K = K_2 K_3 K_4 K_5 \frac{T}{2} \tag{4}$$

The closed loop response is

$$C/R = \frac{G_{Zol}}{1 + G_{Zol}}$$
$$= \frac{K(Z - K_1)(Z + 1)}{Z^3 + Z^2(K - 2) + Z(1 + K - KK_1) - KK_1}$$

g. Root locus. Fig. 45 is a typical root locus plot of the closed-loop poles for K_1 close to unity. The open-loop system contains three poles. Two are at Z equal to one,
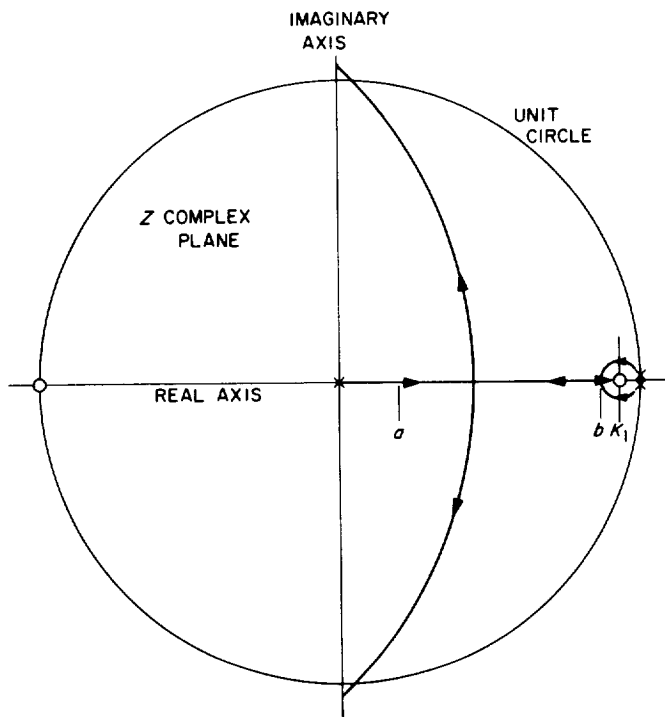
Fig. 45. Typical root locus

Expanding and equating like powers of Z, we have the following simultaneous equations

$$K - 2 = -a - 2b$$

$$1 + K - KK_1 = b^2 + 2ab \qquad (5)$$

$$KK_1 = ab^2$$

from which is obtained

$$a + 1 = \frac{4}{(b+1)^2} \qquad (6)$$

$$b^3 + \left(\frac{K+1}{2}\right) b^2 + (K - 2)b + \frac{K+1}{2} = 0 \qquad (7)$$

Solving Eq. (7) for b in a Taylor series expansion of K gives

$$b = 1 - K - \frac{3}{4} K^2 \cdots \qquad (8)$$

and the third is at the origin. Zeros of the system are at Z equal to minus one and Z equal to K_1. As K increases from zero, the unity poles circle around the zero at K_1 until they meet at point b on the real axis. This is the desired value of K for critical system damping. At this gain, the pole at the origin has moved to point a on the real axis and the denominator of the closed loop response is

$$(Z - a)(Z - b)^2$$

Substituting Eq. (8) into Eq. (6) and then into Eq. (5) gives the approximate relationship between K and K_1 for small values of K.

$$K_1 = 1 - K/2$$

As K is made smaller, the closed loop bandwidth becomes narrower. For a narrow bandwidth K equal to 0.01, K_1 is found to be 0.995. Figure 46 shows a detail of the root locus plot for K_1 equal to 0.995 in the area of critical damping. The pole location for K equal to 0.01 is very
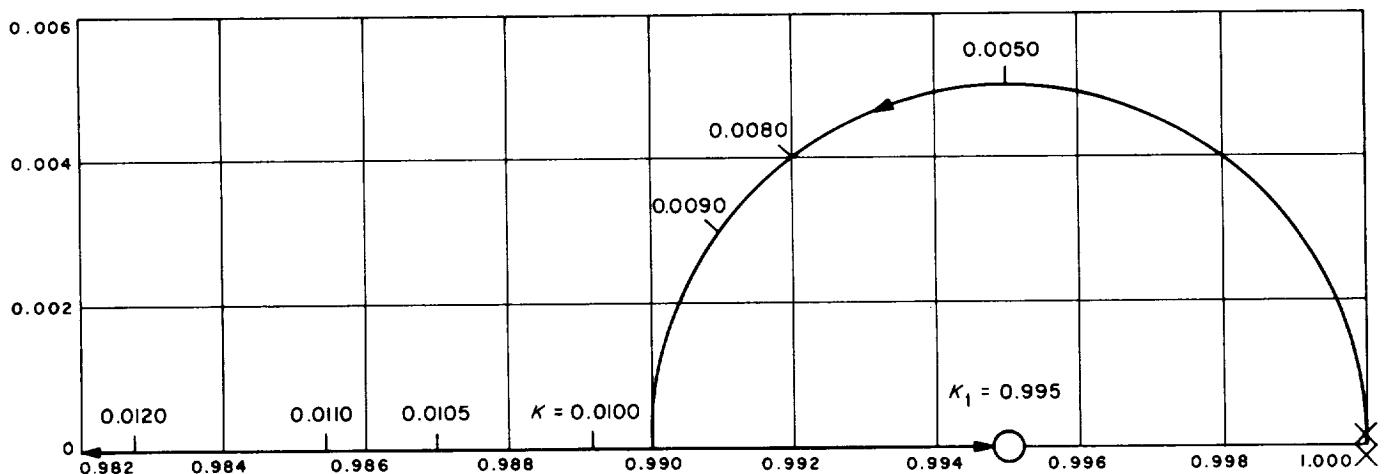

Fig. 46. Root locus detail

close to the desired value of critical damping. In addition, the system is stable for all values in Fig. 45.

h. Conclusion. Having determined the values of K and K_1 for the desired system operation, it is possible to find the computer filter gain constant from Eq. (4) as

$$K_2 = \frac{K}{K_3 K_4 K_5} \frac{2}{T}$$

Thus, for $K = 0.01$

$$K_2 = \frac{(0.01)(2)}{(320 \text{ V/CU})(10 \text{ Hz/V})(0.1 \text{ CU/cycle})(1.48 \text{ ms})}$$
$$= 0.0422$$

Reference

1. Jury, E. K., *Sampled-Data Control Systems,* John Wiley & Sons, Inc., New York, 1958.

6. Analysis and Design of the Symbol-Tracking Loop,
R. C. Tausworthe

a. Introduction. The symbol-tracking loop in the HRT system is implemented as a hybrid digital/analog transition-tracking device. Its function is to provide the cross-correlator with the correct timing information that it requires for correct extraction of data from the SDA output stream. This article describes a mathematical analysis useful for predicting the loop performance, and thereby for choosing appropriate parameters for design.

b. Symbol loop. A schematic diagram of the tracking loop is shown in Fig. 47. The correlator input stream from the SDA is a time-constant-integrated version of the incoming baseband symbol stream. This stream is sampled at a rate, fixed by a VCO, to occur precisely at symbol midtransition times, and converted to digital numbers to be manipulated in the digital hardware of
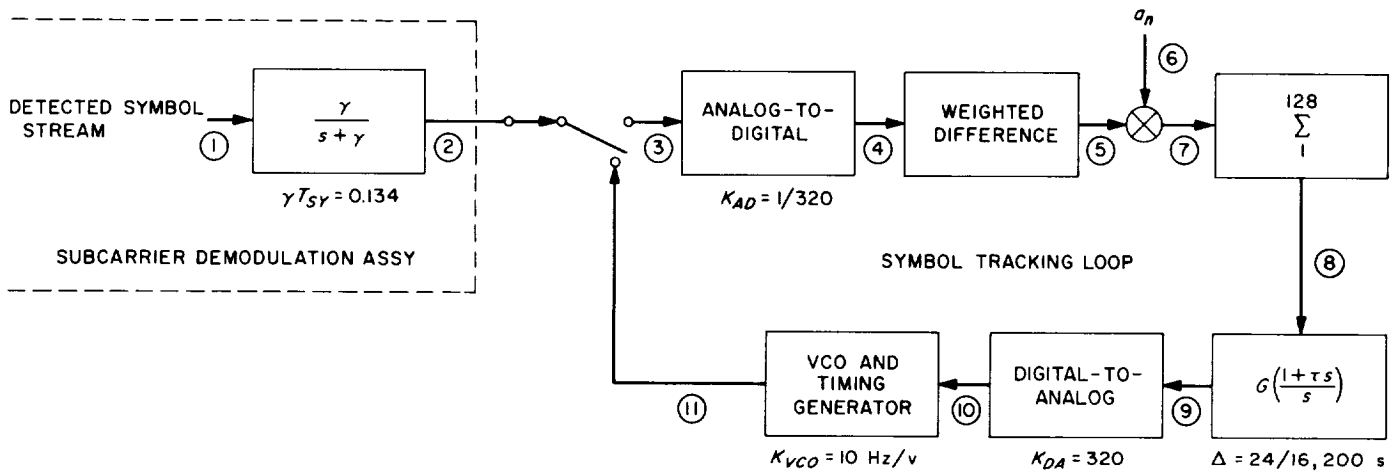
① $x(t) = Ac(t) + n(t),\ |\ c(t)\ |\ = 1,\ S_{nn}(0) = N_0$

② $y(t) = \gamma \exp(-\gamma t) \int_0^t \exp(\gamma u)\, x(u)\, du$

③ $y_k = y(k\, T_{SY}) = \exp(-\gamma T_{SY})\, y_{k-1} + Ac_k + N_k$

where

$$C_k = \gamma \int_0^{T_{SY}} \exp(-\gamma v)\, c(k T_{SY} - v)\, dv$$

$$N_k = \gamma \int_0^{T_{SY}} \exp(-\gamma v)\, n(kT - v)\, dv$$

④ $E_k = K_{AD}\, y_k$

⑤ $\Delta E_k = E_k - [1 - \exp(-\gamma T_{SY})]E_{k-1} = K_{AD}(Ac_k + N_k)$

⑥ $a_k = \begin{cases} + 1 \text{ positive transition detected} \\ - 1 \text{ negative transition detected} \\ 0 \text{ no transition detected} \end{cases}$

⑦ $a_k\, \Delta E_k$

⑧ $z_i = \sum_1^{128} a_k\, \Delta E_k$

⑨ $\approx G\left(\dfrac{1 + \tau p}{p}\right) z(t)$

⑩ $\approx K_{DA}\, G\left(\dfrac{1 + \tau p}{p}\right) z(t)$

⑪ $\text{Sample}\left[\omega_0 t + K_{VCO} K_{DA}\, G\left(\dfrac{1 + \tau p}{p^2}\right) z(t)\right]$

Fig. 47. Symbol tracking loop analysis

the correlator. By differencing adjacent samples in the fashion indicated, the result is a close approximation to the midsymbol integrals required for time-phase corrections to the VCO; however, it is first necessary to adjust these integrals according to the presence and direction of the symbol transition, as done by the transition detector term a_n appearing in Fig. 47. The correlator packs four data words per major cycle; it thereby investigates 128 symbol integrals before interrupting the computer. Computations in the computer implement the usual second-order phase-locked loop filter, and the equipment D/A converter output to the VCO/timing generator completes the loop.

If we follow, in Fig. 47, the operations on the loop input,

$$x(t) = Ac(t) + n(t)$$

where $c(t)$ is the ±1-symbol stream, A its amplitude, and $n(t)$ the white noise with two-sided density N_0, through to the computer input

$$z_n = \sum_{k=1}^{128} a_k \, \Delta E_k$$

then we shall find that z_n is a function of the phase error between the true and estimated transition times.

For near-zero phase errors, we define

$$\alpha A K_{D\Lambda} K_d = \frac{d}{d\phi} \{E[z_n]\}$$

in which α is the effect of mistakes made in the transition detector, and K_d is the detector gain when such errors are absent, where

$$\alpha = (1 - 2P_E)$$

$$= \mathrm{erf}\left(\frac{A^2 T_{SY}}{N_0}\right)^{1/2}$$

$$K_d = 64 \, \frac{\gamma T_{SY}}{\pi} \exp\left(-\gamma T_{SY}/2\right)$$

As for the noise part of z_n, its variance is directly computable as

$$\sigma_N^2 = \frac{N_0 \, \gamma}{2} \left(1 - \exp\left(-2\gamma T_{SY}\right)\right)$$

As viewed by the computer, the sequence of numbers z_n represents sample-and-hold values of the continuous function

$$z(t) = (\alpha A K_{AD} K_d) \, \phi + K_{AD} N(t)$$

which agrees with z_n at the sample instants Δ seconds apart. The noise density at zero frequency is then

$$S_{NN}(0) = 64\Delta \, \sigma_N^2$$

$$= 32 N_0 \Delta \gamma \left(1 - \exp\left(-2\gamma T_{SY}\right)\right)$$

Thus whenever the loop bandwidth w_L is much less than the computer sampling time (i.e., $w_L \Delta \ll 1$), the loop responds as an analog system having an S-curve slope $\alpha A K_{AD} K_d$ and input noise density $S_{NN}(0)$. The resulting phase error variance is thus easily identified as

$$\sigma_\phi^2 = \frac{S_{NN}(0) w_L}{(\alpha A K_d)^2} = \frac{N_0(1 - \exp\left(-2\gamma T_{SY}\right)) \, \pi^2 w_L}{(1 - 2P_E)^2 \, A^2 \gamma T_{SY} \exp\left(-\gamma T_{SY}\right)}$$

$$= \left(\frac{2N_0}{A^2 T_b}\right) \left(\frac{w_L T_b}{2}\right) \frac{\pi^2(1 - \exp\left(-2\gamma T_{SY}\right))}{(1 - 2P_E)^2 \, (\gamma T_{SY}) \exp\left(-\gamma T_{SY}\right)}$$

With this performance measure, the bandwidth can be set, given a particular design $(A^2 T_b/2N_0)$ value T_b, etc., to ensure a particular decorrelation degradation figure

$$\delta^2 = \left(1 - \frac{\sigma_\phi}{\pi(2\pi^{1/2})}\right)^2$$

For a desired bandwidth w_L, the loop constants follow from

$$r = 4\zeta^2$$

$$\tau = \frac{r + 1}{2w_L}$$

$$\alpha A K_{AD} K_{DA} K_d K_{VCO} G = r/\tau^2$$

A typical design follows in the following paragraph c.

c. Design of a symbol tracking loop. In this design we shall assume the following hardware constants:

$$\gamma T_{SY} = 0.134 \qquad K_{VCO} = 200\pi \text{ rad/s/v}$$

$$A = 2v \qquad T_b = 1/16,200$$

$$K_{AD} = 1/320 \qquad T_{SY} = \frac{32}{6} T_b$$

$$K_{DA} = 320 \qquad = 128\, T_{SY}$$

and the following design constants:

$$\zeta = 1 \text{ (critical damping)}$$

$$\delta^2 = -0.1 \text{ dB}$$

$$A^2 T_b/2N_0 = 2 \text{ (giving } P_E^W = 0.01)$$

These parameters produce

$$\sigma_\phi = 0.09 \qquad \tau = 0.416 \text{ sec}$$

$$w_L = 6.63 \text{ Hz} \approx 6 \text{ Hz} \qquad G = 0.0145$$

But since the loop filter is implemented as the difference equation

$$v_n = v_{n-1} + k_2 (z_n + k_1 z_{n-1})$$

we must convert G, τ, and Δ to the machine constants

$$k_1 = - \left(1 + \frac{\Delta}{2\tau} \right)^{-1} \left(1 - \frac{\Delta}{2\tau} \right)$$

$$= -0.99645$$

and

$$k_2 = G \left(\tau + \frac{\Delta}{2} \right) = 0.00601$$

A rigorous discussion of the S-curve and performance derivation will appear in the next issue of SPS, Vol. II.

7. Demonstration Software, *P. H. Schottler*

a. Introduction. The structure of the software subsystem for the high-rate telemetry project was described in SPS 37-48, Vol. II, pp. 92–108. The purpose of this article is to summarize briefly recent software activity in checkout and coding and to further describe the magnetic tape data recording process.

b. Checkout. The software was initially checked out on an SDS 930 computer as part of the demonstration system verification tests. Because the memory cycle time of an SDS 930 is nominally 7/32 that of an SDS 920, this initial check out did not furnish a test of the timing, although it did permit most of the functions performed by the program to be checked out. Since February of this year the software has been undergoing tests on an SDS 920 computer in the Compatibility Test Area, where the timing has been checked out. The results of all of these tests indicate that the structure of the software as reported in SPS 37-48, Vol. II, is satisfactory.

c. Coding. Additional coding has been required both to implement changes in the software suggested by the test results and to finish a number of blocks not previously completed. The changes suggested by the test results are generally minor, but two of the changes deserve some comment. First, a software lock detector for the symbol tracking loop has been added to the symbol acquisition routine (SAR). This lock detector operates on the binary number input to the symbol loop filter. The output of this lock detector is used by routine SAR to determine when to switch between the wide-band acquisition loop and the narrow-band tracking loop, and when to exit the symbol acquisition mode to start the search for word sync.

The second change of consequence is that the format of a typical record on magnetic tape has been modified. Each record on tape now consists of 1038 24-binary-digit words, of which 14 comprise a nondata header (engineering data) and 1024 are data words. While the record length has been increased by six 24-binary-digit words, both the number of data words in each record and the format for a typical data word remain unchanged. A complete record now contains 24,912 bits, or 4152 six-bit characters on tape.

d. Data recording. Recording of data onto magnetic tape in mode 3, the data mode, is controlled by three separate routines, viz., magnetic tape routine A (MTRA) in Fig. 48, magnetic tape routine B (MTRB) in Fig. 49, and magnetic tape end-of record interrupt routine (MEOR) in Fig. 50. Tape routines MTRA and MTRB appear as blocks 13 and 17, respectively, of the data-processing routine (DPR) of mode 3 (SPS 37-48, Vol. II, p. 105, Fig. 16). These two routines are coded as subroutines, and entry is by means of a BRM[5] instruction. The end-of-record interrupt routine MEOR is entered whenever an end-of-record interrupt occurs, that is, whenever the interlace word count reaches zero.
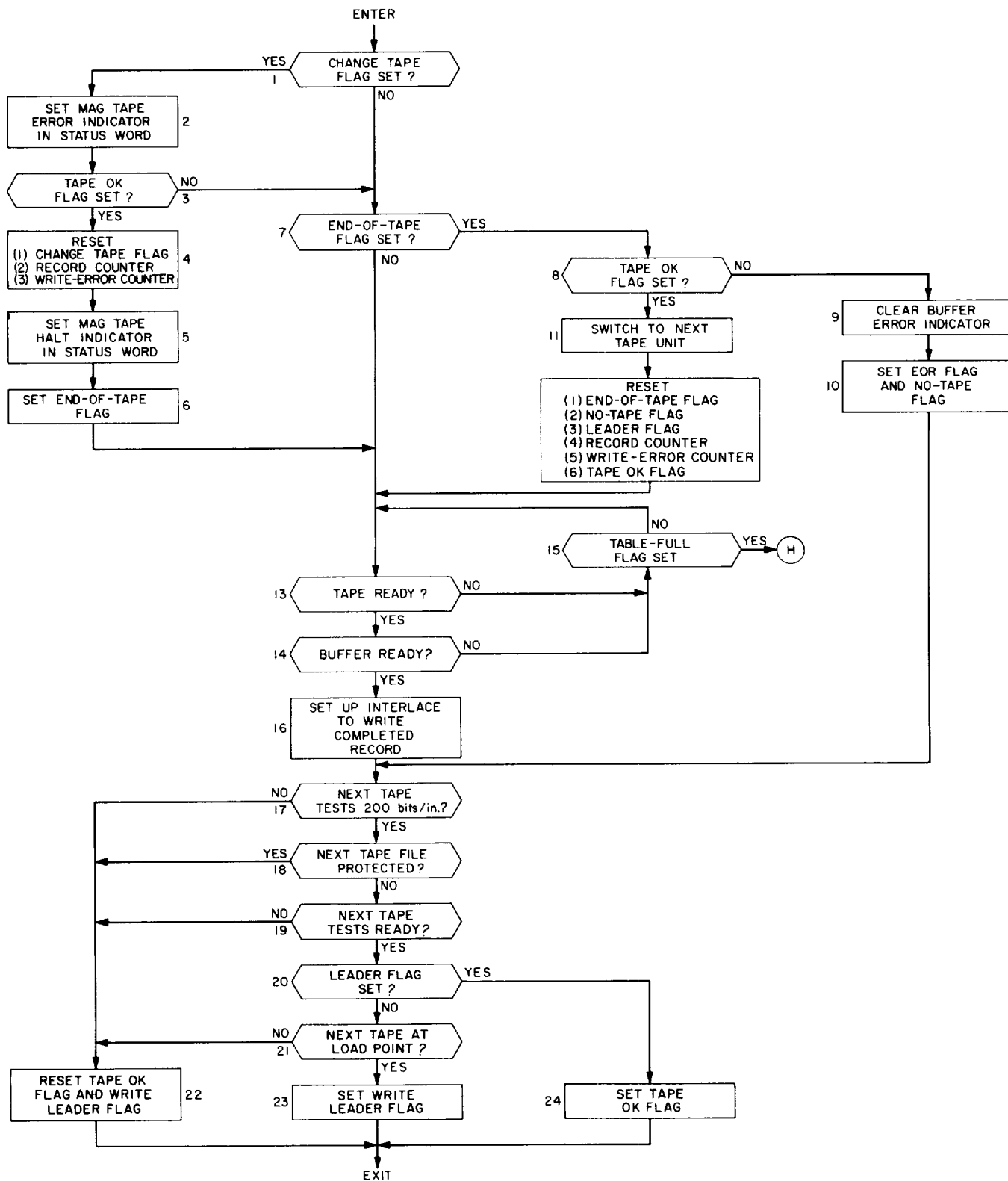
---

[5]BRM = mark place and branch.

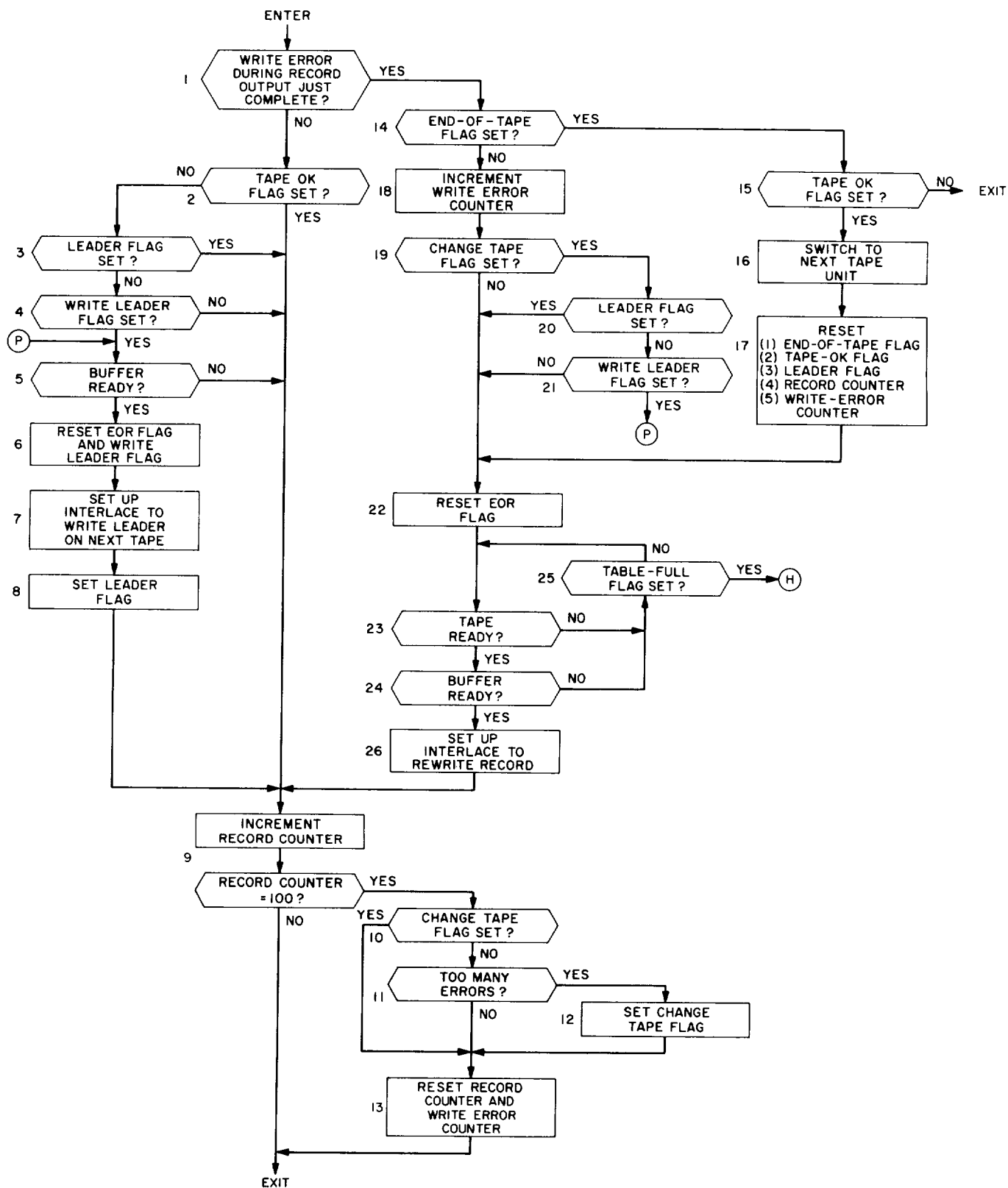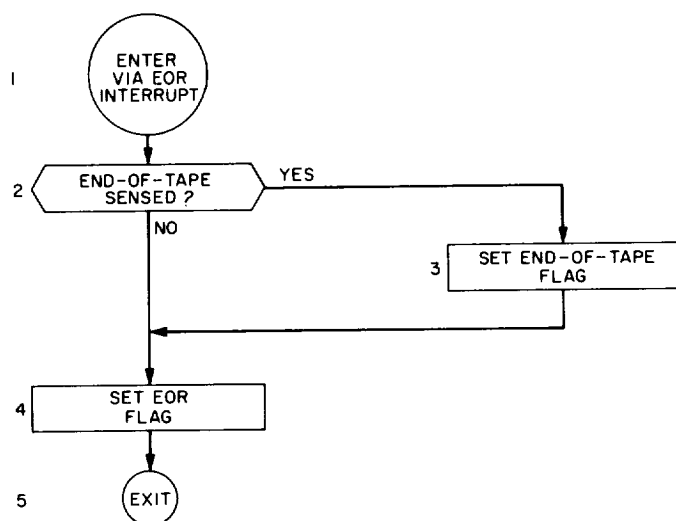**Fig. 48. Mode 3: magnetic tape routine A (MTRA)**

Fig. 49. Mode 3: magnetic tape routine B (MTRB)

ENTER
VIA EOR
INTERRUPT

1

2 END-OF-TAPE
SENSED ? — YES

NO

3 SET END-OF-TAPE
FLAG

4 SET EOR
FLAG

5 EXIT

Fig. 50. Mode 3: magnetic tape end-of-record interrupt routine (MEOR)

The basic philosophy of recording data on magnetic tape is deceptively simple. Each completed record is written once on magnetic tape. If a write error occurs during the first attempt to write any given record, that record is rewritten once on a new section of tape. Except for errors, this rewrite produces two successive identical records on the tape. If the second attempt also results in a *write* error, no third attempt is made because of insufficient time.

While the data-recording process is simple in principle, it is complicated in application because the amount of data to be recorded will occupy many reels of magnetic tape. Since there can be no interruption of the data stream while an operator replaces tapes, it is necessary to have two magnetic tape units, and the program must make provision for switching back and forth between units whenever an *end-of-tape* condition occurs for the tape currently being written on. Furthermore, between successive *end-of-tape* conditions, the program must monitor the status of the next tape and alert the operator accordingly, so as to ensure that the next tape is ready when a switchover does occur.

The three tape routines MTRA, MTRB, and MEOR are most easily understood in terms of the functions performed by the three routines as a whole, rather than as individual routines. Table 6 contains a list of the functions performed by the three routines. Opposite each function are listed the numbers of the blocks in MTRA, MTRB, and MEOR which are directly responsible for implementing that function. A blank indicates that a routine does not participate in a function. The assignment of functions to routines, as shown in Table 14; is precise; that is, routine MTRA participates in functions (1), (4), (7), (8), (9), and (11), but in no others. However, the block numbers listed for a particular routine and function are somewhat arbitrary, as will become clear in the description of the functions which follows.

e. Functions

(1) Initiate first write of completed records on tape. Routine MTRA initiates the first *write* of each completed

Table 14. Mode 3 magnetic tape routines

Function	MTRA	MTRB	MEOR
(1) Initiate first write of completed records on tape	13, 14, 15, 16		
(2) Terminate write operation			4
(3) Initiate rewrite if write error		1, 22, 23, 24, 25, 26	
(4) Monitor status of next tape	17, 18, 19, 20, 21, 22, 23, 24		
(5) Write leader on next tape		1, 2, 3, 4, 5, 6, 7, 8, also 1, 14, 18, 19, 20, 21, 5, 6, 7, 8	
(6) Initiate end-of-tape condition			2, 3
(7) Terminate end-of-tape condition	7, 8, 11, 12	14, 15, 16, 17	
(8) Initiate no-tape condition	7, 8, 9, 10		
(9) Terminate no-tape condition	7, 8, 11, 12		
(10) Initiate change-tape condition		18, 9, 10, 11, 12, 13	
(11) Terminate change-tape condition	1, 2, 3, 4, 5, 6		

record onto tape. To initiate a *write* operation, the program loads the Y buffer interlace with the word count and starting address of the record and then starts the tape moving. Control of the *write* operation then passes to the interlace.

Note that the tape-ready and buffer-ready tests are interlocked with the *table-full* flag. This interlock functions in the event that either the buffer or the tape fails to become ready prior to the next *table-full* indication. Note also that while the program must pass through several blocks in order to reach block 13 and must also pass through several blocks beyond block 16 before exiting routine MRTA, these other blocks do not directly participate in the *write* function and thus are not included.

(2) Terminate write operation. A *write* operation terminates whenever the interlace word count reaches zero causing an end-of-record interrupt to occur. In response to the interrupt, the program enters the end-of-record (EOR) interrupt routine where the EOR flag is set to mark the termination of the *write* operation.

(3) Initiate rewrite if write error. A *write* error during the first attempt to write a given record generally results in a rewrite operation, initiated by routine MTRB. The program tests the Y buffer error indicator for a *write* error, and, if the error indicator is set, resets the EOR flag and then initiates a rewrite in exactly the same fashion as routine MTRA implements function (1).

(4) Monitor status of next tape. The program must monitor the status of the next tape (that is, the tape *not* currently being written on) to ensure that it is ready for data recording when the tape currently being written on fills. Before discussing this monitoring function, however, it is necessary to say something about the format of a typical reel of magnetic tape. Each reel begins with approximately 3.75 in. of blank tape following the reflective load point marker. Following this leader, there is a succession of records recorded in the binary mode at 200 characters per inch. Successive records are separated by an inter-record gap of approximately 0.75 in. of blank tape. A reel normally ends at the first gap following the reflective end-of-reel marker. There is no end-of-file mark recorded on any reel.

Routine MTRA utilizes three flags to acknowledge various states of readiness of the next tape. These flags are defined as follows:

Write leader flag. Assuming that leader has not been written on the next tape, the *write leader* flag is set if the next tape is *ready to have leader written* and reset

otherwise. *Ready to have leader written* is defined as: Next tape tests 200 bits/in., and next tape is not file protected, and next tape tests ready, and next tape is at load point.

Leader flag. The leader flag set indicates that leader has been written on the next tape. A necessary (but not sufficient) condition for leader to be written on the next tape is that the *write* leader flag be set.

Tape OK flag. The tape OK flag set indicates that the next tape is ready for data recording. *Ready for data recording* is defined as: Next tape tests 200 bits/in., and next tape is not file protected, and next tape tests ready, and leader flag is set.

The normal sequence of flags is illustrated in Fig. 51. At time t_0 an *end-of-tape* occurs and all flags are reset. At time t_1 the conditions for the *write leader* flag are met, and that flag is set. At time t_2 *leader* is written on the next tape, and the *write leader* flag reset and the *leader* flag set. At time t_3 the conditions for the tape OK flag are met, and that flag is set. Time t_4 denotes the next *end-of-tape* occurrence. It should be noted that both the *write leader* flag and the *tape OK* flag, once set, may be subsequently reset if one or more of the required conditions ceases. The *leader* flag, on the other hand, once set, remains set until the next *end-of-tape* occurs.

(5) Write leader on next tape. Mode 3 has been designed so as to provide sufficient time to rewrite each data record once in the event that the first *write* attempt produces a *write* error. At the same time, however, the number of records which will need to be rewritten is expected to be small. It follows that the time allotted to the rewrite function will normally be available to the program. The function of *write leader* on the next tape has been assigned to routine MTRB as an alternative to the rewrite function.
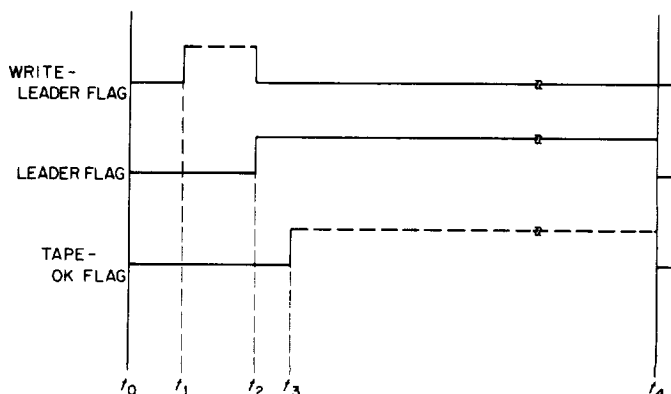

Fig. 51. Normal sequence of tape monitor flags

Following completion of the first *write* attempt for each data record, the program enters routine MTRB. If no *write* error is detected in block 1 of MTRB, the program tests to see if *leader* has been written on the next tape. If *leader* has not been written on the next tape, the program will attempt to do so. Note that at the time *leader* is written on the next tape, the *write leader* flag is reset, and the *leader* flag set, as mentioned previously in the description of function (4).

Under certain conditions, the program may attempt to *write leader* on the next tape even though a *write error* is detected in block 1 of routine MTRB. Since bypassing of the rewrite function in favor of attempting to *write leader* occurs only in the event of a large number of *write* errors, this situation is discussed in the description of function (10).

(6) Initiate end-of-tape condition. An *end-of-tape* condition occurs whenever the reflective end-of-tape marker is passed on the tape currently being written on. After each record is written on magnetic tape, the program tests to see if the end-of-tape marker was passed during the recording of that record. If the marker was passed, the program sets the *end-of-tape* flag.

(7) Terminate end-of-tape condition. Prior to any *write* operation, the program tests the *end-of-tape* flag to see if an *end-of-tape* condition was initiated at the termination of the previous *write* operation. If the *end-of-tape* flag is set, the program will, assuming that the *tape OK* flag is set, switch over to the next tape unit. Since a *write* operation may be either the first write of a completed record or a rewrite, both routines MTRA and MTRB must be able to terminate an *end-of-tape* condition.

(8) Initiate no-tape condition. A *no-tape* condition occurs if the tape currently being written upon reaches the *end-of-tape* marker, and the next tape is not ready for data recording, as indicated by the *tape OK* flag reset. Under these circumstances, the program can neither write more records on the present tape nor switch to the other tape. While a *no-tape* condition is in effect, the program continues to cycle in mode 3, although the data brought into the computer is lost. The status of the next tape is continuously monitored, however, so that data recording can resume as soon as the next tape unit becomes ready.

A *no-tape* condition is initiated by routine MTRA. The buffer error indicator is cleared so that the program can implement function (5) in routine MTRB, if required, the EOR flag is set so that the program will continue to cycle in mode 3, and the *no-tape* flag is set.

(9) Terminate no-tape condition. A *no-tape* condition can only occur simultaneously with an *end-of-tape* condition. When the next tape finally becomes ready for data recording, as indicated by the *tape OK* flag set, the program will switch over to that tape and resume data recording. The termination of a *no-tape* condition is identical to the termination of an *end-of-tape* condition except that this function appears in routine MTRA only.

(10) Initiate change-tape condition. A *change-tape* condition occurs if the number of *write* errors on the tape presently being written on exceeds a certain threshold. For each group of 100 consecutive data records transferred to magnetic tape, the program keeps track of the number of rewrites; that is, the number of records which are written twice because a *write* error occurred during the first write attempt. If in any of these groups the number of rewrites exceeds a threshold, the program initiates a *change-tape* condition. While a *change-tape* condition is in effect, the program attempts to switch over to the next tape even though the tape currently being written on may be nowhere near full. If the next tape is not ready for data recording, the program continues to write on the "bad" tape until such time as the changeover may be accomplished, at which point the *change-tape* condition ceases.

Routine MTRB initiates a *change-tape* condition. The condition is marked by the *change-tape* flag being set. All data records written on tape while a *change-tape* condition is in effect have the magnetic tape error indicator set in the status word. In addition, the final record written on the bad tape has both the magnetic tape error indicator and the magnetic tape halt indicator set. Note that if a *change-tape* condition is in effect, the program may, via blocks 19, 20, and 21 of routine MTRB, bypass the rewrite function in favor of *write leader* on the next tape in an effort to make the next tape ready for data recording.

(11) Terminate change-tape condition. A *change-tape* condition terminates when the program is able to switch to the next tape. Prior to initiating the first *write* of any record on tape, the program tests to see if the *change-tape* flag is set. If the *change-tape* flag is set, the program will, assuming the *tape OK* flag is set, switch to the next tape by initiating a dummy *end-of-tape* condition. There is, however, one final record written on the bad tape.

8. Cross-Correlator Detector, E. Lutz and R. A. Winkelstein

The digital equipment of the high-rate telemetry receiver consists of the cross-correlator detector and the

symbol timing loop. Both subsystems have been extensively tested by Lab Set A and have been found to function satisfactorily. Design and construction have begun on field sets I and II, using JPL Division 33 standard digital modules. These modules are combined in blocks of up to 21 cards to form the basic maintenance replacement unit of the equipment. The field set digital equipment is contained in two cabinets. One cabinet holds the power supplies, analog-to-digital converters, and the frequency synthesizer whose use in the system is described in SPS 37-49, Vol. II, p. 120. The second cabinet contains the digital logic totaling approximately 36 blocks at an average of 19 cards per block.

As an aid in wiring the logic blocks, a computer program using SDS Fortran II has been developed for generation of the block wiring lists. The program is structured to accept information from punched cards containing data directly derived from logic schematics or equations. This information is translated into a pin-to-pin wiring list featuring the shortest possible connections between pins. The present program is designed to accept the four types of Hi-Rel modules shown in Table 15. A total of 21 of

Table 15. Hi-Rel modules

Module	Description	Symbol
FF-33	Hi-Rel flip-flop	F
NG-33	Hi-Rel nand gate	N
PA-33	Hi-Rel power amplifier	P
DC-33	Hi-Rel diode cluster	D

these modules may be assembled into a card cage in any combination.

a. Data format. Table 16 shows the punched card format for the various logic modules. The first field of four columns is reserved to identify the module. Each module type specifies a certain input pattern as shown in that table. Entries into these input fields always refer to logic outputs or pins of the 75-pin connector. Columns 29 through 37 are reserved for logic names if needed. For the NG-33 module a fifth field marked "collector tie" is used only if that particular nand gate is part of a collector tie string; in that case its output is regarded as an input. Moreover, if the output of a nand gate is used as an input, then the internal (optional) pull-up resistor will not be connected. If the fifth input field is left blank, then the internal pull-up resistor is automatically connected. Similarly, in the case of the diode cluster (DC-33) the node can be used as an output or as an input. In addition, a 75-pin connector provides access to the logic inside the card cage.

Fig. 52a shows an example of two cascaded nand gates. Fig. 52b is the corresponding data card showing the second input of the third nand gate in slot 02 connected to the output of nand gate 1 in slot 01.
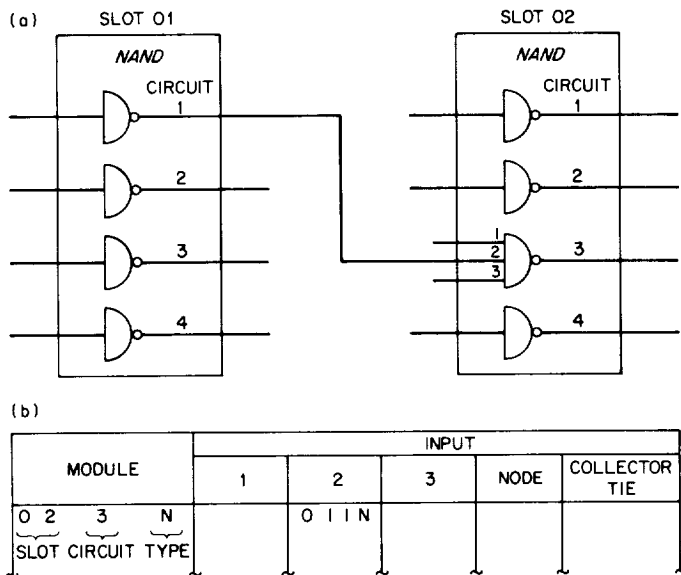
b. Main flow diagram (Fig. 53). One card at a time is read and completely checked for invalid characters or combinations. The information is stored, reformatted, and then printed as part of the documentation. Number pairs are generated by the pin-to-pin translation routine and stored in a list. This process continues until a blank card

Table 16. Data card format

Module				Inputs							Comments								
1 2 3 4	5 6 7 8	9 10 11 12	13 14 15 16	17 18 19 20	21 22 23 24	25 26 27 28	29 30 31 32 33 34 35 36 37
FF-33	SET DIRECT	SET ENABLE	SET TRIGGER	RESET TRIGGER	RESET ENABLE	RESET DIRECT	
NG-33	INPUT 1	INPUT 2	INPUT 3	NODE	COLLECTOR TIE		
PA-33	INPUT 1	INPUT 2	INPUT 3	NODE			
DC-33	INPUT 1	INPUT 2	INPUT 3	NODE			
75-pin CONNECTOR	INPUT						

(a) SLOT 01 — NAND CIRCUIT 1, 2, 3, 4; SLOT 02 — NAND CIRCUIT 1, 2, 3, 4

(b)

MODULE	INPUT			NODE	COLLECTOR TIE
	1	2	3		
0 2 3 N		0 1 1 N			
SLOT CIRCUIT TYPE					

Fig. 52. Two cascaded *nand* gates (a) sample of logic schematic (b) data card for second input for third gate in slot 02
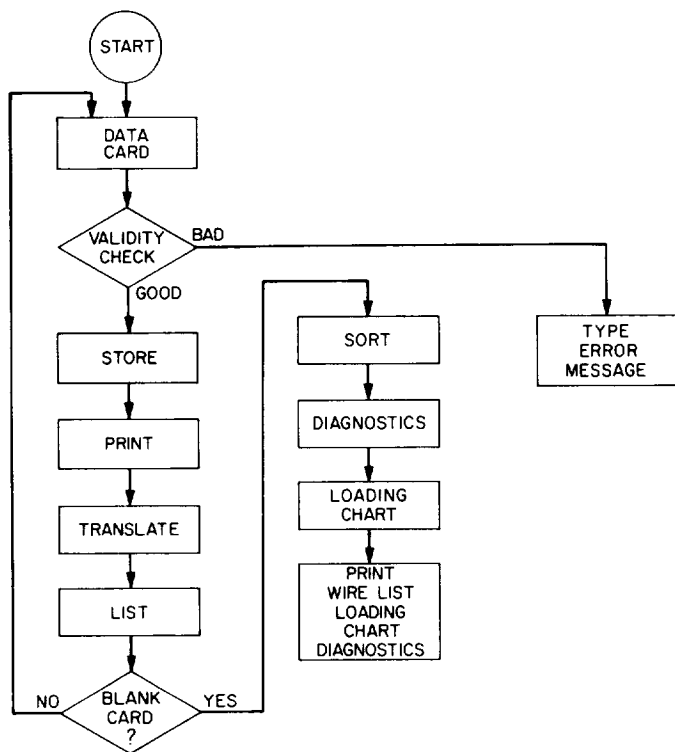

Fig. 53. Main flow diagram

is encountered at the end of the data deck, at which time the program switches to a numerical sort routine. A limited diagnostics routine is incorporated to ensure against

certain logic mistakes, such as unused and missing outputs. The diagnostics are followed by a loading chart routine as an additional convenience.

c. A complete example. The logic example in Fig. 54 is typical. As a convenience, pin numbers are shown inside the logic symbols. The computer results are shown in Fig. 55, where the logic code is an exact duplicate of the input punched card data. In the first column, the 75-pin connector is designated by a C preceded by a pin number, e.g., 005C for pin 5. However, these connector pins shown in columns 2 through 7 are represented by four-digit numbers, e.g., 0005 for pin 5.

In the wiring list a four-digit number is broken down into two groups. The two most significant digits indicate the connector where 00 represents the 75-pin access connector. The second two digits indicate the pins on these connectors. The beginning of a string of connectors in the wiring list is marked by an asterisk.

The loading chart is in many ways similar to the wiring list with the exception of the first column showing the
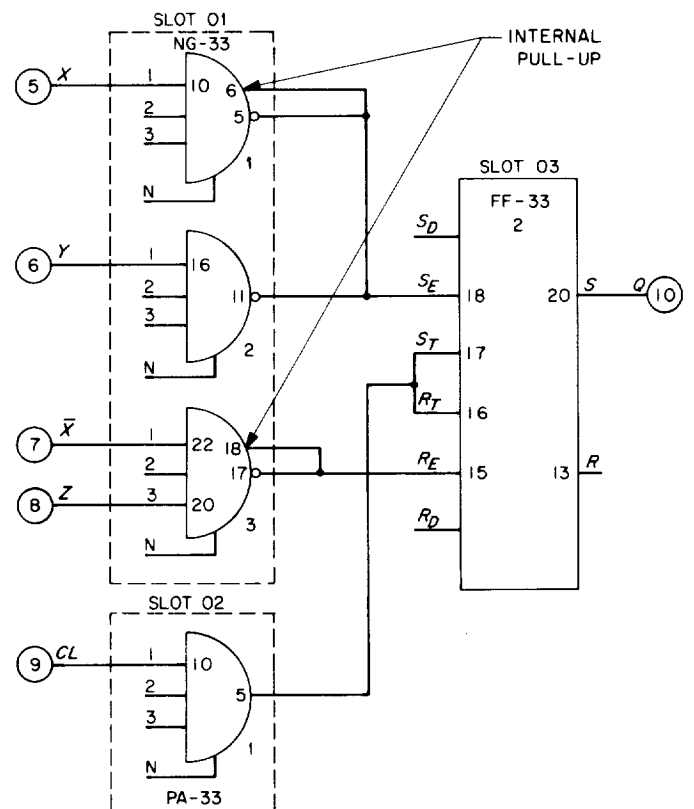
Fig. 54. Complete example

```
        LOGIC CODE      BLOCK    1

   1       2     3      4      5      6      7
 * 005C *     *      *      *      *      *      *      X
 * 006C *     *      *      *      *      *      *      Y
 * 007C *     *      *      *      *      *      *      X'
 * 008C *     *      *      *      *      *      *      Z
 * 009C *     *      *      *      *      *      *      CL
 * 010C * 032S *     *      *      *      *      *      D
 * 011N * 0005 *     *      *      *      *      *
 * 012N * 0006 *     *      *      *      * 011N *
 * 013N * 0007 *   * 0008 *      * 011N *      *
 * 021P * 0009 *     *      *      *      *      *
 * 032F *     * * 011N * 021P * 021P * 013N *      *


            LOADING CHART      BLOCK    1

0005(CPIN05)   0005(CPIN05)   0110(1N  IN1)
0006(CPIN06)   0006(CPIN06)   0116(2N  IN1)
0007(CPIN07)   0007(CPIN07)   0122(3N  IN1)
0008(CPIN08)   0008(CPIN08)   0120(3N  IN3)
0009(CPIN09)   0009(CPIN09)   0210(1P  IN1)
0105(1N  OUT)  0105(1N  OUT)  0106(1NLOAD)  0111(2N OUT)   0318(2FSCLD)
0117(3N  OUT)  0117(3N  OUT)  0118(3NLOAD)  0315(2FRCLD)
0205(1P  OUT)  0205(1P  OUT)  0316(2FRTRG)  0317(2FSTRG)
0320(2F  OUT)  0010(CPIN10)   0320(2F  OUT)


            WIRING LIST      BLOCK    1

 * 0005  0110
 * 0006  0116
 * 0007  0122
 * 0008  0120
 * 0009  0210
 * 0105  0106  0111  0318
 * 0117  0118  0315
 * 0205  0316  0317
 * 0010  0320


        UNUSED OUTPUTS      MISSING OUTPUTS      BLOCK    1

        0313(2FOUT')
```

Fig. 55. Computer results

logic output in a string. In addition, the information shown in brackets is a result of the retranslation process for checkout purposes.

The diagnostics for this example show an unused flip-flop output 0313 [2F OUT'].

d. Utilization. The program in its present form has been used extensively toward the design of the digital correlators for field sets I and II.

With little effort the program can be adapted to generate wire lists using a wide variety of different modules, including integrated circuits.

9. Test Equipment, R. I. Greenberg

a. General. The purpose and functional description of the test equipment were covered in SPS 37-49, Vol. II, p. 115. Evaluation of the prototype unit in the Compatibility Test Area resulted in several test equipment design changes. The tests revealed that the field operational units did not require the degree of flexibility provided with the prototype unit and that several additional functions were required to meet the *Mariner* Mars 1969 requirements. The overall result was a considerably simplified test equipment assembly.

b. Block diagram. A block diagram of the test equipment is given in Fig. 56. This configuration is functionally equivalent to the prototype unit installed in the Compatibility Test Area, with the following external differences.

(1) Addition of a fixed manual code select.

(2) Addition of sync signal outputs.

(3) Assignment of separate channels for the different HRT test points.

c. Changes. Table 17 tabulates the changes made to the prototype design and shows the differences between the prototype and field equipment designs. Those functions deleted were nonessential to the *Mariner* Mars 1969 support requirements.

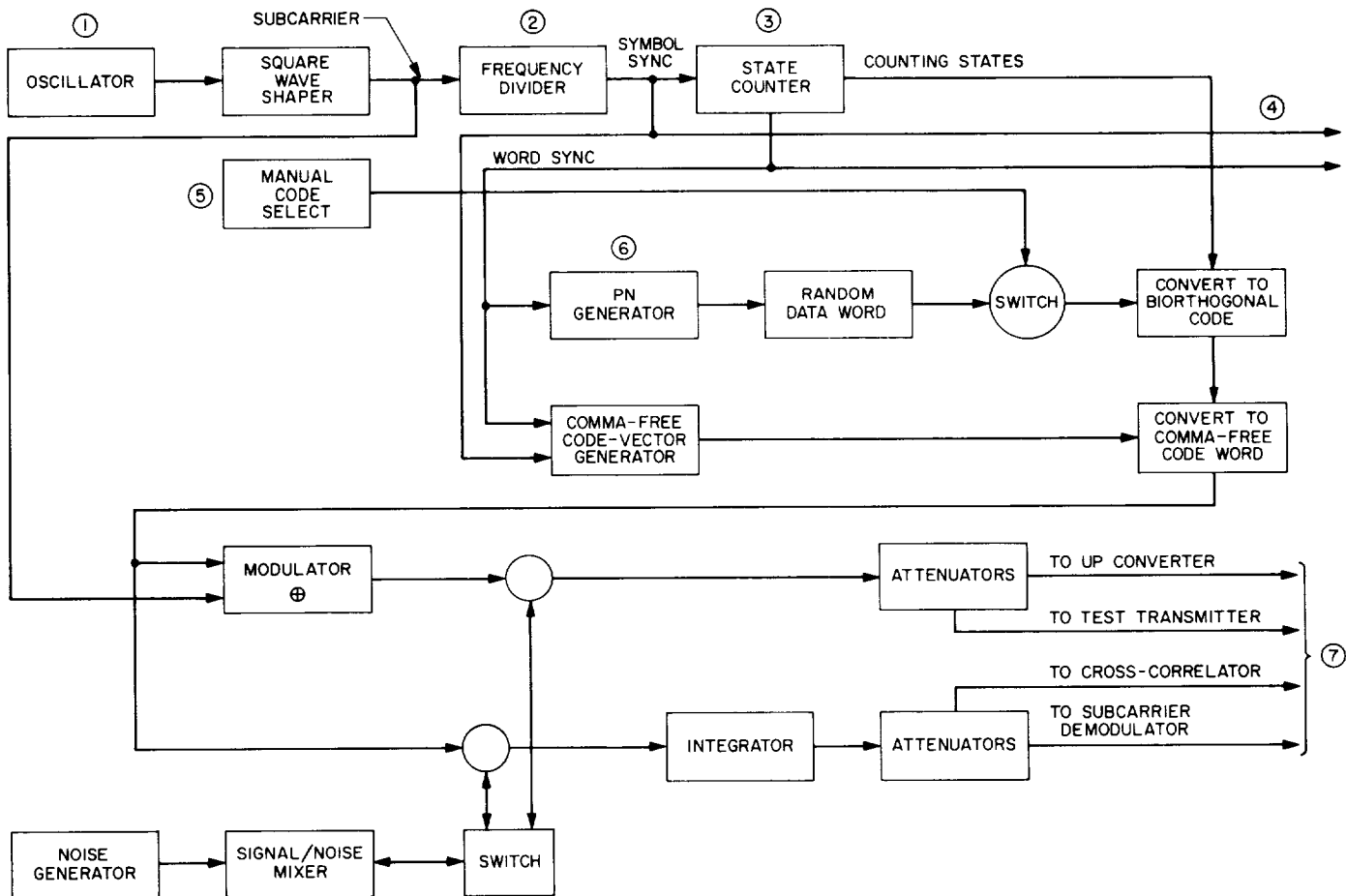The encircled numbers on Table 17 are correlated to those on Fig. 56.

Fig. 56. High-rate telemetry test equipment block diagram

Table 17. Changes to HRT test equipment

Description[a]	Lab unit	Field units
① Oscillator (518.4 kHz required)	Variable oscillator. Too unstable	Fixed oscillator. Very stable
② Subcarrier frequency divider (provides symbol frequency)	Division variable from 1 through 10	Division fixed at 3
③ State counter (provides word sync and biorthogonal coding states)	States could be chosen to number 16, 32, or 64	Only 32 states available
④ Sync signal outputs (word and symbol)	Not available	Symbol and word sync available
⑤ Code word outputs	Random outputs only available	Both random and manual select (fixed code) available
⑥ PN generator provides a bias	All zeros code appears 7 times and other codes appear 8 times during a complete sequence	All codes appear an equal number of times during a complete sequence
⑦ Code outputs		
DC block	Not available	Insertion of capacitors in lines to block DC
Information		
Modulated		
To up converter	Variable in steps of 1 dB	Fixed output: 80 mV p-p
To test transmitter	Variable in steps of 1 dB	1.5 V p-p maximum and variable to 16 dB down
Integrated		
To subcarrier demodulator	Variable in steps of 1 dB	Fixed output: 800 mV infinite bit
To cross-correlator	Variable in steps of 1 dB	Fixed output: 2 V infinite bit

[a] Encircled numbers refer to block diagram (Fig. 56).

V. Operations and Facilities

A. DSN Operations and Analysis

1. An Improved Doppler Frequency Evaluation From Cumulative Count Data, H. D. Palmiter

In the usual method of evaluating doppler frequency from cumulative count data as recorded at DSIF sites, two adjacent counter points are differenced, and the result is divided by the sample interval. This produces an average frequency which is assigned to the time of the center of the sample interval. However, if the actual frequency function has a variation with time of second degree or higher, this linear averaging process introduces a systematic error in the frequency determination even in the absence of noise. If the general functional form of the frequency variation is known, this error is deterministic and can be evaluated and applied as a correction to the data when great accuracy is required, as in the JPL orbit determination program. Another means of accomplishing this correction can be derived from the counter data itself. By combining the information contained in several successive data points, we may generate a kind of augmented count for each frequency determination and then divide by time.

The method investigated here consists of a moving least-squares polynomial fit of suitable degree on an even number of doppler counter samples. The moving origin of the fit is at the midpoint of the sample group where the instantaneous frequency is to be evaluated.

We have

$$C'(t) = a_0 + a_1 t + a_2 t^2 + a_3 t^3 + a_4 t^4 + a_5 t^5 + \cdots$$

where $C'(t)$ is the function which best fits the counter data $C_i(t_i)$ in the least-squares sense.

$$\frac{d}{dt} C'(t) = F'(t) = a_1 + 2a_2 t + 3a_3 t^2 + \cdots$$

and

$$F'(0) = a_1$$

We limit the scheme to an odd-degree fit because going to the next higher (even) degree adds no new information to a_1 in the symmetric case employed here.

Let us designate the data to be fitted as follows:

Time	$-\dfrac{7}{2}\tau$	$-\dfrac{5}{2}\tau$	$-\dfrac{3}{2}\tau$	$-\dfrac{1}{2}\tau$	$+\dfrac{1}{2}\tau$	$+\dfrac{3}{2}\tau$	$+\dfrac{5}{2}\tau$	$+\dfrac{7}{2}\tau$
Data	C_0, R_0	C_1, R_1	C_2, R_2	C_3, R_3	C_4, R_4	C_5, R_5	C_6, R_6	C_7, R_7

where τ is the (constant) sample interval, and the R_i are digital resolver corrections.

The schemes that have been developed are a third-degree fit to the inner six points above and a fifth degree fit to eight points, with two degrees of overdetermination, for smoothing, in each case. The results of the fit expressed algebraically are:

Third degree

$$a_1 = \frac{1}{3024\,\tau}\,[652(C_4 - C_3)_R + 1249(C_5 - C_2)_R$$

$$- 275(C_6 - C_1)_R]$$

Fifth degree

$$a_1 = \frac{1}{549120\,\tau}\,[168445(C_4 - C_3)_R$$

$$+ 249283(C_5 - C_2)_R - 92437(C_6 - C_1)_R$$

$$+ 13573(C_7 - C_0)_R]$$

where $(C_i - C_j)_R$ are the digital resolver-corrected count differences, e.g.,

$$(C_5 - C_2)_R = C_5 - C_2 - \frac{(C_5 - C_2)\,(R_5 - R_2)}{t_5 - t_2},$$

$$t_5 - t_2 = 3\,\tau$$

A subsequent SPS article will present the results of a statistical study of large amounts of doppler data processed by a computer program incorporating these two schemes.

2. A Proposed Method of Evaluating Station Doppler System, F. Borncamp and C. S. Patterson

a. Introduction. When problems of bias, excessive noise, discontinuities, or blunder points are noted in the

doppler data obtained during a mission, four steps must be taken to correct the situation:

(1) Confirm that the problem exists in site equipment and that it is not a failure at the SFOF, in the communication link, or in the spacecraft.

(2) Find the subsystem and module within the subsystem that is causing the fault.

(3) Replace or repair the component.

(4) Test the system to ensure that the problem has been corrected.

There is a need for a test that can be used to confirm that problems exist, ensure that a problem has been corrected, evaluate modifications to the system as to the effect on data, and to be run periodically to ensure nominal performance.

The following tests were designed to provide the above requirements, while using present on-site equipment, involving only minor changes to the system, taking only minimal time to be run, and requiring only limited analysis to interpret the results.

b. Test procedure. The tests involve a setup as shown in Fig. 1. The only nonstandard part of the configuration is the use of the on-site spare exciter loop synthesizer (HP 5100A–HP 5110A), which is used in place of the normal crystal oscillator to control the test transmitter. This provides at the test transmitter output a signal with an exactly known reference frequency. By locking the receiver to this signal, the only portion of the regular doppler system path not included is from the front end of the exciter VCO to the front end of the transmitter.

The equations for the doppler output from this configuration are as follows:

$$D_{(t_1 - t_0)} = \left[\left(\frac{240}{221}\right)(96)\,(f_{(ex-syn)})\frac{f_{R1}}{10^6}\right.$$

$$\left. - 120\,(f_{(spare-syn)})\frac{f_{R2}}{10^6} + f_{R1}\right]\left[\left(\frac{10^6}{f_{R1}}\right)(t_1 - t_0)\right]$$

where

$D_{(t_1-t_0)}$ = accumulated apparent doppler over the interval (t_1-t_0)

$f_{(ex-syn)}$ = frequency output of exciter synthesizer.

$f_{(spare-syn)}$ = frequency output of the spare synthesizer used to control the test transmitter

f_{R1} = reference (rubidium) used to control the exciter synthesizer, the doppler bias, and the clock system controlling the count interval; this is nominally a 1-MHz signal

f_{R2} = reference (rubidium) used to control the spare synthesizer; this is nominally a 1-MHz signal

(t_1-t_0) = the count interval from time (t_0) to time (t_1)
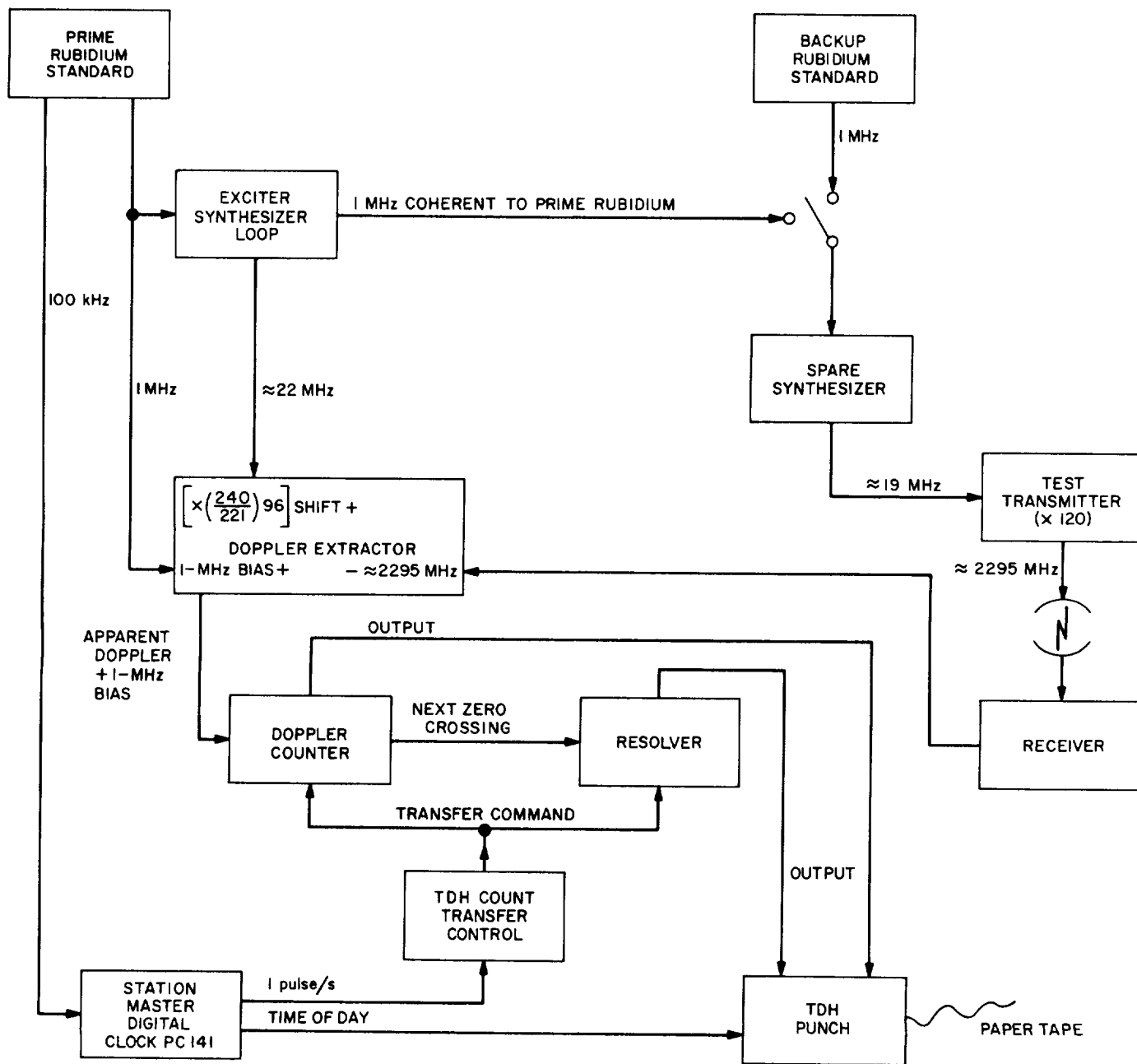

Fig. 1. Doppler system evaluation test setup

If

$$f_{R1} = f_{R2}$$

which can be accomplished by referencing the spare synthesizer to the coherent 1-MHz output on the rear of the exciter synthesizer, then the equation reduces to

$$D_{(t_1-t_0)} = \left[\left(\frac{240}{221} \right) (96) (f_{(ex-syn)}) \right.$$
$$\left. - 120 (f_{(spare-syn)}) + 10^6 \right] (t_1-t_0)$$

If

$$f_{R1} \neq f_{R2}$$

then the equation can be written as

$$D_{(t_1-t_0)} = \left[\frac{240}{221} (96) (f_{(ex-syn)}) \right.$$
$$\left. - 120(f_{(spare-syn)}) + 10^6 \right] (t_1-t_0)$$
$$+ \left[120 (f_{(spare-syn)}) \left(\frac{f_{R1}-f_{R2}}{f_{R1}} \right) \right] (t_1-t_0)$$

The second term is the contribution due to the difference between rubidium standards, and is normally less than 1 Hz for a 1-s count time.

c. Advantages. The above system provides the following three advantages over obtaining two-way lock with a transponder and counting the 1 MHz doppler bias:

(1) Since the frequency is now dependent upon the synthesizers, all digits of the counter can be tested. Typically, a frequency near 1111111.01 Hz is chosen.

(2) The resolver count, which measures the phase at the end of each count cycle which was truncated from the count, can be incremented due to the changing phase of a signal not exactly an integer number of hertz.

(3) If f_{R1} is not the same reference as f_{R2}, the system will show deviations of the prime rubidium standard which would not be detected if the system was coherently locked to a transponder.

Thus, to provide a complete spectrum of tests, a test of this type is necessary as well as the presently used coherent lock on the transponder which provides a check of the transmitter stability. Other tests, such as a constant known frequency being input directly from a synthesizer into the doppler counter or receiver jitter tests, are used to isolate the problem to the subsystem level.

d. Evaluation and use. The procedure has been evaluated at the Pioneer, Woomera and Ascension Island DSSs. It was recently used at Ascension Island DSS to verify the accuracy of a previously faulty doppler counter that had caused 100-Hz doppler accumulation errors on the *Apollo* 501 mission and was correctly repaired prior to the *Apollo* 502 mission. Coherent transponder lock tests run prior to the *Apollo* 501 mission had not detected the doppler-counter failure, although it would have been detected if this new test had been available. During a run of the test conducted at 5 dB above threshold, multiple dropped cycles in the receiver were noted in analyzing this data. This was found to be within the expected cycle loss, since the test was conducted using a 700 Hz bandwidth.

The stations each took several 10 to 20 min runs of 1-s data at various signal levels and bandwidths. The average noise level shown on the tests varied from 0.03 to 0.05 Hz at a -140 dBmW power level, with a 12-Hz bandwidth. In addition to the 1-σ noise figure as obtained above, the data is being retained for spectrum analysis. This will be useful as a base to compare with the spectrum when the system is tracking, such as the work done on the *Pioneer* spacecraft data in determining the spin rate.

At the present time the data is sent to JPL for analysis. It would be advantageous to have the data reduced at the Deep Space Station while it is being taken. The present interim monitor program used on the SDS 920 has the subroutines required to provide the required data from the tracking data handling (TDH) into the computer (i.e., doppler count, resolver value, data condition code, and time). The equations are as outlined, and the standard deviation of the residuals would be computed. In addition, a blunder detector would note the time and value of blunders. If the system temperature, bandwidth, signal level and count time, were entered via the typewriter, the program could also compute the theoretical noise to compare with the value obtained. The availability of on-site reduction should make this test a valuable tool for the Deep Space Stations to use in evaluating their doppler system.

3. Spectral Analysis of *Pioneer VIII* Doppler Frequency Residuals, A. C. Johnson and D. D. Hubiak

a. Introduction. The spectral analysis of doppler frequency residuals from the *Pioneer VIII* tracking data has

provided a technique for the measurement of the *Pioneer VIII* spin rate. The nominal expected spin rate for *Pioneer* spacecraft is 60 rev/min; however, by using a digital reduction technique on the *Pioneer VIII* doppler frequency, the spin rate appears to be nearer 62 rev/min. This article provides the analysis of the doppler frequency residuals, which are defined here as the difference between an observed value $X(t)$ and a detrending function which is a polynomial $Y_n(t)$. The method used to detrend $X(t)$ is to subtract away a polynomial $Y_n(t)$ of degree n. The polynomial $Y_n(t)$ is determined by the method of least squares.

The residuals $R_n(t)$ are then defined as

$$R_n(t) = X(t) - Y_n(t)$$

The adequacy of $Y_n(t)$ as a detrending function is ascertained by inspecting the (relative) power spectrum of $R_n(t)$. Ideally, $R_n(t)$ should exhibit no trend. However, attempts to remove all trend from $X(t)$ by using successively higher degree polynomial detrending functions $Y_n(t)$ have not been successful. Moreover, the trend in $R_n(t)$ exhibits the same characteristics as the trend in $R_{n+i}(t)$ $(n \geq n_0)$.

Part of the trend remaining in $R_n(t)$ has been assumed to be due to the rotation rate of the spacecraft about its spin axis, and results are presented to support this assumption.

b. Finite–discrete–harmonic analysis

Finite Fourier transforms. It is convenient to suppose that the set of residuals $R(t)$ is a complex-valued function of a real variable t, which is periodic of period T, but its values are known only at a discrete set of equally spaced points in a period interval; say at the points

$$0, T/N, 2\,T/N, \cdots, (N - 1)\,T/N$$

of the interval $(0, T)$. Since $R(0) = R(T)$, from the assumed periodicity, there are then N independent data, which may be expected to be used to determine the coefficients of N terms of a finite Fourier series representation of $R(t)$ of the form

$$R(t) = \sum_{k=0}^{N-1} \hat{R}(k) \exp 2\pi\, ikt/T \tag{1}$$

where $i = (-1)^{1/2}$. If the jth point is denoted by

$$t_j = j\,T/N, \qquad j = 0, 1, \cdots, N - 1 \tag{2}$$

so that N independent values $R(j) = R(t_j)$ are prescribed, one may verify that only the N functions

$$1, \quad \exp 2\pi\, it/T, \quad \exp 2\pi\, i2t/T, \cdots, \exp 2\pi\, i(N - 1)t/T \tag{3}$$

are independent over the domain comprising the set of points in Eq. (2); for each of the functions

$$\exp 2\pi\, iNt/T, \qquad \exp 2\pi\, i(N + 1)t/T, \cdots$$

takes on the same values at points in the set in Eq. (2) as does one of the N functions in Eq. (3). For example,

$$\exp 2\pi\, iNt_j/T = \exp 2\pi\, iN(j\,T/N)/T = (\exp 2\pi\, i)^j = 1$$

Similarly

$$\exp 2\pi\, i(N + 1)t_j/T = \exp 2\pi it_j/T$$

It is possible to show that the set of functions in Expression (3) is orthogonal—in the hermitian sense—under summation. As a matter of fact, by noting that the series

$$\sum_{j=0}^{N-1} \exp\, ij\alpha$$

is a geometric series, it follows that

$$\sum_{j=0}^{N-1} \exp\, ij\alpha = \begin{cases} \exp\,[i(N - 1)\alpha/2]\, \dfrac{\sin N\alpha/2}{\sin \alpha/2}, & \alpha \neq 2k\pi \\ N, & \alpha = 2k\pi \end{cases} \tag{4}$$

Making use of Eq. (4), with $\alpha = 2\pi\,(l - k)/N$, one can show that

$$\hat{R}(k) = \frac{1}{N} \sum_{j=0}^{N-1} R(j) \exp\,(-2\pi ikj/N) \tag{5}$$

The discrete forms of formula (1) and formula (5) are Fourier transform pairs. For emphasis, these formulas are rewritten below:

$$\left. \begin{aligned} R(j) &= \sum_{k=0}^{N-1} \hat{R}(k) \exp 2\pi\, ijk/N \\ \hat{R}(k) &= \frac{1}{N} \sum_{j=0}^{N-1} R(j) \exp\,(-2\pi\, ikj/N) \end{aligned} \right\} \tag{6}$$

The real finite Fourier series corresponding to a period interval $(0, T)$ is a trigonometric series of the form:

$$a_0/2 + \sum_{k=0}^{N-1} a_k \cos\left(2\pi \, k t_j/T\right) + b_k \sin\left(2\pi \, k t_j/T\right)$$

$$(7)$$

If one considers the series (1) where, $\hat{R}(k) = a_k - ib_k$, $k > 0$ and $\hat{R}(0) = a_0/2$, then the series (7) is nothing more than the real part of Eq. (1).

Finite–discrete–convolution theorem. Let $R(t)$ and $Q(t)$ be complex valued functions of t, which are both periodic of period T. The expression

$$(R * Q)(\ell) = \sum_{j=0}^{N-1} R(j) \, Q(\ell - j)$$

$$(8)$$

is the convolution of R and Q. From the assumed periodicity of R and Q, it follows that the convolution considered here is cyclic, i.e., the indices of R and Q are interpreted modulo N.

Let $\hat{R}(k)$ and $\hat{Q}(k)$ be the transforms of $R(k)$ and $Q(k)$, respectively. Then, by making use of Eq. (4), one can show that

$$(R * Q)(\ell) = \sum_{k=0}^{N-1} \hat{R}(k) \, \hat{Q}(k) \exp 2\pi \, i\ell k/N$$

$$(9)$$

Equation (9) expresses the convolution of R and Q in terms of their transforms. Also, by making use of Eqs. (9) and (4), one can show that

$$\widehat{(R * Q)}(j) = \hat{R}(j) \, \hat{Q}(j)$$

$$(10)$$

Equation (10) is the convolution theorem which states that the transform of the convolution of R and Q is the product of their transforms.

The covariance function. Denote by $[R(j)]^*$, the complex conjugate of $R(j)$. The expression

$$A_{RQ}(\ell) = \frac{1}{N} \sum_{j=0}^{N-1} [R(j)]^* \, Q(\ell + j)$$

$$(11)$$

is the (cross) covariance of R and Q. Note that Eq. (11) may be written in the form

$$A_{RQ}(\ell) = \frac{1}{N} \sum_{j=0}^{N-1} [R(N - (j+1))]^* \, Q(N - (j+1) + \ell)$$

$$= \frac{1}{N} \sum_{k=0}^{N-1} [R(k)]^* \, Q(k + \ell)$$

and hence by Eq. (9),

$$A_{RQ}(\ell) = \sum_{k=0}^{N-1} [\hat{R}(k)]^* \, \hat{Q}(k) \exp 2\pi \, i\ell k/N$$

$$(12)$$

If $R = Q$ in Eq. (12), the resulting expression, namely

$$A_{RR}(\ell) = \sum_{k=0}^{N-1} |\hat{R}(k)|^2 \exp 2\pi \, i\ell k/N$$

$$(13)$$

is the autocovariance (or autocorrelation) function; and the function

$$A_{RR}(\ell)/A_{RR}(0)$$

is the "normalized" autocovariance (autocorrelation) function. Note that the transform of A_{RR}, namely $|R|^2$, is real. The function $|R|^2$ is the power spectrum of R. If the autocovariance function is real, then Eq. (13) reduces to

$$A_{RR}(\ell) = \sum_{k=0}^{N-1} |\hat{R}(k)|^2 \cos 2\pi \ell k/N$$

$$(15)$$

Mathematical models. It is assumed here that the residuals $R(t)$ may be represented approximately by an expression of the form

$$R(t) = \sum_{\ell=0}^{N-1} a_\ell \cos 2\pi \left(\frac{\ell}{T}\right) t + b_\ell \sin 2\pi \left(\frac{\ell}{T}\right) t$$

$$(16)$$

For such an expression (16), the (finite) discrete Fourier transform is given by

$$\hat{R}(k) = \frac{1}{N} \sum_{j=0}^{N-1} \sum_{\ell=0}^{N-1} R_e \left[C_\ell \exp 2\pi \, i\ell j/N\right] \exp -2\pi \, ijk/N$$

$$(17)$$

where $C_\ell = (a_\ell - ib_\ell)$, and where the notation R_e means "the real part of." Similarly, the notation I_m will mean "the imaginary part of."

Making use of the identity

$$(R_e[Z_1]) \cdot Z_2 = Z_1 \cdot Z_2 + (I_m[Z_1]) \cdot (I_m[Z_2])$$
$$- i(R_e[Z_2]) \cdot (I_m[Z_1])$$

Eq. (17) takes the form

$$\hat{R}(k) = \frac{1}{N} \sum_{l=0}^{N-1} C_l \sum_{j=0}^{N-1} \exp 2\pi\, ij(l - k)/N$$

$$+ \frac{1}{N} \sum_{l=0}^{N-1} \sum_{j=0}^{N-1} [a_l \sin (2\pi l j/N) + b_l$$

$$\times \cos (2\pi l j/N)]\, \sin 2\pi l j k/N$$

$$- \frac{i}{N} \sum_{l=0}^{N-1} \sum_{j=0}^{N-1} [a_l \sin (2\pi\, l j/N) + b_l$$

$$\times \cos (2\pi l j/N)]\, \cos 2\pi l j k/N \qquad (18)$$

By making use of the real part of relation (4) and the trigonometric addition theorems, one can show that the last two terms in Eq. (18) must vanish identically. Again by Eq. (4), the first term in Eq. (18) is

$$C_k = a_k - i b_k$$

Thus,

$$\hat{R}(k) = a_k - i b_k$$

when $R(k)$ is given by Eq. (16); hence the power spectrum of R is

$$|\hat{R}(k)|^2 = a_k^2 + b_k^2, \qquad k = 0, 1, \cdots, N - 1 \quad (19)$$

If $R(t)$ is given by (16), then it is customary to call the term

$$F_l = a_l \cos 2\pi \left(\frac{l}{T}\right) t + b_l \sin 2\pi \left(\frac{l}{T}\right) t$$

a frequency component of $R(t)$ with frequency l/T cycles per unit of time. Thus $R(t)$ contains the frequency component F_l provided $F_l \neq 0$. It follows from Eq. (19) that $R(t)$ contains the frequency component F_l, if, and only if, $|\hat{R}(l)|^2 \neq 0$. Thus the power spectrum is a powerful tool for detecting frequencies in data.

Finite Fourier cosine transform. Formula (15) expresses the autocovariance function as a finite Fourier cosine transform of its power spectrum. One can show that the "inversion" formula is valid; i.e., the power spectrum may be obtained as a finite Fourier cosine transform of the autocovariance function. By multiplying both sides of

Eq. (15) by $\cos 2\pi l j/N$, summing from 0 to $N - 1$, and then making use of the appropriate trigonometric addition theorem and the real part of relation (4), one can show that

$$|\hat{R}(k)|^2 = \frac{2}{N} \sum_{l=0}^{N-1} A_{RR}(l) \cos 2\pi l k/N \qquad (20)$$

which is the representation of the power spectrum as a finite Fourier cosine transform of the autocovariance function.

c. Computations

Doppler frequency. The basic data type is two-way coherent doppler, which is integrated to obtain phase measurements. The doppler frequency is computed from a continuous count doppler in which every other "zero crossing" of a received signal is accumulated. The doppler count measurements are best described in Fig. 2.

The expression for changing doppler measurements into an average doppler frequency F_i (in hertz), over the sample interval $(t_i + TR_i, t_{i+1} + TR_{i+1})$, is given by

$$F_i = \left[\frac{C_{i+1} - C_i}{(t_{i+1} + TR_{i+1}) - (t_i + TR_i)} \right] \text{ in hertz}$$

where

$TR_i =$ "time resolver" count (three digits converted to seconds by multiplying by 10^{-8})

$C_i =$ contents of doppler counter at time $t_i + TR_i$

Calculation of residuals. Doppler frequency residuals are obtained as follows. First, the observation period (TI, TF), is normalized to the interval $(-1, 1)$ by the transformation

$$t'_i = 2 \frac{t_i - TI}{TF - TI}$$

where $t_i = i\Delta t$, and Δt is the spacing between samples. Then the coefficients $A_0, A_1, \cdots, A_N$, in the expression

$$Y_N(t') = A_0 T_0(t') + \cdots + A_N T_N(t')$$

are chosen to minimize the expression:
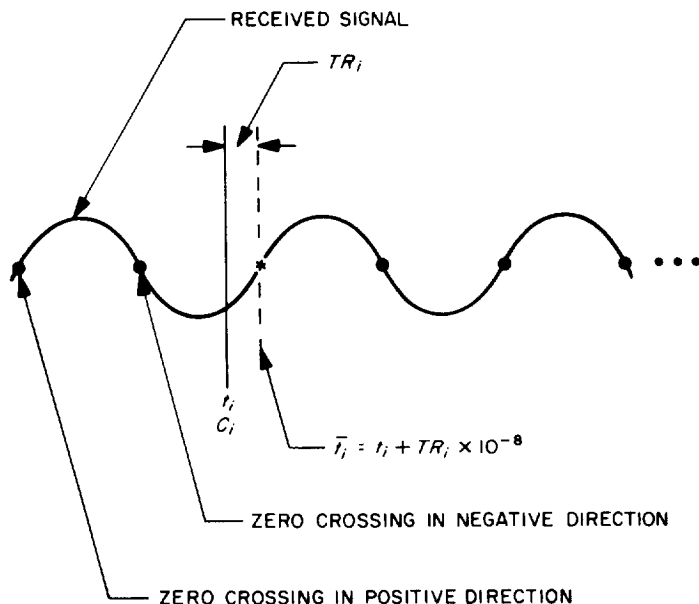
$$\sum_{i=1}^{N} [X(i) - Y_N(t'_i)]^2$$

Fig. 2. Doppler count measurement

where $X(i)$ are the "observed" doppler frequency at times t_i and the T_k's are the Chebyshev polynomials.

The Chebyshev polynomials are given recursively as follows:

$$T_0(X) = 1$$
$$T_1(X) = X$$
$$T_k(X) = 2X\,T_{k-1}(X) - T_{k-2}(X), \qquad k \geq 2$$

As mentioned in the introduction, the use of successively higher degree detrending polynomials $Y_N(t)$, in order to remove all trend from $R_N(t) \equiv X(t) - Y_N(t)$, proved unsuccessful. Figures 3, 4, and 5 are plots of the power spectra of $R_N(t)$ for $N = 10$, 15, and 20, respectively. Note that these power spectra of $R_N(t)$ all exhibit
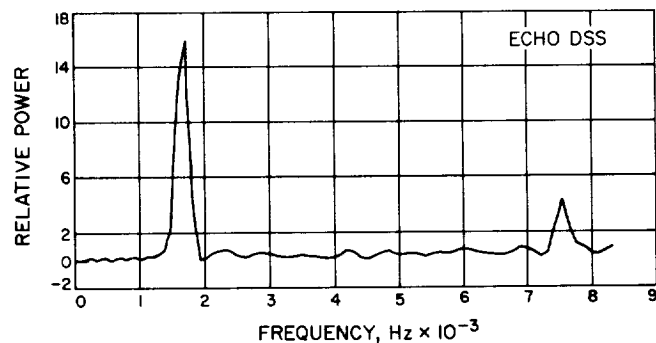

Fig. 4. Power spectrum of $R_{15}(t) = X(t) - Y_{15}(t)$ (pass 01, Dec. 14, 1967)

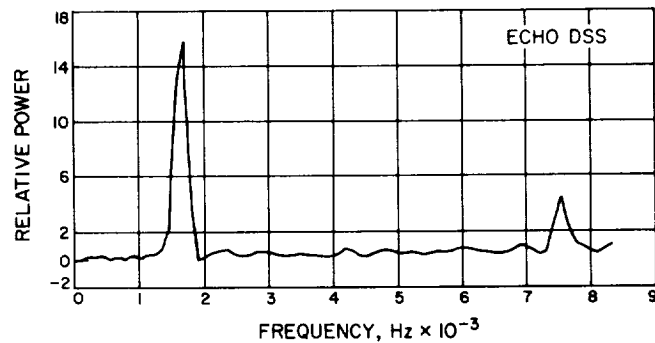Fig. 3. Power spectrum of $R_{10}(t) = X(t) - Y_{10}(t)$ (pass 01, Dec. 14, 1967)

Fig. 5. Power spectrum of $R_{20}(t) = X(t) - Y_{20}(t)$ (pass 01, Dec. 14, 1967)

the same characteristics. Therefore, one can assume that the frequency is truly present and not a part of the data reduction process.

Calculation of the autocorrelation and the power spectrum. The autocorrelation function is calculated from the formula

$$A_{RR}(\ell) = \frac{1}{N} \sum_{j=0}^{N-(\ell+1)} R(j)\, R(\ell + j) \qquad (21)$$

for $\ell = 0, 1, \cdots, M$. The integer M is the maximum "lag index." Note that if $M < N - 1$, and if it is assumed that $R(j) = 0$, for $j > M$, then formula (21) is equivalent to formula (11) with $R = Q$. $A_{RR}(\ell)$ is normalized by dividing $A_{RR}(0)$.

The corresponding power spectrum is calculated by means of formula (20). Formula (20) may be rewritten in the form

$$|\widehat{R}(k)|^2 = \frac{2}{M} \sum_{\ell=0}^{M-1} A_{RR}(\ell) \cos 2\pi f_k t_\ell \qquad (22)$$

Now according to the sampling theorem (Ref. 1) the meaningful range of f_k is the interval $(0, \pi/(2\Delta t))$, and since $M + 1$ values of $A_{RR}(\ell)$ are available, one can select $M + 1$ values of f_k according to

$$f_k = \frac{k}{2M\,\Delta t}, \quad k = 0, 1, \cdots, M \qquad (23)$$

With f_k given by Eq. (23), Eq. (22) now reads

$$|\widehat{R}(k)|^2 = \frac{2}{M} \sum_{\ell=0}^{M-1} A_{RR}(\ell) \cos \frac{\pi k \ell}{M} \qquad (24)$$

Finally, the spectral sequence $[\widehat{R}(k)]^2$ is "smoothed" by Hanning weights to obtain smoothed spectral estimates $[U_k]$, where

$$U_0 = \frac{1}{2}\left(|\widehat{R}(0)|^2 + |\widehat{R}(1)|^2\right)$$

$$U_k = \frac{1}{4}|\widehat{R}(k-1)|^2 + \frac{1}{2}|\widehat{R}(k)|^2 + \frac{1}{4}|\widehat{R}(k+1)|^2,$$

$$k = 1, 2, \cdots, M - 1.$$

$$U_M = \frac{1}{2}\left(|\widehat{R}(M-1)|^2 + |\widehat{R}(M)|^2\right)$$

d. Summary of calculations (Pioneer VIII spin rate analysis). The *Pioneer VIII* spacecraft was injected into a heliocentric orbit on December 13, 1967 with the firing of a solid-propellant third-stage rocket. After third-stage burnout and automatic sequencing, a desired nominal spacecraft spin rate of 60 rev/min is expected. Subsequent telemetry measurements indicate a spacecraft spin rate of approximately 62 rev/min.

It is reasonable to assume that spinning of the spacecraft will introduce a trend in the (observed) doppler frequency data. This trend may then be detected and analyzed via the power spectrum. Based on the above assumption, an alternate method was devised to measure spacecraft spin rate. However, since the maximum sampling rate available is one sample per second, it will be impossible to detect frequencies on the order of 60 rev/min, which is the nominal expected spacecraft spin rate. The method devised is to consider the aliases of detectable frequencies f, where $0 \le f \le f_c$, and where f_c is the cutoff frequency which is known as the Nyquist frequency.

Now for any frequency f in the range $0 \le f \le f_c$, the frequencies which are aliased with f are defined by

$$(2f_c + f), (4f_c \pm f), \cdots, (2nf_c \pm f), n = 0, 1, 2, \cdots \qquad (25)$$

To prove this fact, observe that for $t = 1/2\,f_c$,

$$\cos 2\pi f t = \cos 2\pi (2\,nf_c \pm f) \frac{1}{2f_c}$$

$$= \cos \frac{\pi f}{f_c} \qquad (26)$$

Therefore, all data containing frequencies $2nf_c \pm f$ have the same cosine function as data containing the frequency f, when data are sampled at points $1/2\,f_c$ apart (Ref. 2, pp. 278–282).

Consider now the following example. The power spectrum of the residuals (Fig. 5) indicates the presence of a frequency $f \doteq +0.03274$ Hz. Now the sampling rate is one sample per second so that $f_c = 0.5$ Hz. Thus one of the aliases of f is given by

$$(2nf_c + f)$$

when

$$n = 1$$

$$f_c = 0.5 \text{ Hz}$$

$$f \doteq 0.03274 \text{ Hz}$$

Then, the computed spin rate is

$$[2(1)f_c + f]\,60 = 61.964 \text{ rev/min}$$

with a tolerance of $\pm 60\ (\Delta f) = \pm 0.177$ rev/min, where the resolution

$$\Delta f = \frac{1}{2\,M\Delta t} \qquad (27)$$

This computed value of spin rate lies in the range of telemetry measurements of spacecraft spin rates.[1]

A summary of calculations is presented in Table 1. When $\Delta t = 1$ sec, the computed spin rate generally agrees with the telemetered value. Equation (27) is used to provide the resolution Δf, indicated in Table 1.

The plots of the power spectrum (Figs. 6, 7, and 8) invariably exhibit two dominant peaks. The frequencies corresponding to the peaks are termed in Table 1 "higher dominant frequency" and "lower dominant frequency."

The spacecraft spin rate is always calculated from the frequency corresponding to the peak at the lower end of the frequency scale, since an alias of this frequency appears to be closer to the expected nominal spin rate. The meaning of the frequency corresponding to the peak at the higher end of the frequency scale has not been resolved.

[1]Data supplied by G. Schimmel and M. Erickson of Ames Research Center.

References

1. Blackman, R. B., and Tuckey, J. W., *The Measurement of Power Spectra*, Dover Publications, New York, 1958.

2. Bendat, J. S., and Piersol, A. G., *Measurement and Analysis of Random Data*, John Wiley and Sons, New York, 1966.

3. Gaskell, R. E., *Engineering Mathematics*, Holt, Rinehart, Winston, Inc., New York, 1958.

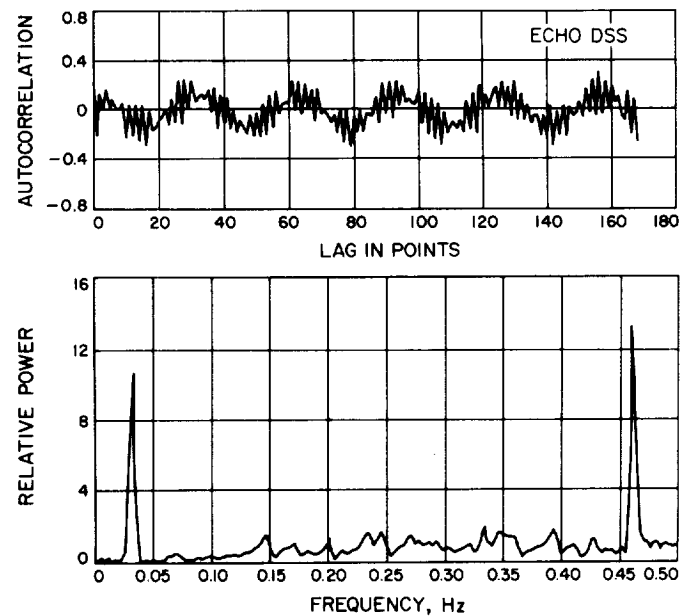4. Lanczos, *Applied Analysis*, Prentice Hall, Inc., Englewood Cliffs, N.J., 1956.

Fig. 6. Autocorrelation and power spectrum of $R_7(t) = X(t) - Y_7(t)$ (pass 02, Dec. 15, 1967, 20% lag index)

Table 1. Results of *Pioneer VIII* spin rate analysis

| Doppler measurement date	Pass Echo DSS	Data rate Time (GMT) From	Data rate Time (GMT) To	Δ t, sec	Number of residuals	Maximum lag index, M	Lower dominant frequency, Hz	Higher dominant frequency, Hz	Mean of $R_7(t)$	Standard deviation of $R_7(t)$	Computed spin rate, rev/min	Telemetry measured spin rate, min	Frequency resolution Δf, Hz
12-15-67	02	06:46:54	07:00:53	1	840	169	0.03274	0.46131	1.14×10^{-4}	5.89×10^{-2}	61.964	61.92	0.00295
12-16-67	03	11:06:22	11:13:59	1	458	92	0.03846	0.45055	1.41×10^{-4}	6.35×10^{-2}	62.307		0.00543
		11:06:22	11:13:59	1	458	230	0.04148	0.44760	1.41×10^{-4}	6.35×10^{-2}	62.488	62.43	0.00217
12-17-67	04	10:47:45	11:01:59	1	855	428	0.04098	0.40281	-7.07×10^{-5}	5.85×10^{-2}	62.456	62.47	0.00116
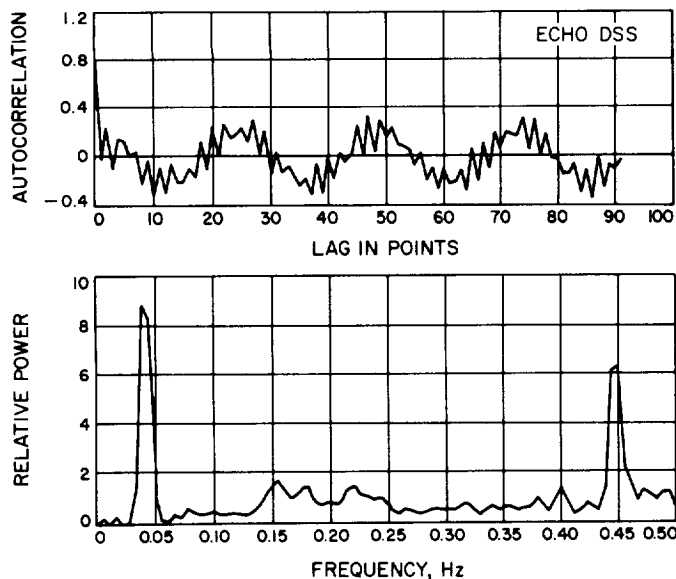
**Fig. 7. Autocorrelation and power spectrum of
$R_7(t) = X(t) - Y_7(t)$ (pass 03, Dec. 16, 1967,
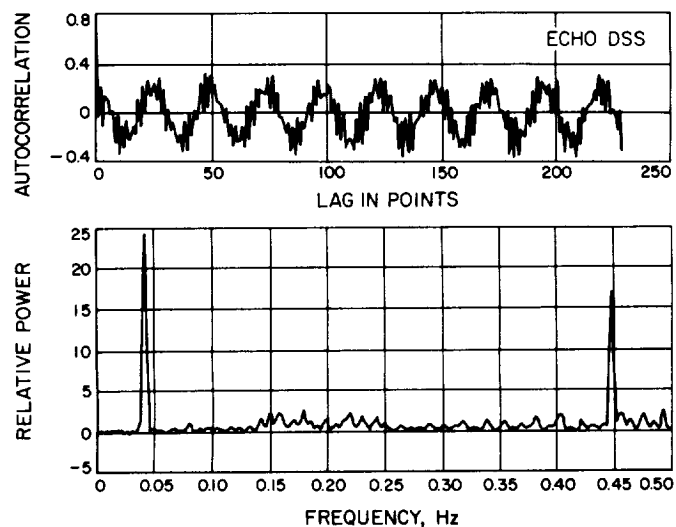20% lag index)**

**Fig. 8. Autocorrelation and power spectrum of
$R_7(t) = X(t) - Y_7(t)$ (pass 03, Dec. 16, 1967,
50% lag index)**

B. GCF Operations

1. Flight Project Support, *F. E. Bond, Jr.*

During March and April 1968 the GCF provided ground communications for the cruise support of the *Pioneer VI, VII,* and *VIII* spacecraft presently in sun-centered orbits. Relay of designated spacecraft data in real-time as received from the tracking stations of the DSIF to the control center at Ames Research Center continues as planned. Operational communications plans, policies, and procedures are presently being formulated for the forthcoming support required for the ninth *Pioneer* spacecraft, *Mariner* extended mission operations, and the *Mariner* Mars 1969 projects.

C. Facility Engineering

1. DSIF Power Facility Engineering, *L. H. Kushner*

a. Introduction. The purpose of this article is to describe one of the types of power systems presently under consideration to support the future configuration of a Deep Space Station. One of the requirements planned for the post-1972 period includes the capability for a high-power transmitter at a 210-ft-antenna Deep Space Station.

b. Anticipated power requirements. Anticipated power requirements (Table 2) are based on all of the loads now existing at the Goldstone 210-ft-antenna Mars Station, plus an operational high-power transmitter. The following is a tabulation of these loads listed by type of required power reliability:

(1) E-bus—electronic equipment; distortion-free; uninterruptible no-break power; mission loads.

Table 2. Required power loads

Load	E-bus power, kW	U-bus power, kW	U-bus (15 min) power, kW	U-bus (24 h) power, kW
Operations bldg.	350	—	200	100
Antenna bldg.	175	1800	200	50
High-power transmitter	—	4000	—	—
Power plant	—	200	—	50
Laboratory bldg.	25	—	—	250
Pump house	—	100	—	—
Area lighting	—	—	—	50
Communications	25	—	—	—
Total	**575**	**6100**	**400**	**500**

Total station load: 7575 kW.
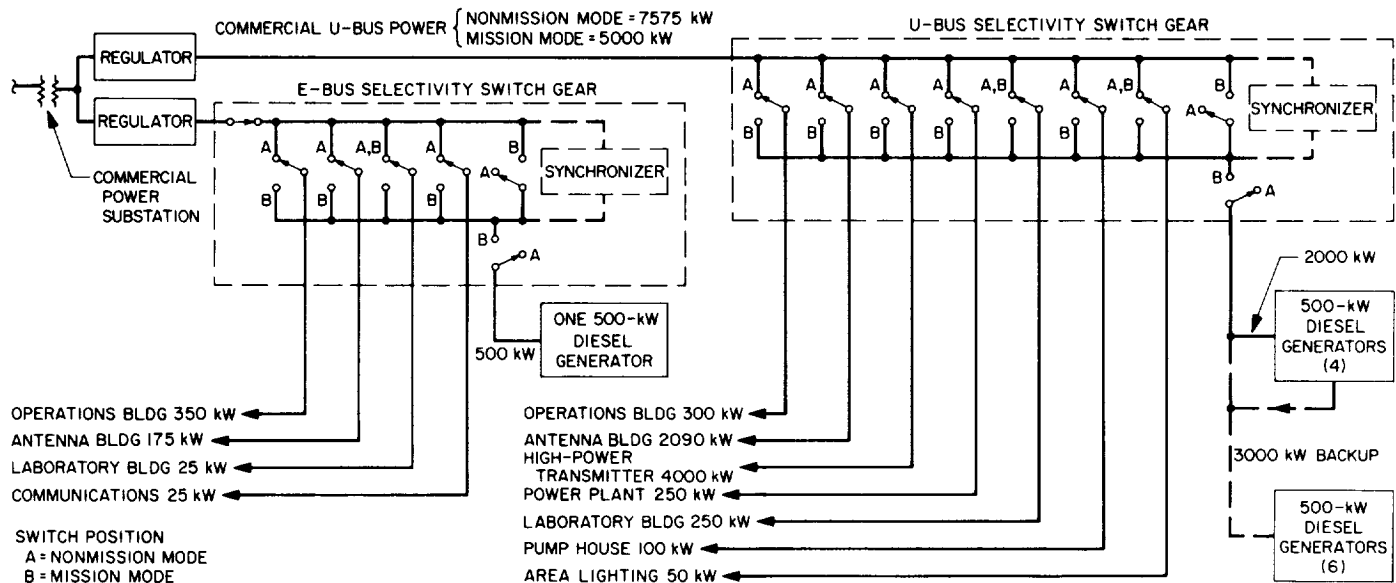Assumed station demand load: 5000 kW.

Fig. 9. One type of power system for mission and nonmission modes

(2) U-bus—bulk-type motor equipment; limited surges permitted; uninterruptible no-break power; mission loads.

(3) U-bus (15 min)—bulk-type motor equipment; limited surges and maximum 15-min downtime permitted; mission loads.

(4) U-bus (24 h)—bulk-type motor equipment; limited surges and downtime in excess of 24 h permitted; nonmission housekeeping loads.

c. Commercial power service. The type of power system under consideration by this report includes the availability of a commercial power service at the station. This commercial power service is derived from the local utility power company and has been integrated with the station's 60-Hz generated power service by means of a feeder selectivity switchgear-distribution network. The two main advantages of an integrated commerical power service are:

(1) Cost is approximately one-eighth that of local generated power.

(2) A separate power source for an emergency back-up service is available.

d. Power system. A type of power system now under consideration is shown in Fig. 9 for nonmission and mission modes.

2. SFOF Uninterruptible Power System, J. G. Grosch

a. Introduction. The SFOF uninterruptible power system described in SPS 37-50, Vol. II, p. 189, is now scheduled for incremental implementation, although the original plan was to secure the system through a single contract. The change in implementation plan results from re-evaluation of the following criteria:

(1) Mission operations plans.

(2) Supporting facilities approval cycles.

(3) Criticality of equipment need as related to mission schedules.

(4) Availability of the SFOF building systems for modification and installation based upon mission related "freeze" periods.

(5) Definition of optimum equipment increments with relation to cost.

b. System installation. At present the uninterruptible power system installation is considered to be the first phase in a three-phase medium-range plan to modernize the SFOF power distribution system and to provide full protection against power anomalies of both minute and extended duration.

The second and third phases will include the following:

Phase II. Construction of an underground power building adjacent to the SFOF, which will house the generating

equipment and facility monitoring system equipment. This phase is anticipated for completion in FY 1969.

Phase III. This final phase will constitute the modernization and upgrading of the building power distribution system and will include the removal of the existing government-owned and leased power generating equipment. This final phase is expected to be completed in FY 1970.

Phase I is to be implemented in four stages:

(1) Installation of a solid-state conversion system.

(2) Provision of an additional battery bank to supplement the existing battery equipment and to provide full capacity for the system.

(3) Procurement of two 1350-kW engine generators for eventual installation in the power building.

(4) The inclusion of the facility central supervisory monitor and control system. This system will provide for central and remote control of all building support systems, such as power, air-conditioning, safety, etc., and will be designed to give warning of impending deterioration of these systems.

Stages (1) and (2) are being implemented; stage (3) is being initiated; and stage (4) is in design.

3. Echo DSS Antenna Mechanical Upgrade Progress, R. McKee

a. Introduction. Modifications of the Echo DSS 85-ft antenna began on February 19, 1968; the completion of structural modifications is scheduled for May 31, with an additional 2 weeks for setting new surface panels.

The purpose of the modifications is (1) to bring the antenna structures up to specification, (2) to increase the structural integrity by high-strength bearing bolting and adding stiffening members to existing steel, and (3) to install the new counterweight assemblies, cable wrapups, high-performance S-band surface panels, and the upper and lower electronics rooms, which will house the transmitter and receiver equipment.

b. Progress to date. The old hour-angle drives have been removed by means of a ramp erected under the antenna pedestal, and new drives have been installed on a new drive support structure. Machinery on the new drives is identical to the machinery removed; however, the main gear boxes on the new drive skids have been

positioned opposite the location on the old drives. This allows the drive pinion to be placed closer to the center of the structure and, with the addition of a three-tooth gear segment at both the east and west ends of the hour angle wheel, will allow the travel of the hour-angle wheel to be increased from ±90 to ±96° from the zenith position.

A typical example of structural changes being made in the antenna pedestal is shown in Fig. 10.

Fig. 10. Structural change in antenna pedestal

The hour-angle wheel has been modified in the yoke area by installing heavier members and filler plates and by welding stiffener plates to the inside edge of the flange (Fig. 11).

The declination drives have been removed to allow replacement of the outrigger supports and support plates for the new declination drives (Fig. 12).

In addition to the new structural members being added to this antenna, all structural connections in the pedestal, hour-angle wheel and declination wheel are being re-bolted, using high-strength bearing bolts. These bolts have a serrated body and must be driven into the holes by means of pneumatic tools or sledge hammers. Hardened washers and heavy hex self-locking nuts complete the fastener assembly. This method of bolting places all fasteners in shear and ensures restriction of movement in the connections and increased structural integrity.
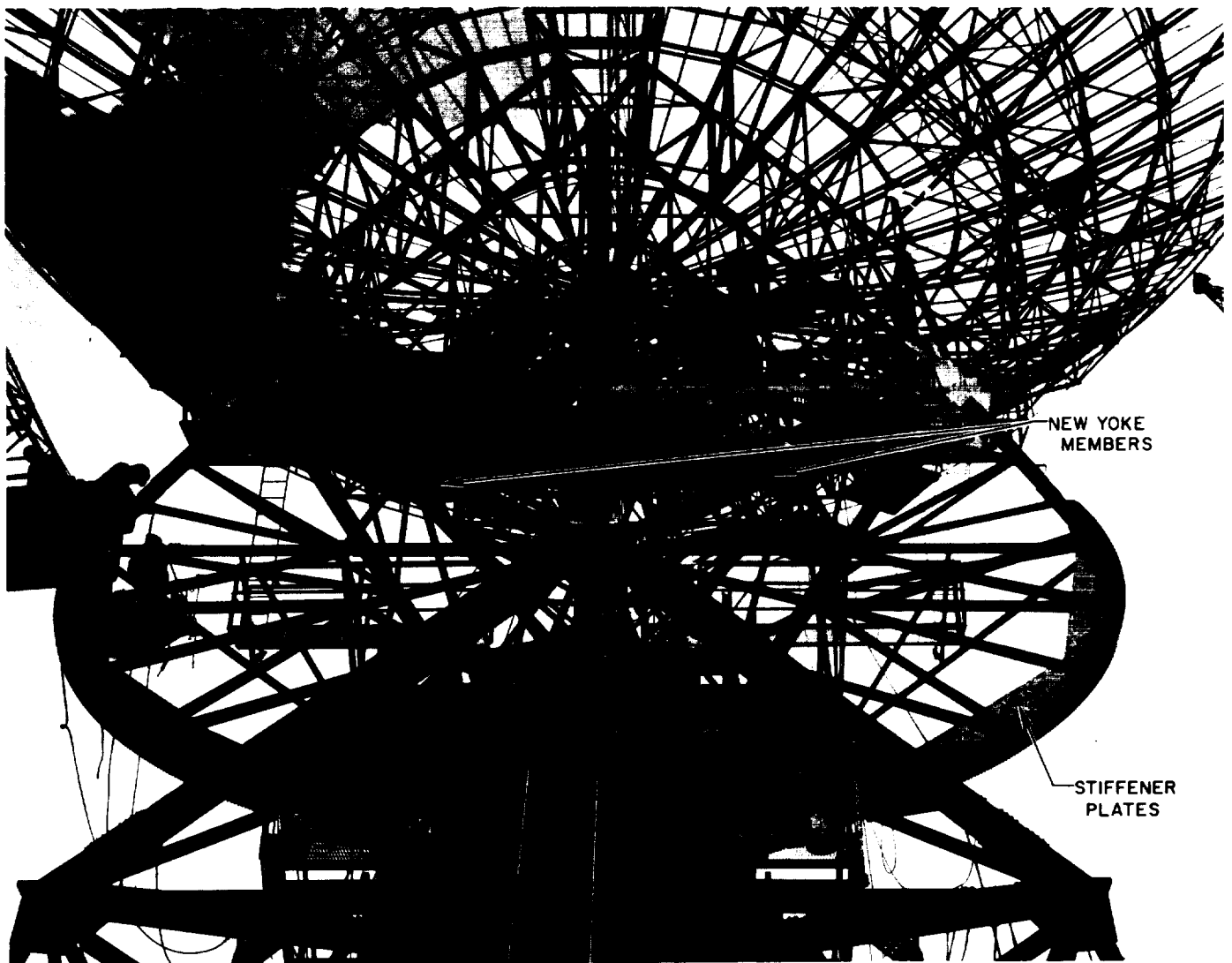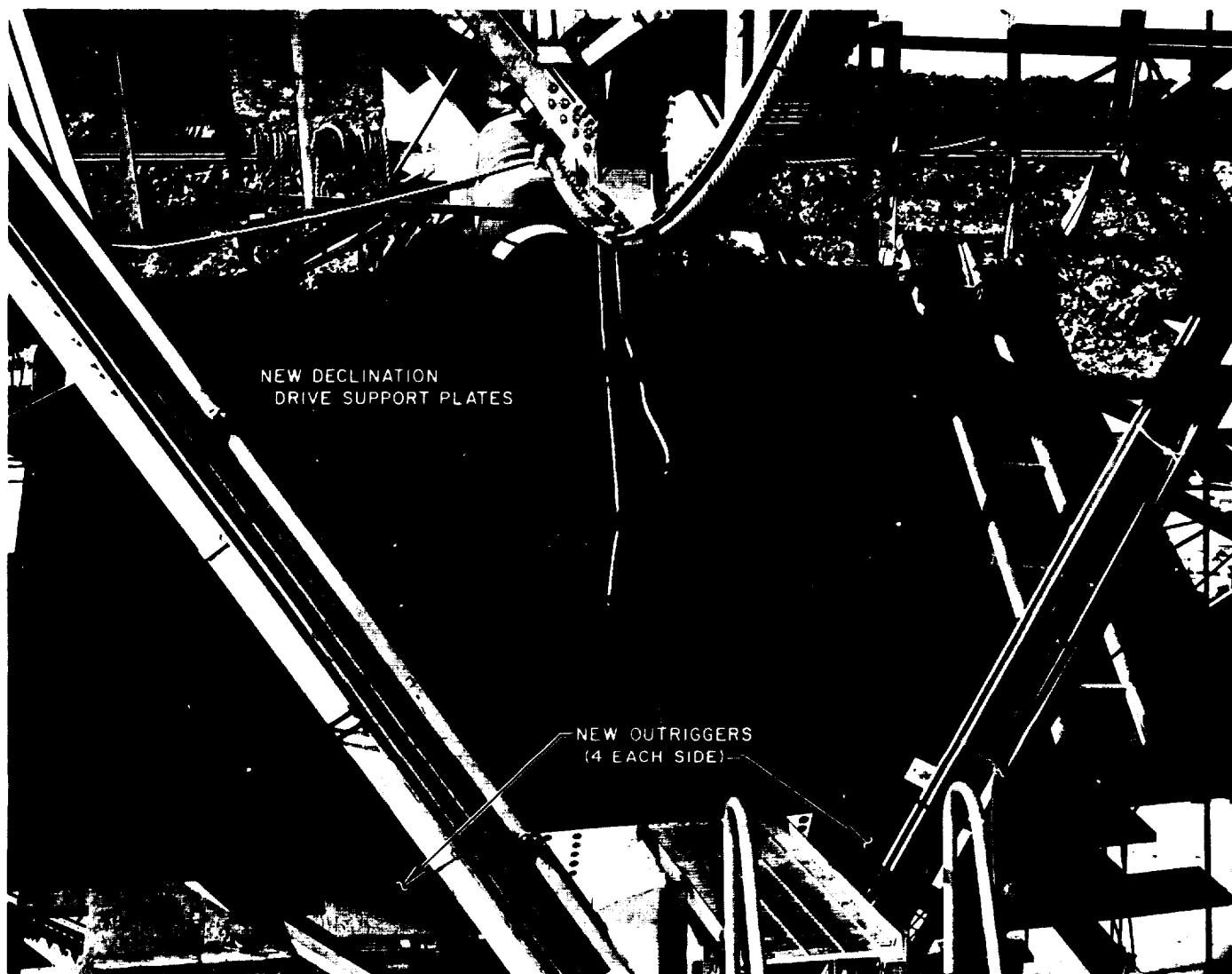
Fig. 11. New yoke members and stiffener plates

Fig. 12. New declination drive support plates and outriggers

4. Woomera DSS Antenna Mechanical Upgrade Progress, M. Kron

The upgrade installation program of the Woomera DSS was initiated in the early part of the calendar year 1965 in order to bring the operational characteristics of the three-legged polar-mounted antennas up to that of the newer four-legged mounts presently installed at the Tidbinbilla, Robledo, and Cebreros DSSs. Figure 13 shows the antenna structure and cable runs as they existed on March 4, 1968, before new components were installed.

In order to accomplish this upgrading, a step-by-step investigation was performed on the antenna structural components and methods of joint fastening to determine the optimum joint design and section properties modifications possible with an existing structure.

The criteria used in reviewing the existing design was a comparison of computer and hand analyses of the

Fig. 13. Antenna structure and cable runs before reinforcing

similar structural components on the newer four-legged mount design. Additional structural steel was added or new members replaced existing members in the pedestal, polar wheel, yoke, etc. In addition to the basic design changes that were made, new drive skids were designed in order to increase the present hour-angle travel by approximately 6 deg. This was accomplished by reversing the main drive reducers to bring the drive pinions closer to each other and then adding a gear segment on both the east and west side of the polar wheel.

The hour-angle drive skid removal ramp was designed to allow the unbolted drive skids to slide down its ways after unbolting. All walkways and platforms have been removed from the drive skid area and replaced with wider ones, which allow greater accessibility around the drive skid areas for maintenance purposes and improve safety conditions.

Figure 14 shows the completed installation of the reinforcing members that were added to the pedestal structure.

5. Venus DSS 400-kW Transmitter Electronics Room Modifications, V. B. Lobb

a. Introduction. In SPS 37-46, Vol. III, p. 145 and SPS 37-49, Vol. II, p. 145, the design study, final design, fabrication, and premodification support work required for the transmitter electronics room were reported. Since then, work has been completed on the Venus DSS modication, as follows:

(1) Installation of new elevation bearings.

(2) Modification of the integral reflector supporting structure.

(3) Installation of the electronics room.

(4) Installation of the counterweight structure and counterweight.

(5) Installation of transmitter for deflection measurements.

(6) Painting of the 85-ft antenna.

b. Elevation bearings. The new bearing has a 312,000-lb static capacity, which is three times the load capacity of the original bearing. Its housing, saddle, and weldments were tripled in stiffness. Both of these factors caused a considerable increase in its size and, likewise, its difficulty in placing. After bearing installation, the elevation axis alignment was checked and found to be aligned to 22 sec of arc.
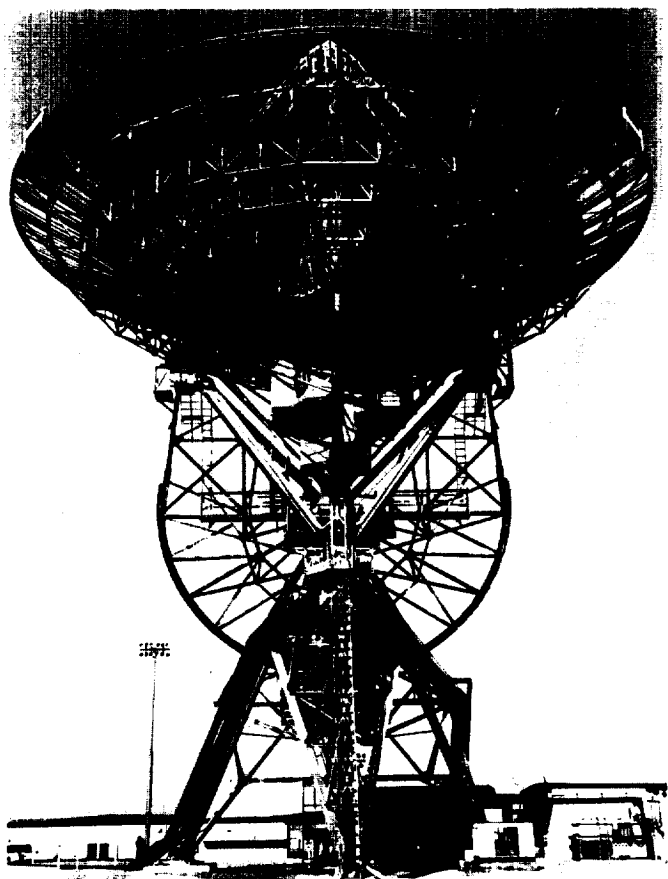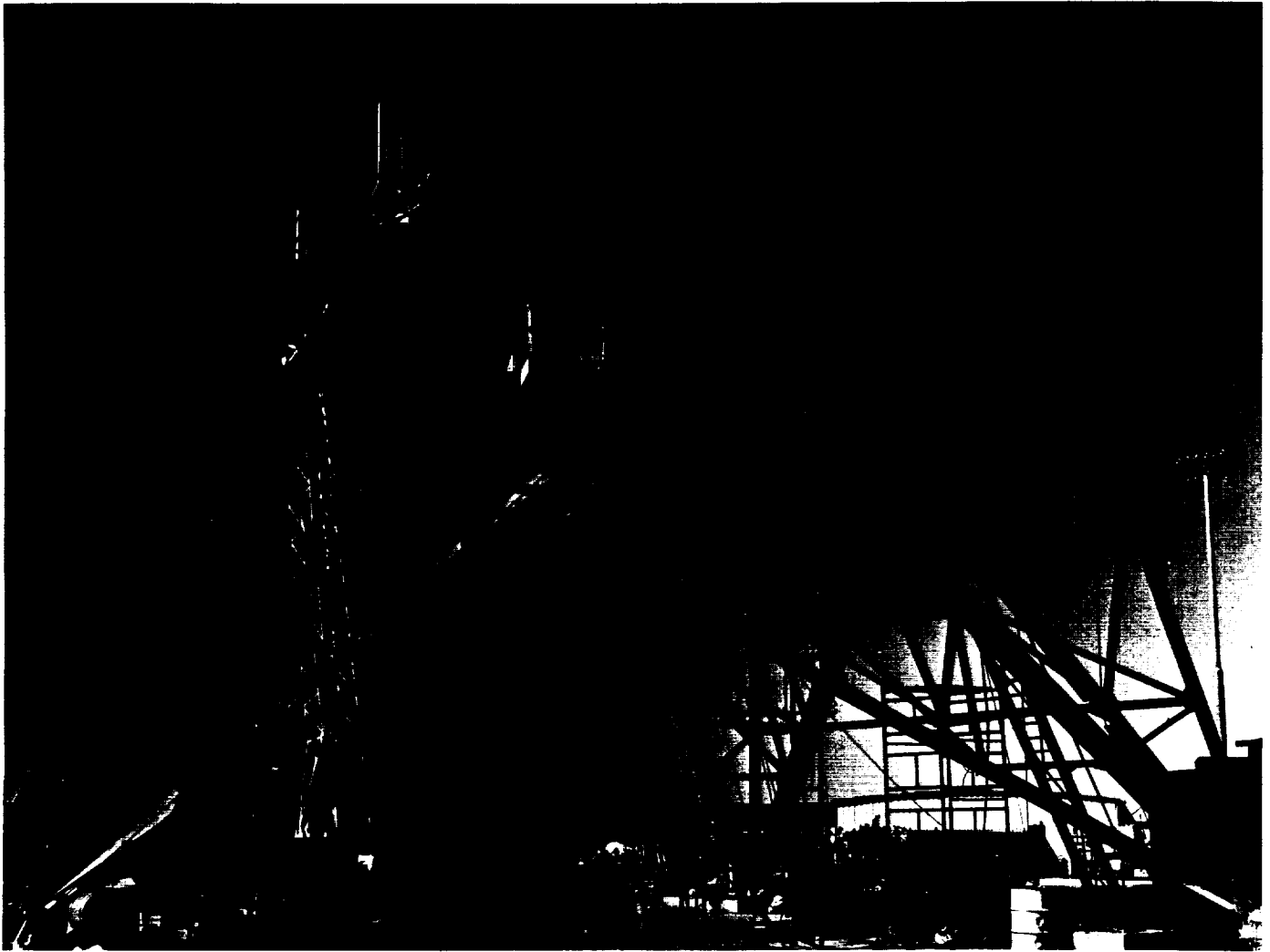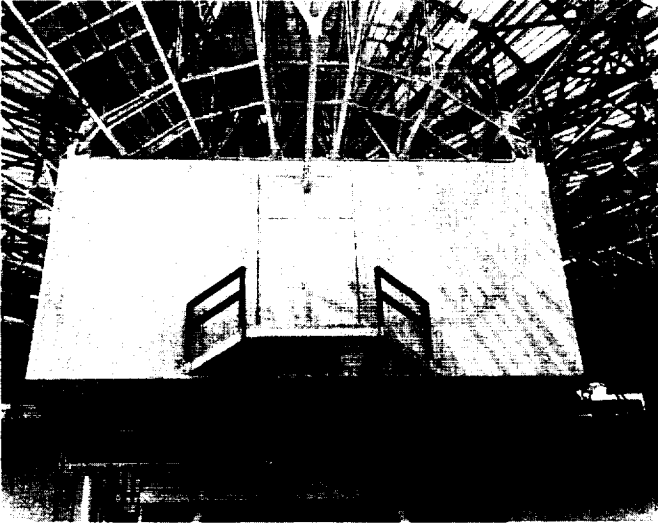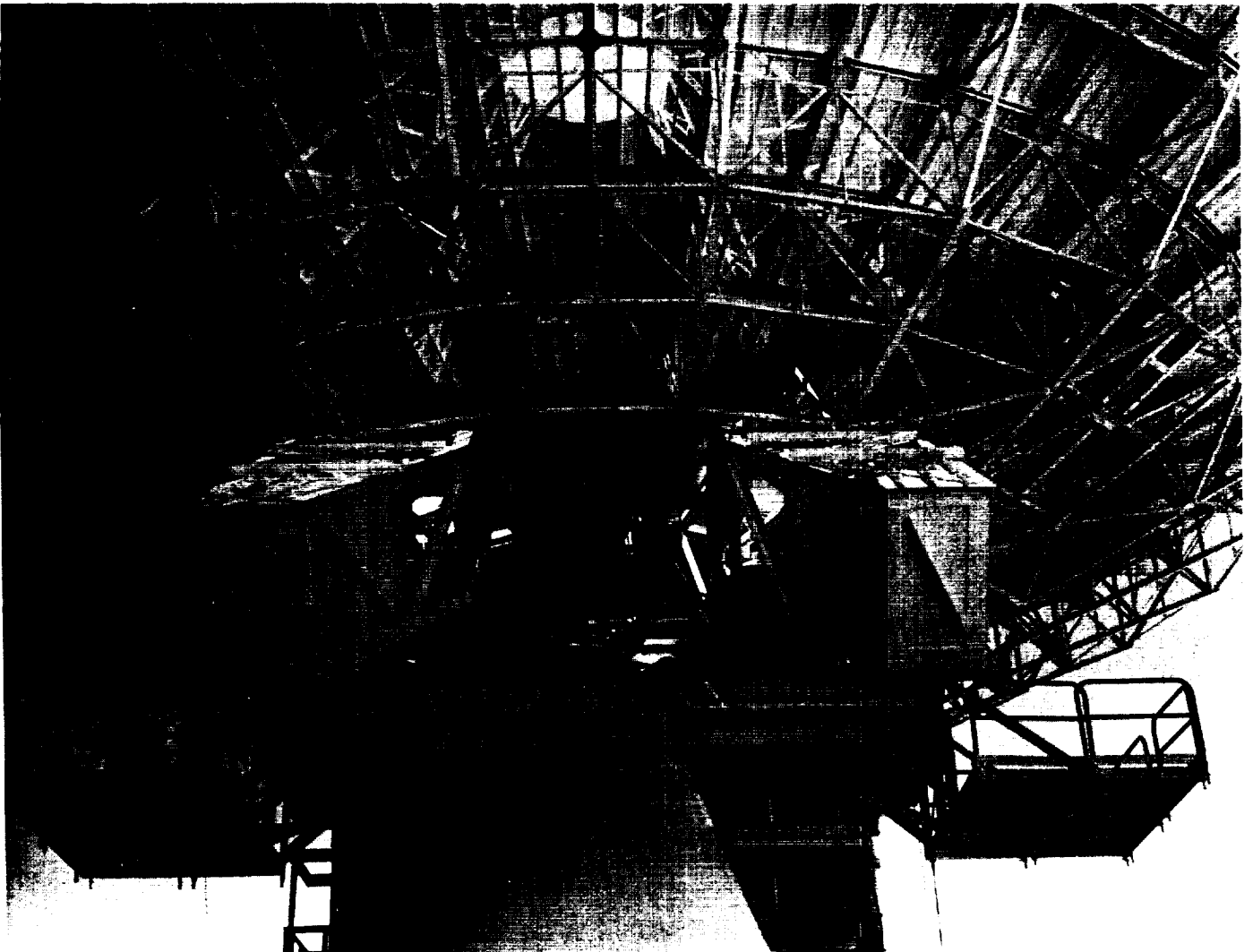
Fig. 14. Reinforcing members added to pedestal

Fig. 15. Venus DSS electronics room

Fig. 16. Counterweight structure

c. Integral reflector supporting structure (square girder). The square girder, which is part of the reflector structure and its supporting structure, had to have material added to its members to increase their section area and stiffness. This was necessary to enable the antenna to retain its parabolic shape after the addition of the room and its equipment. The area of the members of the side truss of the girder (elevation bearing to overhang of the ball-jack screws) was tripled, while the area of the members of the connecting truss between elevation bearings was doubled. To do this, plates from the size of 17 in. wide by 1⅝ in. thick to 4 in. wide by ¼ in. thick were used. The final design computer studies indicate a surface deviation of 0.0276 in. rms at horizon and 0.0277 in. rms at zenith when the surface is set to a perfect parabola at 40-deg elevation. The added material and setting angle not only have maintained the original parabola but have improved its rms surface deviation.

d. Electronics room. The room structure arrived on site as one welded unit (Fig. 15). It was sided with insulated metal panels on all sides except for the surface on the ground. The room is attached at four points to the reflector square girder structure. After installation, the last side was sheeted and the 2-ton, three-way hoist was installed in the room. The hoist has the normal controls, but in addition, it has inching controls to allow it to handle and place the costly klystron tube to within a fraction of an inch.

e. Counterweights. The counterweight structures (Fig. 16) were delivered 90% complete, on a special truck, requiring very little field assembly. Only minor field modifications to the reflector structure were required to accommodate the counterweight structure. The counterweight material is part steel and part lead. This combination was utilized in order to make use of the old steel counterweight material.

f. Transmitter measurement. The transmitter and klystron were placed in the electronics room to check the deflection of the klystron window relative to the cabinet when the antenna is moved from horizon to zenith. The deflections were well within the required tolerances. A special adjustable lifting fixture was fabricated to allow for small height clearance between the hoist and the cabinet and to compensate for the change in the cabinet center of gravity with the klystron not in place.

g. Painting. The 85-ft antenna was painted after all the major modifications were completed. Steel primer, regular and unorganic zinc, were used after sand-blasting and cleaning the structure, and a white semigloss paint was used as a finish coating to reduce thermal effects.

6. Construction Progress at Goldstone DSCC,
W. W. Lord and B. M. Sweetser

a. Water and sewer project. Essentially all construction has been completed on the new water supply and sewage disposal system at the Goldstone DSCC.

Water is pumped from the one-million-gallon Fort Irwin reservoir (Fig. 17b) to reservoirs at the Venus, Echo, Pioneer, and Mars DSSs and the Apollo-STADAN Station. Each of these reservoirs has a capacity of 177,000 gal. Water from these reservoirs is distributed to the use areas by gravity. The Echo DSS reservoir (Fig. 17e) is typical of the installations at each station.

The sewage disposal systems vary from station to station, consisting generally of added septic tank capacity and improved provisions for effluent disposal. Oxidation ponds were constructed at Echo, Pioneer, and Mars DSSs. Representative of these installations are the oxidation ponds at Echo DSS (Fig. 17f).

b. Construction projects. Building projects recently completed are:

(1) A 3200-ft² addition to laboratory building G-18 at Pioneer DSS (Fig. 17d).

(2) A 3200-ft² addition to communications building G-33, at Echo DSS (Fig. 17a).

(3) A 5000-ft² addition to building G-38 for a standards laboratory at Echo DSS (Fig. 17c).

(4) A new security building G-43 at Echo DSS (Fig. 17h).

Other projects in progress are:

(1) Upgrade of collimation tower access road at Pioneer DSS.

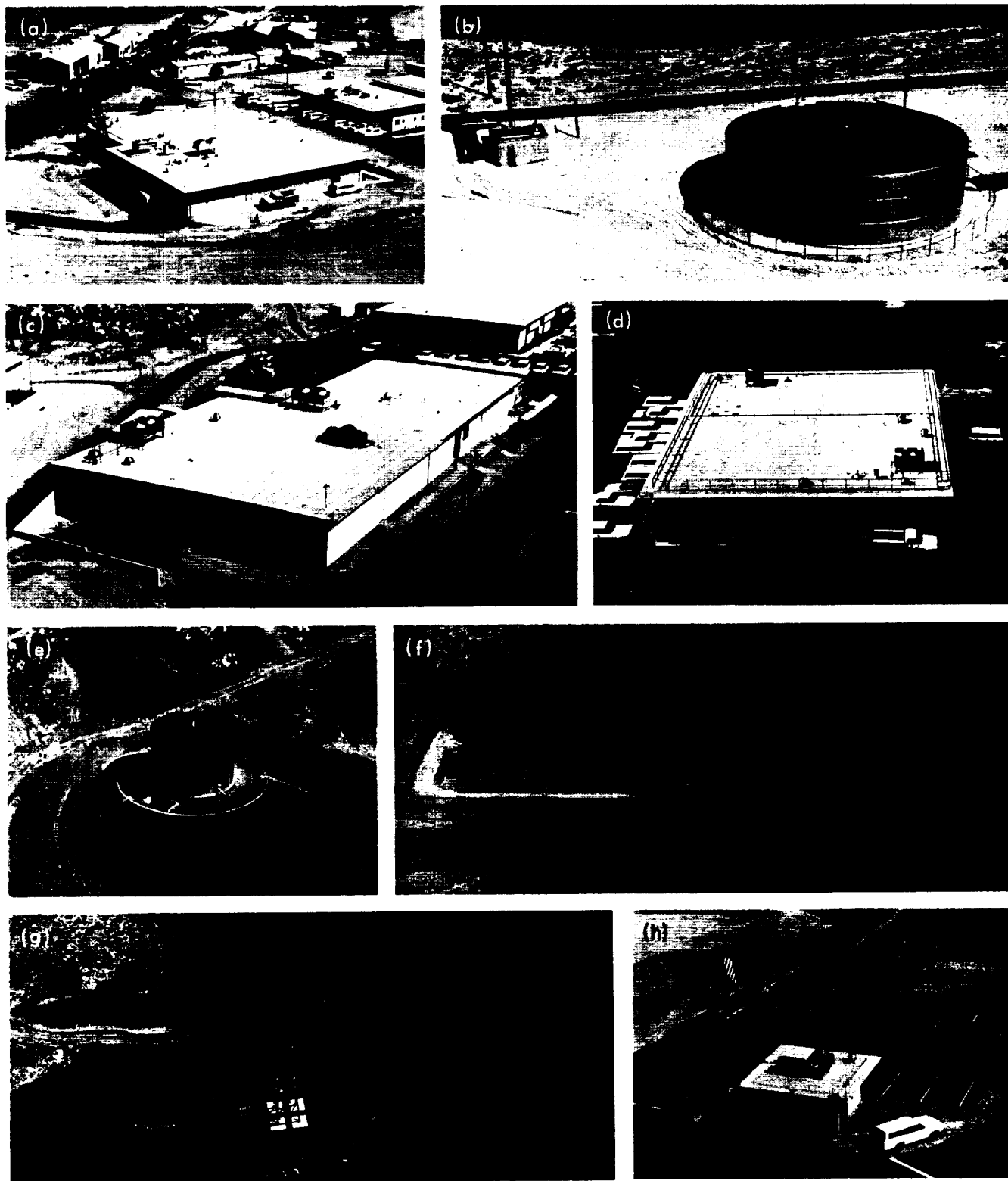(2) Upgrade of collimation tower access road at Venus DSS (Fig. 17g).

Fig. 17. Recent installations at Goldstone DSCC: (a) Echo DSS communication bldg, (b) pump house and reservoir at Fort Irwin, (c) standards laboratory at Echo DSS, (d) laboratory bldg at Pioneer DSS, (e) Echo DSS reservoir, (f) sewage oxidation ponds at Echo DSS, (g) Venus DSS collimation tower road, (h) security control bldg at Echo DSS